SUSPENSION AND CONTROL FOR INTERFEROMETRIC GRAVITATIONAL WAVE DETECTORS

Matthew Edward Husman

Department of Physics and Astronomy,
University of Glasgow.

PRESENTED AS A THESIS FOR THE DEGREE OF PH.D.,
UNIVERSITY OF GLASGOW.

February 2000

ProQuest LLC.
789 East Eisenhower Parkway
P.O. Box 1346
Ann Arbor, MI 48106 – 1346

Acknowledgements

Coming to Glasgow to work on my Ph.D. was one of the most important opportunities I have ever had. I will always be grateful to Professor Jim Hough for the chance. While I know that under his guidance I have learned a great deal about the technical details that follow, I can only hope that I have absorbed a fraction of his knowledge about how to lead a successful team effort. (Newly minted) Professor Norna Robertson has always been there, whether for daily guidance, to act as a sounding board, or even to share experiences in changing cultures.

Mike Plissi and Calum Torrie had been working on suspensions for GEO 600 long before I ever arrived in Glasgow. I count myself fortunate to have been able to work with the two of them on a day to day basis. I think that we all taught each other a great deal and not just about suspension design. These two most helped the culture shock of an ignorant American.

Calum also deserves an additional special mention; sports have always been a major extracurricular interest of mine, and Calum helped teach me Scottish sports.

Everyone in the gravity wave group (past and present) went far out of their way to make me feel welcome. I cannot even begin to cite specifics. The waiting at the emergency room, the daily assistance, the patience, all are well remembered. A huge thanks goes to Paul McNamara, Sharon Twyford, David Clubley, David Palmer, Morag Casey, Geppo Cagnoli, David Robertson, Sheila Rowan, Ken Skeldon, Harry Ward, Ken Strain, Gavin Newton, Steven McIntosh, Peter Sneddon, Bryan Barr, Colin Craig, Allan Latta, and particularly Miss Catherine Macintyre. Of course, Allan deserves the most credit, having put up with sharing an office with me.

I learned a great deal during the portion of my graduate career at Stanford University. Professor Byer has led the gravity wave group and his group taught me the basics of gravity waves. Professor Dan DeBra taught me everything about mechanical design, control, systems engineering, and helped give me the tools to do

this thesis. At Stanford, Eric Gustafson deserves more thanks than he will ever get, and he deserves that thanks from everyone at Stanford. While there is a large group at Stanford as well, I'll particularly express my gratitude to Matthew Lawrence and Bob Shine.

I would like to thank PPARC for the financial support of the gravitational wave research in Glasgow. I would also like to thank Stanford University and the National Science Foundation for supporting me during the period of my research at Stanford University.

While in Glasgow, I have been privileged to spend a year with Jinty McGinty's Glasgow Irish Volleyball Club. I cannot claim that my volleyball was as productive as my research, but it made a welcome physical release. I thank all of the members of the club, especially Andy Thomson and Tam Kerr, for making my wife and me feel so welcome.

There is an additional particular thanks due to Dr. Norna Robertson. I have always felt that communication is extremely important. The greatest ideas in the world have no value if they cannot be explained and then used. Norna is the person most responsible for making sure that in this thesis I clearly say what I intend...mean what I...write...exactly what...for making this thesis readable.

I wish to thank all the family and friends that have helped make me who I am today. I am lucky enough that there are way too many to name them all individually. More than anyone else, I give a big thanks to Mom and Dad. My parents have always allowed me the freedom to find my own way and the support to succeed in doing so. We've almost reached one more hurdle.

Most of all, thanks to my wife, Laura, without whom none of this would have happened at all.

—MEH

Preface

This thesis describes work towards the design of the suspension of the main optical components in the GEO 600 interferometric gravitational wave detector. The focus of the work is the development and application of the pendulum model which is described in detail in chapter 3. Discussions of aspects of the dynamics, the thermal noise performance, and the control of the suspension constitute the subsequent chapters.

Chapter 1 gives a brief introduction to the concept of gravitational waves and their detection. It consists entirely of material from the literature.

Some of the issues in the design of the suspensions for interferometric gravitational wave detectors are described in chapter 2. While there is no inherently original material, it provides the author's interpretations of concepts in the literature.

Chapter 3 explains the theory behind the Lagrangian model of a pendulum suspension written entirely by the author, and also serves as a "user's manual" for the Maple code *Lagran.mws*. The code (a listing of which is in appendix A) is used to draw many of the conclusions in the following chapters.

The dynamic consequences of the pendulum design are considered in chapter 4. Section 4.1 describes the crucial steps in verifying both the Lagrangian model of the author and the force model developed by Dr. Calum Torrie. This work was done by the authors of the two independently developed models in conjunction with Dr. Norna Robertson and is due to be published[1]. The two models proved to be complementary. The Lagrangian model was a more comprehensive analysis tool at the expense of computational complexity. A particular application of the Lagrangian code was the proper inclusion of the cantilever blades. The design of the blades was done with Drs. Mike Plissi, Calum Torrie, and Norna Robertson and is discussed in section 4.2.

The Lagrangian model allows the proper effects of tilt modes and of multiple

stages of pendulums on the level of thermal noise at the mirror to be evaluated. These calculations are covered in chapter 5. The proper method for inclusion of loss (section 5.1) was verified with Dr. Geppo Cagnoli and Prof. J. Hough. The evaluation of noise observed in a suspension as a function of the length of suspension wires covered in section 5.2 was evaluated with Prof. J. Hough.

Chapter 6 describes the design implications for control of the pendulum. The damping of the pendulum resonances, called "local control" and covered in section 6.2, was done in conjunction with Drs. Calum Torrie and Ken Strain. The discussion of higher bandwidth control to be used in cavity locking, named "global control", which includes the modelling of the internal modes of the wires to allow split feedback, results from work with Prof. Jim Hough and Dr. Norna Robertson. The work on cavity fields was done at Stanford University and describes a subset of the work done with Matthew Lawrence et. al.[2].

Chapter 7 summarizes the mechanical parameters of the suspension designed by the suspension working group in Glasgow, based in part on the work in the preceding chapters. The final chapter briefly introduces possible extensions of this work suggested by the author following discussions with Prof. Jim Hough and Dr. Norna Robertson.

Appendix A is the Maple code for the modelling program described in chapter 3. Appendix B is the code used to investigate the centre–of–percussion issues in the cantilever blades which was then incorporated in the main code of appendix A. They are both the work of the author.

Summary

The detection of gravitational radiation is one of the most exciting current endeavours in experimental physics. One method of sensing gravitational waves from astronomical events is to use an interferometer to detect the perturbations in the distance between inertially free masses. This thesis describes some of the work involved in the design of the mechanical suspensions in the UK/German GEO 600 interferometric detector.

The weak interactions between gravitational waves and matter results in very small signal. For detectors on Earth, great care must be taken to reduce the displacement noise of the mirrors of the interferometer. Specifically, these mirrors must be isolated from the seismic motion of the ground and suspended in such a manner that the unavoidable Brownian motion does not exceed the size of the signals to be measured.

In order to predict the performance of a candidate suspension, a computer model of a multiple–stage pendulum has been developed, based on a Lagrangian formulation. This model includes sufficient detail to predict the dynamic and thermal noise performance of the pendulum. The code uses a minimum of assumptions, allowing asymmetric suspensions or suspensions with limited degree of freedom to be analyzed. This feature allows the model to be used to test the robustness of a pendulum design against perturbations in the mechanical parameters which may occur during construction. The model has specifically been designed to include the effect of blade springs which can be used to achieve the necessary additional vertical vibration isolation not provided by a simple wire pendulum.

The predictions of the code have been compared to the results of a force model, written by Dr. Calum Torrie, and to experimental results for a single stage wire pendulum and for a triple stage pendulum using two sets of cantilevers. These comparisons confirm the validity of the Lagrangian model. The Lagrangian code

was then extended to provide a more detailed analysis of the suspension system. This included the proper performance of the blade springs, which has been analyzed and interpreted in terms of the centre of percussion of the springs. Additionally, the code has been used to analyze the cross–coupling between input vertical motion and resulting horizontal output motion due to small imperfections in the pendulum construction. This analysis confirms that the GEO 600 assumption that the cross–coupling would not exceed 0.1% is appropriate. Taking into account this factor, it is predicted that the amount of transmitted seismic noise which will be observed at 50 Hz, the low frequency corner of the detection band, in the measured direction is $2.4 \times 10^{-20}\mathrm{m}/\sqrt{\mathrm{Hz}}$. This is approximately a factor of 3 below the dominant noise at that frequency, the internal thermal noise of the test mass, which is expected to be $7 \times 10^{-20}\mathrm{m}/\sqrt{\mathrm{Hz}}$. This seismic noise is dominated above $\sim$10 Hz by the vertical noise coupling to the measurement direction.

The Lagrangian model has also been used to predict the design of suspension which will result in the lowest pendulum thermal noise. Specifically, a suspension which uses two wires to suspend the optic, one wire in front of the other, has been compared to a four wire suspension equivalent to two loops of wire. This confirms that the four wire suspension is the best choice for GEO 600. The model is also used to compare more general cases, including other suspension geometries which are not suitable for use in the GEO 600 control scheme. The modelling code also allows the full pendulum thermal noise of the triple pendulum observed in the sensed direction at 50 Hz to be predicted at a level of $1.4 \times 10^{-20}\mathrm{m}/\sqrt{\mathrm{Hz}}$.

The thermal noise is reduced away from the resonant frequencies of the pendulum, the reductions being larger the higher the Q of the resonance. These resonant peaks cause unwanted amplification of low frequency motion. The amplitude of these peaks is reduced by application of electronic feedback control. This "local control" must damp the resonances without adding additional noise within the operating frequency band of the system. The successful performance of this local controller has been demonstrated in all degrees of freedom.

Additional modelling has been done to examine other control problems associated with interferometric gravitational wave detection. While the local control can be relatively low bandwidth ($\sim$5 Hz), the "global control" used to maintain the entire interferometer on a dark fringe may require substantially higher bandwidth.

A standing wave model of a wire pendulum has been developed to examine the possiblity of using higher bandwidth actuation in a non–collocated fashion. While this model does not have all the details of the full multi–stage pendulum model, it allows more accurate prediction of performance in the presence of the internal modes of the suspension wires (the 'violin modes'). Finally, one additional question is considered, namely the suitability of the standard RF error signal for locking a resonant optical cavity which has long optical storage times. A model of the cavity fields in a Fabry–Perot cavity which expands upon the standard error signal to include the effects of a moving end mirror has been experimentally verified. This model may be useful in designing a more robust locking algorithm.

In conclusion, the design of the main suspension for GEO 600 has been verified, the parameters of which are presented in this thesis.

Contents

List of Tables

List of Figures

Chapter 1

The Detection of Gravitational Waves

1.1 General Relativity: Gravitational Waves

In the General Theory of Relativity, Einstein[3] proposed that the effects of gravity propagate with a finite velocity. The consequence of this is that, in the weak field limit and far from any source, the solution to the linearized field equations is that of a wave which propagates at the speed of light.

Hulse and Taylor[4] were awarded the Nobel Prize for Physics in 1993 for their discovery of the binary pulsar 1913+16 and subsequent observations of its orbit. The orbital period of this pulsar has been decreasing; from the measurements of this orbit, Taylor[5] calculated the rate at which orbital energy should be lost via gravitational radiation as predicted by General Relativity. From this rate of loss, he calculated the associated rate of orbital inspiral, which agrees with the observed data.

This provided compelling indirect evidence of gravitational waves, but the direct detection of a gravity wave remains one of the most challenging goals of experimental physics. A number of large scale projects around the world are currently working to make this direct observation possible. Their success and further study of these gravity waves will allow some of the predictions of General Relativity to be tested, including the speed of propagation and polarization of the waves. This, in turn, allows the rest mass and the spin of the graviton to be deduced. In addition, every

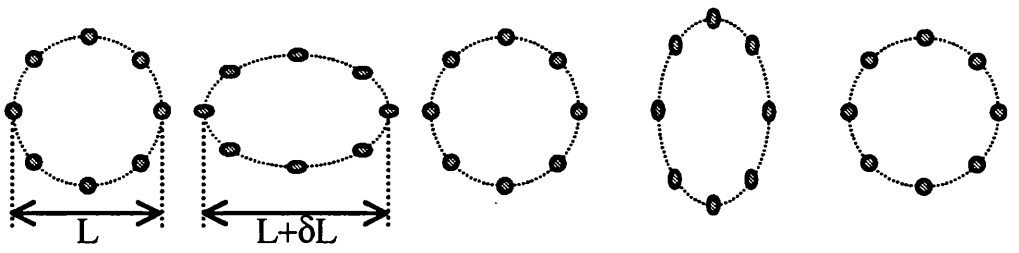

Figure 1.1: Effect of a gravitational wave on a ring of test particles

new 'window' on the universe, which in the past has meant different wavelengths of the electromagnetic spectrum such as X–rays and radio waves, has generated unexpected information about the universe. Beyond the new information about astrophysical events, such as the collapse of stars and the interactions of black holes, which gravity waves will certainly provide, it is possible that even more interesting will be the unanticipated results.

1.1.1 Gravitational Waves

It is informative to draw some analogies between the more familiar electromagnetic radiation and gravitational radiation. In the same fashion that acceleration of charges produce electromagnetic waves, the acceleration of mass produces gravitational waves. For an isolated system, there can be no change in total charge; from this, there can be no electromagnetic monopole radiation. Similarly, the conservation of energy (and thus mass) implies that there can be no monopole gravitational radiation. A particle can have a positive or a negative charge, allowing dipole electromagnetic radiation. Since there can be only positive mass, and due to the conservation of linear and angular momentum, there can be no change in the gravitational dipole moment. Therefore the lowest order moment of gravitational radiation posssible results from a quadrupole distribution of mass. Therefore, only non–axisymmetric accelerations of mass distributions will generate gravitational waves.

Gravitational waves produce a ripple in the curvature of space–time. For an observer on the Earth, these strains would appear as small tidal forces between objects. For a circular ring of test particles, free in inertial space, the effect of a wave travelling perpendicular to the plane of the particles is shown in figure 1.1. During one half period of the gravitational wave, the ring is effectively stretched along one

axis while simultaneously compressed along the perpendicular axis. During the other half of the cycle, the effects are reversed. The amplitude of the wave is equivalent to the strain in space that it produces, h, defined as

$$h = \frac{2\,\delta L}{L} \tag{1.1}$$

as illustrated in figure 1.1. The wave may be expressed in the basis of two linearly independent polarizations. The figure represents the h_+ polarization; the second polarization, named $h_\times$, causes the maximum displacements in the ring of particles to be rotated 45° from that shown in the figure.

1.1.2 Sources

Because gravity is the weakest of the four fundamental forces of nature, generating a 'large' gravitational wave requires extremely large masses accelerating very quickly. The only sources which will generate detectable waves are astronomical. A few candidate sources are described below, with paticular emphasis on those sources which might generate waves in a frequency band detectable by Earth based detectors (above ~10 Hz).

Burst Sources

Sources which emit a few cycles of gravitational radiation at a characteristic frequency are called 'burst' sources. These typically are cataclysmic events in the universe, such as supernova or coalescing binary stars.

Supernovae The stellar explosions called supernovae are classified as either Type I or Type II. A Type I supernovae is thought to occur in a binary system of low mass stars, such as white dwarfs. There are two forms of Type I supernova[6]; the first type is when the larger white dwarf, by accreting mass from its companion, reaches the Chandrasekhar mass limit (where $M_{Ch} = 1.4M_\odot \approx 3\times10^{30}$ kg, and $M_\odot$ represents 1 solar mass). The subsequent collapse and detonation of the larger white dwarf is not expected to generate a significant amount of gravitational radiation. If, however, the two white dwarfs in a binary system are close together and the total mass exceeds the Chandrasekhar mass, the two stars will merge. The resulting stellar object is

highly deformed due to its increased mass and angular momentum. It will collapse asymmetrically with a strong emission of gravitational waves.

A Type II supernova is thought to occur when the iron core of a massive ($\gtrsim 8\ M_\odot$) star collapses into a neutron star or, if the initial mass is large enough, a black hole, again triggering a stellar explosion. If this collapse is asymmetric, due to a significant amount of angular momentum in the stellar core, a strong burst of gravitational radiation will result.

The physics of a supernova event is complicated, making a detailed estimation of the strength of a gravitational wave difficult. Schutz[7] approximates the strain amplitude that might be expected from such an event as

$$h \approx 5 \times 10^{-22} \left(\frac{E}{10^{-3} M_\odot c^2}\right)^{\frac{1}{2}} \left(\frac{15\,\mathrm{Mpc}}{r}\right) \left(\frac{1\,\mathrm{kHz}}{f}\right) \left(\frac{1\,\mathrm{ms}}{\tau}\right)^{\frac{1}{2}}, \qquad (1.2)$$

where E is the total energy radiated, predominantly at a frequency f, over a time scale τ, and where r is the distance to the source. This is scaled based on $\sim$0.1% of the energy available going into the gravitational wave[7]. The event rate of both Type I and Type II supernovae out to the Virgo cluster ($\sim$15 Mpc) has been estimated as several per month[8].

Coalescing Binaries A binary system consists of two stars orbiting their common centre of mass. Compact binary systems consist of two high density stars, e.g. neutron star–neutron star, neutron star–black hole, and black hole–black hole binaries. As these systems lose energy through the emission of gravitational waves, the orbits of the stars decay. As the two stars approach each other, stronger gravitational waves are emitted. The gravitational radiation, emitted at twice the orbital frequency, gradually increases in amplitude and frequency, resulting in a 'chirp' waveform. Once the orbit has decayed so that the stars are within a few stellar radii of each other, the frequency will be in the band that may be detected by ground based gravitational wave detectors. This signal will last for a few seconds before the final coalescence of the stars.

The expected signal strength for two neutron stars coalescing at a distance r

is[9]

$$h \approx 1 \times 10^{-23} \left(\frac{100\,\mathrm{Mpc}}{r}\right) \left(\frac{\mathcal{M}}{M_\odot}\right)^{\frac{5}{3}} \left(\frac{f}{200\,\mathrm{Hz}}\right), \tag{1.3}$$

where the mass parameter $\mathcal{M} = \mu M^{2/3}$, M is the total mass $(M_1 + M_2)$, and μ is the reduced mass, $\frac{M_1 M_2}{M_1 + M_2}$. The time scale, τ, over which this frequency changes is

$$\tau = \frac{f}{\dot{f}} \approx \left(\frac{200\,\mathrm{Hz}}{f}\right)^{\frac{8}{3}} \left(\frac{M_\odot}{\mathcal{M}}\right)^{\frac{5}{3}}. \tag{1.4}$$

If h, f, and τ are measured by a network of three detectors, the value of r can be determined from these equations. The difference in burst arrival time at each detector can be used to determine the direction of the source. If it is also possible to measure the recessional velocity of the source from the optical redshift, there is then a method for determining Hubble's constant, H_0[7].

The primary uncertainty about this type of source is the prediction of their event rate. The number of pulsars in binary systems along with the estimated pulsar birth rate can be used to estimate the event rate at 3 per year out to 200 Mpc[10].

Periodic Sources

Steady sources of gravitational radiation will emit continous, quasi–monochromatic waves. These kind of signals can be detected by a single detector using long averaging times and narrow–band operation, improving the detector sensitivity by the square root of the observation time (when the noise is random). The signal is Doppler shifted due to the relative motion of the detector and the source; the motion of the Earth over these long averaging times will create a characteristic shifting of the signal.

The binary systems just described, long before coalescence, emit continuous gravity waves. These signals will be at frequencies too low to be observed by ground based detectors.

Pulsars Single pulsars can emit gravitational radiation if they spin non–axisymmetrically. The asymmetry is defined in terms of the pulsar's equatorial ellipticity,

ϵ. The strain amplitude of the radiation is then given by[10]

$$h \approx 6 \times 10^{-25} \left(\frac{f_{rot}}{500\,\mathrm{Hz}}\right)^2 \left(\frac{1\,\mathrm{kpc}}{r}\right) \left(\frac{\epsilon}{10^{-6}}\right) \tag{1.5}$$

at twice the frequency of rotation, f_{rot}.

This asymmetry may arise, for example, when a pulsar precesses due to the accretion of angular momentum from a companion star, but it is a poorly known parameter. It is thought to lie between 10^{-4} and 10^{-6}, but could be as low as 10^{-8}[10]. Accurate determination of this would give much information about the structure of pulsars.

Over a year's observing time, the signal detected from such a pulsar can be integrated up to the equivalent of $h = 2 \times 10^{-21}/\sqrt{\mathrm{Hz}}$. There are many catalogued pulsars; of particular interest for the ground based detection of gravity waves is the Crab Pulsar. It is believed to be emitting gravitational radiation at a frequency of $\sim$60 Hz. This pulsar could provide one of the first gravitational wave signals to be detected[11].

Wagoner Stars Wagoner described a method by which a neutron star spins up to the Chandrasekhar–Friedman–Schutz instability point by accretion then becomes non–axisymmetric[12]. The additional angular momentum is then radiated away in the form of gravitational waves. Because the rate of accretion of angular momentum is proportional to the rate of accretion of mass, the gravity wave luminosity of such a star will be proportional to its X–ray luminosity. Discoveries by the Rossi X–Ray Timing Explorer[13] suggest that the gravitational wave signal strength of the X–ray source SCO X–1 could be $h \approx 2 \times 10^{-26}$ at 500 Hz.

Stochastic Sources

A final category of potentially observable gravitational wave signals comes from the stochastic background, the superposition of signals from sources randomly distributed throughout the universe. One possible source of the stochastic background results from primordial gravitational waves produced during or after an inflationary

period immediately following the Big Bang[7]. Another possible source is the production of cosmic strings, which may produce an amplitude of gravitational waves[14]

$$h \approx 2.4 \times 10^{-25} \left(\frac{H_O}{75\,\mathrm{kms^{-1}Mpc^{-1}}}\right) \left(\frac{\Omega_{GW}}{10^{-8}}\right)^{\frac{1}{2}} \left(\frac{100\,\mathrm{Hz}}{f}\right)^{\frac{3}{2}} \left(\frac{B}{2\,\mathrm{Hz}}\right)^{\frac{1}{2}} \tag{1.6}$$

in a bandwidth B about a frequency f, where H_0 is Hubble's constant and Ω_{GW} is the energy density per logarithmic frequency interval required to close the universe.

The stochastic background by its very nature is indistinguishable from other sources of Gaussian noise in a single detector. However, its frequency spectrum will be identical across every detector. By cross–correlating the outputs of two or more detectors, the stochastic background signal can be separated from the random noise. This is best done between detectors separated by reasonably large distances (although less than a fraction of the gravitational wavelength to preserve the coherence of the radiation) to avoid other, local disturbances that might be detected in common between the detectors.

1.2 Gravitational Wave Detection

There are a number of detectors around the world, proposed, being constructed or already in operation, which seek to measure the extremely small strains produced by a gravity wave in space. The major types of detectors can split into two categories: resonant bar detectors and interferometers. Earth based gravitational wave detectors are handicapped by the fact that the Earth does not provide a quiet environment to detect these delicate perturbations. Any form of terrestrial experiment must go to great lengths to vibrationally isolate the detector from its surroundings.

1.2.1 Resonant Bar Detectors

The original detector was a resonant bar developed by Weber in the 1960's[15]. A bar detector uses a massive (~few ton) mechanical resonator, usually a right circular cylinder. A suitably oriented gravitational wave of the correct frequency that passes through the cylinder will excite the fundamental longitudinal mode of the bar (at ~1 kHz), causing a strain in the bar. The resulting motion of the ends of the bar is proportional to the induced gravitational strain.

The effects of seismic noise on the resonant bar are reduced by suspending it from vibration isolation stages (in the same manner as will be discussed in detail in the following chapters for the mirror suspensions of interferometric detectors). Acoustic noise is reduced by placing the detector under vacuum. The sensitivity of the detector is then limited by the noise in the sensor and the thermal noise of the cylinder. The thermal noise is reduced by cooling the detector to cryogenic temperatures (a few Kelvin or below). To reduce the thermal noise further (section 2.5), the bar is made of a material with low mechanical loss (or high quality factor, Q), typically aluminium or niobium. This high Q also ensures that once the cylinder resonance is excited, it will oscillate for a long period of time. This allows the measurement to be time averaged to reduce the effect of sensor noise. This averaging is balanced against the slowly varying level of thermal noise against which the measurement must be made, the effects of which are reduced by shortening the measurement interval. With current technology, this is typically set at a measurement bandwidth of $\sim\frac{1}{100}$ of the resonant frequency of the bar. Because of this, resonant bar detectors are intrinsically narrowband.

Resonant bar detectors have been developed at Stanford, Lousiana State University (ALLEGRO), Rome (NAUTILUS), CERN (EXPLORER), and Perth, Western Australia (NIOBE). Cryogenic bar detectors have achieved strain sensitivities of $h \approx 6 \times 10^{-19}$ over bandwidths of a few Hz at $\sim$1 kHz at a temperature of 4 K[16, 17, 18, 19]. Experimental groups in Padua (AURIGA) and the USA have developed techniques that enable the bars to be cooled further; by reducing the temperature to ultracyrogenic temperatures ($\sim$50 mK), it is expected that a strain sensitivity of order 10^{-20} will ultimately be achieved[20, 21].

A further increase in the sensitivity of a resonant bar detector may be made by changing the bar geometry. A spherical 'bar' is much more massive than a cylindrical bar of the same resonant frequency, which reduces the effects of thermal noise. A sphere also has five usable quadrupole modes which may be used to detect the passing gravitational radiation, as opposed to the cylinder's single mode. The ratio of the amplitudes of these modes may be used to determine the direction and polarization of the incident wave. Spherical detectors have been proposed by experimental groups in the USA (TIGA) and the Netherlands (MiniGrail)[22].

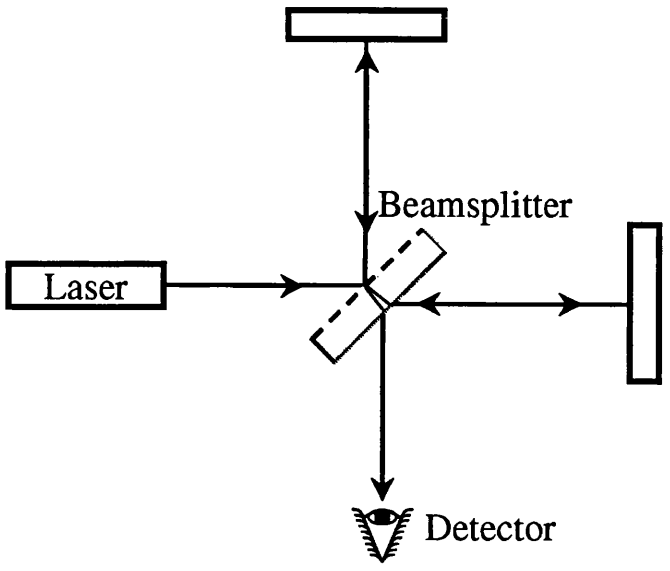

Figure 1.2: A Michelson interferometer.

1.2.2 Interferometeric Detectors

An interferometer uses the interference of light beams typically to measure displacements. An incoming beam is split, so that one component may be used as a reference while another part is used to probe the element under test. The change in interference pattern results in a change in intensity of the output beam which is detected by a photodiode. By using the wavelength of light as a metric, interferometers can easily measure distances on the scales of nanometres and, with care, much more sensitive measurements may be made. The light source used is a laser, a highly collimated, single frequency light, making possible very sensitive interference fringes. Different configurations can be used to measure angles, surfaces, or lengths.

The use of interferometers to detect gravity waves was originally investigated by Forward and Weiss in the 1970's[23, 24]. To use an interferometer to detect gravity waves, two masses are set a distance apart, each resting undisturbed in inertial space. When a gravity wave passes between the masses, the masses will be pushed and pulled. By measuring the distance between these two masses very accurately, the very small effect of the gravity waves may be detected. The simplest Michelson interferometer is shown in figure 1.2. The input beam is split at a beamsplitter, sending one half of the light into each arm. Fortuitously, the quadrupole moment

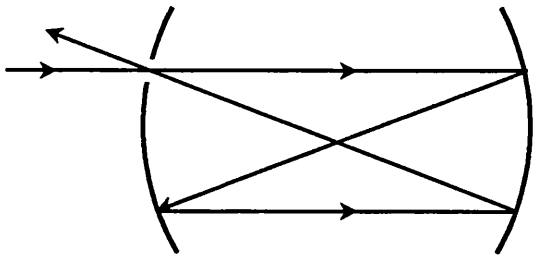

Figure 1.3: Layout of a 'delay-line'. The amount of time the light spends in the arm is increased by reflecting the light repeatedly along the lengths of the arm.

of gravitational radiation means that depending on the direction of the incoming radiation, the arms may actually experience disturbances out of phase with each other, giving rise to a larger signal.

Storage Time

In order to sample as much of the wavefront as possible, to get as large a δL for a given h as possible, an interferometer ought to be made very long. The maximum sensitivity is obtained when the light is stored in the arms of the interferometer for one half of the period of the gravitational wave, or $L_{optical} \approx \lambda_{GW}/4$. For a gravity wave of wavelength 3×10^5 m, this would require an optical path of 75 km. On the Earth, it is physically impractical to build an interferometer where the arms are much longer than $\sim$4 km. The effective length of the arms may instead be increased by causing the light to traverse the arms multiple times before returning to the beamsplitter.

The use of an optical delay line, shown in figure 1.3, was first propsed for use in a gravitational wave detector by Weiss[24]. After reflection of the light at the far end of the interferometer arm, the return of the light to the beam splitter is 'delayed' by reflecting it back down the arm cavity. Multiple non–overlapping beams can be sent between two mirrors, with the light entering and leaving the cavity by a hole in one end mirror. A detector using these delay lines has been developed at the Max–Planck–Institut für Quantenoptik, Garching, Germany[25]. The maximum strain senstivity achieved in a 30 m prototype interferometer was $h \approx 1 \times 10^{-19}/\sqrt{\text{Hz}}$ above 1.5 kHz[26].

Another method of increasing the optical storage time is by use of a resonant

Figure 1.4: A Fabry-Perot cavity. The light enters the cavity through a partially reflecting mirror and is then reflected between the two mirrors of the cavity. Each photon, on average, passes the full length of the cavity many times before exciting the cavity, such that the light power inside the cavity is much greater than the input power.

Fabry–Perot cavity[27] in each arm of the interferometer, a schematic of which is shown in figure 1.4. The use of these cavities in a gravitational wave interferometer was developed in Glasgow[28]. The light enters the cavity by passing through a partially transmitting input mirror. The photons then travel back and forth between the mirrors, on average some multiple number of times, before passing back out of the cavity through the partially transmitting mirror. To obtain the optical resonance necessary requires that the mirrors be held a fixed distance apart from each other. The details of the optical behaviour are examined in section 6.4.

When one of these resonant cavities is used in each arm of an interferometer, each cavity must be kept on resonance. Typically, the laser frequency is adjusted to maintain one cavity on resonance. When a gravity wave changes the length of both cavities, the first control loop changes the frequency of the laser. The length of the second cavity is then adjusted to maintain its resonance. The amount of motion needed to maintain this resonance reflects the total change in length δL and thus the gravity wave signal. A detailed description of the control required involving all the optical components may be found in Sigg[29]. The 10 m Fabry–Perot interferometer at Glasgow has reached an equivalent strain sensitivity of $h \approx 6 \times 10^{-20}/\sqrt{\text{Hz}}$ at about 1 kHz[30]. Another Fabry–Perot interferometer is the 40 m prototype detector at Caltech, which has achieved a displacement noise background below $2 \times 10^{-18}\text{m}/\sqrt{\text{Hz}}$ from 200 Hz to 5 kHz[31].

There are advantages to each scheme. Because the delay lines use non–overlapping beams, the mirrors must be much larger than for comparable Fabry–Perot cavities. The Fabry–Perot cavities also have less difficulty with scattered light, since there is not the problem of scattering light from one beam to the next[25]. However,

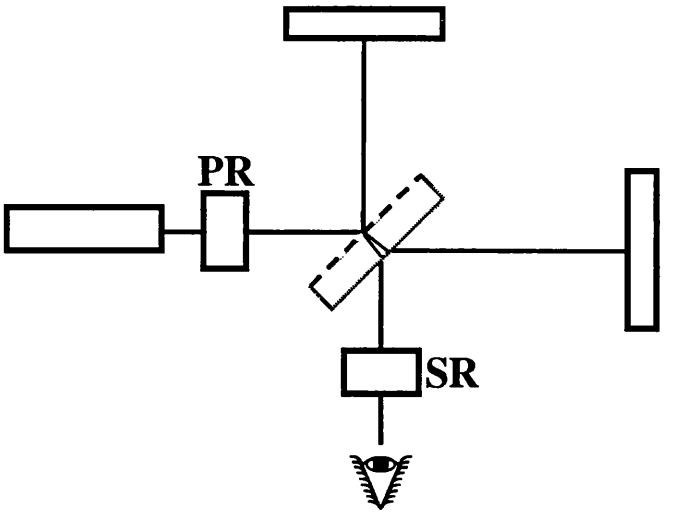

Figure 1.5: Power and signal recycling in a simple Michelson interferometer. Mirror *PR* reflects any exiting laser power back into the interferometer, while mirror *SR* reflects the output signal back into the system.

a Fabry–Perot cavity relies on having a partially transmitting optic, which restricts the material used in the mirror to be transmissive and to have very low absorption. In addition, systems using Fabry–Perot cavities have the additional difficulty that the the cavities must be maintained on resonance, resulting in more complicated control systems.

Power Recycling, Signal Recycling, and Other Configurations

The interferometric signal can be detected most sensitively by operating the interferometer on a dark fringe, when the resulting intensity at the photodetector is a minimum. Since power is conserved, and very little light power is lost in passing through the interferometer, most of the input laser power is reflected from the interferometer back towards the input laser. Since increasing laser power results in better sensitivity (section 1.3.3), rather than 'waste' this reflected power, a partially transmitting mirror can be placed between the input laser and the beam splitter. This allows the entire interferometer to form an optically resonant cavity, much like the Fabry–Perot cavities discussed earlier, with a potentially large increase in power in the interferometer. This is called *power recycling*, and is shown schematically by the mirror labelled *PR* in figure 1.5.

In a similar fashion, the optical perturbation due to the gravity wave may be reflected back into the interferometer to resonantly enhance the output signal. Such a technique is called *signal recycling*, accomplished by mirror *SR* in the figure. A discussion of recycling techniques may be found in Meers[32].

1.2.3 Space Based Detectors

Ground based interferometers are limited at the low frequency end by the practical difficulties of operating on Earth: the increasing difficulty of vibration isolation at lower frequencies, the effects of the curvature of the Earth for longer baseline detectors, and the expense of longer vacuum systems. There is also the fundamental difficulty of gravity gradient noise, described in the next section. The obvious solution to these specific difficulties is to use an interferometric detector in space. Interferometer arms may be made orders of magnitude longer than is practical on Earth. LISA (Laser Interferometric Space Antenna)[33] has been proposed as a cornerstone mission in the Post Horizon 2000 programme in ESA. It will consist of three identical spacecraft positioned in a heliocentric orbit 20° behind the Earth, with each spacecraft forming a vertex of an equilateral triangle. Each spacecraft will be separated from its neighbour by 5×10^9 m and will contain two test masses and two laser transponders (Nd:YAG), allowing the sides of the triangle to form two semi–independent interferometers.

A gravitational wave strain sensitivity of $h \approx 10^{-21}/\sqrt{\text{Hz}}$ is expected to be achieved. LISA should be able to observe gravitational waves occurring in the 0.1 mHz to 0.1 Hz frequency range. Gravitational waves in this frequency band include stellar–mass binary systems with relatively large separations and interactions of massive black holes. Space–bourne detectors will be complementary to ground–based detectors, allowing a broader frequency window to be observed. ESA and NASA are currently discussing a joint mission to launch LISA in ~2008.

1.3 Sensitivity: Noise in Interferometers

There are many things that contribute to the noise budget of a sensitive instrument. For design purposes, it is important to identify the dominant factors. As

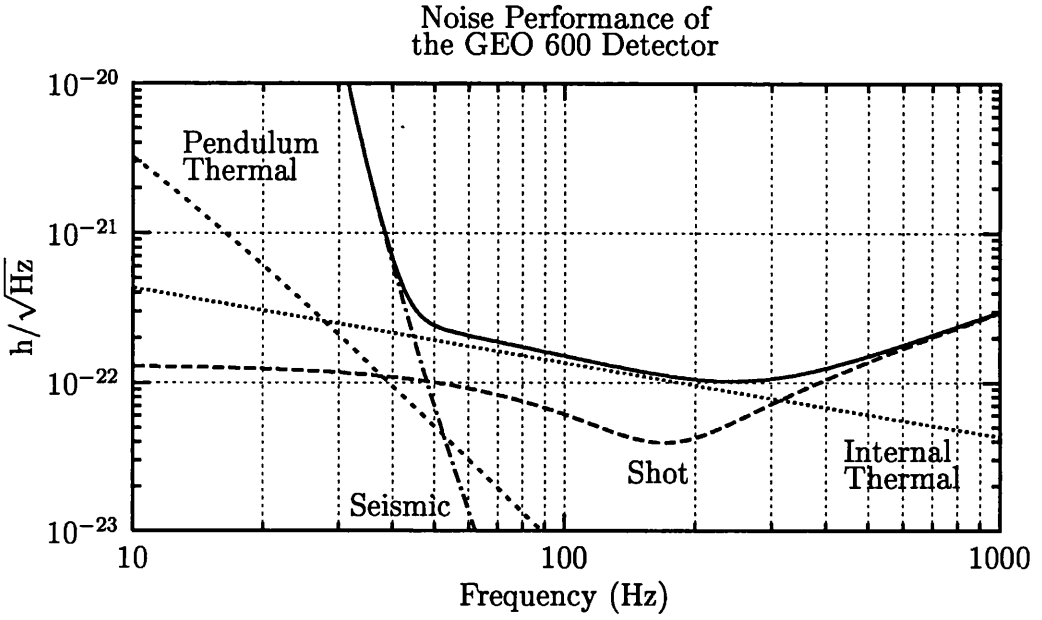

Figure 1.6: Noise curve of the GEO 600 detector

an example, the predicted noise curve for GEO 600[11], the German/UK ground–based interferometric detector, is shown in figure 1.6. The detector will reach its best strain sensitivity in a frequency band starting at approximately 50 Hz, ranging up towards 1 kHz. This figure includes curves representing various noise sources that contribute to the total sensitivity. Some of these factors are calculated using conclusions from later chapters of this work.

There are two different kinds of noise that are relevant in the interferometric detection. The interferometer very sensitively measures the relative displacement of the optics. Therefore, the motion of the optics must be made small enough that the effects of the gravity wave are large enough to be seen. Any noise source that affects the position of the optic is referred to as 'displacement noise'. (The displacement is related to the strain by a factor on the order of the length of the interferometer arms which depends on the specific geometry of the detector. For GEO 600, the equivalent strain noise is $\sim\sqrt{3}/600$ times the displacement noise.) There is then the optical challenge of detecting this small motion. Anything that affects the phase of the laser beam used to detect this is called 'phase noise'. The work described in the following chapters focuses on the actual behaviour of the suspended optics, and therefore the requirements are often expressed in terms of the allowable displacement

noise at the optic which results in the corresponding strain sensitivity shown in the noise curve.

Broadly speaking, the low frequency part of the noise spectrum is dominated by seismic noise, the intermediate region dominated by thermal noise, and the high frequency region dominated by laser noise. Each of these noise sources is briefly introduced here, while the elements that affect the suspension design are examined in more detail in chapter 2.

1.3.1 Mechanical

The low frequency region of the detector sensitivity tends to be dominated by mechanical noise sources, generated by the Earth upon which the detector rests. While careful characterization of the possible sites can result in a better, seismically quieter location, in all cases the ground moves many times more than is acceptable for the size signals to be measured.

Ground Motion

Gravitational wave interferometers sense passing gravitational waves by detecting the apparent motions of the end mirrors; ideally, this assumes that the mirrors are in inertial space. For detectors on Earth, the mirrors are always attached to the ground—far from inertial. The first goal of the mirror suspension will be to ensure that the mirror acts inertially free with respect to the Earth at frequencies where gravity waves are to be detected. That is, the seismic noise of the ground transmitted through the suspension system must be reduced to below the desired measurement sensitivity. The principals of seismic isolation are introduced in the following chapter, while the detailed modelling of isolation performance is described in chapter 3, with the resulting performance covered in chapter 4.

Gravity Gradient

The seismic noise arises from the physical connection between the experiment and the moving ground, which can be reduced by intelligent design by making a soft connection and reducing the effects. There is still the gravitational attraction between mass outside the detector and the measured mirror masses which can 'short circuit'

the vibration isolation. The noise from this effect is referred to as the gravity gradient noise[34]. Given the relatively weak strength of the gravitational attraction, objects that contribute to the gravity gradient need to be either fairly close to the detector, such as workers walking around in the lab, or have a relatively large mass, including storm systems in the atmosphere.

While this could, in principle, be detected and actively cancelled, this has not been attempted or explored in any detail here. Because this is the fundamental limitation only at very low frequencies, compared to the target range of the first generation detectors, it does not affect current detector sensitivity[35, 36]. For advanced detectors, which will strive for greater sensitivity at lower frequencies, the gravity gradient noise will form an eventual limit to the sensitivity.

1.3.2 Thermal

Thermal noise limits the interferometer sensitivity in the mid–frequency band, the lower portion of the detection band. This noise results from the Brownian noise, the k_BT of energy per mode, in the system. This energy is kinetic energy, actual movement of the mirror surface that to the measurement system of the interferometer would be indistinguishable from motion caused by a passing gravitaional wave. The presence of the noise is fundamental, and the integrated quantity may only be reduced by cooling the system, typically to cryogenic temperatures. While this has typically been done for the bar type detectors, first generation interferometers are not planning cooling at this time; it is an option to be considered for next generation detectors. One reason that this is not necessary is because the spectral distribution of this thermal noise can be modified. The details of the relationship between loss in a system and the observed noise and some of the implications for the pendulum design are given in section 2.5, but in short, the noise is concentrated in the resonance of the mode. The less loss there is in the system, the more the noise is concentrated in that resonance and therefore the less noise is observed off–resonance. The noise in the very sharply peaked resonances may be filtered out with narrow band filters if the resonances fall within the operating frequency band of the detector.

Test Mass

The mirror face requires a certain minimum size, expressed as some multiple of the size of the beam, to minimize the amount of light lost to diffraction around the edges of the mirror. A very thin mirror would have low frequency 'drum' modes, where the mirror face moves back and forth like the surface of a drum, whereas a very thick mirror will have its lowest modes where the mirror bends along its length. For the GEO 600 parameters, the lowest frequency mechanical mode of the test mass is approximately 17 kHz[37], well above the detection range of the interferometer.

The mirror material is chosen based on both its thermal and optical properties such as the inherent mechanical loss, the optical loss, and coefficient of thermal expansion. Having chosen the mirror substrate, the issue for suspension design becomes not compromising the inherent loss of the material. Twyford[38] discusses in some detail the state of the research into how this is to be accomplished for GEO 600.

There are a few significant points to highlight with respect to the suspension design. The first issue is that for controlling the orientation of the optics, corrective forces need to be applied. This is commonly done by sending current through coils which act on a magnet attached to the optic. Magnet material is lossy, and attaching magnets to mirrors increases the observed loss. This is one reason why the local control for GEO 600, described in section 6.2, does not act directly on the sensitive optic. The second important point for suspension design involves the method of bonding, as described below.

Suspension

In a similar manner to the internal modes of the mass, the pendulum mode has thermal noise associated with it. The nominal method to minimize the effect of this noise in the frequency band is the same—a very high Q system results in lower noise observed off resonance. If a wire pendulum suspension is clamped in a lossless fashion, the loss observed in the pendulum mode is much less than the inherent loss in the wire material. This is because most of the potential energy is stored in the gravitational potential as the pendulum moves, which is a lossless mechanism (section 2.2.2)[39].

There are, again, a few specific issues that affect the suspension design. First of

all, the system does not swing in a single degree of freedom. In a real pendulum, both the translational motion and the rotational motion of the mirror mass affect the front surface of the mirror seen by the laser beam. This tilt mode of the suspension typically involves the stretching of the wires and thus does not have the 'dilution' of loss described above. Therefore all the modes of the system must be considered. Secondly, in order to maintain the high Q pendulum mode, great care must be taken in how the suspension wires are attached. The intended method of attachment in the GEO 600 suspension is silicate bonding[40]. To use this method will require that the suspension fibres in the final stage of the multiple pendulum be vertical.

Suspension Elements

There will be modes in the suspension that involve almost exclusively motion of the suspension wires. These modes are called 'violin modes', as they are similar to any string under tension. These modes exhibit similar high levels of Q to the losses observed in the other modes of the system, and as such, have a relatively high level of thermal noise at their resonant frequency[41]. (The relatively low mass of the wire compared to the sensed pendulum masses prevents the motion at frequencies away from the resonances from appearing in the interferometer output.) These resonances, and the corresponding thermal noise peaks, are pushed to as high a frequency as possible without over stressing the wires in an effort to remove them from the frequency band of interest.

1.3.3 Laser Noise

Photon Noise

The limitations to the detector sensitivity at higher frequencies tend to come from the laser beam used to make the measurement. The quantized nature of light means that for a certain light power, P, of frequency f, falling on the photodetector, where each photon carries $\hbar f$ of energy, $P/\hbar f$ photons per second fall on the detector. The arrival of each photon at the detector is a statistically independent process where the distribution of the intervals between arrival times forms a Poisson distribution. Simply stated, since it is only possible to count an integral number of photons, if the anticipated number of photons which arrive in a short period of time is a

small number, the relative error of a one more or one fewer photon can be large. Therefore, with a higher power input laser, more photons arrive and the relative error is reduced.

For a simple Michelson interferometer using a delay line in each arm to increase the light storage time, the photon shot noise in the strain, h, is described as[42]

$$h_{shot}(f) = \sqrt{\frac{\hbar\lambda}{\epsilon c P_{in}}}\frac{f}{\sin(\pi f \tau_s)}, \tag{1.7}$$

where $\hbar$ is Plank's constant divided by 2π, λ is the wavelength of the laser light, ϵ is the quantum efficiency of the photodiode, P_{in} is the input power, c is the speed of light, and τ_s is the light storage time. The correct expression for GEO 600 is further modified by the other aspects of the optical layout, specifically the signal recycling. As shown on the noise curve for the GEO 600 parameters using an input laser power of 10 W, this is then the dominant noise source at high frequencies. This is not a fundamental limit, and much work has been done on higher power lasers suitable for use in a gravitational wave interferometric detector[43].

Light Pressure

One other noise source gets worse with increasing laser power. Each photon has momentum, and the resulting radiation pressure exerted on each mirror by the photons reflecting from it, for a lossless mirror, is

$$F_{rad} = \frac{P}{c}. \tag{1.8}$$

The fluctuation in this force is then due to shot noise fluctuation in the power, P. This force, applied to each mirror, causes the mirror to move,

$$x(f) = \frac{1}{m(2\pi f)^2}F(f) = \frac{1}{mf^2}\sqrt{\hbar P_{in}}8\pi^3 c\lambda. \tag{1.9}$$

For first generation detectors such as GEO 600, the laser power is low enough that the radiation pressure noise is far from being a limiting factor.

For future detectors, where the laser power will be increased greatly to reduce the photon shot noise, it is possible that the radiation pressure would become a limiting noise source. For any given frequency, there is an optimal laser power to give the

minimum combination of the noise due to the radiation pressure and that due to the photon shot noise. This limit can be considered a fundamental limitation (for any given frequency) to the achievable noise for interferometric detectors, corresponding to the Heisenberg Uncertainty Principle.

1.3.4 Other Sources

Beyond the three main categories of noise—which result from seismic, thermal, and laser sources—there are any number of other possible sources of noise. One example is that variations in the index of refraction in the optical path of the interferometer can again cause signals indistinguishable from those of a gravity wave. The total optical path seen by the laser beam is a function of how many air molecules the beam passes through. Variations in this number cause noise in the output signal. To minimize this, the entire interferometer must be in vacuum. The required level of vacuum is not extreme, but being in vacuum constrains the choice of materials and bonding agents available to the design of the suspension system.

Any control signal that affects the position of the optics for alignment will also apply noise to the system. This is an important consideration for how control signals are applied to the system. Section 6.2.1 deals with the specific considerations about sensors and actuators for the control that reduce the undesirable effects of high Q pendulum resonances.

Additional care must be taken to avoid noise due to fluctuations in the laser. The effects of intensity fluctuations in the laser are reduced by modulation techniques and by operating the detector on a dark fringe. Errors in beam position and size are reduced by use of a mode cleaner acting as an optical filter.

'Excess' Noise Sources

The noise that appears in the detector that is above the anticipated noise floor is 'excess noise'. Great effort goes into identifying the possible sources of excess noise and then striving to reduce these sources. What is of greatest concern with respect to this work is additional resonances that appear in the physical system. Even with the very large values of isolation, high Q (often poorly modelled) resonances in the middle of the isolation system may cause large peaks in the noise spectrum of the interferometer at their resonant frequency. Whenever possible, the system

is designed to have every internal resonance at a high enough frequency so as not to affect the detection band. When this is not possible, it is often sufficient to ensure that the resonant frequency is above a few hundred Hertz; while this is still within the sensitive frequency band of the detector, the isolation of the system at these frequencies is so great that the resonant peaks do not appear at the output. This is the case, for example, with the internal modes of the smaller cantilever blades described in section 4.2.2. When the internal resonant frequencies can not be made high enough, some extra effort is made to reduce the Q of these resonances. This happens, for example, in the bellows which encloses the passive isolation stack (section 2.2.1).

1.4 Detection

GEO 600 will function as part of the global network of detectors, which include the French–Italian VIRGO project being constructed near Pisa in Italy, the American Laser Interferometer Gravitational–Wave Observatory (LIGO) being built at two sites in the states of Washington and Louisiana, and the Japanese TAMA, near Tokyo, Japan. This worldwide network will allow coincident detection for confirmation of results, as well as providing the geometry needed to locate a source purely by its gravitational radiation, without relying on a source being sighted by other means.

Figure 1.7 compares the anticipated signal strength of potential sources described in section 1.1.2 with the sensitivity of various detection projects. The GEO 600 curve is that introduced in figure 1.6, the broadband sensitivity, which can be enhanced through use of signal recycling at higher frequencies, such as the predicted 500 Hz frequency of the X–ray source SCO X–1, at the expense of reduced bandwidth. Based on the known possible sources, it is clear that it is important to reach the best possible sensitivity.

To that end, this thesis concentrates on the design of the mechanical suspension used for the optics in the GEO 600 interferometric gravitational wave detector. The successful design of the suspension will satisfy requirements involving the vibration isolation, thermal noise of the pendulum modes, and control of the optics. The next chapter will introduce some of the concepts that will be used in the remainder

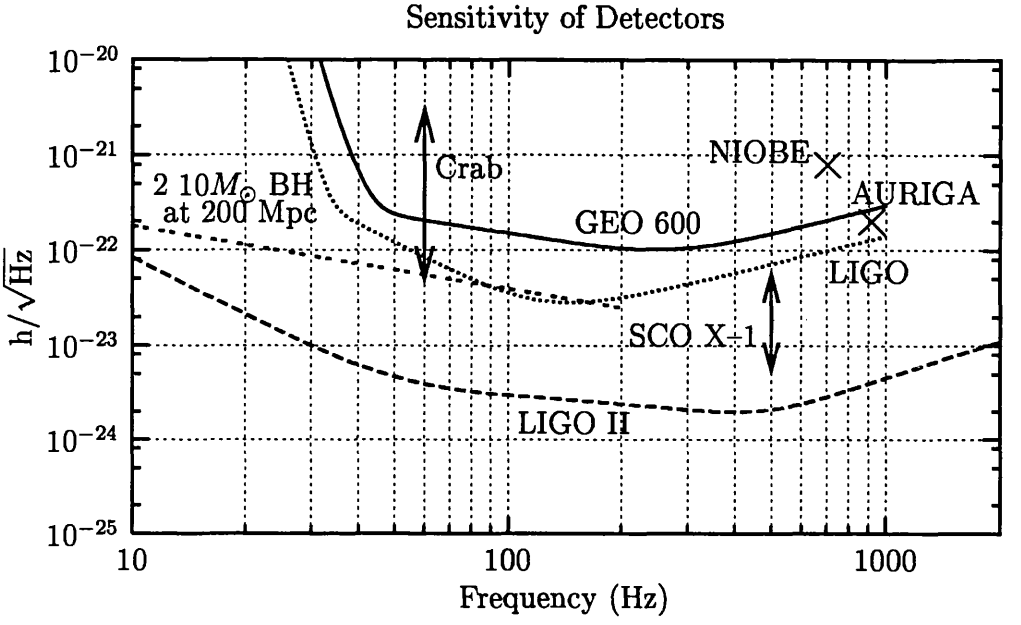

Figure 1.7: Ground–based detection of gravitational wave sources. The figure compares the signal strength of anticipated sources with the sensitivity of various detectors. The GEO 600 curve is the broadband sensitivity, which may be enhanced at higher frequencies at the expense of bandwidth. The LIGO sensitivity is shown as representative of other long baseline interferometric detectors, whereas the LIGO II data illustrates the potential for advanced detectors[44]. Recent sensitivities of the some of the bar detectors are also shown at their most sensitive frequencies[45]. Candidate sources are taken from Schutz[46]. They include the Crab pulsar, shown between an upper limit set by equating the observed loss of energy to the gravitational wave luminosity and a lower limit where its ellipticity would be 10^{-5}, assuming an integration time of one year. The equivalent strength of hypothetical radiation from SCO X–1 is shown based on observation times of one day up to one year, at which point modelling the signal may be difficult. Finally, a representative spectral density curve is shown for a black hole/black hole binary as it approaches coalescence.

of the thesis. After this is a discussion of the computer model used to predict the performance of the suspension. This model is applied in the following three chapters to different aspects of the suspension design: the dynamics of a multi–stage pendulum suspension, including its vibration isolation; the resulting thermal noise; and the electronic control of the suspension. The final parameters of the GEO 600 design are then summarized.

Chapter 2

Mechanical Suspension in Interferometers

There are a large number of sensitive optics in the GEO 600 system. In order to achieve a seismically quiet optic (as described in the following sections), each of these components is 'suspended' in a pendulum system. The specific performance requirements may vary slightly based on where in the optical path a component is, but all the suspended components have a number of issues in common. All suspensions have design constraints that come from the required vibration isolation, the allowable thermal noise, the ability to control the optics, the physical robustness and reliability required when there are many units to be installed, and the limitations due to material and technique constraints.

The detection band for the GEO 600 detector, i.e. the frequency range of greatest sensitivity, ranges from 50 hertz up to a few kilohertz. The various types of noise that limit the sensitivity of the system are introduced throughout this chapter. It has been specified that the system be limited by the internal thermal noise of the test mass at the low frequency corner of the detection band[47]. This sensitivity is anticipated to be a strain of $2 \times 10^{-22}/\sqrt{\text{Hz}}$ at 50 Hz, which with the GEO 600 optical scheme corresponds to a test mass motion of approximately $7 \times 10^{-20}\text{m}/\sqrt{\text{Hz}}$ at 50 Hz. All other noise sources are designed to be below this level (typically by a factor of 10) so as not to significantly increase the observed noise. The requirements on the suspension system are dominated by this low frequency end of the detection band.

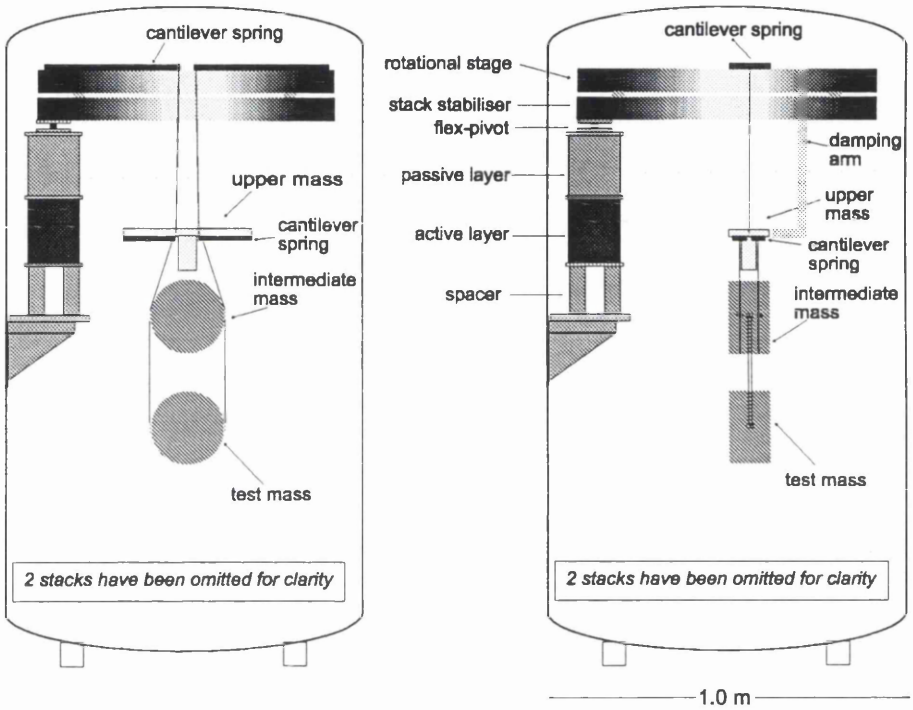

Figure 2.1: GEO 600 main suspension. The figure illustrates a face view (left) and a side view (right) of the total suspension and isolation system. This includes the active and passive isolation stack layers, the interfacing to the pendulum system, and the triple pendulum incorporating two stages of cantilever springs.

This chapter introduces some of the issues that influence suspension design, as well as some of the techniques used to satisfy these issues. The following chapters then address the specifics of modelling the pendulum suspension, and then how that modelling is used to answer problems of seismic isolation, thermal noise, and control. The GEO 600 main suspension will be as shown in figure 2.1. The required isolation will be achieved with a combination of a triple pendulum and a single passive stack layer[48]. The isolation stack is made up of three legs, arranged radially about the vacuum tank. There is also a single active isolation layer which will be used at low frequencies to reduce the rms (root mean square) motion, reduce the effects of the micro–seismic peak, and reduce the low frequency actuation requirements. A flex–pivot on top of each isolation stack leg reduces the rotational stiffness of the leg. The three legs are statically supported by the stack stabilizer.

A rotational stage slides on bearings on top of the stack stabilizer. The pendulum suspension hangs from this rotational stage. There are three stages to this pendulum, the top two of which use cantilever blades to improve the vertical isolation. A damping arm allows control forces to be applied to the top stage of this pendulum. The suspension design was finalized partly based on the work discussed in the following chapters. The final parameters of this design, summarized in chapter 7, are used as a baseline for the worked examples.

2.1 Seismic Noise

Given the desired sensitivity of the detector, the motion of the ground of any potential detector site must be characterized in order to determine the requirements of the suspension. This characterization is done early in the consideration of a site, as it provides one of the fundamental inputs to the design. Representative ground spectra for the site in Ruthe are shown in figure 2.2.

The spectrum of ground motion the world over has certain similar characteristics, although the details can be crucial. Ground motion peaks at what is known as the 'micro–seismic peak', which occurs in the neighbourhood of $\frac{1}{7}$ of a Hertz. This peak is caused by ocean waves crashing on the continental shelf. At frequencies above that of the micro–seismic peak, the spectral density of ground motion as a function of frequency falls up to around 1 Hz, then tends to flatten out until somewhere around

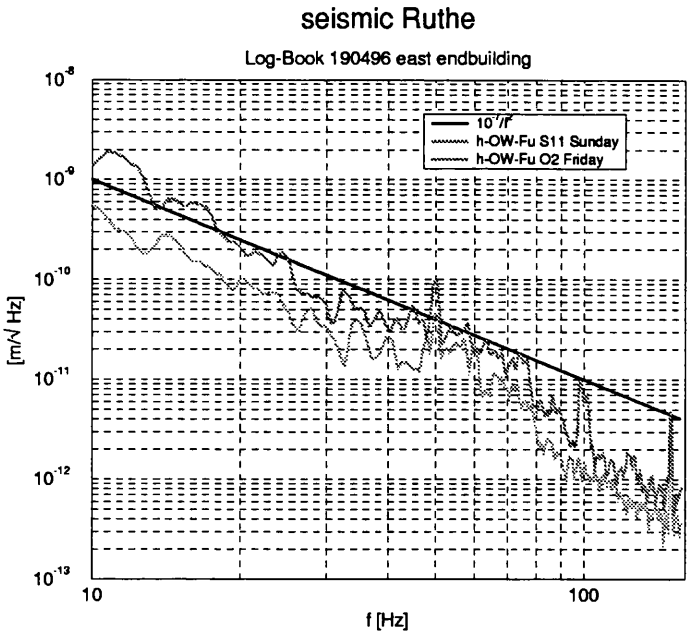

Figure 2.2: Typical ground spectra at the Ruthe site. The horizontal measurements shown here are comparable to the vertical measurements. For the modelling work, the ground spectrum is modelled as $10^{-7}/f^2$ m/$\sqrt{\text{Hz}}$.

10 Hz, then falls with frequency squared (f^{-2}) until well into the measurement band, at which point it ceases to be a limiting factor.

The details of the spectrum vary from site to site and at various times throughout the year. For simple approximation, the ground motion above about 1 Hz is typically written as

$$x_g(f) = x_0 \left(\frac{1}{f}\right)^2 \frac{\text{m}}{\sqrt{\text{Hz}}}, \tag{2.1}$$

where for GEO 600, $x_0 = 10^{-7}\text{m}/\sqrt{\text{Hz}}$. This single asymptote suffices for calculating the performance at the 'target frequency', the lowest frequency corner of the detection band. Since the GEO 600 noise specification is $7 \times 10^{-20}\text{m}/\sqrt{\text{Hz}}$ at 50 Hz, the system will require isolation from ground motion on the order of 6×10^9. While this could be achieved in principle with a single pendulum somewhat over a kilometre in equivalent length, in practice this will be accomplished with a series of isolation stages, both passive and active.

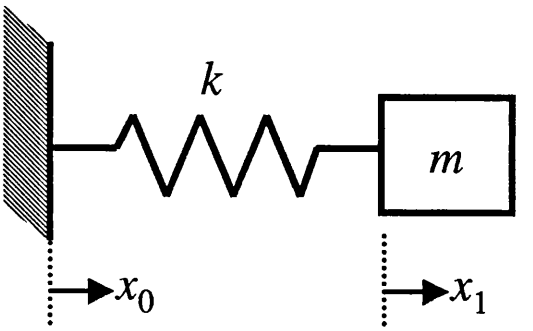

Figure 2.3: A one–dimensional simple harmonic oscillator with spring constant k and mass m. The mass is constrained to move frictionlessly in one direction (horizontal).

2.2 Passive Isolation

Large amounts of isolation can be achieved by cascading passive isolators. Passive isolators are, fundamentally, anything with a resonance. Mechanically, it is typically something heavy on something soft. In concept, the soft linkage between the object being isolated and the base prevents the transmitted force from overcoming the inertia of the object being isolated.

Consider the simple harmoic oscillator shown in figure 2.3, and compare the motion of the input, x_0, with the motion of the output, x_1. The restoring force on the mass, m, is supplied by the spring, with spring constant k. Thus, the equation of motion is

$$m\frac{d^2x_1(t)}{dt^2} = -k\left(x_1(t) - x_0(t)\right). \tag{2.2}$$

This equation can be solved in the frequency domain by taking the Laplace transform (with Laplace variable $s = i\omega$) solving for the ratio of x_1 to x_0. Defining the resonant frequency of the system as $\omega_0^2 = k/m$, the response of the isolated object to input motion is

$$\frac{X_1(s)}{X_0(s)} = \frac{1}{(s/\omega_0)^2 + 1}, \tag{2.3}$$

the magnitude of which is plotted in figure 2.4. At low frequencies, $\omega \to 0$, the expression approaches one, and the output of the system matches closely the input.

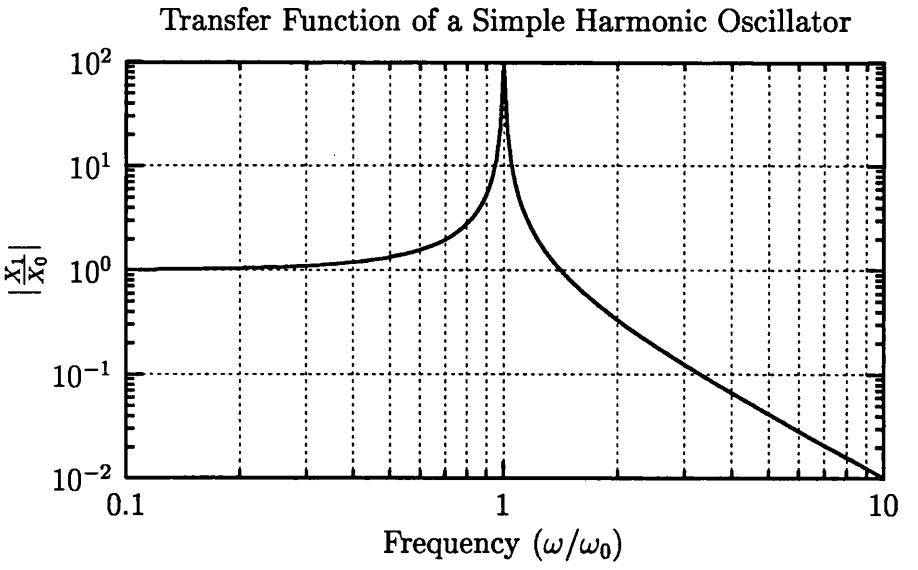

Figure 2.4: Response of a simple harmonic isolator. (Shown here with $Q \sim 100$.)

However, importantly for isolation, at high frequencies ($\omega \gg \omega_0$), the response of the output is $(\omega_0/\omega)^2$. Thus, at frequencies an order of magnitude or more above the resonant frequency of the stage, a great deal of isolation can be achieved.

In any real system, there is some loss in the system, whether this is due to friction, viscous damping, or other mechanism. (In the electrical analogue, the resistance never goes completely to zero.) For the simple oscillator described above, some viscous damping may be introduced as a force proportional to the relative velocity, $F_v = -k_v\,(v_1 - v_0)$. This represents, for example, the motion of this oscillator in air; the faster the mass moves, the proportionally more air molecules it encounters. Then, the equation of motion is

$$m\frac{d^2x_1(t)}{dt^2} = -k\,(x_1(t) - x_0(t)) - k_v\frac{d\,(x_1(t) - x_0(t))}{dt}, \tag{2.4}$$

and the transfer function from ground input to mass output is

$$\frac{X_1(s)}{X_0(s)} = \frac{2\zeta\,(s/\omega_0) + 1}{(s/\omega_0)^2 + 2\zeta\,(s/\omega_0) + 1}, \tag{2.5}$$

where the damping ratio, ζ, is given for this viscously damped case by $\zeta = k_v/2m\omega_0$. Particularly for systems with very little damping, the system is often parametrized

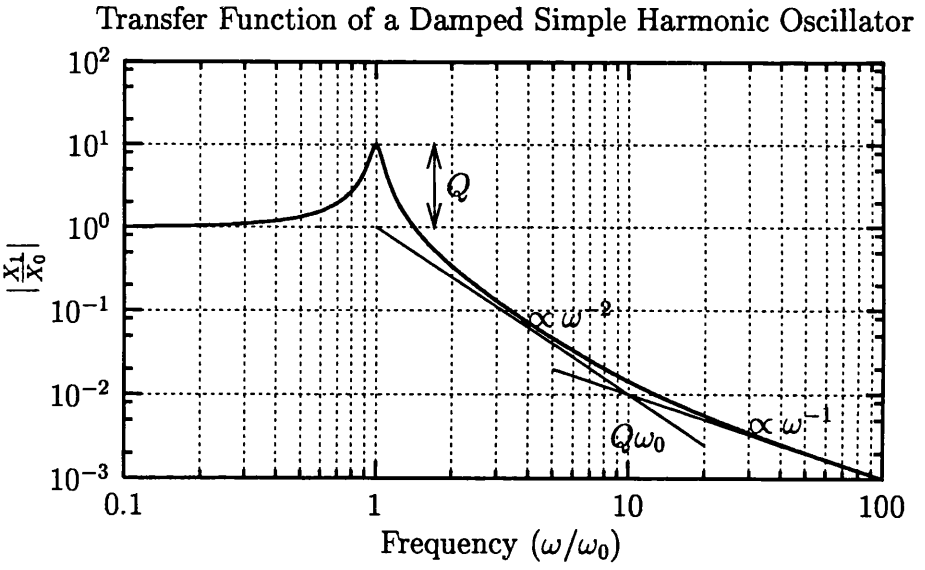

Figure 2.5: Response of a simple harmonic isolator with finite Q

with the quality factor of the resonance, the Q, rather than the damping ratio, ζ, where

$$Q = \frac{1}{2\zeta}. \tag{2.6}$$

The response of a system with $Q \approx 10$ is shown in figure 2.5. There are two important characteristics of the magnitude of the frequency response in contrast to a system with infinite Q. Firstly, the height of the resonant peak at ω_0 is roughly Q times the low frequency response. Secondly, the response of the system is proportional to $(\omega_0/\omega)^2$ above the resonant frequency up to about a frequency $Q\omega_0$. Above this point, the system response falls only as $1/\omega$. These conclusions are drawn for viscously damped systems. For low loss systems, for any form of loss, the system response will fall proportionally to $1/\omega^2$ for frequencies a decade or more above the resonant frequency.

Passive isolation has a number of advantages in comparison to 'active' isolation stages to be discussed shortly. A system is passive in that it supplies no energy to the system and thus requires no energy source. Because it adds no energy to the system, it is guaranteed to be stable. As it has fewer components than an active system, it can be considered more mechanically and electrically reliable. Its performance is

not sensor or actuator limited.

There are, naturally, disadvantages with relying on passive isolation stages. First is the difficulty in reaching very low frequencies—systems have to be very soft and potentially very large to reach low resonant frequencies. Secondly, these very soft systems when supporting a heavy load have a large static sag. For a vertical resonance of $\omega_0^2 = k/m$, and a gravitational loading of mg, the static sag is

$$\frac{mg}{k} = \frac{g}{\omega_0^2},$$

and a system with a lower resonant frequency will have a greater sag. In addition, while small errors in the spring constant, k, only affect the resonant frequency by $\sqrt{k}$, they affect the (potentially very large) sag linearly, complicating the initial setup and alignment. The third complication is the resonance behaviour of these systems. Since the isolator amplifies motion on resonance, any disturbance at that frequency (including the Fourier components from a step input or 'bump') can be very large and can persist for many cycles. Finally, systems designed to be soft typically will be under very high stress and thus more prone to creep.

For the size of isolators that will fit inside a GEO 600 vacuum tank of 1 m in diameter, physically realizable stages will have resonances between 1 and 10 Hz. In order to provide the required isolation of approximately 10^{10} at 50 Hz using such passive isolators would require three to four separate stages of isolation.

2.2.1 Isolation stacks

An isolation 'stack' is just a stack of material, alternating massive layers with soft layers. This forms a series of spring–mass resonances as described above. One practical difficulty is that the entire system has to operate in a vacuum. Metal springs can be made very soft to give the desired low resonant frequencies, but they tend to have very high Q in vacuum. For the isolation stack, which is many layers removed from the sensitive optic and thus does not need high Q for the thermal noise reasons to be discussed in section 2.5, the large values of Q cause large excursions of the stack on resonance. In addition, small disturbances can take minutes to decay. In contrast, most materials that provide the softness required for the resonances needed and that are relatively well damped, such as various types of rubber, are

unsuitable for use in vacuum.

The GEO 600 main suspension will use a single layer passive isolation stack in three legs. The compliance is provided by three plugs of silicone rubber (RTV 615), loaded with graphite to reduce their Q. These are enclosed in a bellows to prevent contamination of the vacuum system. The bellows, in turn, is damped to prevent its resonances from having high Q. The net effect of this isolation stage is to provide a horizontal resonant frequency of $\sim$9 Hz and a vertical resonant frequency of 15 Hz, with a Q of approximately 10[49, 50].

2.2.2 Pendulums

Pendulums are a nearly ideal passive isolation element for a gravitational wave detector, because it is physically simple to provide a resonant frequency on the order of 1 Hz with very low loss. The fundamental angular pendulum resonant frequency for a simple pendulum is $\sqrt{g/L}$, such that for initial work the only relevant design parameter is L, the length of the pendulum. Having a low loss isolator is important with respect to the thermal noise, as discussed in section 2.5. The specific advantage of a pendulum system comes from the 'dilution factor' that relates the loss in a pendulum to the loss in the material[39]. In a pendulum, most of the potential energy is stored in the gravitational field, with a small fraction stored in the bending or stretching of the wire. Since the gravitational field is lossless, the loss seen by the pendulum is only the relative contribution of the lossy components of the stored energy. This dilution factor provides a compelling reason for using pendulums as isolation stages.

There are two obvious shortcomings of a simple pendulum. The first is that while it is physically simple to get a resonant frequency in the neighbourhood of 1 Hz, requiring a length on the order of 30 cm, it becomes difficult to reach frequencies substantially below 1 Hz, except by vastly increasing the size of the system or using more exotic geometries. The difficulty of achieving the total necessary isolation for gravitational wave detectors with any single stage of isolation leads to systems designed with multi–stage pendula. GEO 600 includes a triple pendulum, a modified version of which is in the preliminary design for LIGO II. The second complication is that the pendulum may not be as soft in directions other than the longitudinal. For simple pendula, the vertical resonant frequency, in particular, tends to be in the

10's of Hz range. While the sensed interferometer direction, the longitudinal, is the most sensitive, coupling from other degrees of freedom (specifically vertically as per section 2.4.1) means that isolation is required in every direction.

The pendulum stage is the most common physical unit in the interferometer. Since pendulum stages can be used both to provide a quiet 'test mass' as well as to create a quiet base for actuation (a 'reaction mass'), a number of the suspended optics in GEO 600 actually require parallel triple pendulum suspensions, one for the actual optic and one for the actuators.

Specifically, three pendulum stages are required for the GEO 600 main suspension to allow one stage to be made quiet with respect to thermal noise while two stages are made to include the necessary additional vertical isolation. Chapter 3 describes how multi–stage pendulums are modelled in sufficient detail to allow the necessary conclusions about isolation, thermal noise, and control to be drawn in the following chapters.

2.3 Active Isolation

An active isolation system, by contrast, measures the effect of disturbances on the plant and seeks to compensate for them. This has many potential advantages over a purely passive system. Most importantly is that there is not the inherent connection between size and frequency in the stage. Lower frequency performance will still typically require larger components, but for the same physical size a properly designed active system can act at a lower frequency than a passive system. A second significant advantage of an active system is that it is 'solid'—because it measures and reacts to motion, there is never a large, persistent response to a disturbance such as that caused by the resonant peak of a purely passive system. This helps both because of the smaller range of disturbance that can get through as well as the quicker recovery to a 'quiet' situation from a large disturbance. Another fundamental advantage, although perhaps less significant for gravity wave detectors, is that an active system can detect and reduce disturbances generated by or directly onto the isolated object. A passive system, in constrast, can only reduce disturbances which are transmitted to the system through the isolator.

There are reasons that make active systems less desirable in comparison to passive systems. The most obvious reason is cost: an active system requires some structure to support the plant, as would a passive system, plus the sensors, actuators, and control electronics. Secondly is that systems are 'active' in that they require power, either as a finite on–board supply (battery) or needing some connection to the outside world. Thirdly, the fact that active systems can drive the system in response to a disturbance means that they can potentially drive the system in a mistaken fashion—even driving a system unstable. While proper design will avoid this, changes in the plant or disturbance environment or failures of components can cause all but the most robust control designs to become unstable. A final shortcoming of an active system is that, as in any control system, it can only control what it can measure. Thus, the isolation stage will be limited by the performance of its sensor.

There is no sensor available that is sensitive enough to measure a fully isolated gravitational wave detector mirror; if there were, it would avoid the need for the entire isolation system. Thus active isolation alone will not be appropriate for GEO 600. The ideal solution would be to begin with active isolation stages, where the disturbances are largest and thus easiest to sense, to provide very low frequency noise reduction and provide a solid platform for the later, passive stages. The low frequency disturbances, while not in the frequency detection band, provide the majority of the total (root mean square) motion of the mirrors. These can be reduced most effectively by active isolation.

Active vibration isolation includes both feedback and feedforward control techniques. Feedback control measures the response of a plant and compares this to some desired output to generate an error. The controller then uses this error signal to generate a correction. Disturbances that enter the system cause the output to change, which generates a signal used to eliminate the error. Feedforward seeks to anticipate errors by measuring the disturbance. By modelling how the plant will respond to that disturbance, the correction can be generated before error reaches the output. A schematic depiction of feedback and feedforward in an active vibration isolator is shown in figure 2.6.

Feedforward systems depend on accurate modelling of the plant to achieve good performance, whereas feedback systems tend to be more robust. However, since

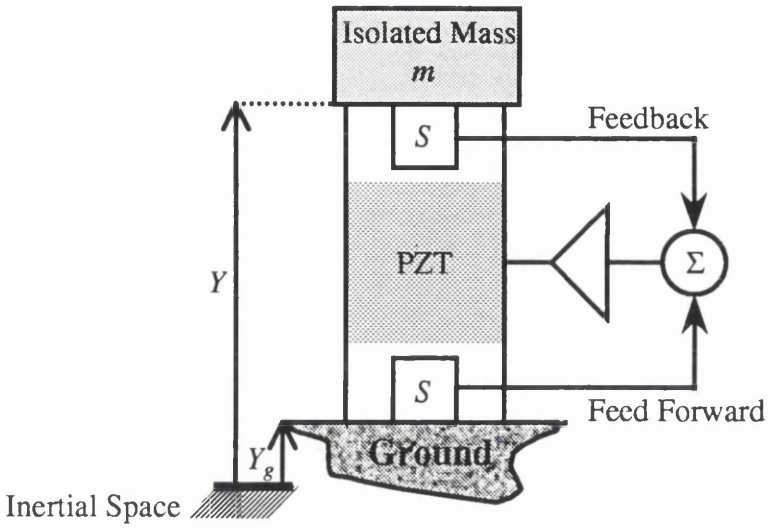

Figure 2.6: A schematic active isolation system. A sensor, S, is attached to the isolated mass. This is typically a small geophone. It provides a feedback signal to an actuator, shown here as a piezo–electric transducer (PZT), which adjusts the position of the mass. A second sensor directly measures the input ground motion to provide a feedforward signal.

there is no direct connection between the output of a feedforward system back to its input, a feedfoward system will not cause instability; even if a system were to undergo severe changes, a feedforward system would only add extra noise to the system. Because a feedforward system anticipates the disturbance before it has time to affect the plant, the effective bandwidth of a feedforward controller can be substantially higher. However, a feedforward system is only effective against the measured disturbances and will do nothing against plant generated disturbances, noise in the controller, or plant resonances. In this fashion, feedforward controllers augment feedback controllers.

2.4 Six Degrees-of-Freedom

Rigid bodies have six degrees of freedom (DOF) in three dimensional space—three translation and three rotation. A multiple–stage pendulum suspension, properly speaking, has a number of rigid body modes equal to the number of masses times six. These different degrees of freedom are not of equal importance to the sensitivity

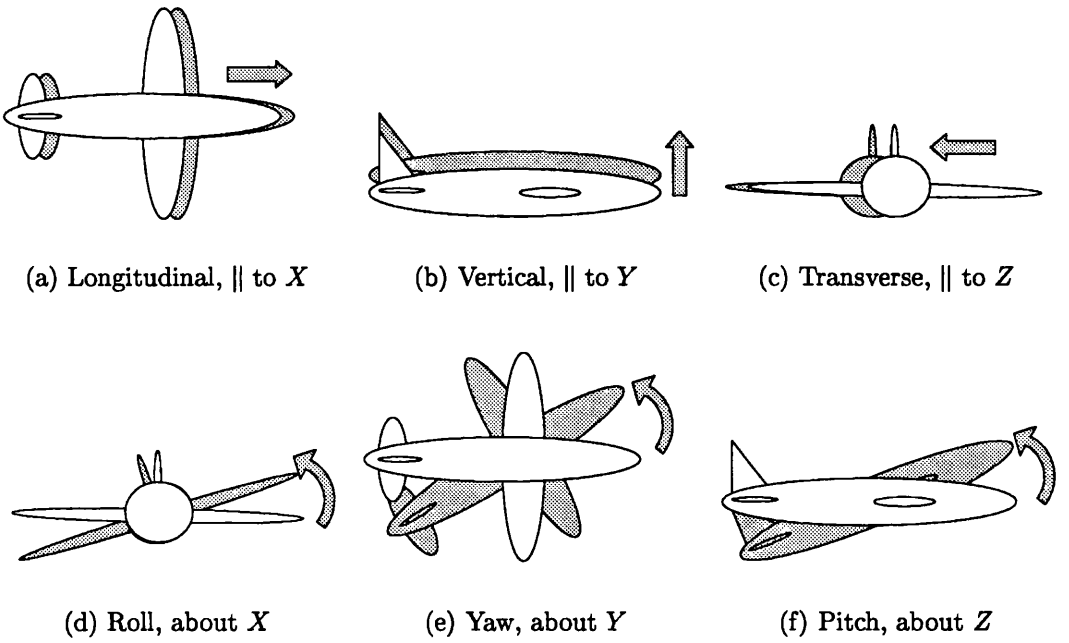

(a) Longitudinal, || to X (b) Vertical, || to Y (c) Transverse, || to Z

(d) Roll, about X (e) Yaw, about Y (f) Pitch, about Z

Figure 2.7: Naming convention of the degrees of freedom of a rigid body. Figures (a) through (c) illustrate translation along a coordinate axis, while (d) through (f) show rotation about the axes.

of the interferometer, but all degrees must be considered to verify the total system performance.

To determine the positions of all the optical components in the GEO 600 system there is a global coordinate system, which is centred on the main beamsplitter. The modelling of each independent suspension is based on a local coordinate system. The naming convention for the motions of an arbitrary body is illustrated in figure 2.7. The positive Y axis is upward, parallel to the pull of gravity, and has translation along which referred to as *vertical* motion; the positive X axis is in the direction of the incoming laser beam, normal to the face of the mirror, and has translation called *longitudinal* motion; the Z axis completes a right handed coordinate system, positive being toward the right when looking out from the face of the mirror toward the incoming beam, and the associated motion is referred to as *transverse*, or *sideways*.

The rotational motions, all defined in a right handed sense, are: *roll*, which is rotation about the X axis; *yaw*, rotation about the Y axis; and *tilt*, rotation about the Z axis.

Note that certain optics do not have an incoming beam normal to the face of the optic; for dynamic modelling, this is unimportant and is why the axes are based off the vertical direction.

Longitudinal/Tilt

The equations of motion of a pendulum in certain degrees of freedom tend to couple together, as explored in detail in section 4.1. Of greatest interest for interferometer sensitivity are the longitudinal and tilt directions. Longitudinal motion couples to first order to a change in optical path length of the interferometer. If the beam strikes the optic at any point not exactly at the same height (vertically) as the centre of mass, tilt motion also couples to the interferometer output to first order. In fact, for most of the multi–stage pendulum systems to be examined, the coupling of tilt and longitudinal motion causes the optic centre of mass to move even for nominally 'tilt' modes.

Sideways/Roll

Mathematically, the sideways and roll directions act the same as the longitudinal and tilt directions, but the parameters are different for realistic suspensions. The

coupling of the beam to the roll direction is very weak, essentially due to imperfections in the surface of the mirror. In addition, since the surface of the mirror is essentially averaged over the beam size, errors of a characteristic length smaller than the beam size do not appear. The first order coupling of sideways motion to the sensed direction is due to the static yaw angle, which can be made small.

Because the wires are attached close to the level of the centre of mass in order to set the coupling in the longitudinal and tilt directions, the wires must be attached at approximately the full width of the mass in the Z direction. This large lever arm, relative to the typical placements in the longitudinal direction for tilt, results in a much higher roll frequency.

Yaw

Yaw motion of the mass couples to optical path length in the same manner as tilt motion, except that for systems that are bilaterally symmetric about the vertical axis, yaw motion does not couple to any other degree of freedom. For essentially vertical wires long with respect to the mass dimensions, yaw tends to be a soft degree of freedom.

Vertical

The vertical degree of freedom is, in many ways, the most interesting direction. While in principal there is no interferometer sensitivity to motion in the vertical direction, there is fundamental coupling to this degree of freedom for any long baseline interferometer, as discussed below. Unless the other isolation stages provide significantly more isolation in the vertical direction than in the horizontal direction, simple wire pendulums do not provide sufficient vertical isolation.

For a system with vertical wires, the restoring force is the extension spring constant of the wires times the number of wires. This spring constant, $k_s = \frac{EArea}{L}$, is proportional to the Young's Modulus of the material, E, and the cross sectional area of the wires, and inversely proportional to the length, L. For a given choice of material, the Young's Modulus is set, while the length is established by the calculations for motion in the longitudinal degree of freedom. Thus, to have a low vertical resonant frequency and a greater isolation requires that the area of the wire be made as small as possible. Since the stress in the wire goes as the loading divided

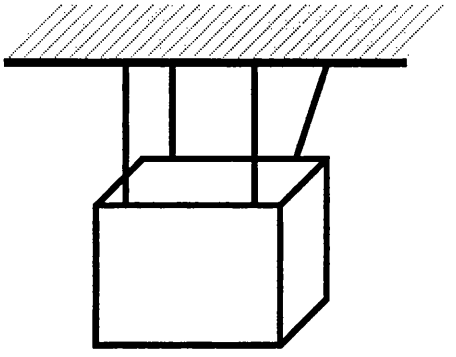

Figure 2.8: Misalignment in a pendulum suspension. One wire is not attached parallel to the other wires.

by the area, this also increases the stress on the wires. So the wire size (diameter) is chosen to give the maximum permissable stress which then effectively establishes the vertical resonant frequency. For materials such as steel, with a Young's Modulus of 1.65×10^{11} N/m and using 25% of the yield stress of 1.5 GPa, a 30 cm pendulum has a vertical resonance of 38 Hz.

2.4.1 Vertical to Horizontal Coupling

In any real physical system, mechanical imperfections will cause motion in one direction to couple to motion in other directions. For example, in figure 2.8, the misalignment of one end of a wire means that vertical motion of the upper connection stretches all of the wires, of which all but one wire gives a purely vertical force on the lower connection, while the misaligned wire gives an unbalanced horizontal force. Similarly, unbalanced tensions in the wires, static twists in the wires, or any other physical imperfections causes similar difficulties. Usually the amount of the cross–coupling, defined as the ratio of the transfer functions from vertical input to horizontal output and from vertical input to vertical output, is extremely small, such that as long as the system provides some isolation in every direction, the motions due to these cross couplings are not significant.

However, for long baseline interferometers, such as full scale gravitational wave detectors, the local verticals at each end of the interferometer—the direction of the gravitational field—are not parallel. This implies that any pure vertical motion locally appears as a horizontal motion of the mirror with respect to the input beam

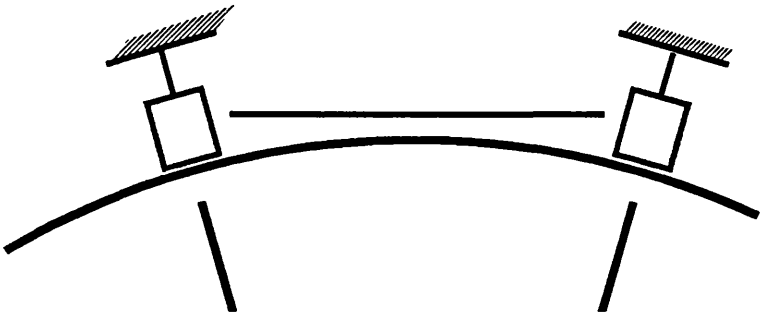

Figure 2.9: The local vertical and the earth's curvature

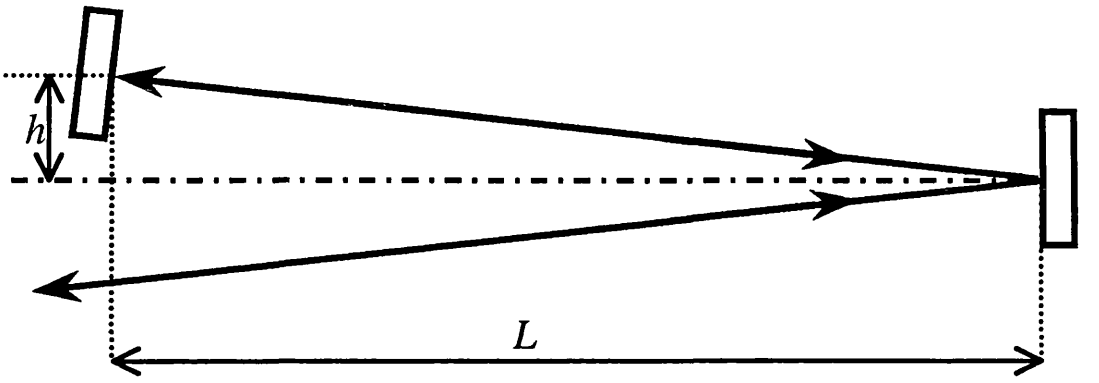

Figure 2.10: Light in one arm of GEO 600

(figure 2.9). The amount of cross–coupling is

$$\frac{X_{beam}}{Y_{mass}} = \frac{L/2}{r_{Earth}}. \tag{2.7}$$

For a 600 m baseline interferometer, such as GEO 600, with the radius of the earth $r_{Earth} = 6 \times 10^3$ km, this causes a cross–coupling of 5×10^{-5}.

The specific optical path of the interferometer can cause additional couplings. In order to increase the effective arm length of the interferometer while using a fixed 600 m long vacuum tube, each arm of the GEO 600 system uses a four pass delay line as shown in figure 2.10. The beam enters each arm, reflects off a mirror at the far end, returns the length of the tube where it reflects off another mirror. The beam then returns along the input path, passing a total of four times down the length of the tube. The return beam ends up $2h = 30$ cm above the incoming beam, to allow

the near mirror to not block the incoming beam. This forces the near mirror to be at an angle h/L to reflect the beam back along the incoming path. This angle causes vertical motion of the near mirror to appear as horizontal motion of the beam at a level of 3×10^{-4}. While it is possible to arrange the optics so that the incoming beam is at an angle, allowing the face of the far mirror to be vertical, this would require mirrors at the input end to be angled, such that this calculation provides an appropriate conservative limit. This level of cross–coupling is present regardless of the form of the pendulum suspension.

The net effect is that while there are cross couplings between every degree of freedom, the difficulty in getting as much isolation in the vertical direction as in the horizontal directions, plus the fundamental coupling from vertical to horizontal, means that this is the most important coupling to evaluate and model. To this point, GEO 600 has assumed that the total cross–coupling comparing vertical to horizontal outputs, including the optical path effects just described plus any additional couplings due to potential misalignments, will be less than 0.1%.

2.4.2 Vertical Isolators: Cantilever Blades

If there is on the order of 0.1% cross coupling between degrees of freedom and the longitudinal resonance of a suspension is approximately 1 Hz while the vertical resonance is approximately 20 Hz, the horizontal isolation of a single pendulum at 50 Hz is on the order of $(1/50)^2$, while the vertical isolation is $(20/50)^2$. If, as is typical, the input vertical motion is comparable to the input horizontal motion, then, including the cross coupling,

$$\left(\frac{0.1}{100}\right)\left(\frac{20}{50}\right)^2 \leq \left(\frac{1}{50}\right)^2,$$

the contribution of the vertical motion to the sensitive direction is less than the horizontal motion. However, for a triple pendulum, an order of magnitude estimate suggests that

$$\left(\frac{0.1}{100}\right)\left(\frac{20}{50}\right)^6 > \left(\frac{1}{50}\right)^6,$$

and the sensed motion along the beam will be dominated by the resulting vertical motion of the mass. This implies that the vertical isolation for a purely wire based

pendulum, barring substantially greater vertical isolation in other stages, would be insufficient.

The pendulum wires being angled in any direction away from vertical causes the restoring force to become softer, as described in the modelling work in section 4.1.1. Except for systems that then use much longer wires and thus result in very wide systems, this degree of freedom can not be made soft enough to permit the expected coupling. Some other method must be used to soften the system in the vertical direction.

In addition, since there is always some coupling between degrees of freedom, due to mechanical imperfections if nothing else, it would be unwise to do a large amount of vertical isolation at one stage and very little everywhere else. The direction that is less well isolated at each stage would couple to, and reduce the effectiveness of the isolation for, the other directions. Therefore it is desired to introduce additional vertical resonances in the middle of the multi–stage pendulum. The compliance introduced by these vertical resonances could affect other degrees of freedom, but this is not necessary and, if it introduces loss and therefore thermal noise, may be undesirable.

One method used to get this extra vertical compliance is a soft spring, specifically a cantilever blade. The specific design for the lower cantilever blades in the GEO 600 main suspension is shown in figure 2.11. These blades have been adapted from the design of the cantilever blades used in VIRGO[51]. They are designed as pure vertical isolators, although introduced in pairs they end up affecting some tilt and roll motions. These may be shaped into an appropriate form[52], for example curved about an axis parallel to its base to allow the blade to be soft with respect to vertical and horizontal movement and rotation about that axis. For the purposes described here, the blades are designed to be flat under load, so that they act as very stiff in five degrees of freedom and soft with respect to vertical deflection. This softness leads to the bladees being highly stressed, in the same manner as the suspension wires. The blades are thus designed to be (approximately) triangular so as to have constant stress—the load lines travel evenly, in straight lines, from the tip of the triangle to all points of the base. For the blades coming to a point, either a single wire or a set of closely spaced wires may connect at the tip.

For a trapezoidal blade geometry, which includes a triangle as a limiting case,

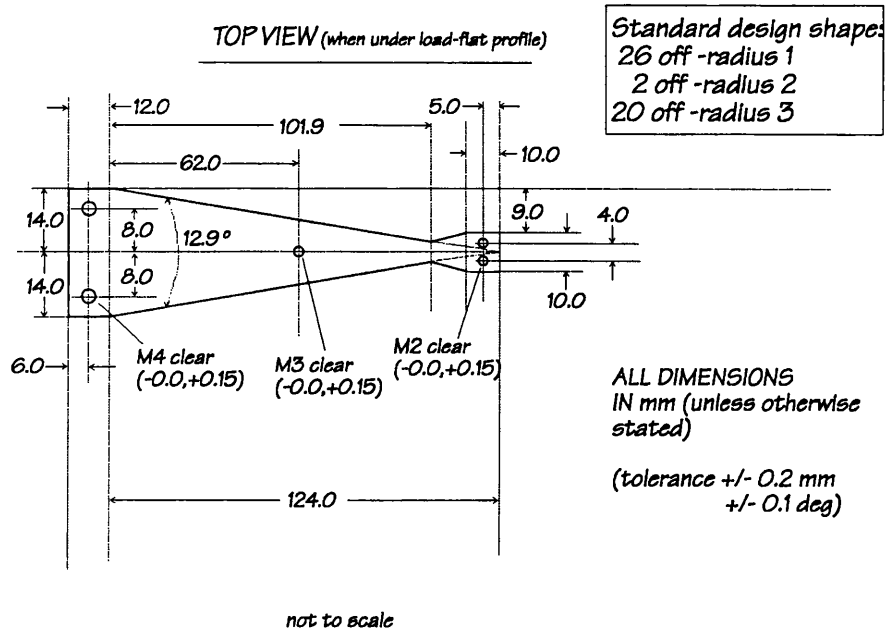

(a)

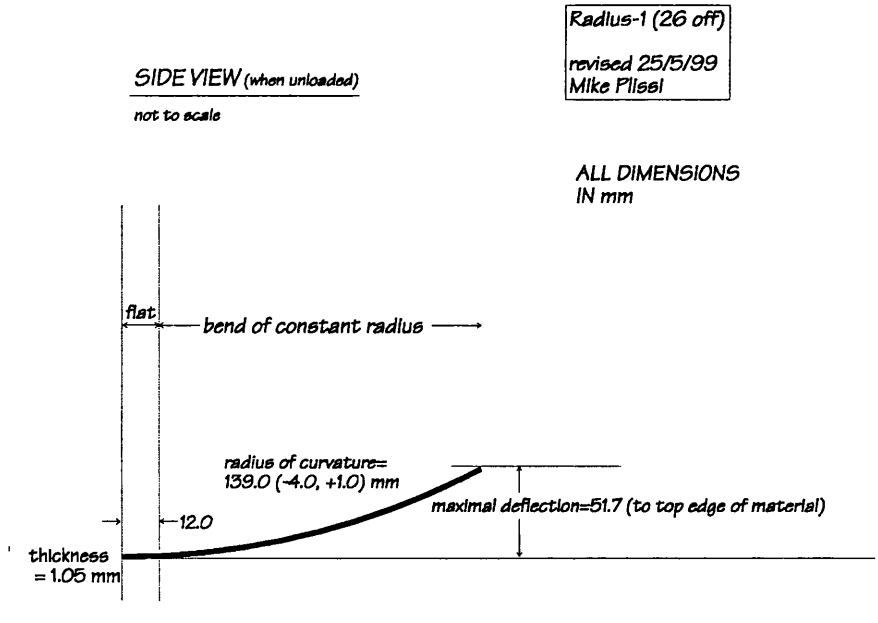

(b)

Figure 2.11: A cantilever blade. This is the mechanical design of the lower cantilever blades used in the GEO 600 triple pendulum suspension (from M. Plissi).

the spring constant of the blade is

$$k_{cant} = \frac{Eah^3}{4l^3\alpha}, \tag{2.8}$$

where E gives the Young's modulus of the cantilever material, a is the base width of the cantilever, h the thickness, l the length, and α a geometrical factor. This factor for a trapezoid is

$$\alpha = \frac{3}{2(1-\beta)}\left(3 - \frac{2}{1-\beta}\left(1 + \frac{\beta^2 \ln \beta}{1-\beta}\right)\right), \tag{2.9}$$

where $\beta = b/a$, and b represents the width at the tip of the blade[53]. The value of α ranges from 1.5 for a triangle to 1.0 for a rectangular blade. Since the actual blades are not exactly trapezoids, having extra width for the clamping of the wires, this factor α is calculated approximately then experimentally verified.

For vertical wires and an ideal, vertical only, cantilever, the appropriate vertical spring constant will be the series sum of the wire and the much softer blade, which will be dominated by the blade. For angled wires and other degrees of freedom, the exact effect of the blades is calculated as in section 3.5. A more detailed examination of the performance of the blades is in section 4.2.2.

2.5 Thermal Noise

The displacement noise in the optics due to the thermally driven fluctuations in the position of the mirror surface is the limiting noise source in the middle frequency band of the detector. In particular, the low end of the detection band is defined by the frequency at which all other noise sources can be reduced below the thermal noise of the test mass. The particular frequency distribution of this noise is a function of the loss of the system.

There are two different types of resonances which contribute thermal noise to the overall noise budget of the system. The higher frequency internal modes of the test mass all add noise in the detection band below their resonant frequencies, while the low frequency modes of the suspension system contribute noise above their resonance. For purposes of the suspension design, the internal modes of the suspended masses are essentially fixed and give a thermal noise level which provides

a target noise floor. The noise contributed by the pendulum modes will be affected by the design of the suspension described in the following chapters.

There is also noise contributed by internal modes of the suspension elements (this includes the 'violin' modes of the pendulum wires). These modes causes additional noise above the noise floor of the detector. Every effort is made to move the frequencies of these modes away from the detection band of the detector.

2.5.1 Fluctuation Dissipation

Every mode of a system has $k_B T$ of thermally averaged energy[54]. This leaves unspecified the spectral distribution of this noise. Callen et. al.[55, 56] determined the relationship between the thermal fluctuations in the system and the dissipation in the system. In particular, the fluctuating thermal force is proportional to the impedance of a system, Z, such that

$$F_{Th}^2(\omega) = 4k_B T \Re\left(Z(\omega)\right). \tag{2.10}$$

The impedance is given by the force required at a point in the system to cause a specific velocity at the same impinging point, $Z = F/v$. This can be expressed in a more useful form by using

$$F_{Th}^2 = \|Z\|^2 v_{Th}^2, \tag{2.11}$$

and writing the power spectral density of the thermal displacement as

$$x_{Th}^2(\omega) = \frac{4k_B T}{\omega^2} \Re\left(Y(\omega)\right) \text{ per Hz}, \tag{2.12}$$

where $Y(\omega)$ is the mechanical admittance, $Y(\omega) = 1/Z(\omega) = v/F$.

Returning to the simple oscillator described in section 2.2, the equation of motion for the damped system, equation 2.4, driven by an input force F with no ground input ($x_0 = 0$) is

$$m\frac{d^2 x_1(t)}{dt^2} = -kx_1(t) - k_v \frac{dx_1(t)}{dt} + F. \tag{2.13}$$

A sinusoidal driving force, $F = F_0 e^{i\omega t}$, will cause the system, after all transients

have died away, to move at the same frequency, such that $x \propto e^{i\omega t}$. Substituting this steady–state repsonse into equation 2.13 gives

$$-m\omega^2 x = -\left(k + i\omega k_v\right) x + F. \tag{2.14}$$

This can be written with a spring constant with an imaginary component as

$$\frac{F}{m} = \left(\omega^2 - \frac{k}{m}\left(1 + i\phi(\omega)\right)\right) x, \tag{2.15}$$

where $\phi(\omega)$ is the loss angle, the angular amount that the system lags behind the driving force.

From equation 2.15, the admittance of the system can be calculated as

$$\frac{v}{F} = \frac{i\omega x}{F} = \frac{i\omega m}{\omega^2 - \frac{k}{m}\left(1 + i\phi(\omega)\right)}, \tag{2.16}$$

which can be inserted into the fluctuation dissipation theorem to give the resulting thermal noise.

This ϕ is related to the Q of the system, the quality factor of a resonance seen in equation 2.6, by

$$Q = \frac{1}{\phi}. \tag{2.17}$$

Typical values of this loss function at room temperature can range from 10^{-3}, for most metals, down to a few times 10^{-9}, for sapphire, but can be a strong function of temperature[57]. The material chosen for the GEO 600 transmissive optics is Suprasil 1, supplied by Heraeus, which has a loss factor of 2×10^{-7} at the internal mode frequencies of the test mass (tens of kilohertz) as measured in the lab in GEO[58, 59]. The proper contribution of the thermal noise from all of the various modes of the test mass based on this loss factor defines the noise requirement at 50 Hz to be $7 \times 10^{-20}\mathrm{m}/\sqrt{\mathrm{Hz}}$[48, 38].

2.5.2 Mechanical Damping

From equation 2.16, if the loss, ϕ, equals zero, the real part of the admittance, and hence the thermal noise, equals zero. Therefore, the presence of any loss in the

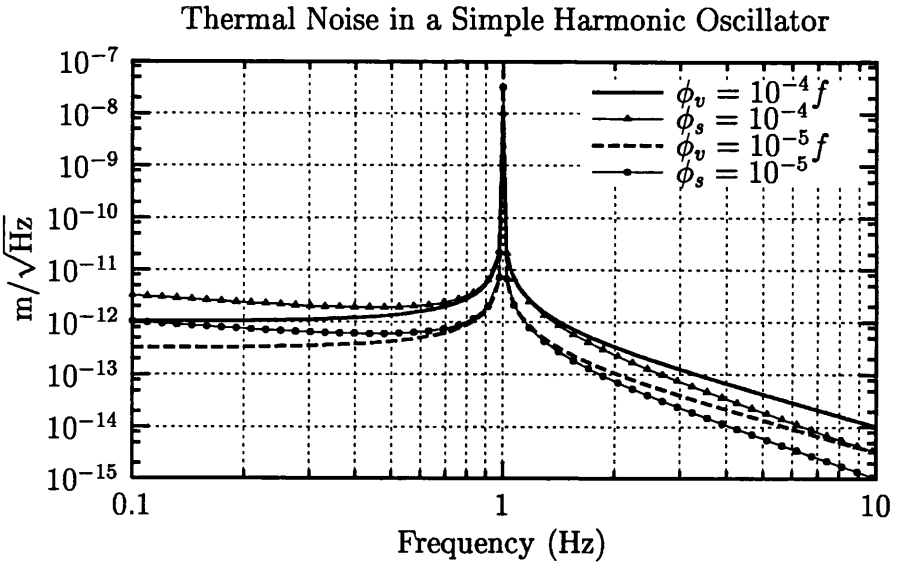

Figure 2.12: Viscous versus structural damping. The figures shows the displacement thermal noise for a simple harmonic oscillator with resonant frequency of 1 Hz, comparing the effects of viscous damping, where $\phi \propto f$, to those of structural damping, where ϕ is constant, for two different values of Q.

system results in a broadband thermal noise.

For the viscous damping considered so far, $\phi(\omega) \propto \omega$. Viscous damping accurately describes some systems, such as motion through a viscous medium. This form of damping does not represent the observed behaviour in many cases however. A more accurate model for most problems of interest in the design of suspensions is given by $\phi(\omega) = \phi_0$, a constant, over a wide range of frequencies[60]. This form of damping is referred to as 'structural damping'.

The displacement noise spectrum of a single degree of freedom oscillator with resonance at 1 Hz is shown in figure 2.12. There are four different cases shown, comparing the effects of viscous damping to structural damping at two different levels of loss. In comparing viscous to structural damping, the losses are chosen to be equal on resonance, such that $\phi_v(\omega_0) = \phi_{v0}\omega_0 = \phi_s$. One pair of curves is plotted for a loss on resonance of 10^{-4}, while the other pair is for a loss on resonance of 10^{-5}.

It can be seen that there is a large peak in the thermal noise spectrum at the

resonant frequency. Far above the resonant frequency, the thermal noise falls proportionally to $(1/f)^2$ for the viscously damped cause, and proportionally to $(1/f)^{5/2}$ for the structurally damped case. Below the resonant frequency, the noise in the viscously damped case is constant, while for the structurally damped case it is proportional to $(1/f)^{1/2}$. Regardless of the exact form of the damping, having less loss concentrates more of the thermal energy into the resonant peak resulting in a lower level of thermal noise off resonance.

To achieve the sensitivity desired in GEO 600 will require systems with very low loss, such that the Q of the pendulum resonance, where $Q = 1/\phi$ at the resonance, must exceed $\sim 10^7$[61]. The exact frequency dependence of the loss can be difficult to experimentally measure, since the effects off resonance are so small. For the control work to be described, this amount of loss is small enough that the controllers can be designed assuming it to be zero. This simple analysis of a single stage, single degree of freedom oscillator must be expanded to examine the noise in a complex, multiple degree of freedom system. This is done for the GEO 600 suspension in section 5.3.

2.5.3 Electronic ('Cold') Damping

The large resonant peaks in the isolation can be measured and suppressed. This reduces the Q seen in the transfer function between, say, seismic input and pendulum motion, but does not increase the off resonance thermal noise of the system since the energy is removed externally, rather than in a internally lossy way, such as by friction. This can be called 'cold' damping, since the observed thermal noise is lower than would be expected for a given Q, equivalent to lowering the temperature of the system.

The ability to do this is important to the operation of the detector. While the thermal noise requirements of the system force the resonances to have high Q, the resulting large amplitude motion would force the detection scheme to operate over an unfeasibly large range. Damping the system also reduces the time required for the system to recover from a disturbance by orders of magnitude. How this is accomplished in the GEO 600 suspension is described in chapter 6.

2.6 Design of Suspensions

A suspension was to be designed to meet the GEO 600 requirements as introduced in this chapter. To predict the performance of a candidate pendulum suspension, a modelling code was developed which is described in detail in chapter 3. The following chapter uses the code to examine the dynamics of the pendulum system as well as other important aspects of the design, such as the cross–coupling and the behaviour of the cantilevers. Chapter 5 then applies the code to address some of the thermal noise aspects of the pendulum design.

Chapter 3

Lagrangian Model

Lagran.mws, the code of which is in Appendix A, is the modelling program that has been developed to calculate the dynamics and thermal noise performance of a multi–stage pendulum system. It uses an energy method, the Lagrangian formulation[62], for the equations of motion. The *mws* extension refers to a '*M*aple *W*ork*S*heet'. *Maple V*[63] is a symbolic mathematics package developed by Waterloo Maple and available on a variety of platforms, including IBM PC compatibles and Unix. The code was developed using release 4 of *Maple V* on a desktop PC using a Pentium II-MMX processor running at 350 MHz and using 384 Mb of RAM. (Full calculations use on the order of 150 Mb of RAM.) Versions of this code have been run on UNIX platforms using release 5. Conclusions that are drawn from the modelling work, particularly those with application to the GEO 600 suspensions, are discussed in the following chapters, particularly chapter 4 for the pendulum dynamics and chapter 5 for the thermal noise results.

This chapter will describe how the modelling is done, including both the theoretical treatment of the problem as well as some of the programming details involved in making the code tractable. In the hope that this program will continue to assist in the design of future suspensions, this chapter will serve as a 'user's manual'. The organization of this chapter will largely follow the organization of the code, although a few topics will be rearranged for clarity. One example is modelling misalignments. The large variety of misalignments tend to be implemented at different points throughout the code. Because of this, and because misalignments are a complication of the basic problem, their treatment is deferred until after full discussion

of a more basic model.

As the model was developed, the symbolic capabilities were used to generate symbolic equations of motion, which allowed comparison with other worked examples, specifically as described in section 4.1 and in Torrie[50]. With the continued evolution of the code, the expressions become more complicated and substantially less intuitive. Because of this, the current version of the code, by default, explicitly outputs very few intermediate steps. To examine any of these steps, one can take advantage of the Maple convention that uses a ';' to terminate a line and show the output and a ':' to terminate a line suppressing the output. It should be noted that some intermediate steps, which are often not simplified until after the numeric calculations, result in very long expressions.

The Lagrangian, L, is defined to be the kinetic energy of the system minus the potential energy of the system,

$$L = KE - PE. \tag{3.1}$$

The energies are written in terms of generalized coordinates of the system, q_i. There is one coordinate for each degree of freedom of the system. Once the Lagrangian is written out, the equation of motion for each coordinate can be expressed as:

$$\frac{d}{dt}\left(\frac{\partial L}{\partial \dot{q}_i}\right) = \frac{\partial L}{\partial q_i}. \tag{3.2}$$

3.1 Coordinates

Any inertial coordinate system is appropriate for these calculations. As we are concerned with the positions of the masses in the multi–stage pendulum, the first choice will be the (x, y, z) positions of the centre of mass of each pendulum mass and the rotations about those same centres of mass, (ψ, ϕ, θ), which are about the X, Y, and Z axes, respectively. The centre of this coordinate system is defined along the nominal line of symmetry in the X and Z directions, level with the top of the top-most wires (see figure 3.1). Note that the Y axis is defined to be parallel to the local gravitational field. The X axis is in the direction of the input optical beam, although the beam itself is not necessarily perpendicular to the vertical axis for long baseline interferometers.

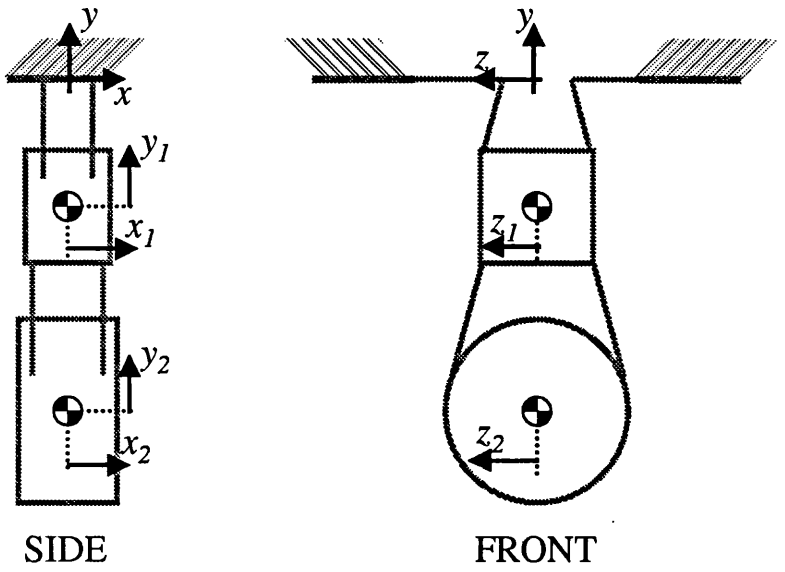

Figure 3.1: The coordinate system for *Lagran.mws*. Illustrates the global coordinates used for each suspension, (x, y, z), and defines the state variables for each pendulum mass, (x_i, y_i, z_i).

In practice, the coordinates as finally used will not be 'global', all referencing the same origin, but instead will be redefined so that each coordinate is measured relative to the nominal position of each mass. This is how each q_i is initially defined, then redefined as

$$q_i \rightarrow q_i + q_{i0},$$

where the q_{i0} give the coordinates of the equilibrium position. In this fashion, the resulting q_i can be guaranteed to be small, allowing first order expansion in the generalized coordinates. The masses are numbered from top down; in a three stage pendulum, the centre of mass of the optic will be at position (x_3, y_3, z_3).

One useful set of coordinates would be the modal coordinates, particularly for evaluation of the loss or 'Q' of each mode. Since, as will be shown, the mode shapes are not obvious and because the physical positions of the masses are the variables measured, modal coordinates have not been implemented.

All the calculations that follow depend on the suspension elements, which will initially be described as wires. The various wires will bend, twist, and stretch which will lead to the forces. The stored energy will be integrated along the wire, where

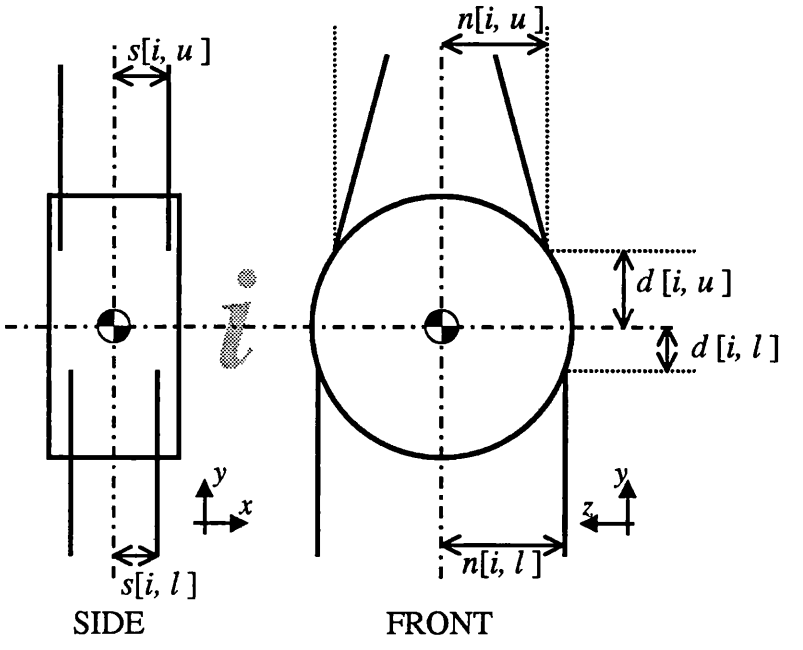

Figure 3.2: Attachment points of wires. The variables s, n, and d show the distances from a wire attachment to the respective centre of mass.

the boundary conditions will be the location of the endpoints of the wire.

The modelling code does not *rely* on any symmetries in the suspension, but recognizing there are often symmetries present, uses them to simplify the inputs. For example, in a two or four wire suspension, the code will place the wires symmetrically about the X and Z axes, requiring only two inputs, the distances from each axis. This is easily changed as necessary. The code does not make any assumptions about forces of symmetric wires canceling or adding; each wire is calculated independently. Thus the results are still correct for any input geometry.

The end of each wire is referenced to the centre of the mass to which it is attached. The endpoint of the first wire is located a distance s from the centre of mass along the X direction; a distance n along the Z direction; and a distance d in the Y direction, as in figure 3.2. With the centre of mass being located at (x, y, z), the end of the first wire is at $(x + s, y + d, z + n)$. The naming convention is

$$\beta[i, w]$$

where $\beta \in \{s, d, n\}$, i refers to the pendulum mass, and w refers to the direction:

'u' for the bottom end of an 'upper' wire, leading to mass $i-1$, and 'l' for the top end of a 'lower' wire, leading to mass $i+1$.

The sign convention for the first wire in any stage is positive s toward positive X and positive n toward positive Z. Since for static stability, wires toward the higher stage in the pendulum chain are typically attached above the centre of mass while those leading to a lower stage are attached below the centre of mass, the convention is that $d[i,u]$ is measured positive above the centre of mass, while $d[i,l]$ is positive for attachments below the centre of mass.

The default locations of the wires, relative to the centre of mass, are

$$\vec{w}_1 = (+s, +d, +n) \tag{3.3}$$

$$\vec{w}_2 = (-s, +d, -n) \tag{3.4}$$

$$\vec{w}_3 = (+s, +d, -n) \tag{3.5}$$

$$\vec{w}_4 = (-s, +d, +n) \tag{3.6}$$

$\vec{w}$ representing the vector to the attachment point. Initially, four wire attachments are assumed. The wires are numbered so that both kinds of symmetric two wire suspensions can be simply input. For one loop of wire, one wire is at each outer edge of the mirror face by setting $s=0$ and $n=t_r$, the test mass radius. For two short wires which are attached to the top of the test mass, one wire behind the other, $n=0$ while s is set equal to the half separation of the wires (and $d=t_r$).

The locations in three dimensional space for these wire connections including displacement and rotation of the masses have the following form:

$$\vec{w}_{i,u,1} = \begin{pmatrix} x_i + s[i,u]\cos(\phi_i)\cos(\theta_i) - d[i,u]\sin(\theta_i) + n[i,u]\sin(\phi_i), \\ y_i - (\sum_{j=1}^{i} H_j) + d[i,u]\cos(\theta_i)\cos(\psi_i) + s[i,u]\sin(\theta_i) \\ \quad - n[i,u]\sin(\psi_i), \\ z_i + n[i,u]\cos(\phi_i)\cos(\psi_i) + d[i,u]\sin(\psi_i) - s[i,u]\sin(\phi_i) \end{pmatrix} \tag{3.7}$$

for $\vec{w}_{i,u,1}$ representing the wire connection for the ith mass, the $u$pper connection, wire number 1. With appropriate permutations in signs of the coefficients, as can be seen in the code, wires numbered two to four follow. For input cases where this symmetry does not hold, the definitions of these points are changed. For cases with fewer than four wires, the extra connections are ignored.

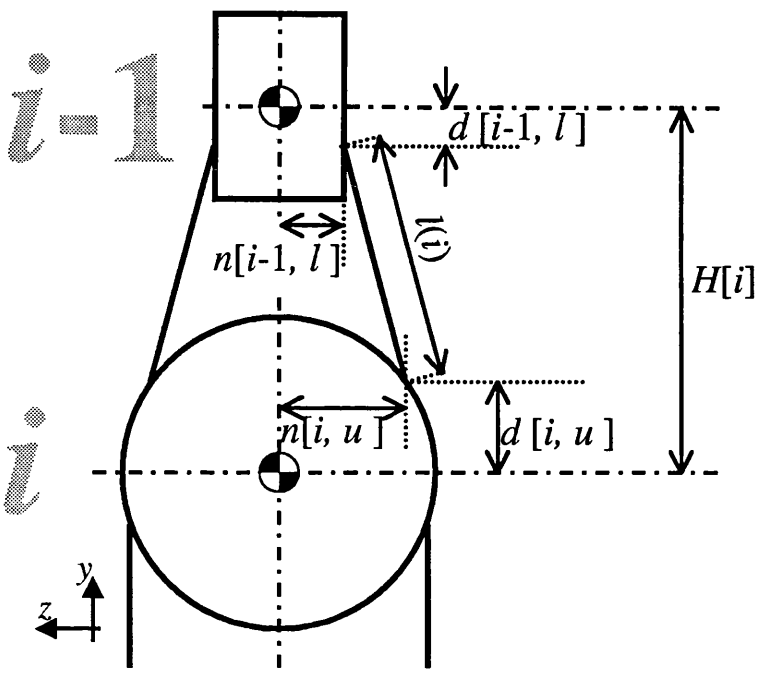

Figure 3.3: The height difference between the centres of mass of the two masses can be calculated from known parameters. $l(i)$ is the (input) length of the wires in the ith stage, and H is the (calculated) height between one mass and the preceding.

The other variable in the Y coordinate is the vertical height between each stage. With the above definitions, the vertical height of each stage, $H[i]$, can be defined such that

$$l_i^2 = (s[i-1,l] - s[i,u])^2 + (n[i-1,l] - n[i,u])^2 + (H[i] - d[i-1,l] - d[i,u])^2 \tag{3.8}$$

the Pythagorean length of the unloaded straight wire, as shown in figure 3.3.

3.2 Inputs

The specific parameters for the model are input toward the beginning of the code. There is some compromise in the naming convention between how concise and how readable the code is. There are two kinds of inputs, broadly speaking. System definitions, which use a Maple assignment statement, such as

$$NumPen := 3; \tag{3.9}$$

are used to define the problem to be solved, in terms of number of pendulum stages, number of wires, and so forth. From a coding perspective, these are variables that control logical branching (*if*) statements and looping (*while* statements). The key is the :=, which in the Maple language defines *NumPen*, anywhere it appears, to be replaced with 3, in the above example. These system definitions include:

- *NumPen*, the number of pendulum stages ranging from 1 to 3 and numbered from top down,
- *'# of wires,u'*, *'# of wires,m'*, and *'# of wires,l'*, the number of wires of the uppermost, middle, and lower stages, respectively, and
- *NumCanU* and *NumCanM*, the number of cantilever blades at the uppermost and middle stages.

Note the Maple convention of using single quotes (' ') to declare an arbitrary string as a variable name. If any of these variables are unused, such as *'# of wires,l'* for a one or two stage pendulum, the code should ignore them, although setting them to zero is appropriate.

The last system parameter is named *Symmetric* and takes a Boolean value of 1 for symmetric systems and 0 for non-symmetric systems. A symmetric system, for purposes of this code, is one for which:

- The equilibrium position is a pure vertical motion away from the model definition. This means that the code solves for the balance of tension and gravity by minimizing with respect to the vertical position of each mass, ignoring any possible X-Z motion or rotation.
- The potentially coupled equations of motion assume only certain cross terms. Specifically, the equations of vertical motion are only functions of the y_i coordinates; the equations of yaw are functions only of the ϕ_i; the longitudinal and tilt motions are coupled equations of only x_i and θ_i; and the transverse and roll motions are coupled equations only in z_i and ψ_i.

Defining a symmetric system as non-symmetric gives the same result, with the usual limits on numerical accuracy, and can be used to verify whether a system is symmetric, by this definition. When possible the flag should be set to symmetric as there is a large saving in computation time. Systems that fit this definition of symmetric include those which are symmetric about both the X and the Z axes, which cover the 'usual' one, two, and four wire pendulum suspensions.

The other category of inputs to the system is the specific set of parameters. These parameters are input in Maple as

$$vars := tr = 0.09, `d[0]` = 0.001, `n[0]` = 0.03, \ldots \tag{3.10}$$

The key Maple difference is that the variables *vars* is assigned, using :=, to a collection of parameters, each of which is set using =. Most of the terms used in the derivation are solved generically, such as the shape of the wire in terms of its endpoints. Then the variable *vars* is substituted into these expressions to get the numbers for each case modelled. The other important convention illustrated here is that Maple uses [ ] to indicate matrix elements, which it prints as subscripts ($\alpha[i] \rightarrow \alpha_i$). Some variables use this to generate subscripts in the output ($A_{x1,x1}$). Maple will not allow, for example, the assumption that d_0 is real since this is interpreted as one element of a matrix. Thus many variables are named using character strings and brackets, such as $'d[0]'$.

Because there are potentially a large number of inputs for each case, common derived variables are grouped in *vars_equations*. For example, the moments of inertia of a cylindrical test mass are

$$I_\theta = m_{TM}\left(\frac{t_r^2}{4}+\frac{t_x^2}{12}\right) \tag{3.11}$$

$$I_\phi = m_{TM}\left(\frac{t_r^2}{4}+\frac{t_x^2}{12}\right) \tag{3.12}$$

$$I_\psi = m_{TM}\frac{t_r^2}{2} \tag{3.13}$$

with m_{TM} being the mass of the test mass, t_r being the test mass radius, and t_x being the test mass thickness (in the X direction). These expressions are defined in *vars_equations*, under the assumption that the test mass is cylindrical. The specifics of the test mass, including t_r, t_x, and m_{TM}, are defined in the variable *vars*. The list *vars_equations* include:

- the moments of inertia of all the pendulum masses, $Ipitch[i]$, $Iyaw[i]$, and $Iroll[i]$
- the extension spring constants of the three wires, $ks_i = \frac{E[wire_i]Area}{Length[i]}$
- the area moments of the wires, $Iwire[i] = \frac{\pi(r[wire_i])^4}{4}$ for a round wire
- the torsion spring constants of wires, $kt_i = \frac{E[wire_i]Iwire[i]}{Length[i](1+\sigma[i])}$
- the cantilever spring constants, $k[cant, u]$ and $k[cant, l]$, in Nm^{-1}
- g, the earth's gravitational constant, as $9.8\mathrm{ms}^{-2}$
- and $H[i]$, the height of each pendulum stage, defined in terms of the inputs in *vars*.

The remaining inputs are set in the variable *vars*. The way the Maple substitution command, *subs*, works, the variables are substituted in the order they are listed in *vars*. Thus to use the terms defined in *vars_equations*, they must be listed first

$$vars := vars\_equations, E[wire1] = \ldots \tag{3.14}$$

Thus when $Ipitch[1]$ is used, the command

$$subs(vars, Ipitch[1])$$

first substitutes the definition of $Ipitch[1]$ from *vars_equations* in terms of the mass and sizes, then substitutes the mass and sizes from the rest of *vars*.

Variables included in *vars*, all in SI (mks) units, are

- the Young's Modulus of the material for each wire, $E[wire_i]$
- the radius of each wire, $r[wire_i]$
- Poisson's ratio for each wire material, $sigma[i]$
- the wire offsets, s, n, and d, as defined in the section on coordinates, section 3.1
- the mass of each pendulum mass, '$mass[i]$', either as a function of the sizes or as a number in kg.
- the length of the wires for each stage, $Length[i]$
- and the dimensions of each mass, for a cubical mass, ix, iy, and iz, or for a cylindrical mass, tr and tx.

Strictly speaking, the Lagrangian as defined here is for a conservative system, a system with no loss. The only loss modelled in the system is the intrinsic loss of the wire material. This is expressed as a complex part of the Young's Modulus,

$$E_i = E_{0,i}\,(1 + i\alpha_i(\omega)) \tag{3.15}$$

as discussed in section 2.5. The important thing in the calculation is that the α_i are the only variables maintained as symbolic until the very last step. This means that the loss in each and every stage may be a completely arbitrary function of frequency, not restricted to the standard viscous and structural damping terms. For example, one example included in the code shows a structural loss which is constant in frequency plus a thermoelastic loss as a function of ω for the third stage wires. Given the noise requirement that losses in the system be small, it follows that the

α_i are small, allowing the various expansions that will be used. These $\alpha_i(\omega)$ are the final inputs and are defined as

$$loss := alpha1(\omega) = \ldots, alpha2(\omega) = \ldots$$

There is also a *loss0* defined, with all the $\alpha_i = 0$, used to greatly simplify calculations where the loss is unimportant.

3.3 Kinetic Energy

The kinetic energy of this system is straightforward, consisting of the translational and rotational kinetic energy of the pendulum masses:

$$KE = \frac{1}{2}m_i(\dot{x_i}^2 + \dot{y_i}^2 + \dot{z_i}^2) + \frac{1}{2}I_{\phi_i}\dot{\phi_i}^2 + \frac{1}{2}I_{\psi_i}\dot{\psi_i}^2 + \frac{1}{2}I_{\theta_i}\dot{\theta_i}^2. \tag{3.16}$$

This has some implicit assumptions about the system.

Firstly, the masses themselves are rigid and thus all their mass moves with the centre of mass. As noted in the discussion about thermal noise in section 4.5, the internal modes of the optics are all in the region of 10 kHz and above, which implies that for frequencies up to the lowest part of the detection band, where this model will be used, the masses can be treated as rigid. This is not strictly true for the uppermost mass, which does not have an optimized cylindrical geometry, however the modes in this mass will still be at least a few hundred Hertz and thus far above the frequencies modelled here (and above the isolation corner frequency near 50 Hz). Specifically for the GEO 600 mass, the structural mode of the mass will be over 300 Hz (section 7.3.3).

The second basic assumption is that there are no other elements in the system that have kinetic energy, with the exception of the cantilever blades as discussed in section 3.5. The primary thing this assumption ignores is the modes of the suspension wires, the 'violin modes'. This is a potentially more problematic assumption since the relevant frequencies could stretch from a few tens of Hertz upwards. For a number of reasons, both scientific and practical, the assumption that these modes can be ignored is used. Because the mass of the wires is very small compared to

the mass of the pendulum masses, for control purposes the dynamics are dominated by the pendulum masses. It is noted that right at the frequency of these wire resonances, the response of the system is affected, both in terms of control dynamics and thermal noise. This is accepted as a shortcoming of the model due to the computational complexity of including the wires properly. While the effects of the wires could have been included for a simple system, enough other complexities were already in the code to render a calculation which included the violin modes numerically intractable. Alternative methods can be used to model these effects, as described in section 6.3.3.

3.4 Potential Energy

There are a number of relevant potential energy terms in the Lagrangian. The code is designed to be as general as possible. For practical designs for interferometer suspensions, certain terms have greater significance. For example, the stored energy due to the bending of the wires can be commented out for calculation of the resonant frequencies of many systems, with no substantial loss of accuracy.

3.4.1 Gravity

These suspensions are constructed in the earth's gravitational field. This, together with the assumption that the suspension elements (wires or flexures) are massless, means that the potential energy due to the gravitational field is

$$PE_g = m_i y_i g. \tag{3.17}$$

Naturally, the gravitational potential leads to a downward force on the masses. This is balanced in equilibrium by a static force proportional to the extension in the wires called tension. (The details of how this is done in the code is described in section 3.6.) The gravitational field is conservative (lossless), which implies that energy stored in this field does not contribute to the thermal noise.

3.4.2 Twisting

The suspension wires, when they twist, cause a restoring force as in a torsional pendulum. For a beam that is twisted, the potential energy is the sum of the energy for each wire in each stage, giving[64]:

$$PE_t = \sum_{i,j} \frac{1}{2} k_{t,ij} (\phi_i - \phi_{i-1})^2 \tag{3.18}$$

where

$$k_t = \frac{EI}{(1+\sigma)l}. \tag{3.19}$$

In these expressions, k_t is the torsional spring constant, E is the Young's Modulus and σ is the Poisson ratio of the wire material, and I is the area moment of the wire. The material constants are determined by the choice of the material, the length l is chosen to set the longitudinal mode, and I by the geometry of the wire. Two typical choices are a round wire of radius r, with $I = \pi r^4/4$, or a flexure, thin in the longitudinal bending direction, with width a, thickness b, and $I = a^3 b/12$.

It is clear that for a single wire, in a torsional pendulum, the twisting which the wire experiences is the differential rotation of the ends of the wire, hence $\phi_i - \phi_{i-1}$. In a system with multiple wires, which are perhaps not straight, differential rotation of the stages clearly bends and stretches the wires as well as twists them. For small motions, these can be calculated independently, and the amount of twist in each wire is still the differential rotation of the stages at each end.

There is no energy stored in rotation for any motion except yaw. Even for yaw motion, in a suspension with multiple wires, the terms due to twisting of round wires are usually not dominant.

3.4.3 Bending

While the dominant terms for pendulum dynamics are gravity, or tension, and the extension of the wires, the solution of the bending potential illustrates one subtlety in the extension of the wires and will be discussed first.

Given an initially straight vertical wire, ζ is the coordinate along the length of the wire (parallel to the Y-axis). The variables $\eta(\zeta)$ and $\chi(\zeta)$ represent the

transverse displacement of the wire, in the X and Z directions, away from the initial wire position. The potential energy stored in the bending of a beam in a plane is determined by the fourth order beam equation[64]:

$$EI_X\eta^{(iv)}(\zeta) - T\eta^{(ii)}(\zeta) = 0 \tag{3.20}$$

where E is the Young's modulus, I the area moment of the wire or flexure in the appropriate plane, and T the tension in the wire. There is an identical equation for bending in the Y-Z plane, which involves $\chi(\zeta)$ and I_Z. The bending of a beam can be split into uncoupled equations, as done here, when describing its bending along its principal axes. As long as the wire or flexure has principal axes parallel to the X and Z axes, true for round wires or constant rectangular cross section flexures soft in the longitudinal direction, this solution holds. This equation does not require that the total displacement be small, which it will not necessarily be, only that the local bending be small, which it will for sensible suspensions. The solution to the beam equation (3.20) is:

$$\eta(\zeta) = \alpha e^{-\kappa\zeta} + \beta e^{+\kappa\zeta} + \gamma\zeta + \delta \tag{3.21}$$

where $\kappa = \frac{1}{\lambda}$, and

$$\lambda = \sqrt{\frac{EI}{T}} \tag{3.22}$$

is the characteristic bending length, E and I are the Young's modulus and area moment of the wire, as usual, and T is the tension in the wire. With no tension, when the bottom end of a hanging wire is deflected, the stiffness of the wire insures that the entire wire bends forming an arc. The characteristic bending length is the length over which the bending of the wire occurs; for a long wire under tension ($l \gg \lambda$), if the bottom end of the wire is deflected, the wire bends mostly at the top, with the rest of the wire nearly straight. Note that the tension can only be accurately determined by solving equation 3.21 for the wire shape to get the stretching of the wire, as discussed further in the next section (3.4.4).

The boundary conditions for this equation for each wire are straightforward. The position of each endpoint is exactly that defined in the description of the coordinates,

section 3.1, in terms of x and z directions. The y coordinates of the points gives the range of ζ. How the wire is attached at these points is unspecified in the initial setup. Wires are sometimes clamped between two flat surfaces or welded or bonded, again onto a flat surface. This is typically flush with a vertical surface of the mass. (If necessary, this can be changed for specific cases.) While the optics will be cylindrical, even here the wires are connected to a flat ground on the side of the mass. This same condition is approximately true for wire attachments using 'breakoffs', small pieces attached to the side of a mass to explicitly determine where a wire loop comes in contact with the mass. The wire curves around the breakoff such that at the point of contact the slope is tangent to the breakoff. For nearly vertical wires, this tangent is approximately vertical. This gives the boundary condition for the slope of the wire—it is equal to the 'slope' of the mass, which is the angle in the proper direction. Thus, the boundary conditions for η, corresponding to bending of the wire parallel to the X axis, are:

$$\eta(0) = (\vec{w}_u)_x \tag{3.23}$$

$$\eta\left((\vec{w}_u)_y - (\vec{w}_l)_y\right) = (\vec{w}_l)_x \tag{3.24}$$

$$\eta'(0) = \theta_u \tag{3.25}$$

$$\eta'\left((\vec{w}_u)_y - (\vec{w}_l)_y\right) = \theta_l \tag{3.26}$$

The boundary conditions in the other direction, bending parallel to the Z axis, are similar, replacing x coordinates with z and θ with ψ, for the equations in $\chi(\zeta)$.

The stored energy of the jth deformed wire in the ith stage is:

$$PE_{bend,ij} = \frac{1}{2}E_i \int_0^{\delta y_j} \left(I_{i,\eta} \left(\frac{\partial^2}{\partial \zeta^2} \eta_j(\zeta) \right)^2 + I_{i,\chi} \left(\frac{\partial^2}{\partial \zeta^2} \chi_j(\zeta) \right)^2 \right) d\zeta \tag{3.27}$$

where the variables are as before, I being the area moment with respect to each transverse direction, and δy_j being the vertical component of the wire length. The second derivative with respect to ζ gives the curvature in each direction along the wire. The curvature times the Young's modulus and area moment gives the stored energy, which is integrated along the wire.

It should be noted that for readability in the code, the potential energy terms are listed in order. The integral of the curvature for the bending energy is shown,

although this is actually a place holder in the code. The real calculation of the bending energy, in the manner described above, is further along in the code.

3.4.4 Stretching

The wires also act as springs in extension. The stiffness of the wires is equal to the stiffness of the material, the Young's modulus, E, times the cross sectional area, $A = \pi r^2$ for a round wire, divided by the length:

$$k_s = \frac{EA}{l}. \tag{3.28}$$

With that spring constant, the stored energy becomes $\int_0^l Fx\ dx$, which for constant sized wires gives the potential energy for the entire system as:

$$PE_{stretch} = \frac{1}{2} k_{s,ij} (\delta l_{ij})^2. \tag{3.29}$$

During development, the length of the wire was initially defined as the geometric distance between the two end points of the wire,

$$\begin{aligned} l_i &= \sqrt{(x_u - x_l)^2 + (y_u - y_l)^2 + (z_u + z_l)^2} && (3.30) \\ &= f_{geom}(\vec{w}_l, \vec{w}_u). && (3.31) \end{aligned}$$

The initial length, l_0, is an input variable used in this expression to determine the initial y_i.

This function for the geometrical distance, f_{geom}, is not sufficiently accurate as a length measurement to be used for thermal noise calculations. The actual length of the wire must be found by solving for the shape of the wire as a deformed beam loaded under tension, similar to what is done in the bending calculation in section 3.4.3. The case for a single vertical wire and a simple translation is shown in figure 3.4, where the difference in length is obvious. The manner in which it is calculated merits some discussion.

For this small displacement, x, the distance between the endpoints is $l_{geom} = \sqrt{l_0^2 + x^2}$. The proper shape of the wire could be taken directly from equations 3.21–3.26. Knowing the shape of the beam, in terms of $\eta(\zeta)$ and $\chi(\zeta)$, the length of

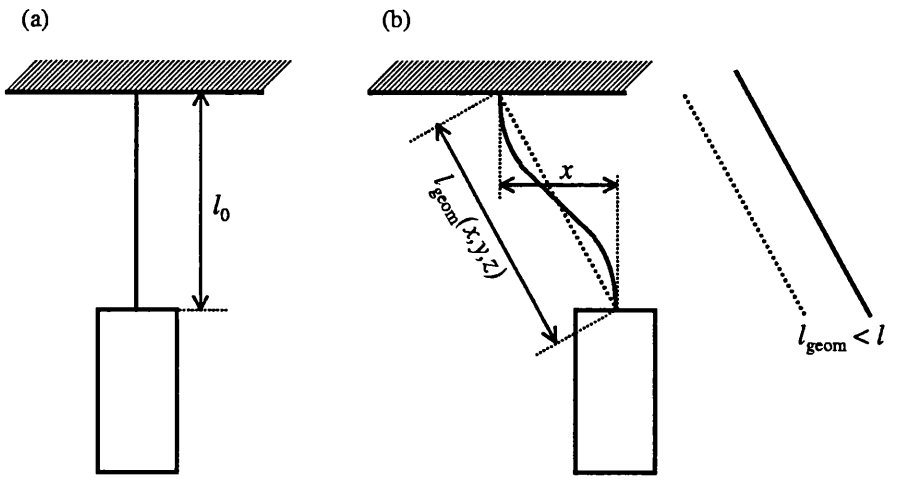

Figure 3.4: Length of a deformed wire. Figure (a) shows a vertical wire of length l_0. (b) shows the wire after the bottom end point has been displaced to the right a distance x and lines illustrating the distance between the end points versus the proper length of the wire.

the deformed wire is just

$$l_i = f_{4th}(\vec{w}_l, \vec{w}_u) = \int_0^{\delta y} \sqrt{1 + \left(\frac{\partial}{\partial\zeta}\eta(\zeta)\right)^2 + \left(\frac{\partial}{\partial\zeta}\chi(\zeta)\right)^2}\, d\zeta, \qquad (3.32)$$

the Pythagorean distance for each vertical $d\zeta$ integrated from the top to the bottom of the wire. It would be computationally desirable to expand this, as a binomial expansion, to remove the square root. Unfortunately, there is no guarantee that $\frac{\partial\eta}{\partial\zeta}$ and $\frac{\partial\chi}{\partial\zeta}$ are small. The solution to this is to use a different coordinate system for solving the wire shape.

Rather then integrating along a vertical axis, with the limits being the y coordinate distance between the end points of the wires, an axis which lies along the straight line connecting the end points of the wire is used. This corresponds to the dashed line shown in figure 3.4. The length of this line, as already calculated, is simply l_{geom}. The boundary conditions to the beam equation are also updated. By defining the new axis to pass through the end points of the wire, the displacements

are defined to be zero, as:

$$\eta(0) = 0 \tag{3.33}$$

$$\eta(l_{geom}) = 0 \tag{3.34}$$

$$\chi(0) = 0 \tag{3.35}$$

$$\text{and } \chi(l_{geom}) = 0. \tag{3.36}$$

The wires are still assumed to connect flush with the surface of each mass. With these new coordinates, however, the slopes are not identically equal to the angle of the mass. Instead, the slope of the wire at each end is the rotation of the mass combined with the slope of the new axis. For small angles, the slope due to the rotation of the mass is $\tan(\theta_i) = \theta_i$ or $\tan(\psi_i) = \psi_i$, respectively for η and χ; the angle of each axis is simply $\frac{x_u - x_l}{y_u - y_l}$ and $\frac{z_u - z_l}{y_u - y_l}$. With this choice of coordinate system, the slopes are guaranteed to be small, allowing the expansion of equation 3.32 into

$$l_i = f_{4th}(\vec{w_l}, \vec{w_u}) = \int_0^{l_{geom}} 1 + \frac{1}{2}\left(\frac{\partial}{\partial\zeta}\eta(\zeta)\right)^2 + \frac{1}{2}\left(\frac{\partial}{\partial\zeta}\chi(\zeta)\right)^2 d\zeta \tag{3.37}$$

While this may still be a complicated expression for a general wire orientation, it can be solved analytically by the code.

The last point to note is that the solution of η and χ relies on the tension in the wire, which is defined as $k_s\delta l$ and thus depends on the length. For small displacements from equilibrium, with the tension being linear with changes in length, the changes in tension are very small and can be ignored. In initially solving for the equilibrium, the static tension is unknown. In this case, the geometric distance is used to calculate δl and thus an approximate tension, which is used to calculate the proper wire shape and thus the proper length and tension. If it were necessary, this could be iterated, using the newly calculated tension to recalculate the wire shape. Generally this is not required.

For typical wire suspensions, where the wire length is many times the characteristic bending length, λ, the proper integrated wire length is not greatly different from the geometric distance between the endpoints. Therefore, the magnitude of the restoring force is not substantially different. The importance comes when considering the loss in the system. If the pendulum mass were to oscillate along the arc

of a circle, the geometric distance would remain the same while the static tension would provide the restoring force. If the integrated length of the wire were not used, with no dynamic change in the length of the wire there would be apparently no loss due to extension. From a calculation of the shape of the wire, the actual change in length in the wire and hence the resulting contribution to the observed loss can be obtained.

3.5 Cantilevers

The cantilever blades are used in the upper stages of the pendulum suspension, where their possible thermal noise contributions are filtered by the lower stages of the pendulum. The initial assumption is that the blades act as pure vertical springs, with one soft direction and infinitely stiff in all others. The cantilever coordinates are defined relative to their equilibrium position, which is designed to be level. The coordinate, $yc[w,i]$, is the distance, normal to the flat blade, of the tip of the blade from the equilibrium, w referring to which set of blades, u upper or l lower, and i to which blade of the set. As defined in section 3.1, the input $d[j,l]$ gives the distance below the centre of mass of the wire attachment. A cantilever motion in the positive direction moves this point upward, effectively replacing $d[j,l]$ with $d[j,l] - yc[w,i]$.

The potential energy of the cantilevers, acting as pure springs, is simply

$$PE_{cant} = \sum_{i=1}^{NumCan} \frac{1}{2} k_{cant} \left(yc[w,i]\right)^2 . \tag{3.38}$$

In an effort to use the coordinates of the pendulum masses as the only relevant variables, the cantilever coordinates were originally to be eliminated, by first minimizing the potential energy with respect to them as

$$\frac{\partial PE}{\partial yc[u,i]} = f(x_j, y_j, z_j, \ldots, yc[u,i]) = 0, \tag{3.39}$$

giving a set of equations in terms of the centre of mass coordinates and each cantilever coordinate, and then substituting. The order of expansion of these equations that is required to include loss accurately is high enough that this method of solution proved to be computationally intractable.

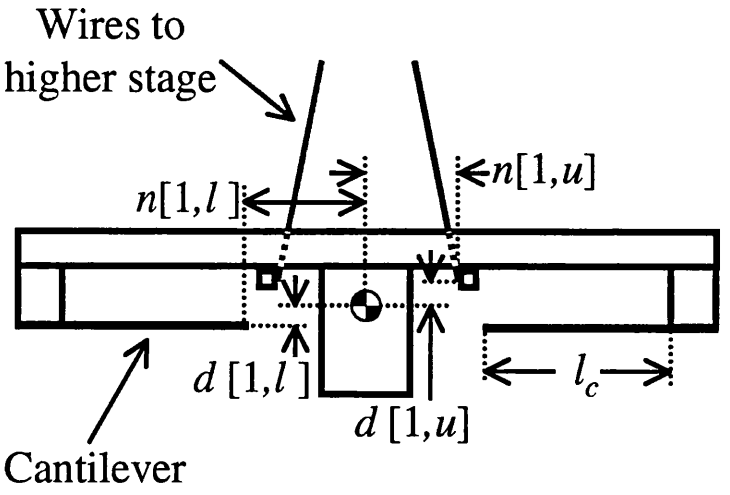

Figure 3.5: The input parameters for a system with cantilevers. The lower wires are attached at the tip of the cantilever blades, which are shown with length l_c. Even though the mass may have a more complicated geometry in order to support the cantilevers, the parameters of the wire spacings, s, n, and d, are defined exactly as in other stages.

Instead, the way the cantilevers are currently included in the code is the same manner as described in the discussion on their behaviour with respect to their centre of percussion in section 4.2.2. This had the added advantage of giving a more realistic model of these non-ideal blades. Each cantilever coordinate is another state variable of the system. The kinetic energy of the cantilevers is included. The blades are assumed to remain flat as they bend. While this is not strictly accurate, this will not cause any great errors since the kinetic energy of the blades is small compared to the energy in the masses (as verified in section 4.2.2). The base of a cantilever moves the same amount as the point of the mass to which it is attached. This point is very similar in terms of input parameters to the relevant wire attachment point, except instead of being a distance $n[l, i]$ from the centre of mass in the z direction, it is a distance $n[l, i]$ plus the length of the cantilever blade, l_c. The position of the tip of the cantilever is the same as the position of the wire connection. Both of these are shown in figure 3.5.

Given the positions of both ends of the cantilever blade, and assuming it does not deform (remains flat), the kinetic energy is a straightforward calculation. A nearly triangular blade has it's centre of mass $\sim \frac{1}{3}$ of the distance from the base to

the tip of the blade. Thus the motion of the centre of mass is then

$$\vec{x}_{blade} = \frac{2\vec{x}_{base} + \vec{x}_{tip}}{3}. \tag{3.40}$$

The velocity is then the time derivative of this expression. The rotation of the blade, Ω, is just the rotation of the stage to which it is attached plus the relative rotation of the blade, $\arcsin(yc[w,i]/l_c) \approx yc[w,i]/l_c$ for these small motions. The total kinetic energy is then, naturally

$$KE_{blade} = \frac{1}{2} m_{blade} \vec{v}_{blade}^2 + \frac{1}{2} I_{blade} \Omega_{blade}^2, \tag{3.41}$$

which is included in the total kinetic energy of the system. Because the cantilevers only move in the one direction, their rotation in the other directions is a rigid body rotation equal to the rotation of the mass. This has the effect of changing I_{yaw} and I_{pitch} for the masses, but the contribution is small and ignored here.

3.6 Equilibrium

To ensure small motion in all variables, permitting a low order expansion of the equations of motion, this expansion is done about the equilibrium point of the system. First this point needs to be determined. The equilibrium is the point of minimum potential energy with respect to the free parameters. In principle, the partial derivatives of the potential energy, PE, with respect to $q_i \in \{x_j, y_j, z_j, \theta_j, \phi_j, \psi_j\}$ for $j = 1$ to $NumPen$ (plus the cantilever coordinates, $q_i \in \{yc[u,j], yc[l,k]\}$), are all set equal to 0. This leads to a large number of simultaneous numerical equations. A considerably easier problem to solve results from knowing that for pendulum systems, the equilibrium comes from the tension in the wires balancing the force of gravity. The tension comes primarily with the masses sagging downwards. Therefore, the numerical problem that is solved sets all the cantilever positions in a stage to be equal ($yc[u,i] = yc[u,1]$ and $yc[l,i] = yc[l,1]$), then defines the $gravity\_eqs$ to be

$$\frac{\partial PE}{\partial q_i} = 0, \forall q_i \in \{y_1, y_2, y_3, yc[u,1], yc[l,1]\}. \tag{3.42}$$

As noted earlier, the potential energy depends on the tension, which depends on the position, a recursive difficulty. Thus here the tension is explicitly set equal to the spring constant times the geometrical distance between the wire end points, not the proper integrated length of the wire (section 3.4.4). Also to speed the problem numerically, it is realized that the bending potential, which is crucial for the loss calculation, contributes very little to the static equilibrium calculation. Instead of the full potential energy, what is used is an 'equilibrium potential energy' variable,

$$PE\_eq = PE_{grav} + PE_{twist} + PE_{stretch} + PE_{cantilevers}. \tag{3.43}$$

This has all the numeric inputs substituted to form *PE_num*. The solution of the set of equations 3.42, y_{i0}, is assigned to the variable *offset_values*, along with $x_{i0}, z_{i0}, \ldots$ set equal to 0.

For a *Symmetric* system as defined in section 3.2, this solution of *offset_values* is the equilibrium position. For a non-symmetric system (*Symmetric* = *0*), the potential energy (*PE_num*) is multivariate Taylor series expanded to second order about the *offset_values* in the first step of a gradient search for the minimum. The expansion is done to all the state variables of the system, giving the expression

$$PE\_MT2 = \vec{q}_i \mathbf{P} \vec{q}_i + \mathbf{Q} \vec{q}_i. \tag{3.44}$$

This is minimized by setting the derivative with respect to $\vec{q}$ equal to zero, giving

$$\vec{q}_i = \mathbf{P}^{-1} \mathbf{Q} \tag{3.45}$$

for the new solution of *offset_values*. This procedure can be iterated to reach a minimum. For any system which basically involves pendulum wires under tension, this reaches the global minimum.

By minimizing the potential energy, there is no particular constraint on the geometry of the system. The one restriction is that the wires may not buckle, which in practice means all the wires must be under tension. As a practical note, this means that if one wire is defined to be longer than any other wire, the initial calculation of *offset_values* may give a solution where the long wire is not under tension and the iteration will fail. It may still be possible, by manually setting an initial set of

values where all wires are under tension, to iterate to the correct solution.

The minimum gives the equilibrium position in terms of all the variables, q_{i0}. With these, the equilibrium lengths of all the wires can be calculated (using the proper integrated length of the wires) and thus the static tensions as $T = k_s(l_{eq} - l_0)$. To insure small perturbations about this equilibrium, every state variable is replaced by the variable plus offset,

$$q_i \rightarrow q_i + q_{i0}, \tag{3.46}$$

and all further work is done with this new definition of the q_i.

Most of the physical inputs are straightforward inputs to the code, easily measurable, such as the masses of the stages and the lengths of the wires. The exception is the cantilevers, for they are designed to be flat under load. For the desired parameters of the GEO 600 system, prior to loading, the cantilevers can deflect up to six centimetres. To simplify this input, the code provides a shortcut for the cantilevers. Since the cantilevers act in a pure vertical direction, in equilibrium they balance gravity with no other geometric factors. So the initial offset position of the cantilevers which results in them being flat under load is simply

$$yc[u,i]_0 = \frac{\sum_{j=1}^{NumPen} m_j g}{k_{c,u}(NumCanU)}, \tag{3.47}$$

with a similar expression for any lower cantilevers. Thus before the equilibrium calculation is begun, the cantilever coordinates are adjusted with the above offset.

The final subtlety in the equilibrium calculations comes from an understanding of loss and tension. The restoring force from the stretching of a wire is

$$\begin{aligned} k_s \delta l &= k_s(l(q_i) - l_0) && (3.48)\\ &= k_s(l(q_i) - l_{eq} + l_{eq} - l_0) && (3.49)\\ &= k_s\left(l(q_i) - l_{eq}\right) + k_s(l_{eq} - l_0) && (3.50)\\ &= k_s\left(l(q_i) - l_{eq}\right) + T_0 && (3.51) \end{aligned}$$

with T_0 being what is called the static tension. Any loss terms associated with this force enter through the Young's modulus and thus through the spring constant, k_s. T_0 is a constant force in the wire and has no loss. This set of substitutions is done

in the stretching potential energy term in order to calculate the proper loss.

The total potential energy for a potentially asymmetric multi–stage pendulum system ends up with many, many terms. Calculations that are done on these long expressions can use a large amount of memory (easily over one hundred megabytes of RAM, a restrictive amount for a desktop PC system). To limit the amount of memory actively used at any time, the potential energy is broken up into parts,

$$\frac{\partial L}{\partial q_i} = \frac{\partial KE}{\partial q_i} - \frac{\partial PE}{\partial q_i} \tag{3.52}$$

$$= \frac{\partial KE}{\partial q_i} - \frac{\partial}{\partial q_i}\left(\sum_j PEnum_j\right). \tag{3.53}$$

The exact terms in each $PEnum_j$ are somewhat arbitrary. $PEnum1$ corresponds to the gravitational and twisting potential terms. $PEnum2$ and $PEnum3$ are the cantilever potentials, for upper and intermediate blades. $PEnum4$ up to $PEnum6$ as necessary gives the bending potential for each stage of the pendulum. The remaining $PEnum_i$ are the stretching potential for each wire, one value of i for each wire.

3.7 State Space Equations

With the kinetic and potential energy of the system solved in detail in terms of small perturbations about equilibrium, the Lagrangian equations of motion,

$$\frac{d}{dt}\frac{\partial L}{\partial \dot{q}_i} - \frac{\partial L}{\partial q_i} = 0, \tag{3.54}$$

can now be solved. Appreciating that the kinetic energy is only a function of the $\dot{q}_i$ and not of the q_i, while the potential energy is a function of q_i and not of $\dot{q}_i$, the equations of motion for each q_i are then

$$\frac{d}{dt}\frac{\partial KE}{\partial \dot{q}_i} = -\frac{\partial PE}{\partial q_i}. \tag{3.55}$$

Each side of this equation is Taylor expanded to first order in terms of the q_i and $\dot{q}_i$. As this is about the equilibrium, the zeroth order terms should be identically zero, so only the first order terms are generated. Equation 3.55 can then be rewritten in

matrix form as

$$\frac{d}{dt}\left(\mathbf{M}\dot{\vec{q}}\right) = -\mathbf{K}\vec{q}. \tag{3.56}$$

This expresses the system in terms of a mass matrix, **M**, and a stiffness matrix, **K**. For a constant coefficient mass matrix, usual for these systems, this gives

$$\mathbf{M}\ddot{\vec{q}} = -\mathbf{K}\vec{q}. \tag{3.57}$$

This is the step that takes a large amount of computational time. To speed up the calculations, the definition of *Symmetric* is recalled. The appropriate cross-couplings are assumed when *Symmetric* = 1. This implies, for example, that

$$\frac{d}{dt}y_i = c_{ij}y_j + 0x_j + 0z_j + \dots .$$

When *Symmetric* = 1, the code only calculates the assumed non–zero terms and simply sets the other terms equal to zero. (For a single stage pendulum with no cantilevers and no inputs, taking advantage of the stiffness matrix being symmetric means that for *Symmetric* = 0, there are $\frac{6\times6+6}{2} = 21$ elements that are solved for, whereas for *Symmetric* = 1 there are only $1 + 1 + \frac{2\times2+2}{2} + \frac{2\times2+2}{2} = 8$ terms to be solved. These are $k_{yy}, k_{\phi\phi}, k_{xx}, k_{x\theta}, k_{\theta\theta}, k_{zz}, k_{z\psi}$, and $k_{\psi\psi}$.)

For a system with no cantilever blades, the mass matrix is diagonal, consisting of the masses and moments of inertia of the pendulum stages. Most of the computation time is spent on the calculations of the **K** matrix. (Looking ahead to the state space $[\mathbf{A}, \mathbf{B}, \mathbf{C}, \mathbf{D}]$ formulation in equations 3.67–3.68, the coefficients are named A_{q_i,q_j}.) The equations are expanded to first order in each variable, such that

$$A_{q_i,q_j} = -\frac{\partial^2 PE}{\partial q_i \partial q_j}. \tag{3.58}$$

These terms are solved to first order in terms of the losses, that is

$$A_{q_i,q_j} = c_{ij} + \sum c_{ij,k}\alpha_k(\omega). \tag{3.59}$$

The state vector is defined as

$$\vec{q}^T = \begin{bmatrix} x_1 & y_1 & z_1 & \theta_1 & \phi_1 & \psi_1 & \cdots & yc[u,1] & \cdots & yc[l,1] & \cdots & x_0 & y_0 & z_0 & \theta_0 \end{bmatrix} \tag{3.60}$$

of dimension $n \times 1$, for n total states. The state variables include the coordinates for each stage of the pendulum, $yc[u,i]$ and $yc[l,i]$ for the necessary cantilevers, and ground motions as inputs, x_0, y_0, z_0, and θ_0. For consistency in the state space formulation, these inputs are included as state variables in $\vec{q}$ with the corresponding elements of the mass matrix identically 1, giving

$$\mathbf{M}\ddot{\vec{q}} = -\mathbf{K}\vec{q} + \mathbf{B}_{In} \tag{3.61}$$

where $(\mathbf{M}^{-1}\mathbf{B}_{In})^T = \begin{bmatrix} 0 & \cdots & 0 & \ddot{x}_0 & \ddot{y}_0 & \ddot{z}_0 & \ddot{\theta}_0 \end{bmatrix}$.

This matrix equation is converted to a set of first order differential equations, a set of state space equations[65]. The solutions to such a set of equations may be visualized as a trajectory in the state space. This is a generally convenient form for a number of reasons, including the relative simplicity of numerically modelling first order differential equations plus the compactness in handling systems with more than one input or output, as shall be shown. In addition, the states provide a complete internal description of the system, allowing the behaviour of each mass and each degree of freedom to be modelled, not just the measured outputs. The state vector is redefined as

$$\vec{x} = \begin{bmatrix} \vec{q} \\ \dot{\vec{q}} \end{bmatrix} \tag{3.62}$$

Since $\frac{d\vec{q}}{dt} = \dot{\vec{q}}$ and $\frac{d\dot{\vec{q}}}{dt} = \ddot{\vec{q}}$, this results in the first order set of equations

$$\frac{d}{dt}\vec{x} = \begin{bmatrix} \mathbf{0}_{n\times n} & \mathbf{I}_{n\times n} \\ -\mathbf{M}^{-1}\mathbf{K} & \mathbf{0}_{n\times n} \end{bmatrix} \vec{x} + \begin{bmatrix} \mathbf{0}_{n\times n} \\ \mathbf{M}^{-1}\mathbf{B}_{In} \end{bmatrix} \tag{3.63}$$

where $\mathbf{0}$ represents the zero matrix of appropriate dimension and $\mathbf{I}$ the identity matrix.

Rewriting the inputs as a vector

$$\vec{u} = \begin{bmatrix} x_0 \\ y_0 \\ z_0 \\ \theta_0 \end{bmatrix}$$

allows the driving term in the set of equations to be written in a vector form

$$\mathbf{M}^{-1}\mathbf{B}_{In} = \begin{bmatrix} \mathbf{0}_{(n-4)\times 4} \\ \mathbf{I}_{4\times 4} \end{bmatrix} \vec{u}. \tag{3.64}$$

In a similar fashion, the desired outputs of the system are written as a vector $\vec{y}$. Each output is a function of the states of the system, since the state variables by definition fully describe the system. With appropriate small angle approximations, the outputs are linear combinations of the state variables and possibly inputs, such as

- the translational motion of the test mass, $\vec{y}_1 = x_{TM}$
- the sensed motion of a spot a distance d below the centre of mass of a test mass, $\vec{y}_2 = x_{TM} + d\theta_{TM}$
- the motion of a GEO 600 shadow sensor, located on the top surface of the uppermost mass l_ψ away from the centre of mass in the Z direction and l_θ away in the X direction, $\vec{y}_3 = y_1 + l_\theta\theta_1 + l_\psi\psi_1$
- the signal from the above, which is the relative motion between the sensor attached to the ground and the mass, $\vec{y}_4 = y_0 - \vec{y}_3$

or any other outputs that are necessary. These are written succinctly as $\vec{y} = \mathbf{C}\vec{x} + \mathbf{D}\vec{u}$. Note that for a great many cases of interest, $\mathbf{D}$ is identically zero.

To this point, the system has been modelled as if it were a conservative system with a complex Young's modulus, leading to a complex stiffness matrix, $\mathbf{K}$. In analysing the frequency response of a system (Bode plots, for example), the system is in principle driven at a frequency ω until all transients have died away, leaving every state of the system oscillating at the same frequency, $\vec{q}(t) = \vec{q}_0 e^{i\omega t}$. Since each

element of $-\mathbf{M}^{-1}\mathbf{K}$ has been numerically expanded as $c_{ij} + i\sum c_{ij,k}\alpha_k(\omega)$, where the coefficients c are real, this leads to the set of equations in 3.63 being

$$\begin{aligned}\ddot{\vec{q}} &= (-\mathbf{M}^{-1}\mathbf{K})\vec{q} \\ &= \Re(-\mathbf{M}^{-1}\mathbf{K})\vec{q} + i\Im(-\mathbf{M}^{-1}\mathbf{K})\vec{q}\,\frac{\omega}{\omega},\end{aligned}$$

but since $\dot{\vec{q}} = \frac{d}{dt}(\vec{q}_0 e^{i\omega t}) = i\omega\vec{q}$, this gives

$$\ddot{\vec{q}} = \Re(-\mathbf{M}^{-1}\mathbf{K})\vec{q} + \Im(-\mathbf{M}^{-1}\mathbf{K})\frac{\dot{\vec{q}}}{\omega}. \tag{3.65}$$

Combining this with the definition of $\vec{x}$ from equation 3.62 gives the set of equations

$$\frac{d}{dt}\vec{x} = \begin{bmatrix} \mathbf{0}_{n\times n} & \mathbf{I}_{n\times n} \\ \Re(-\mathbf{M}^{-1}\mathbf{K}) & \frac{1}{\omega}\Im(-\mathbf{M}^{-1}\mathbf{K}) \end{bmatrix}\vec{x} + \begin{bmatrix} \mathbf{0}_{(2n-4)\times n} \\ \mathbf{I}_{4\times 4} \end{bmatrix}\vec{u}. \tag{3.66}$$

This equation and the corresponding relation for the outputs, y, can be written concisely in the canonical state space form as

$$\dot{\vec{x}} = \mathbf{A}\vec{x} + \mathbf{B}\vec{u} \tag{3.67}$$

$$\vec{y} = \mathbf{C}\vec{x} + \mathbf{D}\vec{u}. \tag{3.68}$$

The functional part of the code generates this **A** matrix and the **B** matrix for the ground motion inputs, x_0, y_0, z_0, and θ_0. If desired, the components of these matrices can be taken from Maple and translated, for example, to a Matlab compatible form to take advantage of available control packages.

3.8 Inputs and Outputs

Given the set of state space equations 3.67–3.68, the system can be numerically modelled in terms of dynamic response. It can be particularly useful to calculate the performance in the frequency domain. Applying the Laplace transform to the

state space equations for constant coefficient matrices would yield

$$\begin{aligned} \mathcal{L}(\dot{\vec{x}}(t)) &= \mathcal{L}(\mathbf{A}\vec{x}(t) + \mathbf{B}\vec{u}(t)) \\ s\vec{X}(s) &= \mathbf{A}\vec{X}(s) + \mathbf{B}\vec{U}(s) \end{aligned} \tag{3.69}$$

and

$$\begin{aligned} \mathcal{L}(\vec{y}(t)) &= \mathcal{L}(\mathbf{C}\vec{x}(t) + \mathbf{D}\vec{u}(t)) \\ \vec{Y}(s) &= \mathbf{C}\vec{X}(s) + \mathbf{D}\vec{U}(s) \end{aligned} \tag{3.70}$$

with Laplace variable s. Because of the allowed arbitrary nature of the loss function, these matrices may be a function of frequency and may not be a constant with respect to the Laplace transform. As a Bode response calculates the output due to a constant frequency input after all transients have died away, in steady state these matrices are constant for the given ω. (Given a smooth loss function and low levels of loss, this approximation should be good even for not strictly steady state conditions.) Then the equations 3.69 and 3.70 can be solved algebraically to give

$$\frac{\vec{Y}(s)}{\vec{U}(s)} = \mathbf{C}\left(s\mathbf{I} - \mathbf{A}\right)^{-1}\mathbf{B} + \mathbf{D}, \tag{3.71}$$

where $s = i\omega$, which is the set of transfer functions of the system from all the inputs in $\vec{u}$ to all the outputs in $\vec{y}$.

It is only at this stage that the loss functions, α_i, are substituted into the dynamics matrix $\mathbf{A}$ or the resulting transfer function expression. By first solving and expanding in terms of the α_i, arbitrary (small) loss functions are easily included. In addition, if constant coefficient matrices are desired for control design or other reasons, viscous damping or zero loss can be substituted without recalculating the entire system dynamics.

The state space formulation can easily deal with multiple input, multiple output (MIMO) systems. The Maple code generates representative inputs from the top of the suspension. These are nominally from the ground, $\mathbf{B}_{gr}$, although in practice from the top of an isolation stack, the rotation stage in GEO 600, or some other interface. These inputs are used to calculate the isolation performance of the suspension or cross coupling in isolation. The corresponding outputs are initially state

variables, such as x_{TM} for calculating longitudinal motion of the system from either longitudinal input or vertical input through cross-coupling. The elements of the corresponding row of the output matrix, **C**, are for this case all zeros except for the relevant state. The term describing direct coupling of input to output, the **D** matrix, is identically zero for these cases.

Recognizing that the **B** matrix gives the coefficients for inputs in the equations of motion, it is a simple matter to state other useful inputs. For control purposes, the system applies force (through a coil-magnet pair) onto one of the pendulum masses. From Newton's second law of motion, $F = m\ddot{x}$, a coil which applies a force purely in the X direction to the top mass has a corresponding column in the **B** matrix in which the element corresponding to x_1 is $\frac{1}{m}$ with all other elements zero. Forces which do not push directly through the centre of mass tend to have a column in **B** which has two (or more) non-zero elements. For example, a longitudinal force applied a distance d below the centre of mass would have the x_i term being $1/m$ and the θ_i term being d/I_θ. These are particularly useful inputs for calculating the performance of the control servos.

Another, just as simple, category of inputs is used for calculating the thermal noise performance. By the fluctuation dissipation theorem, the thermal noise seen at a point is directly related to the impedance seen at that point, $Z = \frac{F}{v}$, as discussed in section 2.5. The model can now directly calculate the admittance, $Y = \frac{1}{Z} = \frac{v}{F}$, calculating the transfer function from the force applied at a point to the resultant velocity at that same point. The relevant column for **B** is exactly as described for any other input force. The desired output is still a state of the system, although a velocity rather than a position variable. With the frequency dependence of the admittance calculated, it is straightforward to get the thermal noise. The fluctuation dissipation theorem gives the velocity thermal noise; as requirements for this problem are usually given in terms of displacement noise, the desired expression is

$$x_{TN} = \sqrt{\frac{4k_B T \Re(Y)}{\omega^2}}, \text{ in } \frac{m}{\sqrt{Hz}} \tag{3.72}$$

as explored in detail in chapter 5.

Calculating the transfer functions by evaluating the matrix expression

$$\mathbf{C}\,(s\mathbf{I}-\mathbf{A})^{-1}\,\mathbf{B}+\mathbf{D}$$

is not necessarily the most numerically efficient. There are algorithms that may be better; they are not used in this Maple code. For a large dynamics matrix $\mathbf{A}$ (which for a triple pendulum system with 2 upper cantilevers, 4 lower cantilevers, and 4 ground inputs would have $(3 \times 6 + 2 + 4 + 4) \times 2 = 36$ states), it is impractical to do the matrix inversion symbolically. If all states are necessary, such as for general asymmetric systems, the coefficients of the $[\mathbf{A}, \mathbf{B}, \mathbf{C}, \mathbf{D}]$, as well as the definitions of the loss variables, α_i, can be copied over to another package such as Matlab[66]. To maintain the general nature of the loss functions, the supplied 'bode.m' function cannot be used. Instead, a new function is defined, which upon taking the frequency argument ω calculates the proper $[\mathbf{A}, \mathbf{B}, \mathbf{C}, \mathbf{D}]$ for that frequency, and passes these 'constant coefficient' matrices to 'bode.m' for evaluation only at that frequency.

There are cases where a smaller dynamics matrix can be used. For a symmetric system where only pure vertical motion is of interest, the only relevant states are the y_i and the cantilever coordinates. There is a routine toward the end of the Maple code that extracts the appropriate states from the total $\mathbf{A}$ and creates smaller $\mathbf{B}, \mathbf{C}$, and $\mathbf{D}$ matrices. For selected cases the matrix inversion can be done symbolically, and then the loss function is included resulting in a straightforward expression for the desired transfer function in terms of ω.

3.9 Misalignments and Other Classes of Input

Because the code generates equations of motion from scratch for each new model, any assumptions made in the inputs are easily changed. Because of the wide possible variety of changes, it is impossible to collect all the changes in a simple header file. Instead the possible changes are all through the setup portions of the code. With an understanding of how the code works, it should be clear what needs to be changed for any desired setup. Some, it is re-emphasized some, of the kinds of changes are described briefly here.

Number of Stages The most straightforward change involves the number of pendulum stages. The code could have been written with purely numbered stages, rather than occasionally referring explicitly to the uppermost mass and so forth. It was not coded this way partially for readability and party due to its historical development. The extension of the code to four or more stages should be very clear.

Wire Connections Most pendulum suspensions used in gravity wave interferometers are two or four wire suspensions. This leads to symmetric systems which can be simply suspended on wire loops and which are designed to be soft in as many degrees of freedom as possible. Alternatively, a wire based pendulum could be built to be stiff in the non-critical degrees of freedom while soft in the longitudinal direction. For a six degree of freedom single stage pendulum, five wires are used to constrain the other degrees of freedom. The various loops in the modelling code count from 1 to *'# of wires,u'*, which can be set to 5. An extra input has to be defined. The section of code that describes the coordinates of the wire points, as per section 3.1, requires one additional line for the upper connection and one line for the lower connection, with appropriate values. With this change, the code now models five wire suspensions. An example of such a suspension is evaluated in section 4.4. For simple misalignments, rather than adding an entire new connection, one of the defined connections can have a small offset added to it.

Wire Lengths In one of these five wire suspensions, to keep the tensions and thus the violin modes the same in each wire is likely to require the wires to be different lengths. Alternatively, the wire lengths in any suspension may vary slightly, due for example to the difficulty in accurately welding the fused silica fibres in the final stage of a suspension. In this case, rather than using $\delta l = l(q_i) - l_1$, where l_1 is the input length of the first stage wires, l_1 can be replaced in the definition of δl by the necessary length for each wire. This can be done with a *case* like structure for the different wires, or a conditional *if* for a simple permutation. Logically, this gives

$$l_j = l_0 + \begin{cases} 0 & \text{for } j \neq 1 \\ \delta & \text{for } j = 1 \end{cases},$$

which is implemented in Maple as

$$l_j = l_0 + \text{`if`}(j = 1, delta, 0).$$

The first argument of 'if' is the logical test, followed by the value for true, and lastly the value for false.

Spring Constants This same conditional statement can be used to vary any other parameter, such as the extension spring constant of the wires. In the definition of the stretching potential, the *ks1* can be multiplied by the same form of conditional statement to get small variations in the constant of one wire. Note that changes to the definitions in potential energy should be done to both PE and PE_{eq} in order to find the proper equilibrium position as well.

Flexures Flexures of constant cross section can be used instead of round wires. Strictly speaking, the flexures need to have their principal axes parallel to the X and Z axes, which would be true for a rectangular strip soft in the longitudinal direction. To implement this requires a number of changes. The cross section influences the torsional and stretching spring constants. It also affects the moments in the calculation for the shape of the wire, affecting both the bending and stretching energies. Although some care must be taken to ensure completeness, these changes are all straightforward.

Split Pendulums The code was designed to model a multi–stage pendulum constructed in a single chain, one stage connected below another. The code can, with simple modifications, solve other geometries. For example, consider the modelling of a two stage pendulum hanging in front of a two stage reaction pendulum, both suspended from a common uppermost mass, as illustrated in figure 3.6. This system could be modelled in four simple steps. Firstly, for a symmetric system, the equilibrium position of the full system, balancing gravity and tension, is simple to calculate, and the explicit statement of this equilibrium position would replace the numerical solution in the code. The next step involves modelling three elements of this pendulum, the uppermost mass and the two masses comprising one of the lower pendulums. The coefficients of the dynamics matrix, **A**, would be correct with no

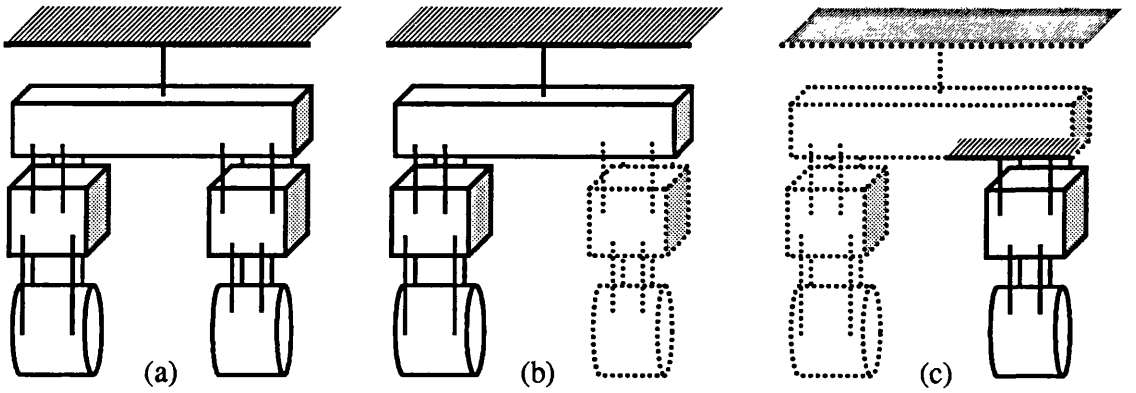

Figure 3.6: Split pendulum configuration with common uppermost mass. Figure (a) shows a two stage pendulum and a (not necessarily identical) two stage reaction mass pendulum hanging from a common uppermost mass. Figures (b) and (c) show the subsystems that can be modelled using the unmodified code to give the correct results for the full system.

other changes—the influence of the motion of the lower masses on the uppermost masses would be calculated correctly, and vice versa. This intermediate result is saved. Thirdly, the other lower two stage pendulum is modelled using the uppermost mass as the input state (so as not to remodel the effects of the uppermost wires in the suspension). Finally, these results are concatenated with the previous results; using $\vec{q}_1$ to represent the state vector associated with the uppermost mass, and $\vec{q}_2$ and $\vec{q}_3$ the states for the two stage pendulums, the results would be

$$\begin{aligned} \ddot{\vec{q}}_1 &= \mathbf{A}_{11}\vec{q}_1 + \mathbf{A}_{12}\vec{q}_2 \\ \ddot{\vec{q}}_2 &= \mathbf{A}_{21}\vec{q}_1 + \mathbf{A}_{22}\vec{q}_2, \end{aligned}$$

and

$$\ddot{\vec{q}}_3 = \mathbf{A}_{31}\vec{q}_1 + \mathbf{A}_{33}\vec{q}_3.$$

Using the symmetry of the stiffness matrices, the effects of $\vec{q}_3$ on $\vec{q}_1$ can be calculated, and all these results can be combined to give

$$\begin{aligned}
\ddot{\vec{q}}_1 &= \mathbf{A}_{11}\vec{q}_1 + \mathbf{A}_{12}\vec{q}_2 + \mathbf{A}_{13}\vec{q}_3 \\
\ddot{\vec{q}}_2 &= \mathbf{A}_{21}\vec{q}_1 + \mathbf{A}_{22}\vec{q}_2 \\
\ddot{\vec{q}}_3 &= \mathbf{A}_{31}\vec{q}_1 + \mathbf{A}_{33}\vec{q}_3
\end{aligned}$$

with no other changes to the modelling code. If this method proved unsatisfactory, the logic of the code could be extended by adding wire connections in the relevant locations to generate an arbitrary geometry. The functions that calculate the different energy terms can be used to easily extend this.

3.10 Summary

The Maple code *Lagran.mws* solves the dynamic equations of motion for a wide class of pendulum suspensions for gravitational wave interferometers. Its power and flexibility lead to complexity. Thus, as with any computational tool, it is not intended to be used without some supervision. It has some basic error checking but not the rigorous error trapping that might be expected with commercial software. (A simple example is that if the code fails to converge to an equilibrium position, it will continue spending many hours attempting to continue the calculations symbolically.) Used with other tools and intelligent design, it can describe the dynamics to a sufficient degree to enable design of feedback controllers, sensitivity analysis of mechanical construction, and thermal noise performance based on loss in every elastic stage. Some of the conclusions that can be drawn are described in the following chapters.

Chapter 4

Pendulums

In this chapter, various aspects of the applications of the Lagrangian model of a multiple pendulum system are discussed. The model underwent extensive verification, both theoretical and experimental, as described in section 4.1. Cantilever blades were implemented to improve the vertical isolation of the pendulum suspension. The cantilevers do not act as ideal vertical springs, due to their finite mass and inertia. This limitation to the isolation achieved when not using the centre of percussion is covered in section 4.2. This explains how these effects are built into the modelling, as well as outlining the design changes that resulted from an understanding of this problem. The vertical isolation which is achieved by use of the cantilevers is judged to be sufficient for GEO 600 based on an assumed level of cross-coupling. The sensitivity of this cross-coupling parameter to imperfections in the mechanical construction of the system is explored by the Lagrangian model in section 4.3. As opposed to a suspension fundamentally soft in every degree of freedom, an alternative method would be to construct a suspension stiff in the non–critical degrees of freedom. An example of such a reduced degree of freedom suspension is examined in section 4.4. The chapter concludes with a few comments on the range of validity of the model and the resulting transmitted seismic noise.

4.1 Modelling

4.1.1 Force

One technique for writing the equations of motion of a system is by way of Newton's equations, drawing a free body diagram and writing out the various forces that are in the system. This method was used by Calum I. Torrie to generate one model used in the triple pendulum suspension, details of which may be found in Torrie[50], [1]. This work was done in conjunction with the development of the Lagrangian code by the author. The two methods proved complementary. Some terms appeared in the Lagrangian output that were not initially obvious. The force model provided explanation and understanding of how each term affected the result.

The work done on the force model generated equations of motion for a system symmetric about the X and Z axes as a function of the mechanical parameters of the system. These equations were input into a Matlab m-file in a state-space form, making them very simple to use and fully compatible with already existing Matlab tools for the GEO controller design. The Matlab toolboxes rely on the system being linear and time invariant and therefore having constant coefficient state space matricies. In order to generate appropriate matrices, this model cannot handle structural loss terms where the coefficient of the velocity terms in the **A** matrix are a function of frequency. Since the bending and the twisting of the wires contribute very little to the restoring forces—their significant contribution being to the loss terms—they have been neglected for this force modelling. Lastly, the exact details of the behaviour of the cantilevers based on the angle of the wires is complicated. For purely vertical wires, the apparent extensional spring constant of the wire, for all degrees of freedom, may be replaced by the spring constant of the series connection of the wire and the cantilever to which it is attached. While this is not strictly true for wires angled away from the vertical, for the small angles used in the GEO designs, this same approximate replacement is sufficient.

By restricting the class of inputs, the force model can explicitly establish equations of motions in terms of the input parameters. By avoiding the need for recalculating for every system, the code is substantially easier to read and runs many, many times faster. This allows parameter searches to be done much more conveniently. Because of this, some of the conclusions on the control to be discussed in

section 6.2 use outputs from the Matlab force model. This is only done after careful cross checking with the Lagrangian model and with due consideration of the relevant approximations.

4.1.2 Evaluation of the Models

Both models, the force and Lagrangian, were rigorously evaluated against each other and against earlier modelling work done for the double pendulum suspensions such as used in the Glasgow 10 m prototype[67, 30]. This earlier modelling work evaluated the dynamics for a slightly more restricted class of pendulum systems. Specific features that were added for both new models included the angling of the wires away from vertical and the inclusion of the cantilever blades.

During the evolution of the Lagrangian code (in particular, while the lengths of the wires were calculated as the geometrical distance rather than the integrated length of the wires), it was possible to generate symbolic equations of motion to be explicitly compared to the other modelling techniques. This allowed evaluation of the equations of motion for a single stage pendulum.

Vertical wires in a pendulum

The simplest example pendulum suspension has four vertical wires breaking off from a mass in the plane level with the centre of mass. In this case, the equations of motion due to the simple extension of the wires can be calculated in a straightforward manner from Newton's second law of motion. The resulting resonant frequencies are given by

$$\omega^2_{vertical} = \frac{4k}{m} \tag{4.1}$$

$$\omega^2_{longitudinal} = \frac{g}{l} \tag{4.2}$$

$$\omega^2_{tilt} = \frac{4ks^2}{I_Y} \tag{4.3}$$

$$\omega^2_{yaw} = \frac{mg(s^2+n^2)}{lI_Z} \tag{4.4}$$

where $\omega = 2\pi f$, f = resonant frequency, the I give the moments of inertia about the respective axes, k = the extension spring constant of each wire, m = mass and

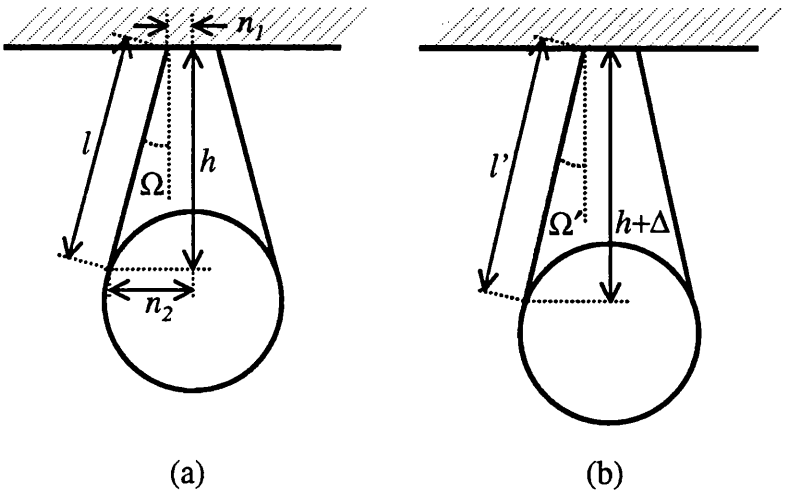

Figure 4.1: A single pendulum suspension on four angled wires. The wires make an initial angle Ω with the vertical, in figure (a). After the mass is displaced downwards a distance y to the position in (b), the new angle is Ω'.

g = the acceleration due to gravity. The variables s and n are the half separations of the wires in the X and Z directions, as described in section 3.1. The expressions for transverse and roll modes are similar to those of longitudinal and tilt.

Vertical Motion

Now consider the equation for vertical motion for the same single pendulum where the four wires are all at an angle Ω in the Y-Z plane with respect to the vertical, as shown in figure 4.1. The equilibrium position is found by setting the time derivatives to zero, as

$$m\frac{d^2y}{dt^2} = 0 = 4T_0\cos(\Omega) - mg. \tag{4.5}$$

From this the static tension, T_0, is found to be

$$T_0 = \frac{mg}{4\cos\Omega}, \tag{4.6}$$

where the angle Ω is determined by

$$\cos\Omega = \frac{h}{l}. \tag{4.7}$$

In this equilibrium position, the length of the wire is given by

$$l^2 = (n_2 - n_1)^2 + h^2. \tag{4.8}$$

The calculation of this equilibrium deserves some consideration with respect to the Lagrangian code. The equilibrium tension comes from some initial extension of the wire. Force models typically take this input geometry and assign the appropriate tension, T_0, to the wires. The Lagrangian code takes this input geometry, assigning the initial length of the wire to l_0, and calculates the extension needed to get the correct tension. Therefore in the equilibrium position, the Lagrangian model has $l = l_0 + \delta l_{eq}$. Typical values of δl_{eq} are less than a millimetre. This equilibrium value of l is what is usually input into a force model and what is measured on a physical suspension, and the use of l_0 versus l can cause slight differences between models.

When the mass is moved downwards a small amount Δ, the vertical equation of motion becomes

$$m\frac{d^2y}{dt^2} = 4T' \cos\Omega' - mg, \tag{4.9}$$

where the tension in the wires becomes

$$T' = T_0 + k\delta l, \tag{4.10}$$

the initial tension in the wire plus the force due to the extension in the wires, and it is projected along the new angle Ω'. In this new configuration, the length of the wire has increased to $l' = l + \delta l$, such that

$$l'^2 = (l + \delta l)^2 = (t_2 - t_1)^2 + (h + \Delta)^2. \tag{4.11}$$

Recalling the discussion from section 3.4.4, in the Lagrangian model this length is written as

$$l' = l_0 + \delta l_{eq} + \delta l.$$

How this is done is important for the correct evaluation of thermal noise, as will be described in section 5.1.1. The change in the length of the wire is found by

subtracting equation 4.8 from 4.11, leaving $2h\Delta + \Delta^2 = 2l\delta l + \delta l^2$, which when substituting equation 4.7 gives, to first order in Δ,

$$\delta l = \frac{h\Delta}{l} = \Delta \cos\Omega. \tag{4.12}$$

The angle in the disturbed configuration, Ω', is given by

$$\cos\Omega' = \frac{h+\Delta}{l'}$$

which, upon substituting equations 4.12 and 4.7 and expanding to first order in y, gives

$$\begin{aligned} \cos\Omega' &= \frac{h+\Delta}{l+\delta l} \\ &= \frac{h+\Delta}{l+\Delta\cos\Omega} \\ &= \frac{h}{l} + \frac{\Delta}{l} - \frac{h}{l}\frac{\Delta}{l}\cos\Omega \\ &= \cos\Omega + \frac{\Delta}{l}\sin^2\Omega. \end{aligned} \tag{4.13}$$

Using the expressions for the new angle, equation 4.13, and new tension, equation 4.10, in the equation of motion, equation 4.9, gives

$$\begin{aligned} m\frac{d^2y}{dt^2} &= 4T'\cos\Omega' - mg \\ &= 4(T_0 + k\delta l)\left(\cos\Omega + \frac{\Delta}{l}\sin^2\Omega\right) - mg \end{aligned} \tag{4.14}$$

which upon substitution of the original tension (equation 4.6) and the expression for δl (equation 4.12) and noting that $y = -\Delta$, gives the final equation to first order in y as

$$m\frac{d^2y}{dt^2} = -\left(4k\cos^2\Omega + mg\frac{\sin^2\Omega}{\cos\Omega}\right)y. \tag{4.15}$$

There are two terms to the restoring force in the vertical direction. One comes simply from the extension of the wires; vertical motion is multiplied by $\cos\Omega$ to get the change in wire length, whose force is projected back to the vertical direction by

again multiplying by $\cos\Omega$. The second term comes from the fact that the original tension in the wire, T_0, which no longer acts in the same direction, does not exactly cancel the pull of gravity. Therefore there is a component of restoring force that is proportional to T_0 which is proportional to g for vertical motion when the wires in a pendulum are not vertical.

Other degrees of freedom for a single stage pendulum

In a similar fashion, the equations of motion and thus resonant frequencies of the other degrees of freedom for this pendulum can be calculated. The resulting frequencies are given by

$$\omega^2_{vertical} = \frac{4k\cos^2\Omega}{m} + \frac{g}{l}\frac{\sin^2\Omega}{\cos\Omega} \tag{4.16}$$

$$\omega^2_{longitudinal} = \frac{g}{l\cos\Omega} \tag{4.17}$$

$$\omega^2_{tilt} = \frac{4ks^2\cos^2\Omega}{I_Y} + \frac{mgs^2\sin^2\Omega}{I_Y l\cos\Omega} \tag{4.18}$$

$$\omega^2_{yaw} = \frac{4mg\left(s^2\cos^2\Omega + n_1 n_2\right)}{lI_Z\cos\Omega} + \frac{4ks^2\sin^2\Omega}{I_Z}. \tag{4.19}$$

In comparing equations 4.16-4.19 with the same equations for vertical wires ($\Omega = 0$, or equations 4.1–4.4), some of the terms appear straightforward. For example, the frequency in the longitudinal direction is based on the vertical height of the pendulum, so for a length l at angle Ω from vertical, the height is $l\cos\Omega$, which is the term that appears in the denominator in equation 4.17. It was initially less obvious that there should be additional terms in the vertical, roll, and tilt equations which depend upon g/l. It can now be seen that these terms come from changes in the angles of the wires when the pendulum moves.

4.1.3 Coupling

For the cases examined so far, the equations of motion for each of vertical, longitudinal, tilt, and yaw have been independent, the restoring force for each depending only on the corresponding displacement. (Note that this is not strictly true when the effects of the bending of the wires is included, but that this coupling between the equations of motion is small.) When the wires are attached to a mass in a

plane parallel to the X-Z plane and above or below the centre of mass (for the model inputs defined in section 3.2, $d \neq 0$), certain couplings between the degrees of freedom are introduced. For a four wire suspension with the wires attached in plane with the centre of mass, the torque introduced by the front set of wires due to a vertical or longitudinal motion is cancelled by the torque from the rear pair of wires. When attached above or below the centre of mass, there is a net torque for a longitudinal displacement and therefore tilt motion. The coupled set of equations for longitudinal and tilt motion become

$$\frac{d^2}{dt^2}\begin{bmatrix} x \\ \theta \end{bmatrix} = \begin{bmatrix} A_{11} & A_{12} \\ A_{21} & A_{22} \end{bmatrix}\begin{bmatrix} x \\ \theta \end{bmatrix} \tag{4.20}$$

where

$$A_{11} = -\frac{g}{l\cos\Omega} \tag{4.21}$$

$$A_{12} = \frac{gd}{l\cos\Omega} \tag{4.22}$$

$$A_{21} = \frac{mgd}{I_Y l\cos\Omega} \text{and} \tag{4.23}$$

$$A_{22} = -\frac{4ks^2\cos^2\Omega}{I_Y} - \frac{mgs^2\sin^2\Omega}{lI_Y\cos\Omega} - \frac{mgd}{I_Y} - \frac{mgd^2}{lI_Y\cos\Omega}. \tag{4.24}$$

In this case, the resonant frequencies are the eigenvalues of this dynamics matrix $[A]$.

Similarly, angling the wires away from vertical introduces coupling between degrees of freedom. The cases examined so far, with the wires angled in the Y-Z plane, cause the equations of motion for transverse and roll motions to be coupled even for $d = 0$. For GEO 600 designs, for thermal noise reasons it is never appropriate for the wires to be angled in the X-Z plane, although the Lagrangian code can calculate such systems. The longitudinal and tilt equations for wires angled in the X-Z plane would be very similar to the following sideways and roll equations for $d \neq 0$ when the wires are angled in the Y-Z plane, shown here for completeness as

$$\frac{d^2}{dt^2}\begin{bmatrix} z \\ \psi \end{bmatrix} = \begin{bmatrix} \tilde{A}_{11} & \tilde{A}_{12} \\ \tilde{A}_{21} & \tilde{A}_{22} \end{bmatrix}\begin{bmatrix} z \\ \psi \end{bmatrix} \tag{4.25}$$

with the elements of the $[\tilde{A}]$ matrix as

$$\tilde{A}_{11} = -\frac{g\cos\Omega}{l} - \frac{4k\sin^2\Omega}{m} \tag{4.26}$$

$$\tilde{A}_{12} = -\frac{gd\cos\Omega}{l} + \frac{gs\sin\Omega}{l} - \frac{4kd\sin^2\Omega}{m} - \frac{4ks\sin\Omega\cos\Omega}{m} \tag{4.27}$$

$$\tilde{A}_{21} = \frac{mgd}{lI_X} - \frac{mgs\sin\Omega}{lI_X} + \frac{4kd\sin^2\Omega}{I_X} + \frac{4ks\sin\Omega\cos\Omega}{I_X} \tag{4.28}$$

$$\tilde{A}_{22} = \frac{mgs\sin\Omega}{I_X\cos\Omega} - \frac{mgd}{I_X} - \frac{mgd^2\cos\Omega}{lI_X} - \frac{mgs^2\sin^2\Omega}{lI_X\cos\Omega} - \frac{4kd^2\sin^2\Omega}{I_X} + \frac{2mgds\sin\Omega}{lI_X} - \frac{8kds\sin\Omega\cos\Omega}{I_X} - \frac{4ks^2\cos^2\Omega}{I_X}. \tag{4.29}$$

Based on these equations, which were the result of the detailed cross checking between the two modelling methods, the nominal cross couplings in a pendulum suspension were defined. When the variable *Symmetric* is set in the Lagrangian code, the same couplings shown in these equations are assumed: longitudinal coupling with tilt and sideways with roll. The vertical equation and the yaw equation remain uncoupled for this class of inputs. The sensitivity of this assumption is tested in section 4.3.

4.1.4 Experimental Verification

To test the models, a single pendulum was set up on a four wire suspension. The resonant frequencies were obtained by exciting the pendulum and measuring the Fourier response from an accelerometer attached to the mass. The experimental results were obtained for four different examples. The first case investigated had four vertical wires breaking off level with the centre of mass, which corresponds to equations 4.1–4.4. Secondly the wires were angled in the Y-Z plane at two different angles to introduce the new terms in the equations 4.16–4.19. Finally, further coupling was introduced by having the wires break off above the plane through the centre of mass (equations 4.20– 4.29). For all of these cases, the mass, m, was 20 kg. The various cases and parameters for each are summarized in table 4.1.

The initial theoretical predictions gave frequency values that were too high compared to the measured values for the frequencies where the dominant force was due to the spring constant, k. Most of the physical parameters of this system are known

with confidence; the single unverified input is the spring constant of the wire,

$$k_s = \frac{E\pi r^2}{l} \tag{4.30}$$

where r is the radius of the wire, l is the length of the wire (both of which are simple to measure), and E is the Young's modulus. For these experiments, the suspension wires were made of stainless steel 302, from 280 to 350 μm diameter. In the first set of predictions, a reference value of Young's Modulus of 2.0×10^{11} Pa was used[68]. To account for these discrepancies, an attempt was then made to calculate the Young's modulus based on the observed vertical frequencies, the frequencies which depend most dominantly on the Young's modulus. This calculated modulus was then used to predict the other frequencies. However, this value over corrects, predicting frequencies for tilt, yaw, and roll that were too low compared with the measured values. It was then postulated that some of the vertical frequencies might be affected by coupling to the support structure which was not completely rigid; this idea was supported by some simple adjustments to the experimental setup. Thus it was decided to independently measure the modulus of the wire by measuring the vertical and yaw frequencies of a one wire pendulum, whose restoring forces are directly proportional to the modulus of the wire with a minimum of geometrical factors. This one wire pendulum was as long as practical (8 m), and was mounted directly to the building to minimize the effects of the support structure. This length also allowded a large amount of wire to be averaged, reducing the effects of any kinks or other defects in the wire. These measured frequencies each gave a value for E of $\sim 1.7 \times 10^{11}$ Pa.

This value was used in table 4.1, where the theoretical predictions agree with the measured results within experimental error (10%) except for the vertical frequencies for the first three cases. In these cases, it is believed that the support structure still couples with the pendulum to give a lower frequency, as varying the bracing on the test structure caused the measured vertical frequency to vary significantly. The last case was measured on a different support structure which was noticeably stiffer and consequently gives better agreement.

This experimental verification was logically extended, first to a double pendulum system suspended on wires, then to a triple pendulum, a triple pendulum with one stage of cantilevers, and finally to a triple pendulum suspension using two stages

	All values in (Hz)					
	Tilt	Longitudinal	Roll	Sideways	Rotation	Vertical
Case 1:						
Experiment	*7*	*0.94*	*20.3*	*0.94*	*1.8*	*11.3*
Theory	7.6	0.96	22.2	0.96	1.78	14.3
Case 2:						
Experiment	*4.4*	*1.0*	*19*	*1*	*1.9*	*11.9*
Theory	4.5	1.01	21.8	1.01	2.02	13.74
Case 3:						
Experiment	*3.6*	*0.81*	*16*	*0.8*	*1.3*	*10.2*
Theory	3.6	0.82	17.6	0.8	1.37	11.1
Case 4:						
Experiment	*3.9*	*0.84*	*18.5*	*0.8*	*1.4*	*11.4*
Theory	3.9	0.85	19.9	0.8	1.5	11.4

	l	s	n_1	n_2	d
Case 1	0.26m	0.025m	0.047m	0.133m	0
Case 2	0.27m	0.04m	0.133m	0.133m	0
Case 3	0.40m	0.025m	0	0.133m	0
Case 4	0.36m	0.025m	0	0.133m	0.032m

Table 4.1: Results from single pendulum experiment. The model predictions and the measured results are compared for various cases, chosen to emphasize different terms in the equations.

	Theoretical	Experimental
Tilt/Longitudinal	3.6, 2.7, 2.4 1.34, 0.5, 0.6	3.5, 2.6, 2.2 1.4, 0.6
Sideways/Roll	52, 3.3, 2.5 1.4, 0.9, 0.6	 1.4, 1.0, 0.6
Yaw	3.1, 1.6, 0.4	3.1, 1.6
Vertical	36, 3.8, 1.0	37, 3.7, 1.0

Table 4.2: Resonant frequencies from the prototype triple pendulum

of cantilever blades. The final set of experiments was to measure the frequencies of a prototype GEO 600 main suspension. It is very difficult to measure the actual isolation in a multi–stage isolation system. To measure the full isolation of the GEO isolation system would require the sensitivity of the full GEO interferometer. Therefore, the measurement of the resonant frequencies will establish the predicted levels of isolation in the system. The predicted and measured frequencies for the GEO 600 prototype suspension are summarized in table 4.2. The specific parameters were chosen to meet the GEO 600 requirements through the use of this modelling work. Specific examples of how these parameters affect the vibration isolation follow in the remainder of this chapter. The agreement with theory is for the most part excellent. Due to the experimental setup, the sideways modes were difficult to detect. Additionally, the cluster of modes near 0.5 Hz made it difficult to explicitly resolve all the modes.

The validation of the Lagrangian modelling, both from consistency with the force model and by comparison with experiment, gave a firm basis for extending the code to a wider class of problems. The remainder of this chapter and all of chapter 5 could only be done with the capabilities of the Lagrangian code.

4.2 Centre of Percussion

The concept of 'centre of percussion' influences the isolation performance achieved in these multi–stage pendulum systems. A compound pendulum is a rigid body constrained to rotate about a fixed axis[69]. The centre of percussion in figure 4.2 is the point P, located a distance

$$l_{CP} \equiv l_{CM} + \frac{k^2}{l_{CM}} \tag{4.31}$$

from the axis, where l_{CM} is the distance to the centre of mass and k is the radius of gyration, defined by

$$I_{CM} = mk^2 \tag{4.32}$$

where I_{CM} is the moment of inertia about the centre of mass. This distance is the length of the equivalent simple pendulum, which therefore has a resonant angular

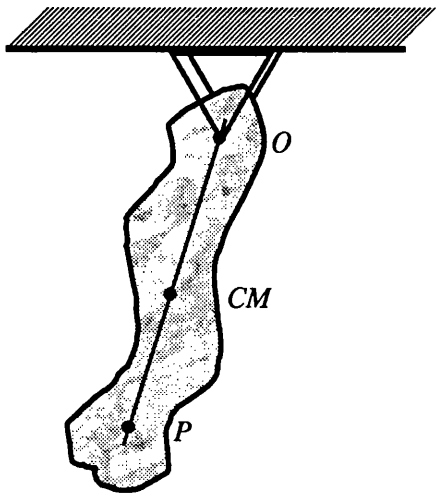

Figure 4.2: A compound pendulum. The diagram depicts a rigid body with mass and moment of inertia which pivots about a point O, has a centre of mass located at CM, and has centre of percussion located at P.

frequency $\omega_0^2 = g/l_{CP}$. For a pendulum consisting of a mass on a long wire, such as is typical for suspensions in gravity wave interferometers, the length of the stage is long compared to the dimension of the mass, meaning that l_{CP} is approximately the same as the length of the wire.

4.2.1 Isolation in Compound Pendulums

The transfer function of interest for isolation is the ratio of the horizontal motion at the output to the horizontal motion at the ground input. For a simple pendulum, a point mass at the end of a wire, the isolation well above the resonant frequency is $(f_0/f)^2$. For a compound pendulum, the observed output depends on where on the mass the horizontal motion is observed. The motion at the centre of percussion is exactly that of a simple pendulum. Thus for a sinusoidal input of arbitrarily high frequency, the motion at the centre of percussion is very close to zero. Because the pendulum is a rigid body, the motion above the centre of percussion is a fraction of the motion at the top of the pendulum. Similarly, the motion below the centre of percussion is as if the pendulum pivots about that point of zero motion. That is, at arbitrarily high frequency, the motion at a point a distance l from the rotational

axis along the vector $\vec{OP}$ is

$$\frac{x_l}{x_0} = \frac{l_{CP} - l}{l_{CP}}. \tag{4.33}$$

This intuitive description is extended to describe the behaviour at all frequencies as

$$X_l(\omega) = \frac{l_{CP} - l}{l_{CP}} X_0(\omega) + \frac{l}{l_{CP}} X_{CP}(\omega), \tag{4.34}$$

from the geometry of the straight line connecting O and P. The motion at the centre of percussion is that of the equivalent length simple pendulum,

$$\frac{X_{CP}}{X_0} = \frac{1}{1 - (f/f_0)^2}. \tag{4.35}$$

The observed horizontal transfer functions for a point at distance l from the axis is found by combining equations 4.34-4.35 to get

$$\frac{X_l}{X_0} = \frac{\left(1 - \frac{l}{l_{CP}}\right)\left(1 - \left(\frac{f}{f_0}\right)^2\right) + \frac{l}{l_{CP}}}{1 - \left(\frac{f}{f_0}\right)^2}. \tag{4.36}$$

The response of a family of points with different l across the surface of the pendulum are plotted in figure 4.3. The important feature is that the transfer function reaches a constant value at high frequencies, depending on the distance from the centre of percussion. It is also worth noting that for points above the centre of percussion, the isolation has a significant 'dip', where the isolation is (in a very narrow band) much better than the nominal $(f_0/f)^2$. This dip is essentially as deep as the resonance peak is high (the value of Q). In theory, if additional isolation was needed at a target frequency, this dip could be tuned to achieve extra isolation, trusting the isolation from all the other stages, which continues to improve at higher frequencies, to work for higher frequencies where this stage's isolation would plateau. Due to the narrowness of this peak and the consequent difficulty in tuning it, this seems an unlikely course of action. For example, the best isolation for a given frequency

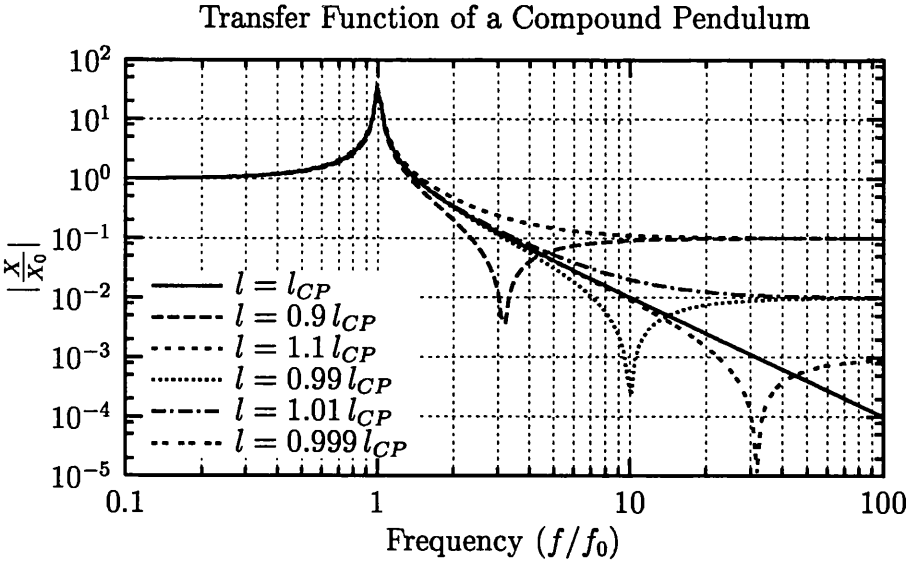

Figure 4.3: The transfer function of a compound pendulum. Above the resonant frequency, the isolation initially improves as $\frac{1}{f^2}$ but levels off at a frequency which depends on the distance from the centre of percussion.

occurs at a point a distance l from the axis such that

$$\frac{l_{CP}}{l_{CP} - l} = \left(\frac{f}{f_0}\right)^2 . \tag{4.37}$$

For a resonance at $f_0 = 1\ Hz$ with $Q = 10^5$ with desired performance at 50 Hz, the distance to the centre of percussion is given by $\sqrt{g/l_{CP}} = 2\pi f_0$, or $l_{CP} \approx 0.25$ m. The peak performance at 50 Hz occurs at about 1.0004 times this distance, or approximately 0.1 mm below the centre of percussion. To take maximum advantage of this improved isolation, the location would have to be tuned to within roughly $(0.1\text{mm})/Q$, or something like 1 nm.

The same issues regarding centre of percussion affect multi–stage pendulums. A double pendulum would normally be expected to see isolation proportional to $1/f^4$ above both resonant frequencies of the system, a factor of $1/f^2$ from each pendulum stage. When the lower stage pendulum, whether it is a rigid body or a simple 'ideal' pendulum, is not attached at the centre of percussion of the upper rigid body pendulum, the combined system will not have the full $1/f^4$ isolation at high frequencies; instead, the system will have isolation that improves at no better

rate than $1/f^2$.

4.2.2 Cantilevers

To this point the cantilever blades have been described as vertically compliant elements designed to enhance the vertical isolation of the total suspension system. Their treatment in the Lagrangian model as described in section 3.5 actually treats the cantilevers more realistically as elements with mass and inertia. The consequence of this is that the cantilevers do not give the $(f_0/f)^2$ isolation of a spring–mass resonance to as high a frequency as might be expected for a high Q resonance. This is because the cantilever–wire vertical system may be considered just like the multi–stage pendulum described above, where the connection between the stages is not at the centre of percussion. As in the previous example, the isolation from the cantilever stage reaches a maximum value, rather than continuing to improve with frequency.

The Maple code shown in Appendix B calculates the vertical transfer function of a cantilever blade such as used in GEO 600 suspending a wire pendulum, including the kinetic energy due to the translation and rotation of the blade. It is this treatment which is generalized to all degrees of freedom that is included in the Lagrangian code.

The blades are nearly triangular, as described in section 2.4.2, modified to allow clamping of wires and dampers. Although the exact parameters for the spring constant and moment of inertia are complicated for the particular shape of the blade, fitting the blade parameter α based on the measured resonance (section 2.4.2) gives a sufficiently accurate prediction for the cantilever behaviour. For a flat triangular blade of constant thickness and of length l_c, the centre of mass is

$$l_{CM} = \frac{l_c}{3} \tag{4.38}$$

from the base of the blade. Since the blades to be used have extra mass at the tip, both because they widen to allow for clamping and due to the clamp itself, this expression is not exact but gives satisfactory results.

The coordinates used to model the cantilevers are shown in figure 4.4. The input to the system is the motion of the base of the blade, y_0. One coordinate is the

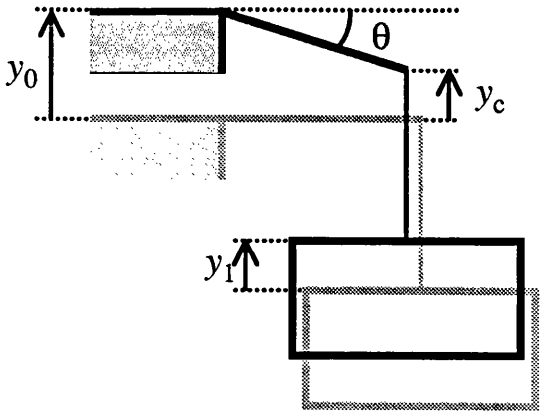

Figure 4.4: Coordinates for cantilever modelling. The variables y_0 and y_1 measure the displacement of the base and the suspended mass, while y_c measures the motion of the tip of the blade. All of these variables are measured in inertial space from their respective initial positions.

vertical motion of the mass of the pendulum, y_1, at the other end of the wire from the tip of the cantilever. The remaining state variable is the motion of the tip of the blade, y_c. All these variables are measured with respect to their initial positions.

The potential energy of the system is given by the two springs, the cantilever, with spring constant k_c, and the extension of the wire, which has spring constant k_w. Thus,

$$PE = \frac{1}{2}k_c\left(y_c - y_0\right)^2 + \frac{1}{2}k_w\left(y_1 - y_c\right)^2. \tag{4.39}$$

The position of the centre of mass of the blade is the weighted average of the position of the base of the blade and the position of the tip,

$$y_{CM} = \frac{\left(l_c - l_{CM}\right)y_0 + l_{CM}y_c}{l_c}. \tag{4.40}$$

The rotation of the cantilever is given by, for small angles, the slope of the blade, shown in figure 4.4 as

$$\theta_{cant} = \frac{y_c - y_0}{l_c}. \tag{4.41}$$

The time derivatives of equations 4.40 and 4.41 give the translational and rotational

velocities, which give the kinetic energy of the system, due to both the cantilever of mass m_c and pendulum of mass m_1. By substituting for l_{CM} from equation 4.38, this kinetic energy is given by

$$KE = \frac{1}{2}m_1\dot{y}_1^2 + \frac{1}{2}m_c\left(\frac{2}{3}\dot{y}_0 + \frac{1}{3}\dot{y}_c\right) + \frac{1}{2}I_{cant}\left(\frac{\dot{y}_c - \dot{y}_0}{l_c}\right)^2. \tag{4.42}$$

The moment of inertia of such a triangular blade is given by $I_{cant} = m_c l_c^2/18$. Expressing the Lagrangian as the difference in kinetic and potential energies the appropriate equations of motion can be derived. Solving these, by way of Laplace transforms, gives

$$\frac{Y_1}{Y_0} = \frac{k_w\left((2m_c l_c^2 - 9I_{cant})\omega^2 + 9k_c l_c^2\right)}{\left(9I_{cant}^2 m_1 + m_c l_c^2 m_1\right)\omega^4 - \left(9I_{cant}k_w + m_c l_c^2 k_w + 9(k_w + k_c)l_c^2 m_1\right)\omega^2 + 9k_c k_w l_c^2}. \tag{4.43}$$

To investigate the isolation provided by a set of cantilevers, the vertical transmissivity was measured. The experiments were performed in the tank which was eventually used to house the prototype of the entire suspension system, including vibration isolation stacks, rotation stage, and triple pendulum (described in chapter 7). Each test was done by mounting the cantilevers rigidly to the support structure attached to the stacks and suspending a single wire pendulum stage beneath it. Consistency checks were performed later on the final triple pendulum prototype. Each of the three legs of the prototype stack sits on top of a three–axis piezoelectric (PZT) actuator, normally used to investigate active vibration isolation. For these experiments, the PZT stacks were used to vertically vibrationally excite the entire structure. Two piezoelectric accelerometers were used to measure the resulting excitation through the prototype stack. One accelerometer was at the fixed end of the cantilevers while the other was attached to the suspended pendulum mass, as near as possible to the vertically symmetric axis. The thin wire which carried the signal from the suspended mass was attached to the top of the system with slack so as not to have added any stiffness to the system. A dynamic signal analyzer was used to convert the two channels of data into the resulting transfer functions.

The cantilever blades as originally designed were of maraging steel, 2 mm thick, 37 cm long, and with a base of 8.2 cm, giving a spring constant of 739 N/m, as

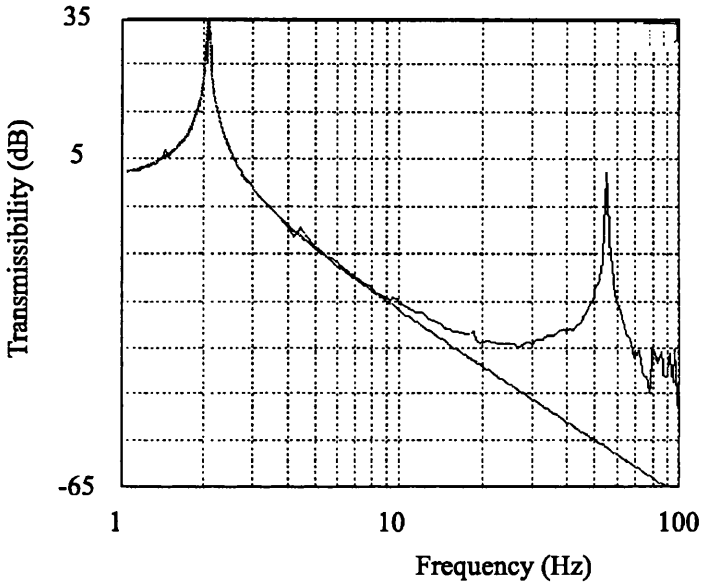

Figure 4.5: Transfer function of the original upper cantilever blades. Comparing the measured data to an idealized isolator clearly shows the first blade resonance at $\sim$2 Hz, a region of $(f_0/f)^2$ isolation, followed by a levelling off of the isolation. The data also shows the presence of the first internal mode of the blade at 54 Hz.

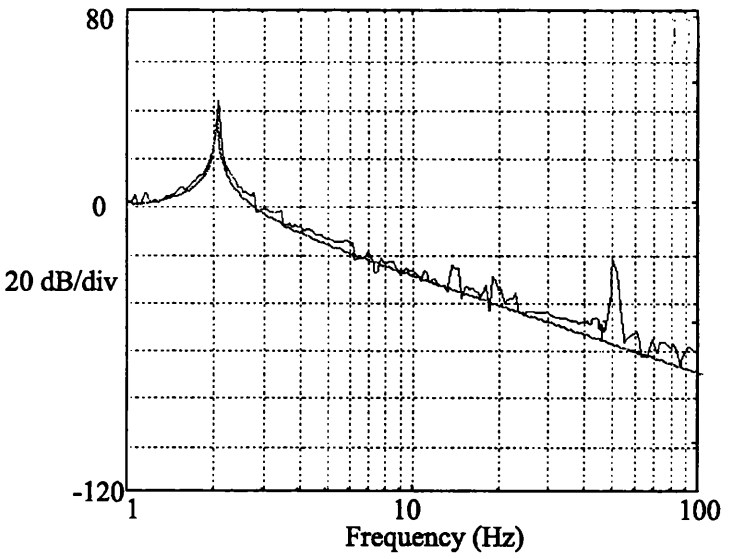

Figure 4.6: Transfer function of the lower cantilever blades. The isolation is very close to the ideal $(f_0/f)^2$ until past the critical frequency of 50 Hz.

per section 2.4.2. The measured transfer function of the original upper cantilever blade design is shown in figure 4.5. This is measured using a suspended mass equivalent to the mass of the individual stage suspended by the blades in the final suspension. That is to say that two upper cantilever blades are measured supporting a mass equal to that of the uppermost mass, 5.6 kg. Some features of this predicted transfer function can be seen. The response at low frequencies matches that of a mass–spring oscillator, a resonant peak followed by a curve falling as $(f_0/f)^2$. The problem with this design is that the slope levels off, giving no further isolation, above approximately 20 Hz. It is further complicated by the first internal resonance of the blade occurring very close to 50 Hz. This is not exactly coincidence—the region of flattening out depends on the blade geometry, as does the internal resonance—but no explicit relationship between the internal resonance and the roll off of isolation is explored here. While the curve does have the large resonant peak superimposed on the isolation, it is clear that this is not the only limitation to the isolation and that the curve is no longer falling with frequency squared. This effect is due to the point of attachment of the wires not being at the centre of percussion of the blade, relative to the input motion at the base of the blade. While the same effect occurs in the

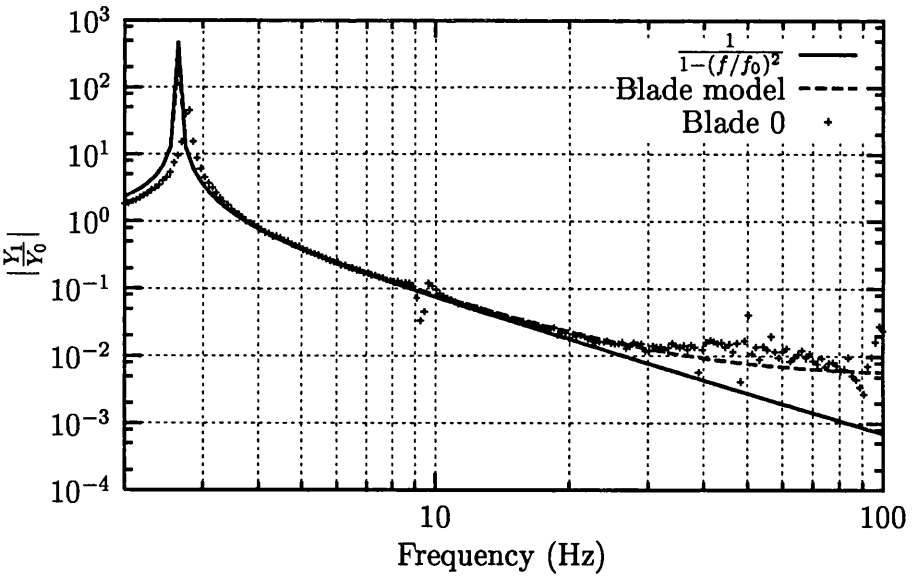

Figure 4.7: Transfer function of the new cantilever blade. The figure shows the measured isolation as well as that predicted by $(f_0/f)^2$ performance and the improved model using the mass and inertia of the blade. While the fundamental resonant frequency of this blade is actually higher than that of the original blade (see figure 4.5), the realized isolation at 50 Hz is better.

lower set of blades, due to the smaller size of the blades (a length of 12.4 cm, base of 28 mm, and thickness of 1 mm) as well as the higher frequency resonance, the transfer function shown in figure 4.6 shows the desired isolation up to well past the critical point at 50 Hz. Note that the first uncoupled resonant frequency is defined to be 3 Hz, the resonant frequency of the four cantilevers supporting the mass of the next stage (5.6 kg). Experimentally, mounting the blades in place required that they be flat, which they do only under the weight of the total mass suspended below (two stages); therefore, additional weight was added to the suspended mass. This causes the measured resonant frequency in figure 4.6 to be a factor of $\sqrt{2}$ lower, or approximately 2.1 Hz.

Since the upper cantilever blades were no longer achieving the intended isolation, the vertical vibration isolation of the entire system was insufficient. This led to a redesign of the upper blades for the GEO 600 suspension. The new design for the upper blades used smaller blades, with a length of 24 cm and a base of 4 cm, resulting in a slightly higher initial resonance frequency of 2.6 Hz. With the blades being smaller, the mass of the blade relative to the pendulum mass is less and

the distance from the centre of percussion is less, resulting in better performance at 50 Hz. Better high frequency isolation is thus achieved even though the fundamental resonance is higher. In addition, this change increases the first internal mode of the blade from ~55 Hz to near 130 Hz. This new blade design provides 'ideal' isolation up to ~30 Hz, and will provide sufficient isolation at 50 Hz for the GEO 600 suspension[48]. The internal mode of the blade, while at a higher frequency than in the original design, still requires to be damped. This will be done with a small resonant damper, currently under development. The behaviour of the new blade design is shown in figure 4.7.

If it were necessary to improve the isolation further at high frequencies, to reduce sensitivity to internal resonances, or if moderate improvements in isolation between 30–50 Hz were required for advanced configurations, minor modifications of the blades could provide additional performance. This could be done by modifying the location of the centre of percussion, as described below.

The centre of percussion is defined with respect to a driving point and as such is symmetric; for any system, the centre of percussion for an input at point A is located at B, and for an input at B, the centre of percussion is at point A. As before, the distance to the centre of percussion for the triangle shown in figure 4.8 is defined as

$$l_{CP} = l_{CM} + \frac{k^2}{l_{CM}}. \tag{4.44}$$

For a triangular blade, the distance from the base to the centre of mass is $l_c/3$ (equation 4.38). The moment of inertia for rotation about the base is easy to calculate as

$$I_0 = \frac{ml^2}{6}. \tag{4.45}$$

The parallel axis theorem gives the moment about the centre of mass,

$$I_{CM} = \frac{ml^2}{18}. \tag{4.46}$$

These equations 4.44–4.46 give the distance to the centre of percussion from the

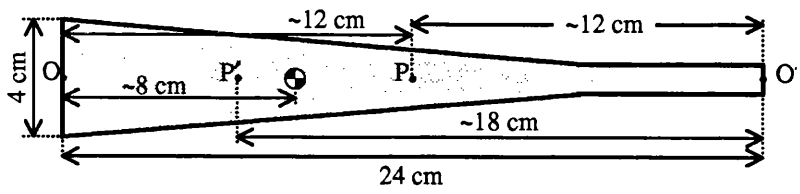

Figure 4.8: Centre of percussion of triangular blades. For the GEO 600 upper blades, the centre of percussion calculated with respect to the base is ~0.12 m from the base, such that the distance from the tip of the blade where the wires are mounted to this point is also ~0.12 m. The distance to the centre of percussion calculated with respect to the tip of the blade is ~0.18 m

base as

$$l_{CP} = \frac{l}{2}. \tag{4.47}$$

For a GEO 600 blade of length 24 cm, this means the wires are attached approximately 12 cm from the centre of percussion ($l - l_{COP}$).

There are fundamentally two ways this could be adjusted (within the basic triangular blade geometry). Additional mass could be added at the base of the blade, such that the centre of percussion with respect to the tip would be where the blade is mounted. This solution is complicated by the question of how to mount the blade without constraining the connection of the base. Alternatively, more mass could be added at the tip of the blade, which would move the centre of mass and the centre of percussion measured with respect to the base toward the tip of the blade. The simplest way to do this without changing the geometric position of the wires would be to make a larger triangle, such that $(l_{CP})_{new} = l$, and attach the wires to the appropriate point in the middle of the triangle. This is a poor solution, since by loading the triangle in the middle there is no longer the constant stress in the blade material, which is what drove the choice of triangular geometry in the first place.

A better solution is to add mass to the tip of the blade. The triangle would simply be extended with a narrow 'nose' as shown in figure 4.9. While this blade will have the same fundamental frequency and stress, due to the triangle being the same, there is a difficulty in that the extra mass on the soft end of the blade will cause the first internal mode to decrease. This mode is not at so high a frequency that it can be ignored in the GEO design; reducing it is not desired. The advantage

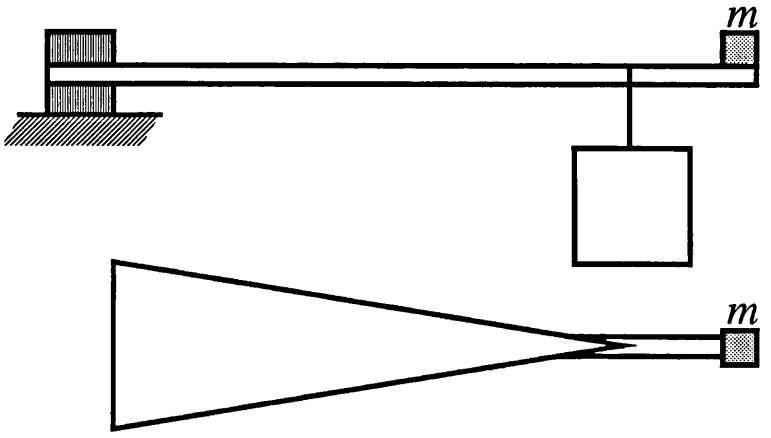

Figure 4.9: Cantilever blade with extra mass on tip. This moves the centre of percussion, with respect to the base, closer to the tip of the blade.

is that this is a very simple redesign. To locate the centre of percussion at the tip of the blade, imagine adding a mass m a distance d off the tip of the blade. As will be shown, the necessary mass can be small, implying the mass of the neck should not be ignored; in practice, the adjustment is simple enough that an approximate figure will allow a starting point for experimental tuning. The centre of mass of the combined system is located a distance

$$\tilde{l}_{CM} = \frac{\left(\frac{1}{3}\right) l m_c + (l+d)m}{m_c + m} \tag{4.48}$$

from the base of the blade. The moment of inertia measured from the base is

$$\tilde{I} = I_0 + m(l+d)^2 \tag{4.49}$$

where I_0 is as in equation 4.45, $m_c l^2/6$. Using the parallel axis theorem to solve the moment about the centre of mass,

$$\tilde{I}_{CM} = \left(I_0 + m(l+d)^2\right)(m_c + m)\tilde{l}_{CM}^2. \tag{4.50}$$

This moment of inertia inserted into the definition of radius of gyration gives

$$\tilde{k}^2 = \frac{\frac{m_c l^2}{6} + m(l+d)^2}{m_c + m} - \tilde{l}_{CM}^2. \tag{4.51}$$

Knowing that the distance to the centre of percussion is $\tilde{l}_{CM} + \frac{\tilde{k}^2}{\tilde{l}_{CM}}$, and that this distance is desired to be equal to the length of the blade, the resulting equation is

$$l = \frac{\frac{m_c l^2}{6} + m(l+d)^2}{\frac{m_c l}{3} + (l+d)m}, \tag{4.52}$$

which solving for the added mass m gives

$$m = \frac{m_c l^2}{6d(l+d)}. \tag{4.53}$$

For the parameters of the GEO 600 upper blades, $l = 0.24$m and $m_c = 0.084$kg, with an extra length of $d = 0.055$m (the distance somewhat arbitrarily added to an experimental design), this gives an extra mass of $m \approx 0.050$ kg to be added to the tip. Since the mass of a tip of this length is roughly 0.010 kg, although not concentrated at distance d, and since the wire clamps also add mass near the tip of the blade, it is expected that the best performance will require substantially less that 0.050 kg to be added at this distance. The results from adding mass to the tip are shown in figure 4.10. The various curves show the isolation measured for an upper GEO 600 blade versus the isolation for the blade with the extra tip added on, and with various masses added to this tip. Also shown is an ideal isolator, with isolation $(f_0/f)^2$ of the same resonant frequency. It is easy to see in principle that the isolation can be improved towards the ideal. It is also clear that with additional mass added, the internal mode moves to lower frequencies. When more mass than required is added, a dip in the isolation is shown, just as anticipated for a point located closer to the bending axis than the resulting centre of percussion. If a design such as this were to be chosen, a careful tradeoff between the internal mode and the isolation would have to be made. Since the best results are achieved with very little additional mass, the next iteration of such a design could use a shorter tip. The example blade constructed for this test had an unnecessarily long neck. It could not be used as a simple replacement in the current GEO 600 design, since the

long neck would interfere with the desired wire spacing. A shorter neck would allow a new blade to fit in the GEO 600 suspension by replacing the original blade with no other changes.

The same modelling technique incorporating the effects of the centres of percussion can be extended to the full GEO 600 suspension. Two cantilever spring stages in a three stage wire pendulum give the vertical isolation shown in figure 4.11. Note that for the assumed 0.1% coupling from vertical motion to horizontal motion, this vertical motion is the limiting source of seismic noise. The predicted level of isolation for cantilevers with mass and inertia is compared with the idealized case of three coupled ideal isolators. This suggests that at 50 Hz, the isolation is a factor of 3.4 worse than the ideal case supposed. The other new feature this curve shows is the pair of high frequency (~500 Hz) resonances. These are the bounce modes of the cantilevers, where the cantilevers move out of phase with the lower mass of each stage, stretching the wires between the cantilevers and the mass. While this identifies another set of possible noise peaks in the spectrum, in practice, since the internal modes of the blades are not included in the model, these bounce modes are not accurately modelled by this method.

This same model can be used to estimate the effect of the internal modes of the cantilevers on the output spectrum. The displacement noise level in the vertical direction can be estimated for the expected resonant frequencies of the upper blades, ~130 Hz, as the transmission shown in figure 4.11, 1.7×10^{-7}, times the performance of the stack, $(15/f)^2$ (section 2.2.1), times the input ground spectrum, $\frac{10^{-7}}{f^2}\mathrm{m}/\sqrt{\mathrm{Hz}}$, to give $1.2\times10^{-20}\mathrm{m}/\sqrt{\mathrm{Hz}}$. Allowing for a 0.1% coupling to the horizontal direction and a Q factor of 10^4 as is typical for steels such as maraging, the height of this peak is $1.2\times10^{-19}\mathrm{m}/\sqrt{\mathrm{Hz}}$, well above the noise floor of the detector. Thus this peak should be damped. The resonance of the lower blades, occuring closer to ~270 Hz, gives a peak of only $1.7\times10^{-23}\mathrm{m}/\sqrt{\mathrm{Hz}}$, which should not appear in the output signal. (With the levels of approximation, this peak might appear, but should not significantly degrade performance.) For each of these cantilever modes, the net contribution of these resonances to the rms motion of the optic is small enough to be ignored.

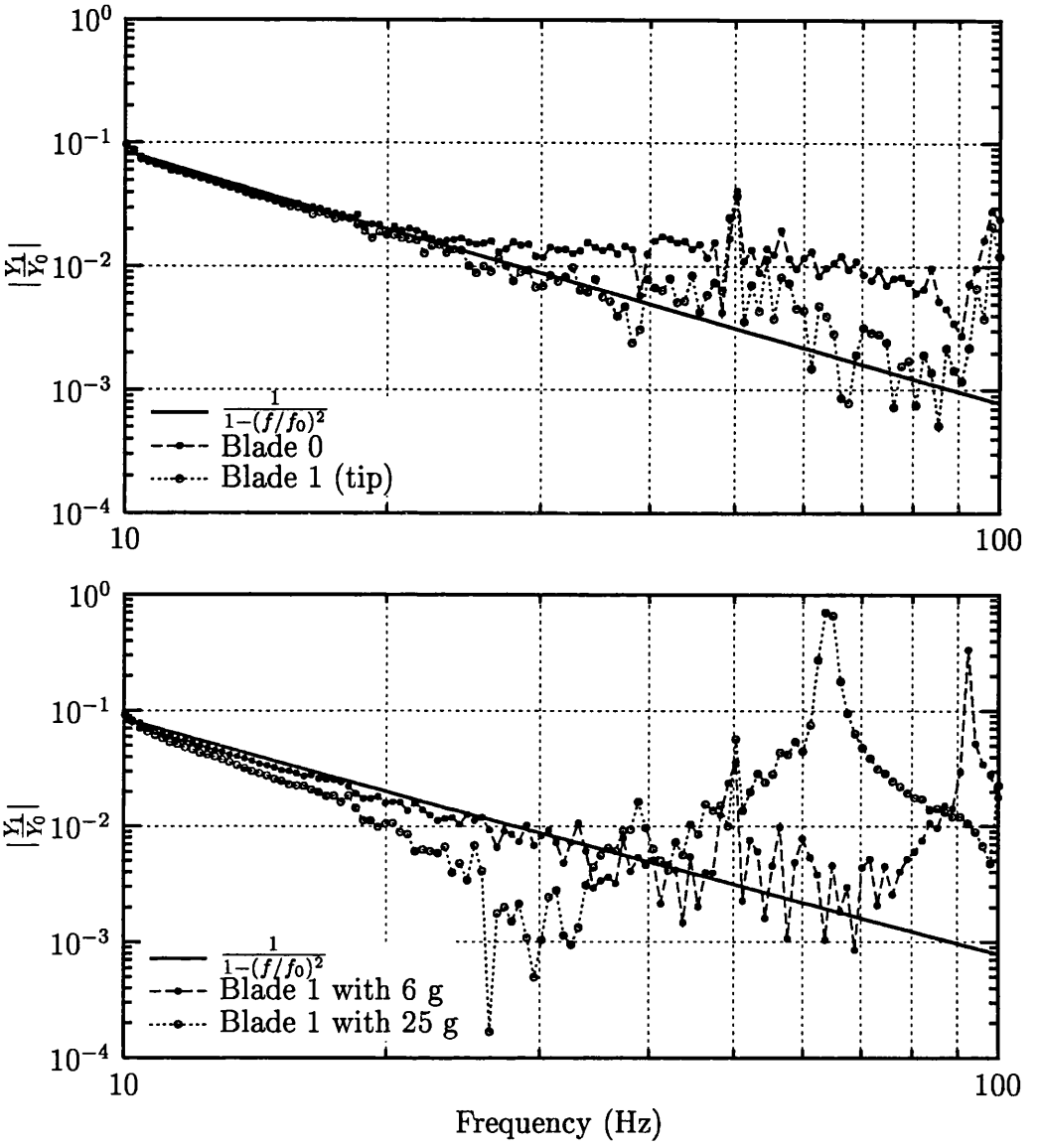

Figure 4.10: Transfer function of a cantilever stage, adjusting the centre of percussion. By careful choice of the added mass, the blade can demonstrate improved isolation. The upper plot shows the measured performancee of the GEO 600 upper blade (blade 0) compared to a new blade which has a tip added on to the end of the blade. By comparing these to the modelled performance of a massless isolator, it can be seen that the new blade provides better isolation. The lower plot shows the performance when additional mass is added onto the tip of the new blade. While this can affect the transmission at lower frequencies, it also reduces the frequency of the first internal mode of the blade, which appears as the peak in the transmission.

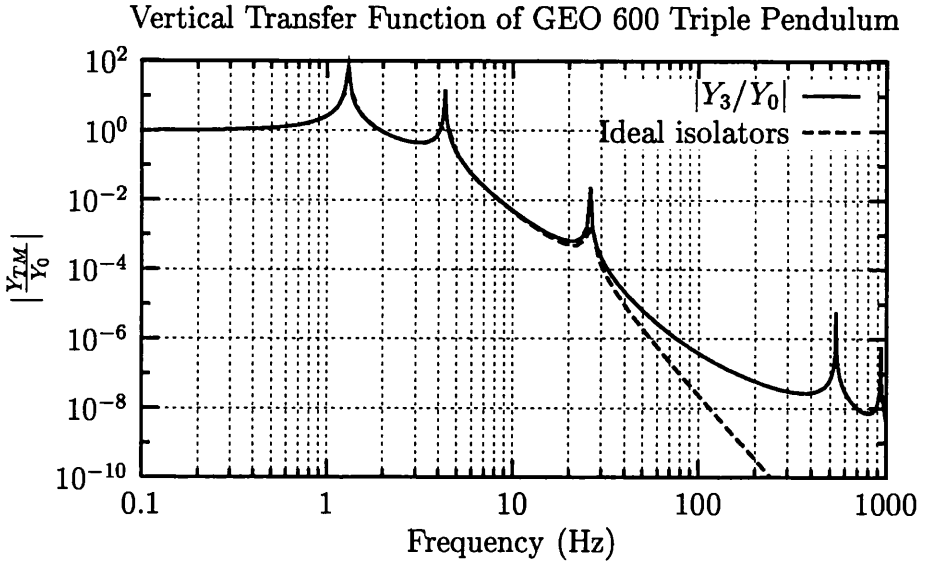

Figure 4.11: Vertical isolation for a triple pendulum with two cantilever stages. This is illustrated in comparison with ideal (massless) isolators. The two very high frequency modes arise where a set of cantilevers move out of phase with the next lower mass.

4.3 Cross–Coupling

The required vertical isolation in the suspension system has been calculated from the displacement noise tolerable in the measurement direction divided by a cross–coupling factor from the vertical to the horizontal. There is some inherent value of cross–coupling due to the optical configuration (section 2.4.1) and the achievable values of cross coupling have been assumed to not greatly exceed this level. While this assumption was made conservative for earlier designs, for the GEO 600 suspension, this factor directly determines the predicted noise performance for the frequencies where transmitted vertical seismic noise dominates. In addition, this factor is always assumed as a constant value, whereas in the physical system, the different values of the vertical and horizontal resonant frequencies mean that the amount of cross–coupling will be dependent on frequency.

Based on the symbolic modelling work from section 4.1, it can be seen that a perfectly symmetric system will have no cross–coupling from vertical to horizontal. As discussed in section 7.2.2, the way the GEO suspension will achieve the necessary thermal noise performance in its final stage pendulum is by use of silicate bonded

fibres[38]. Specifically, small attachments will be bonded onto the test mass, and drawn fibres will be welded onto these attachments. It is unclear to exactly what level of accuracy four different fibres may be welded to the same length. Once the fibres are attached, it may be difficult to tune their lengths. Even without this challenge, simple symmetric designs in the laboratory often require a fair bit of adjustment to achieve the desired static position. It is obvious that a particular 'nominal' position may be achieved by a happy combination of many errors; a single stage pendulum on four cantilevers may be level either due to all four cantilevers being identical or with every cantilever different but compensated by four differing wires. The Lagrangian code for the first time allows theoretical predictions of the effects of this kind of misalignment.

There are as many possible physical imperfections as there are parameters in the system. A few selected misalignments will be examined to calculate their effect on cross–coupling compared to the assumed value. It is presumed that the effects of errors in upper stages of the pendulum suspension will be isolated by the remaining pendulum stages. In addition, errors in the steel wires can be corrected, within limits, on the experimental apparatus by reclamping to adjust length, tension, and location of attachment. It is primarily offsets in the lowest stage of the suspension that are likely to cause difficulties. The methods by which such misalignments or parameter variations can be input to the code are described in section 3.9.

The amount of static extension in equilibrium of the final stage wires should be less than 1 mm. As the static tension is directly proportional to this extension, having the static tension in all four wires to within 1% would require the wire lengths be balanced to the order of 10 μm. By measuring the resonant frequency and thus the tension, wires that can be clamped under tension might well be adjusted to near this level of accuracy. For welding wires not under tension, this is a great challenge. The important question is how close to the same length do the wires have to be. Figure 4.12 shows the cross–coupling, the ratio between vertical output motion and horizontal output motion for the same vertical input motion, when one wire is 0.25 mm longer than the other three wires. This case, as with the following cases, is calculated based on numbers very similar to those to be used in the final stage of the GEO 600 main suspension. The parameters are for four wires hanging vertically, separated by 0.010 m in the beam direction ($s = 0.005$). Each wire is

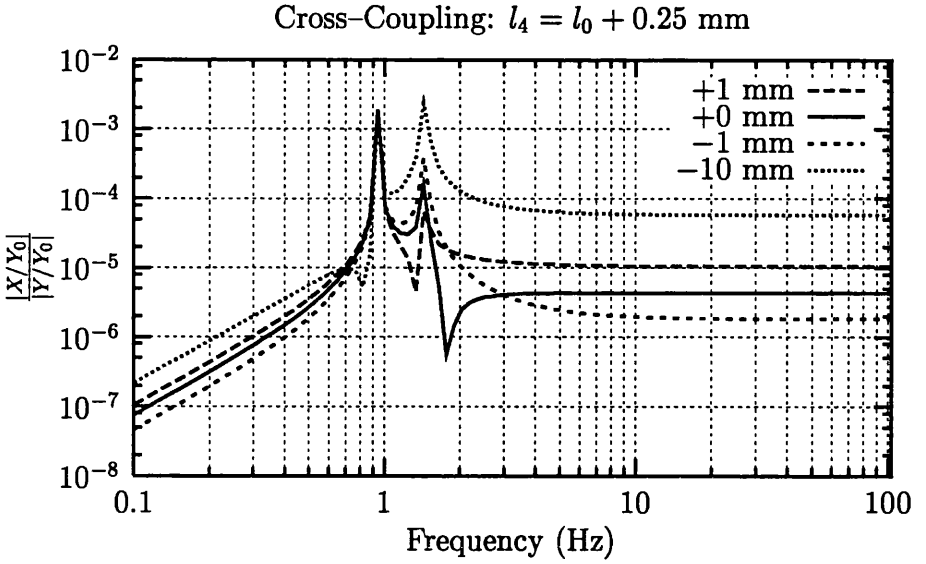

Figure 4.12: Cross–coupling in final stage of GEO 600 with 0.25 mm error in wire length. The data shown is the cross–coupling observed at a point level with the centre of mass, as well as points above and below the centre of mass, which introduces the effects of tilt.

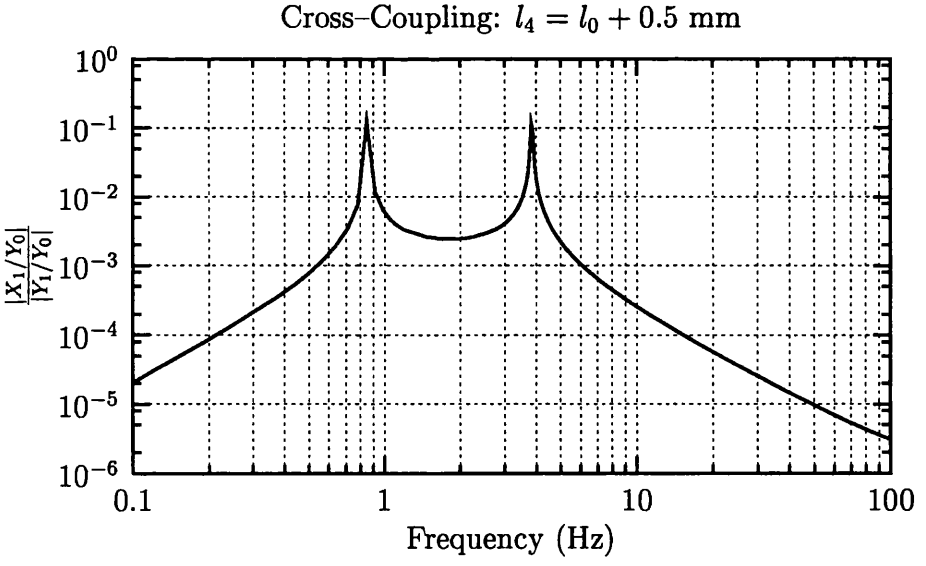

Figure 4.13: Cross–coupling in final stage of GEO 600 with 0.5 mm error in wire length. The data shown is the cross–coupling observed at a point on the front face level with the centre of mass.

attached 1 mm above the plane of the centre of mass and is attached to a breakoff on a flat polished on the side of the mirror, giving a separation in the transverse direction between wires of 0.175 m ($n = 0.0875$). Each wire is made of fused silica of radius 140 μm with Young's modulus of 7×10^{10} N/m. The mirror masses are right circular cylinders of radius 0.09 m, length 0.10 m, and mass 5.8 kg with horizontal flats along both sides. The static tensions in the four wires are 14.57, 14.47, 13.02, and 12.93 N. These differing tensions cause the mirror to move in the beam direction as well as tilt when given a pure vertical input. Because the beam should be located at the minimum of the thermal noise for the longitudinal and tilt modes, which is offset from the centre of mass, the inputs are chosen to show the coupling as seen directly not only level with the centre of mass, but also above and below the centre of mass. This allows determination of a maximum anticipated value for the cross–coupling allowing for errors in beam positioning.

Two things are important. Firstly, at frequencies well above all the resonances of the system, the vertical and horizontal motions are being attenuated as the same function of frequency, giving effectively constant cross–coupling. The shape of the curves suggests that for systems that strive for isolation performance at frequencies closer to the system resonances, the cross–coupling may be much greater than the level predicted at high frequencies. This might be the case for systems that aim for lower frequency performance without correspondingly lower resonant frequencies, instead using a large number of stages which only achieve moderate levels of isolation per stage. Secondly, at 50 Hz, the values of cross–coupling for this level of misalignment plus the misalignment from consideration of the optical path, 3×10^{-4} (section 2.4.1), is well below the 0.1% assumed for GEO 600, even for beam positions up to 10 mm away from the centre of mass. Next, figure 4.13 shows the same inputs where that misaligned wire is 0.5 mm longer than specified. In this case, the static tensions in the wires are 18.93, 14.85, 12.83, and 8.68 N. Again, the assumed 0.1% is an appropriate, conservative value. For errors substantially larger than this, one wire in the suspension will actually become slack, causing much greater difficulties.

Another class of misalignment on the final stage of the pendulum could be the location of the wire attachments. A specific type of misalignment is shown in figure 4.14, where one of the wire connections is modelled as being offset along the beam axis. To compound this, the spring constant of the same wire is varied. The

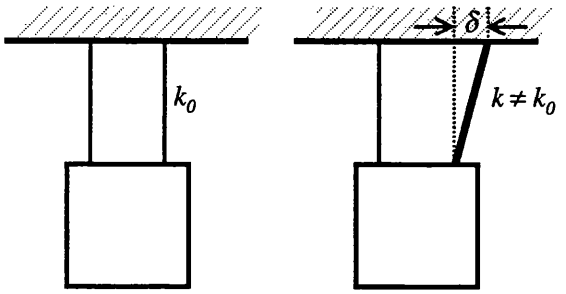

Figure 4.14: Variations in wire attachment and spring constant.

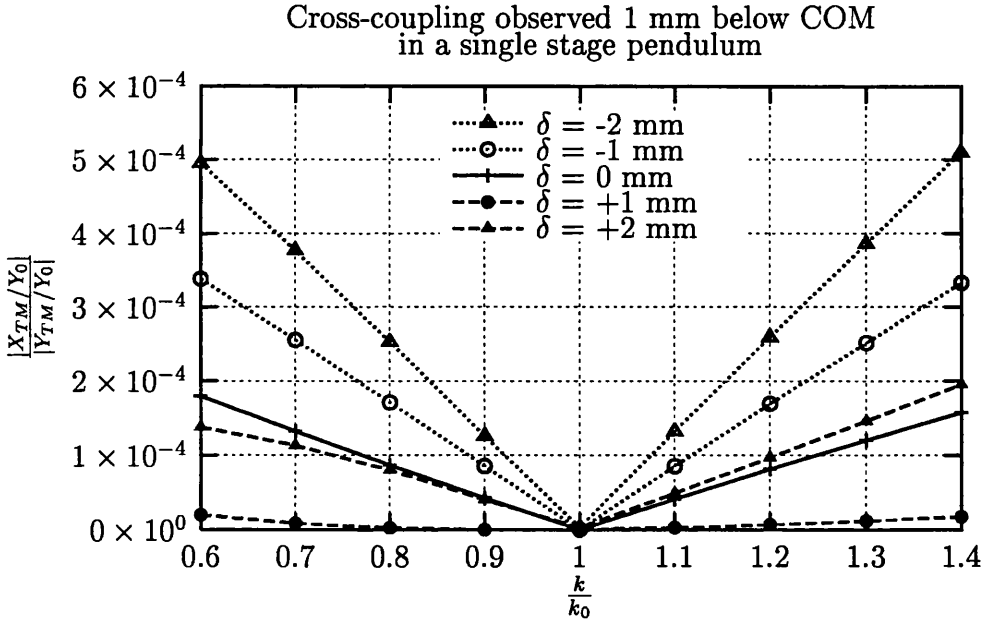

Figure 4.15: Cross–coupling in final stage of GEO 600 due to variations in wire attachment and spring constant. The different curves represent different locations for the upper attachment of one wire while the abscissa gives the variation in the spring constant of the same wire.

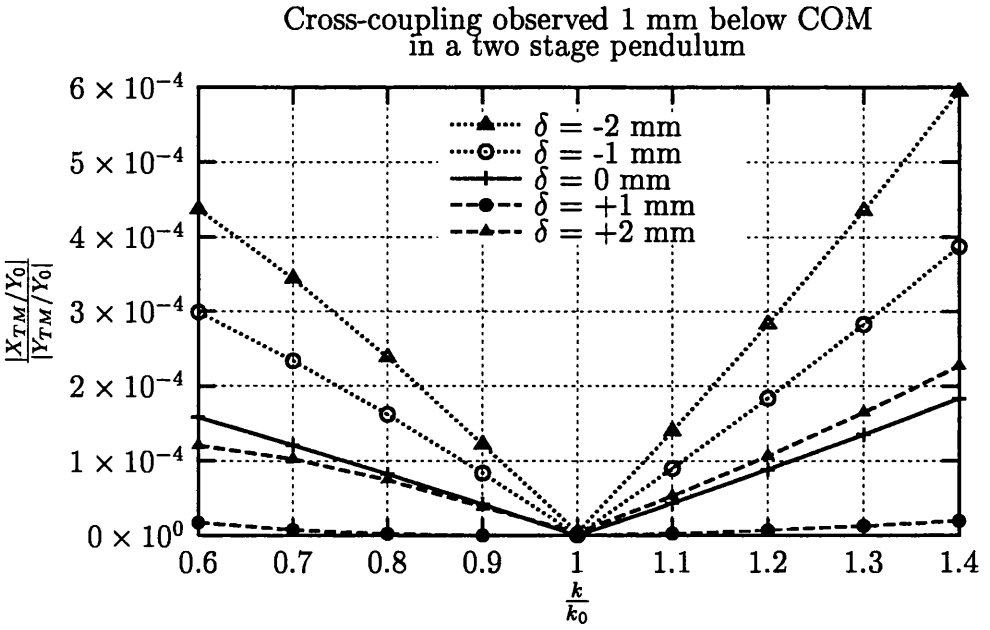

Figure 4.16: Cross–coupling in final two stages of GEO 600 due to variations in wire attachment and spring constant.

extension spring constant is directly proportional to the cross sectional area of the wire, and it is very possible that the drawn fused silica fibres will vary in cross section. The levels of cross coupling at 50 Hz for this example are shown in figure 4.15 as a function of this offset and a normalized variation in spring constant. The ratio of horizontal output, seen 1 mm below the centre of mass, to vertical output for a given vertical input is plotted. Again, for this category of misalignment, the assumed total cross–coupling of 0.1% is appropriate even for offsets in wire position on the order of 2 mm, out of a 10 mm wire separation, and spring constants that vary by 40%.

This calculation may not accurately illustrate the situation for a multi–stage pendulum. A misalignment in a wire connection may affect the alignment of all the masses in a multi–stage suspension, where the upper connection of the wire is not rigid. Figure 4.16 illustrates the modelled cross–coupling for the a two stage pendulum, using the parameters of the lower two stages of the GEO 600 suspension. Again, the errors are assumed in the final stage of the suspension, where the fibres will make corrections most difficult. The modelled offset, δ, is an error in the X coordinate of the upper connection of one lower fibre while varying the spring

constant of the same fibre. The data are different than for the single pendulum case, but the assumed 0.1% is still appropriate except for very large errors in the parameters.

4.4 Reduced DOF Suspensions

Another application of the modelling code is to examine radically different suspension designs. Because of the effects of cross–coupling and due to the philosophy of the control design, in GEO 600 it is considered desirable to make the suspension system as soft as possible in all degrees of freedom. This way, first of all, every degree of freedom is isolated so that any cross–couplings do not compromise the isolation in the desired direction. Secondly, the controller design is made simpler. While the details of the control design are left to section 6.2, the idea in GEO 600 is to have the local control loops for each degree of freedom act on the same low frequency band. This gives the system its great degree of robustness, since mild variations in any degree of freedom do not substantially degrade performance for any of the (identical) control loops.

Another design possibility would be a suspension soft not in as many degrees of freedom as possible, but only soft in a reduced number of degrees of freedom, those actually requiring the isolation. Such a design would be made as stiff as possible in the remaining degrees of freedom. The low frequency isolation resonances need to be damped, since with very little isolation at low frequencies, high Q values lead to a large amount of (rms) motion. For the higher frequency resonances, the isolation provided by the other stages plus the reduced input from less ground motion at these frequencies means substantially less motion on resonance and less rms motion. This suggests that these higher frequency resonances, those in the less crucial degrees of freedom, would not necessarily have to be damped.

One significant advantage of this kind of suspension would be the considerably simplified local control structure. Only the longitudinal degree of freedom needs to be damped, reducing the number of electronic channels by a factor of six. Because the suspension is too stiff to move much in the remaining degrees of freedom, it does not require dynamic alignment in the final stage. The principle difficulty is that, since there is much less isolation in the other directions, there must not be substantial

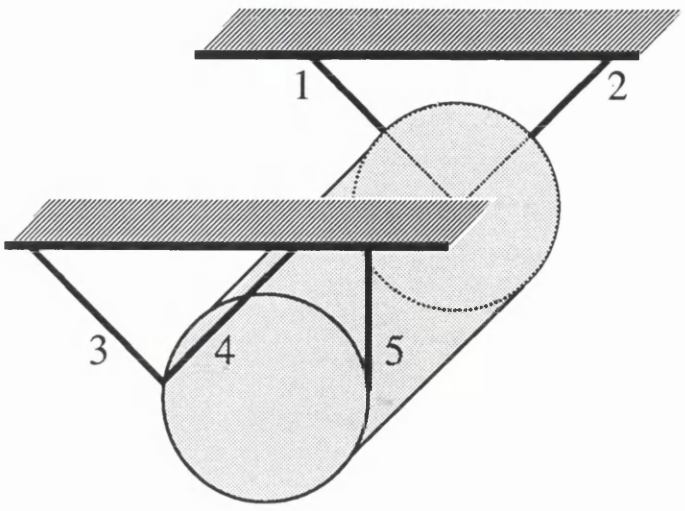

Figure 4.17: A five wire, reduced DOF suspension. The wire angles and sizes are chosen to give the same tension in each wire.

cross coupling between the degrees of freedom. Because of this tight restriction, these reduced degree of freedom principles would not necessarily be applied at every stage in a multiple stage system. They can be used in an outer stage, where a very long range is needed in just one direction. One example would be compensating for changes in length of a long baseline beam tube due to temperature changes; a lead screw could translate the entire suspension a large distance along the beam with no (deliberate) motion in any other direction. These ideas could also be used in a very sensitive inner stage specifically to avoid the need to apply control and possible disturbance in other directions.

At least two different methods of restricting the soft degrees of freedom can be modelled using the Lagrangian code with slight modifications. A wire, acting as a rod stiff in tension and soft in all other degrees of freedom, can constrain one degree of freedom. A flexure, envisioned as a thin rectangular sheet, is soft in bending but stiff in three other degrees of freedom—translation along the two long dimensions of the flexure and in rotation about the axis perpendicular to the surface of the flexure.

4.4.1 Wires

A possible five wire suspension is shown in figure 4.17. There is a 'V' at the front end of the suspension, an offset 'V' at the rear of the suspension, and the fifth wire

is vertical, mirroring the offset point at the rear of the suspension. The two pairs of wires, being at right angles to each other, constrain motion in the Y-Z plane at both the front and rear of the mass. By preventing relative motion in the Y-Z plane from front to rear, this constrains tilt and yaw motion of the mass, while the fifth (vertical) wire acting with the offset pair of wires constrains roll motion. In calculating the tension in each wire, the net forces must balance vertically with the pull of gravity. In addition, the tensions balance in tilt, front and rear, and balance in roll, left to right, such that for wires angled at 45°, and knowing that the tensions in each angled pair of wires in the figure are equal, $T_1 = T_2$ and $T_3 = T_4$,

$$\frac{2T_1}{\sqrt{2}} + \frac{2T_3}{\sqrt{2}} + T_5 = mg \tag{4.54}$$

$$\frac{2T_1}{\sqrt{2}} = \frac{2T_3}{\sqrt{2}} + T_5 \tag{4.55}$$

$$\frac{2T_3}{\sqrt{2}} = T_5. \tag{4.56}$$

From this, $T_5 = mg/4$, $T_3 = T_4 = \sqrt{2}mg/8$, and $T_1 = T_2 = \sqrt{2}mg/4$. To get the same violin modes (discussed in more detail in the following section) in each wire requires that the cross-sectional area of the wires be in the same proportions as the tensions.

The above system was modelled using a vertical height (length of wire 5) equal to 0.28 m, the same length as the final stage wires in the main GEO suspension. As anticipated, the longitudinal degree of freedom is soft, with a resonant frequency of 1.0 Hz, while the other degrees of freedom are much stiffer, being resonant at 7.3, 10.1, 10.3, 10..8, and 15.3 Hz. Because the wires have some bending stiffness, they do not act purely as one dimensional constraining elements, causing a slight amount of cross coupling between vertical and horizontal ($\sim 4 \times 10^{-6}$) even for a system built perfectly as described above. The greatest concern for these systems is how much tighter the requirements are for aligning the beam. A small offset in the beam location away from the centre of mass couples angular motion of the test mass into sensed displacement. For a system soft in all degrees of freedom, this rotational motion is well isolated. In this reduced DOF suspension, this rotational motion can be substantially larger. Thus for this example, a beam centring offset of only

0.1 mm above the centre of mass increases the observed vertical to horizontal cross–coupling to 3.8×10^{-4}. This level of cross–coupling for a five wire suspension with no perturbations can be compared with the 'soft' suspension modelled in figure 4.12, where there is a significant error (0.25 mm) in one wire length. The five wire suspension where the beam is offset 0.1 mm from the centre of mass exhibits nearly ten times the cross–coupling that the misaligned four wire suspension does when the beam is offset 10 mm from the centre of mass.

This same sensitivity to beam alignment is required for the thermal noise reasons discussed in the following chapter. In section 5.2, it will be seen that higher frequency modes will introduce much more thermal noise when the beam is misaligned a small amount than will the lower frequency modes of a soft suspension.

Because the system couples so weakly to roll motion, a symmetric system could be designed using four wires in two vees, which remains soft in the roll direction as well as the longitudinal direction. Again, this would not fit with the GEO 600 control strategy in the triple pendulum. Modelling this is a straightforward variation in the Lagrangian code.

4.4.2 Flexures

Another construction uses two flexures, one behind the other. The simplest flexure is a thin, rectangular sheet, arranged to bend in the longitudinal direction while remaining stiff in the transverse and vertial directions. By constraining X-Z motion at the front and back of the mass, as in the wire suspensions, the tilt motion is also constrained. One other possible advantage of flexures is with regards to the internal modes of the suspension elements as described in section 4.5. The modelling code can simply represent flexures of constant cross section, such as short ribbons. Flexures are of great interest with respect to their thermal noise performance. One particular difficulty is that using two flexures actually overconstrains the system. If the flexures are not perfectly parallel, the soft degree of freedom of the two flexures is not quite the same. This could cause substantially more thermal noise, by coupling to the stiffer direction of the flexure. How some of these ideas may be extended are suggested in section 8.2.

4.5 Internal Modes

As with any model, it is important to recognize what approximations have been made and thus what limitations may apply to the results of a model. The single largest effect not included in all the modelling discussed to this point is the internal modes, both in the suspension elements and in the masses. This is particularly true when realizing that the local control actuators, acting on the upmost mass as described in section 6.2, are to affect the motion of the lower two masses. The Lagrangian model accurately describes the dynamics for frequencies below the resonances of the wires, which tend to be at 100 Hz and higher, but is not appropriate at or above these frequencies. This allows the low frequency local control to be designed using this model, but higher bandwidth control applied at the upper masses can not be accurately characterized by this modelling technique. In a similar fashion, the thermal noise floor in the system has two main contributors, as per section 1.3.2, the noise from the pendulum suspension and the noise from the test mass itself. The Lagrangian code can accurately calculate the thermal noise in the suspension at these lower frequencies, but does not address the noise resulting from the test mass, whose calculation is based on the higher frequency modes of the test mass.

The dynamic modes modelled by the Lagrangian code are rigid body modes. All the kinetic energy terms are expressed as point masses with inertia. The internal modes are fundamentally continuous modes. They can be approximated in a finite element fashion, by breaking a continuous mass into many small elements. Accurately modelling the first n internal modes can be done by using enough elements. Another approach is to model a continuous system, which in principle allows all the modes to be calculated, an example of which is described in sction 6.3.3. This section will address these internal modes and confirm under which circumstances the modelling work described to this point may be used.

4.5.1 Suspension Elements

Any wire in the suspension system, examined in isolation, is exactly analogous to a wire in a stringed musical instrument. The wire fixed at each end loaded under tension leads to 'violin modes' in the wire. The same effects that allow low loss pendulum modes ensure that the violin modes also have low loss and a

corresponding high resonance Q—specifically $Q_{violin} = \frac{1}{2}Q_{pend}$ (when the tilting mode of the pendulum has been constrained)[41]. The low mass of the suspension wires compared to the pendulum masses means that the potentially large motions of the wires has a reduced effect on the pendulum masses, however the height of the resonant peaks is such that these resonances can still appear in the output signal.

The violin modes occur at frequencies[70, 71]

$$\omega_n \approx \frac{n\pi}{l}\sqrt{\frac{T}{\rho}} \tag{4.57}$$

where T is the tension in the wire, ρ is the linear density, and l is the length. The tension, being set by the suspended mass divided by the number of wires for vertical wires, is essentially fixed. The linear density is simply the material density times the cross sectional area of the wires, A. In order to make the violin modes as high a frequency as possible in an effort to remove them from the measurement band, the area of the wires should be made small. This is consistent with reducing the thermal noise by reducing the stiffness of the wire. Minimizing the area is limited by the allowable amount of stress in the suspension wires, usually expressed as a fraction of the breaking stress

$$S = \frac{T}{A} \leq nS_{breaking}. \tag{4.58}$$

Overstressing the wires is a poor idea in terms of mechanical robustness. If the wire is stressed within a small factor of its breaking stress, any bends or defects in the wire cause stress concentrations which could exceed the nominal breaking stress. This is a particular concern in the design of wire clamps. Even without catastrophic failures, greater stress in a wire will cause more 'creep'. The difficulty in quantifying this is that creep is usually measured over long time frames, as a fractional length change per month or even year. This gives very little insight as to how the stress in a wire contributes to noise in the measurement frequency band. Maraging steel is an alloy that seems to have exceptionally low levels of creep, which can therefore be used under greater relative stress levels, at least with respect to creep noise. For standard grades of steel, as used in the upper stages of GEO 600 and in the prototype work, the maximum allowable stress is set as $\frac{1}{3}$ of the tensile stress,

1.5 GPa for ANSI302 stainless steel and an anticipated value on the order of 2–4.5 GPa for the fused silica fibres[72, 73]. This results in violin mode frequencies for the three stages of approximately 200, 500, and 500 Hz and the integral harmonics of these frequencies, based on the final parameters in section 7.3. Naturally, only the modes in the lowest stage directly affect the output, the other stages being filtered by the lower pendulums.

4.5.2 Masses

Of less importance to the modelling work described here is the internal modes of the masses being supported. The optics have a minimum size based on the size of the beam and the desire to lose a minimum of light off the edges of the mirror. The aspect ratio of the right circularly cylindrical optics is chosen to minimize the thermal noise seen on the front surface of the test mass. This involves the shape and resonant frequency of the internal modes, where a longer cylinder gives lower frequency longitudinal and bending modes and a wider cylinder gives lower drum modes[74]. For GEO 600, the test mass is of radius 9 cm and length 10 cm, which has its first internal mode at $\sim$17 kHz. This is an important source of noise, as per section 1.3.2, but the comparatively high frequency suggests that it does not compromise any of the prior modelling results. It can have an effect for very high bandwidth control as discussed in section 6.3.2.

4.6 Conclusions

Based on the internal modes of the system, the Lagrangian model can be used with confidence up past the low frequency end of the detection band, 50 Hz. This allows the determination of the total seismic noise transmitted through the isolation system to be made.

From section 2.1, the ground noise spectrum is modelled as flat below 1 Hz at a level of $10^{-7}\mathrm{m}/\sqrt{\mathrm{Hz}}$ and falls as $1/f^2$ at higher frequencies. The single layer passive isolation stacks are modelled to act as ideal viscously damped isolators (section 2.2),

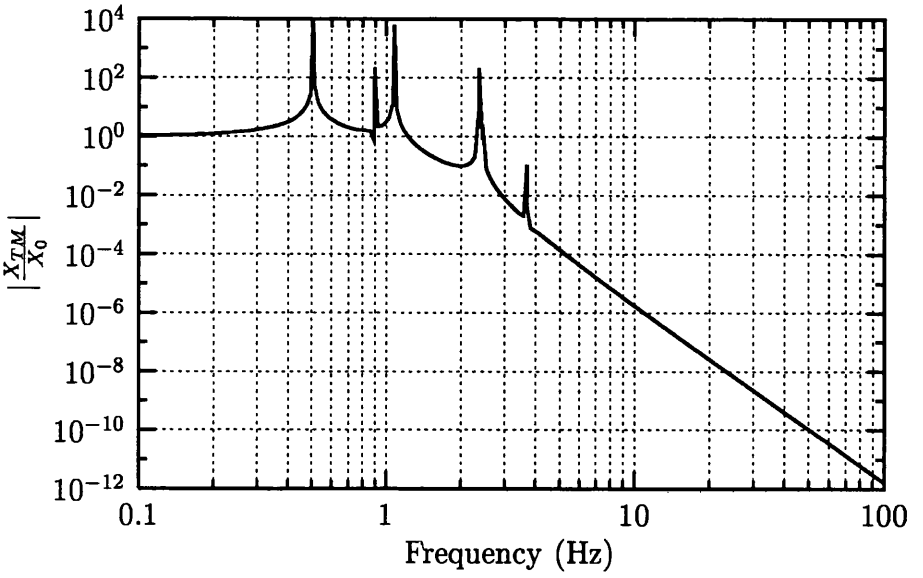

Figure 4.18: Horizontal isolation for the triple pendulum suspension.

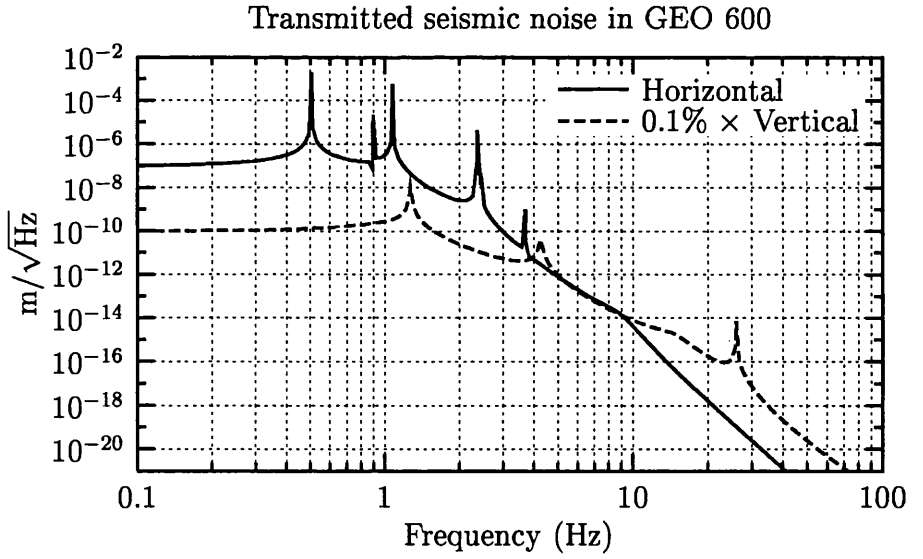

Figure 4.19: Total transmitted seismic noise in the main suspension. At low frequencies, the noise is dominated by trasmitted horizontal ground motion; above ~10 Hz, the noise is dominated by vertically transmitted motion which couples to the sensed direction at a level of 0.1%.

such that

$$\frac{X_{out}}{X_{in}} = \frac{1}{1 + i\,0.3\,(f/f_0) - (f/f_0)^2}\,, \tag{4.59}$$

where the resonant frequency, f_0, in the horizontal direction is 9 Hz and in the vertical direction is 15 Hz. The mass between the stack layer and the pendulum (the stack stabilizer and the rotational stage) is large enough compared to the mass of the pendulum that the stack and pendulum may be modelled as uncoupled. The transfer function of the pendulum is then calculated. The isolation in the horizontal direction is shown in figure 4.18, which shows the longitudinal and tilt resonances at 0.51, 0.90, 1.08, 2.36, 2.44, and 3.69 Hz. The vertical transmission was calculated for figure 4.11 and shows resonances at 1.27, 4.25, and 26.0 Hz. The product of the ground spectrum, the stack isolation, and the pendulum transfer function gives the total seismic noise transmitted to the final optic. Based on a cross–coupling of 0.1%, verified as appropriate in section 4.3, the total transmitted seismic noise of the optic is the quadrature sum of the transmitted horizontal noise and 0.1% of the transmitted vertical noise. This noise is plotted in figure 4.19; the noise is dominated by transmission in the horizontal direction at low frequencies, while above ~10 Hz the vertically transmitted noise dominates. This gives a displacement noise of the optic at 50 Hz of $2.4 \times 10^{-20}\mathrm{m}/\sqrt{\mathrm{Hz}}$, a factor of ~3 below the the internal thermal noise of the test mass of $7 \times 10^{-20}\mathrm{m}/\sqrt{\mathrm{Hz}}$.

Chapter 5

Thermal Noise Results

The Lagrangian code described in chapter 3, by properly treating all the dynamics terms in a multi–stage pendulum, allows the thermal noise observed in a system to be calculated. The significance is that this code allows the contributions from all degrees of freedom and from every stage of the pendulum to be properly included. Thermal noise calculations use the fluctuation dissipation theorem as described in section 2.5.1. In this chapter, details of how the proper loss is calculated in the code are covered, then two specific applications of the code are described.

The fundamental resonance of a pendulum, which is specified for isolation purposes, is determined by the equivalent length of the stage, not necessarily the length of the wires. More important is the vertical distance from the suspension point to the centre of mass. In particular, when the test mass has dimensions smaller than the pendulum lengths, approximately the same longitudinal mode frequency can be obtained by attaching 'long' wires to the sides of the mass, approximately level with the centre of mass, or by attaching 'short' wires directly off the top of the mass. The performance consequences of this kind of variation in suspension geometry are explored using this code in section 5.2.

Symbolically solving the noise in a multi–stage pendulum can be done in principle, although the expressions become much more complicated. With this modelling work, it is straightforward to calculate the performance for the entire system, including exploring the effects of loss in each stage of the pendulum. Such an investigation can establish requirements on all the stages. In particular, the code shows the contribution of loss in the cantilever blades. This depends on the specific geometry

and is difficult to manually calculate. The code is used to calculate the predicted thermal noise in the GEO 600 suspension system is section 5.3.

There are additional applications of the code to thermal noise problems which are not explored in detail here. One final straightforward use of the code could extend the results about cross–coupling of section 4.3. The code not only quantifies the amount of cross-coupling from (e.g.) vertical input to horizontal output for a given set of misalignments, but also can calculate the effect of the 'vertical' thermal noise that is seen in the horizontal direction.

5.1 Loss in *Lagran.mws*

The fluctuation dissipation theorem introduced in section 2.5.1 relates the frequency distribution of thermal noise in a system to the mechanical impedance. Specifically, equation 2.12 gives the displacement spectral density as

$$x_{Th}^2(\omega) = \frac{4k_B T}{\omega^2} \Re\left(Y(\omega)\right) \text{ per Hz}, \tag{5.1}$$

where k_B is Boltzman's constant, T the absolute temperature, and Y the admittance (the inverse of the impedance) measured at the point of interest. The mechanical admittance is the resulting velocity due to an input force at that same point,

$$Y(\omega) = \frac{v}{F}, \tag{5.2}$$

which is simple to calculate based on the techniques described in section 3.8. For an optical beam impinging on the test mass a distance d below the centre of mass, the output velocity is $\dot{x}_{TM} + d\dot{\theta}_{TM}$, given by the output matrix, $\mathbf{C}$, as the sparse row vector all zero except for a 1 corresponding to the $\dot{x}$ state and a d corresponding to the $\dot{\theta}$ state. The corresponding force is input at the same location; to obtain the driving terms in the equations of motion requires dividing by the appropriate mass or moment. The input vector is then

$$\mathbf{B} = \begin{bmatrix} 0 & 0 \\ 0 & \mathbf{M}^{-1} \end{bmatrix} \mathbf{C}^T \tag{5.3}$$

where M is the mass matrix of the system. With these definitions, the admittance and thus the observed thermal noise can be calculated as per section 3.8.

5.1.1 Gravity and Conservative Forces

Because the gravitational field is conservative—that is to say, it is lossless—energy stored in the gravitational field is not dissipated and thus does not contribute to the thermal noise. Since the Lagrangian formulation is designed for lossless systems, the introduction of lossy elements has to be done carefully in modifying the equations of motion of chapter 3.

Properly speaking, the force of gravity, being purely vertical, does not provide the restoring force in a swinging pendulum. The tension in the wire, which at equilibrium balances the gravitational force, is the dominant term in the equation of motion. The equilibrium tension results from the static extension of the wire times the extension spring constant of the wire. For the simplest case, a pendulum hanging on a single vertical wire, the potential energy allowing only vertical motion is

$$PE = mgy + \frac{1}{2}k_s y^2, \tag{5.4}$$

where in this case the change in wire length, δl, is equal to $-y$. Minimizing this with respect to y gives the equilibrium change in wire length as

$$\delta l_{eq} = -y_{eq} = \frac{mg}{k_s}. \tag{5.5}$$

Therefore the static tension, T_0, equals $k_s \delta l_{eq}$ and is solved for numerically at the same time the equilibrium is determined. While k_s is a function of the Young's Modulus, and thus has loss as a function of frequency, in steady-state equilibrium this loss is zero.

The dynamic length of the wire as determined in section 3.4.4 can be expressed as

$$\begin{aligned} l(x(t)) &= l_0 + \delta l & (5.6)\\ &= l_0 + \delta l_{eq} + \delta l(x). & (5.7) \end{aligned}$$

The potential energy involving δl is rewritten as $\delta l_{eq} + \delta l(x)$. The forces in the equations of motion appear as $k_s \delta l$. It is now clear that this force is made up of a constant force, the static tension $= k_s \delta l_{eq}$, and a dynamic force due to additional changes in wire length $= k_s \delta l(x)$. Only this dynamic component of the force exhibits loss. This is easily seen by examining the vertical equation of motion for a single wire pendulum, where the static tension balances the force of gravity while the additional change in wire length provides the restoring force and associated loss. To implement this in the equations of motion, the expression $k_s \delta l_{eq}$ is everywhere replaced by T_0 before any numerical substitution.

5.1.2 Implementation of α

The variables α_i in the Lagrangian code represent the loss angle for each stage as the imaginary component of the Young's modulus,

$$E_{wire1} = E_{0,1}\left(1 + i\alpha_1(\omega)\right), \tag{5.8}$$

or more generally, as the imaginary component of the spring constant for cantilever stages

$$k_{cant,u} = k_{u,0}\left(1 + i\alpha_u(\omega)\right). \tag{5.9}$$

These are the only variables that are maintained as symbolic until the very last step of the calculation because they are functions of frequency. This allows the α_i to be completely arbitrary functions. The only complication is in the numerical evaluation of large symbolic matrices. For viscous loss, where $\alpha_i \propto \omega$, the resulting **A** matrix has constant coefficients, and the calculations of the transfer function, using for example Matlab's bode.m routine, are simple. For other (more realistic) loss functions, the simplest method to generate transfer functions as a function of frequency is using a copy of **A** where the α_i are explicitly evaluated at every frequency.

The typical loss function for these wire suspensions is represented by a constant (structural) loss term plus loss due to thermoelastic damping[75, 76]. The is the function used for loss in the final stage for all of the modelling done in the following

sections. The expression used for the loss is[77]

$$\alpha_i(\omega) = \phi_c + \phi_{TE}(\omega) \tag{5.10}$$

$$= \phi_c + \frac{\Delta\tau\omega}{1+\tau^2\omega^2} \tag{5.11}$$

where

$$\Delta = \frac{E\,\alpha_{TE}^2\,T}{\rho\,c_{Sp}} \text{ and} \tag{5.12}$$

$$\tau = = \frac{1}{2\pi f_{char}}, \tag{5.13}$$

where for cylindrical wires

$$\tau = 7.32 \times 10^{-2}\,\frac{\rho\,c_{Sp}\,d^2}{k}. \tag{5.14}$$

In these expressions 5.12–5.14, where all values are for fused silica, $\alpha_{TE} = 5 \times 10^{-7}$ is the coefficient of thermal expansion, $E = 7 \times 10^{10}$ N m^{-2} is the Young's modulus, $T = 300$ K is the (absolute) temperature, $\rho = 2200$ kg m^{-3} is the density, $c_{Sp} = 772$ J kg^{-1} K^{-1} is the specific heat capacity, $k = 1.38$ J m^{-1}s^{-1}K^{-1} is the thermal conductivity, and d the thickness over which the bending occurs, the diameter of the wire. For the GEO 600 fused silica fibres, with $r = 154$ μm, this gives the thermoelastic peak at 19 Hz.

The use of a constant loss term, ϕ_c, represents the presence of structural damping. For thin fibres (such as used in the final stage of the GEO suspension), the observed damping will be dominated by dissipation in the surface of the fibre[75]. The loss in the bulk material, ϕ_{bulk} is related to the loss in the fibre by

$$\phi_c = \phi_{bulk}\left(1 + 8\frac{d_s}{d}\right) \tag{5.15}$$

for round wires, where d_s is a characteristic dissipation depth. The bulk loss used is that reported by Gretarsson,

$$\phi_{bulk} = 3.47 \times 10^{-8}, \tag{5.16}$$

consistent with the lowest dissipation measured in fused silica[78, 57]. The value

reported for the dissipation depth is

$$d_s = 167\,\mu\text{m} \tag{5.17}$$

over a range which includes the size of the GEO fibres.

The loss in the earlier stages of the pendulum can be input in the same fashion, but as the details are considerably less important, they are input simply as structurally damped terms α_i = constant, except where otherwise noted.

5.2 Length of Suspension Wires

The optimum suspension for a gravitational wave detector is the suspension that results in the lowest displacement noise of the optic, in terms of both seismic isolation and pendulum thermal noise. The total seismic isolation results from the many layers of vibration isolation while the pendulum thermal noise is dominated by the behaviour of the final stage pendulum. The question that this modelling work can be used to answer is what form of suspension gives the lowest amount of pendulum thermal noise. In particular, the relative merits of shorter wires versus longer wires may be compared. In addition, the effects of using more thin wires as compared to using fewer thicker wires to support the same mass may be evaluated.

The seismic isolation performance of a pendulum stage depends on the resonant frequency of the longitudinal mode. For a single wire attached at the centre of mass of the suspended object, this frequency is $(1/2\pi)\sqrt{g/l}$. When the length of the wire, l, is substantially larger than the radius of the suspended mirror, t_r, virtually the same resonant frequency is obtained using a wire of length $l - t_r$ attached to the top of the test mass. This would then give nearly equivalent vibration isolation in the same physical height. Therefore, the question is which suspension exhibits less thermal noise.

5.2.1 Two Wires and Two Loops of Wires

For the GEO 600 control architecture described in chapter 6, it is necessary to be able to control the tilt motion of the test mass from a higher stage in the suspension. Using a single wire to suspend the optic is insufficient as there is no stiffness in the

tilt direction and therefore no ability to apply the necessary control to the optic. There must be at least two wires, one in front of the other (in the parameters of the modelling section, $s \neq 0$).

The GEO 600 main mirror has a radius $t_r = 9$ cm, a length $t_x = 10$ cm, and mass 5.6 kg. In the GEO triple pendulum, the length of wires for the final stage is 28 cm; therefore, to investigate the best final stage suspension, an equivalent pendulum length of 28 cm is used. The total cross sectional area of the circular fibres necessary to support this test mass depends on the breaking stress of the material and to what level it is considered appropriate to load the wire. The breaking stress of fused silica is an area of active research; at the time this modelling was done, an estimate of breaking stress of 600 MPa was used. To load this to ~30% of the breaking stress, two fibres of radius 212 μm were modelled. In principle, two fibres of this radius could be of length 19 cm and attached to the top of the test mass or of length 28 cm and attached in a plane level with the centre of mass of the test mass. The loss assumed in section 5.1.2 is to be used, a constant (structural) term plus thermoelastic damping.

The resulting thermal noise for this stage in isolation is shown in figure 5.1. The total pendulum thermal noise observed on the face of the pendulum is a combination of all the pendulum modes which couple to the output, principally longitudinal and tilt. To address the fundamental question of which method results in a lower level of thermal noise, it is desired to examine the effect of only the longitudinal mode. Since for a general point on the front surface of the mirror, the longitudinal and tilt modes each contribute uncorrelated noise to the observed output, this corresponds to the point of minimum thermal noise calculated on the front surface of the mirror. The minimum point will depend on the mode shape and thus on the chosen spacing of the wires. In attempting to analyse the effect of only the longitudinal mode, this spacing need only be small compared to the size of the test mass. The exact tilt frequency will not affect the minimum noise obtained at high frequencies. Separating these two wires symmetrically about the centre of mass by 1 cm ($s = 0.005$) gives, for wires mounted off the top of the mass, a resonant tilt frequency of 4.7 Hz and a longitudinal frequency of 1.2 Hz. The minimum observed loss is at a point 0.8 mm below the centre of mass. When the two longer wires are attached in a plane at the same height as the centre of mass with the same separation, the resulting tilt

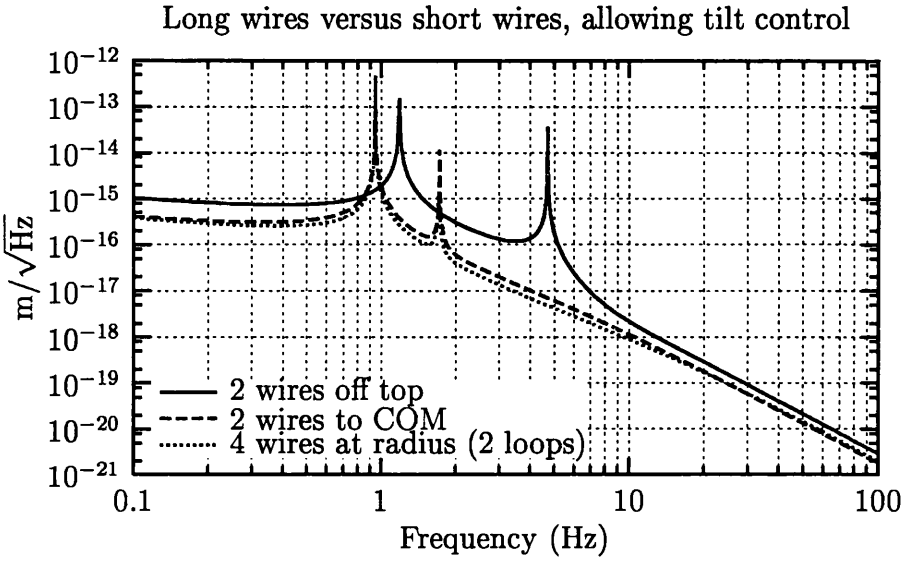

Figure 5.1: Two short wires versus two long wires. The thermal noise on the front surface of a GEO sized mass suspended using two short wires attached to the top of the mass is compared to the thermal noise for the same setup using longer wires attached level with the centre of mass. The data are calculated for the point of minimum motion on the surface of the mass, which for these cases is a fraction of a millimetre below the height of the centre of mass.

frequency is only 1.7 Hz while the longitudinal mode is resonant at 0.95 Hz. The minimum thermal noise is observed at a point 0.3 mm below the centre of mass. (The minimum is not seen at the height of the centre of mass because the finite bending stiffness of the wires cause the two modes to couple slightly, even when the wires are attached in a plane level with the centre of mass.)

The peak in the thermal noise at the tilt resonant frequency is clearly visible. At higher frequencies, the resulting noise is dominated by the noise from the longitudinal mode. The effects of the slightly different mode frequencies and less bending stiffness in the longer wires means that supporting the test mass with the longer wires results in less thermal noise at higher frequencies. At the 50 Hz frequency of most interest to GEO, the two long wire case exhibits a noise of $1.33 \times 10^{-20}\mathrm{m}/\sqrt{\mathrm{Hz}}$ while the suspension using two wires fixed to the top of the mass has a thermal noise of $2.13 \times 10^{-20}\mathrm{m}/\sqrt{\mathrm{Hz}}$.

It is impractical to drill through the test mass to allow the suspension wires to be attached near the centre of mass. (In addition, this would likely compromise the losses for the internal modes of the test mass.) Instead, the appropriate suspension to use these longer wires is a four wire suspension. This case is also plotted in figure 5.1, where all four wires are attached in a plane level with the centre of mass, one pair located 1 cm in front of the other pair, and where all the wires are attached on the outer radius of the mass ($n = t_r$). This is analogous to using two loops of wire to support the mass. The suspension wires are thinner, by a factor of $\sqrt{2}$, to support the same load across twice as many wires. The suspension has identical longitudinal and tilt resonant frequencies to that of the suspension with two wires attached near the centre of mass.

The bending stiffness of a wire may be expressed as[39]

$$k_b = \frac{T}{2L}\sqrt{\frac{EI}{TL^2}} \tag{5.18}$$

where T is the tension in the wire, E the Young's modulus, I the area moment of inertia, and L the length. The moment, for round wires, is proportional to r^4. For the four wire suspension compared to the two wire suspension, there is one half the tension and the radius is $1/\sqrt{2}$ times the two wire radius, implying the moment is 1/4 the moment of the two wire case. Thus the bending constant for one of

the four wires should be $\sqrt{2}/4$ times the moment for one of the wires in the two wire case. There are twice as many wires, suggesting that the total bending spring constant for the four wire case is $\sqrt{2}/2$ that of the two wire case. Since the wires are thinner, however, the surface effects cause the loss to be greater (section 5.1.2). For this example, the greater loss has more effect than the weaker stiffness and the thermal noise increases. The relative importance of these two effects is not obvious and depends on the specifics of the parameters. The minimum loss for the four wire suspension at 50 Hz is observed 0.2 mm below the centre of mass at a level of $1.46 \times 10^{-20}\mathrm{m}/\sqrt{\mathrm{Hz}}$, 10% worse than for two wires attached near the centre of mass but still ~30% better than for two wires attached off the top of the mass.

For these cases, the tilt modes of the pendulum are nearly pure rocking modes about the centre of mass and the minimum point of thermal noise is very close to the height of the centre of mass. The thermal noise observed when the beam is at the height of the centre of mass is a few percent worse than the optimum values quoted above.

As this method of suspension minimizes the amount of pendulum thermal noise for a practical suspension and allows the necessary tilt control of the mass, a four wire suspension is what will be used in GEO 600.

5.2.2 One Wire Suspensions

In order to maintain low loss for the internal modes of the test mass, it is usually considered undesirable to attach alignment actuators directly to the test mass. Therefore tilt alignment in the GEO 600 suspension acts on the upper stages of the multi–stage suspension, requiring at least two suspension wires as calculated above. If it were to be acceptable to provide the control directly on the test mass, it would be important to reconsider the best suspension solution with respect to pendulum thermal noise. A single wire of radius 300 μm can support the modelled mass at the same fraction of breaking stress as considered for the earlier cases. The comparison of the minimum thermal noise observed on the front face of the test mass using a single 19 cm wire attached to the top of the mass as compared to a longer 28 cm wire attached at the centre of mass of the optic is in figure 5.2. The respective longitudinal mode frequencies are 1.1 and 0.95 Hz. The tilt modes are now resonant at 4.3 and 0.50 Hz. The substantially different mode shapes that result with a single

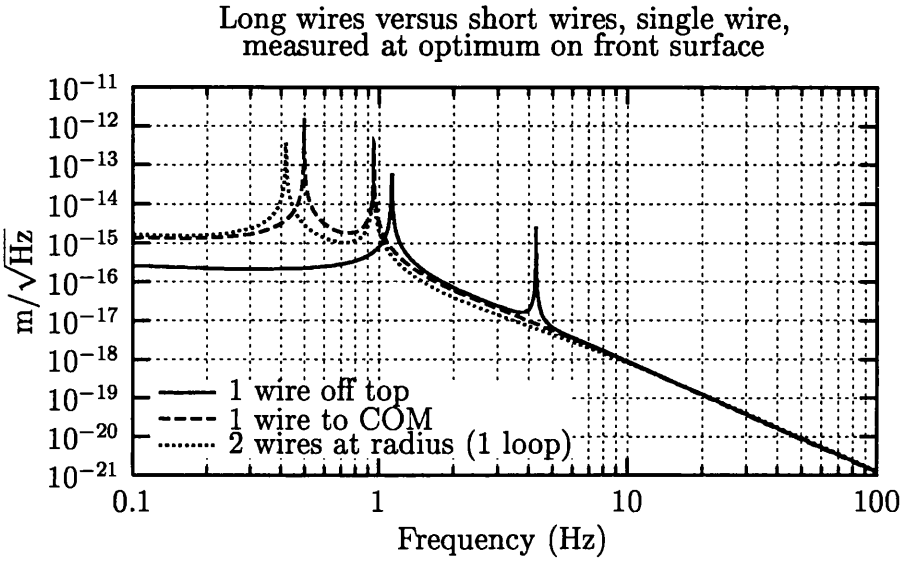

Figure 5.2: One short wire versus one long wire. When control can be applied directly on the test mass, a single wire may be used to suspend the optic. The minimum thermal noise on the front surface of the mass is evaluated for a suspension using one short wire attached to the top of the mass versus one longer wire attached to the centre of mass. This is further compared to two wires attached at the radius of the mass (one loop of wire). These values are calculated, again, for the location on the surface of the mass where the thermal noise is at a minimum.

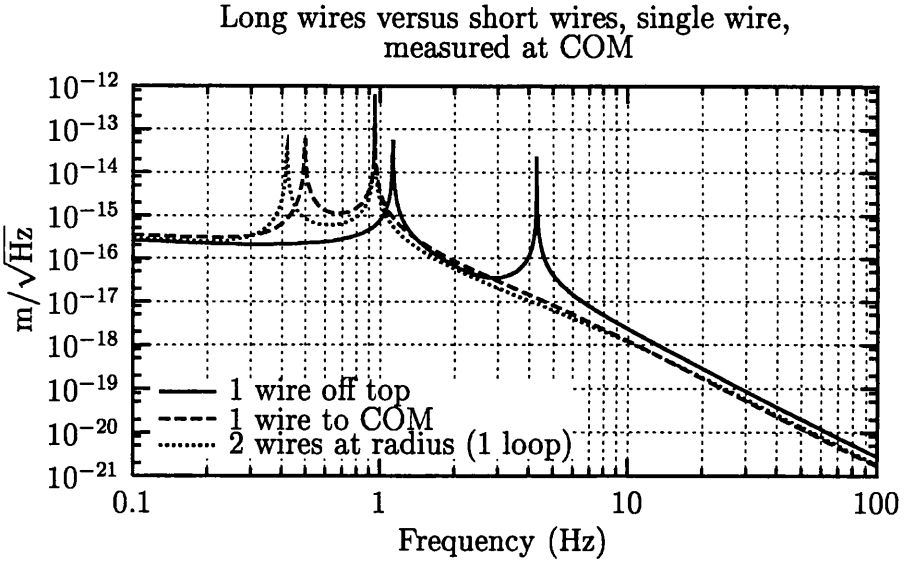

Figure 5.3: One short wire versus one long wire, measured at COM. The same modelling parameters are used as in figure 5.2, but the resulting thermal noise seen at the centre of the optic, rather than at the optimum point, is plotted.

wire cause the minimum thermal noise to be observed much further from the centre of mass than in the two wire suspensions. The minimum is found 12.3 mm below the centre of mass for the short wire suspension and 10.3 mm below for the longer wire to the centre of mass. As with the suspensions modelled previously, using the longer wire results in less thermal noise, $8.5 \times 10^{-21}\mathrm{m}/\sqrt{\mathrm{Hz}}$ at 50 Hz as compared to $8.8 \times 10^{-21}\mathrm{m}/\sqrt{\mathrm{Hz}}$ for the wire mounted off the top of the mass.

As before, a single long wire could not in practice be attached in the middle of the optic. It would instead be replaced by two wires near the radius of the mass, equivalent to a single loop of wire. These two wires would again be of radius $212(= 150\sqrt{2})$ μm. The longitudinal and tilt modes would be resonant at 0.95 and 0.42 Hz, and the minimum noise would be observed on the front face at a point 10.3 mm below the centre of mass. In this case, the increase in the loss in the fibre due to the increasing effect of the surface losses is sufficient to give a worse level of thermal noise than for either of the single wire cases, $9.4 \times 10^{-21}\mathrm{m}/\sqrt{\mathrm{Hz}}$. This data is also plotted in figure 5.2.

When there are suspension wires separated in the longitudinal direction, as in section 5.2.1, the tilting stiffness is dominated by the relative extension of these

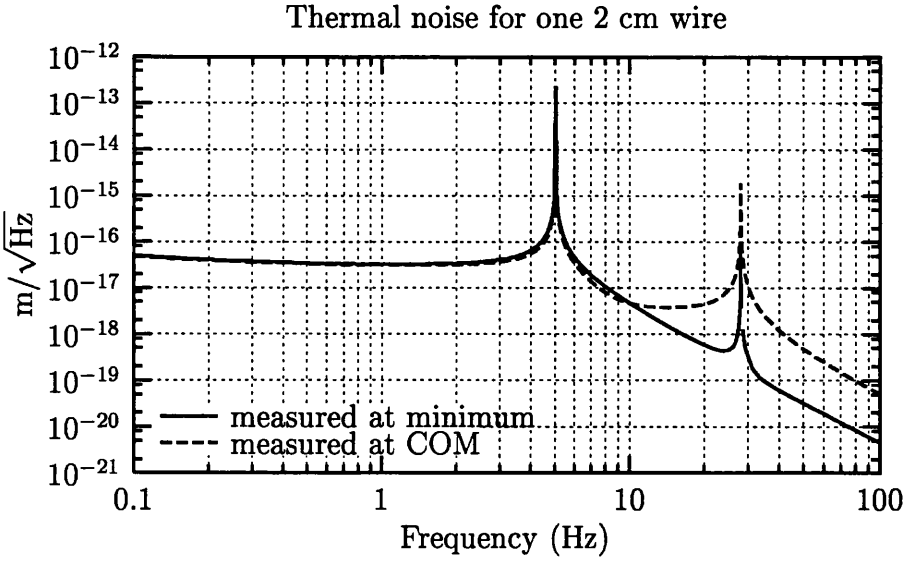

Figure 5.4: Thermal noise in a very short suspension. The observed thermal noise across the face of the GEO mass supported on a single 2 cm fibre.

wires. In the cases in this section, the tilting stiffness comes from the angling of the wires away from the vertical as the mass rotates. This results in substantially different mode shapes, which is why the point on the front surface which exhibits the minimum thermal noise is much further from the centre of the optic than for the earlier cases. The thermal noise for these cases is substantially higher when the output is observed at the centre of mass, as plotted in figure 5.3. The suspension using a single wire mounted off the top of the mass exhibits over twice the level of thermal noise at the centre of the optic as opposed to its optimum 12.3 mm below the centre, $1.98 \times 10^{-20}\mathrm{m}/\sqrt{\mathrm{Hz}}$ at 50 Hz as compared to $8.84 \times 10^{-21}\mathrm{m}/\sqrt{\mathrm{Hz}}$. The other two cases, one wire attached to the centre of mass and two wires attached at the outer radius, also exhibit more thermal noise performance measured at the centre of the optic—$1.21 \times 10^{-20}\mathrm{m}/\sqrt{\mathrm{Hz}}$ and $1.34 \times 10^{-20}\mathrm{m}/\sqrt{\mathrm{Hz}}$ at 50 Hz, respectively.

5.2.3 Short Suspensions

It has been suggested that very short wires should be used to eliminate the violin modes of the suspension wires from the detection band. However, it must be ascertained whether such a suspension can obtain comparable pendulum thermal

noise performance. The thought is that there is a point on the surface of the mass where the combined effect of the longitudinal and tilt mode can give a minimum in the observed thermal noise. To examine this possibility, a suspension for a GEO sized mass is modelled supported on a much shorter single wire. A 2 cm long wire, of radius 300 μm as before, supports the mass off the top of the suspension. The resulting thermal noise on the front face of the optic is shown in figure 5.4.

Were the wire to be completely rigid, such that the wire and mass combination pivoted perfectly about the upper suspension point, the resulting centre of percussion (section 4.2) would be located 2.6 cm below the centre of mass of the optic. By comparison, the minimum thermal noise is located at a point 2.8 cm below the centre of mass of the optic. At this point, at frequencies away from the resonant peaks, the performance is completely determined by the behaviour of the longitudinal mode. Except near the tilt frequency of 28 Hz, the thermal noise is that of the longitudinal mode at 5.0 Hz. The best noise observed for this case, $3.2 \times 10^{-20}\mathrm{m}/\sqrt{\mathrm{Hz}}$, is substantially worse than for the other cases detailed due to the higher resonant frequencies. The additional difficulty is that this minimum occurs over 1/4 of the radius away from the centre of mass. Assuming that the size of the mirror has been chosen to be as small as possible with respect to the optical beam, this point will be too far from the centre of the mirror to be useful. If the beam were to be centred on the optic for this suspension, the resulting thermal noise would include the effects of the tilt mode and be much worse—$4.8 \times 10^{-19}\mathrm{m}/\sqrt{\mathrm{Hz}}$ at 50 Hz.

One particular advantage of this kind of suspension is that it would be comparatively simple to replace the suspension wire with a short flexure. Flexures can be made at the same fraction of breaking stress (that is, with the same cross sectional area) but much thinner in the critical direction. This can make the flexure much softer in bending, and presumably improve the thermal noise performance. The Lagrangian code can model the effects of flexures by changing the definition of the area moment of inertia of the wire. However, the results presented here are sensitive to the exact values of loss. The loss in the suspension elements depends on the surface effects, and it is not clear at this time what is the proper loss function to use for a flexure. A brief discussion of how flexure systems may affect thermal noise performance and other aspects of suspension design is included in the chapter summarizing possible future work (section 8.2).

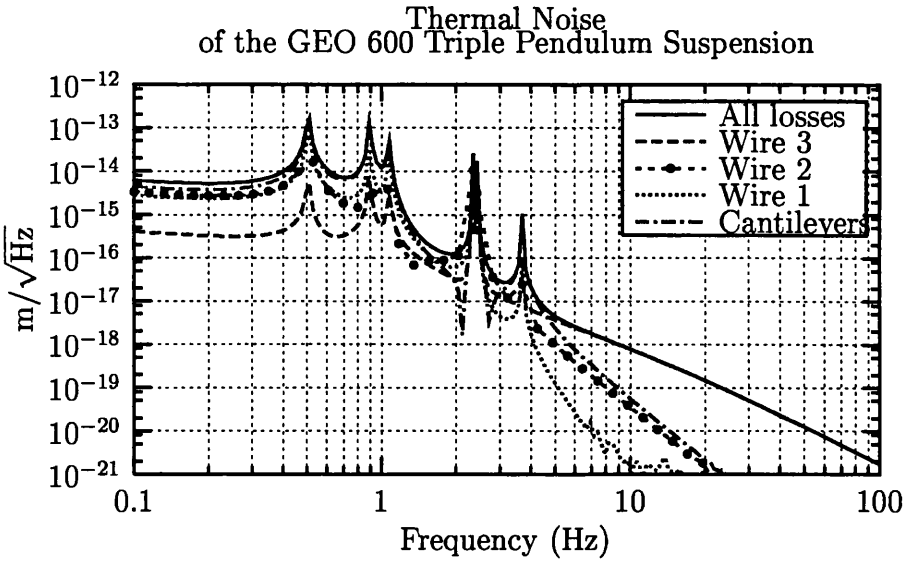

Figure 5.5: Thermal noise in the GEO 600 pendulum. The data illustrates the contribution to the noise for the loss associated with each set of wires and with the cantilevers, as well as the total noise. The curve labelled 'wire 3' is calculated using non–zero loss only in the third (lowest) stage of wires; that labelled 'wire 2' uses non–zero loss only in the intermediate stage wires; and that labelled 'wire 1' only has loss in the uppermost wires in the system. The final curve is plotted for loss only in both sets of cantilevers.

5.3 Thermal Noise in a Multi–stage Pendulum

The final figure of merit is the overall thermal noise in a triple stage GEO 600 suspension. The Lagrangian code allows arbitrary loss in every stage of the system, accounting for the observed noise from all longitudinal and tilt modes. In particular, the intrinsic loss in the cantilever blades can be included, with the correct coupling to the output of the system. This allows for the first time the determination of the maximum allowable loss in every stage of the pendulum.

5.3.1 Longitudinal and Tilt

The resulting thermal noise in the longitudinal direction for the GEO 600 parameters is shown in figure 5.5. This includes all the noise that results from pendulum motion in the longitudinal and tilt modes. These curves are calculated using structural plus thermoelastic loss in the final stage of the pendulum, and structural loss of 10^{-5} for

the other two wire stages. The cantilever blades are input with a structural loss of 10^{-4}. These figures for the stages other than the final stage are extremely conservative, but as the data show, even these values are acceptable because of the isolation that the final stage of the pendulum provides. To illustrate the effects of loss in each individual stage, various curves are plotted showing the resulting thermal noise for the loss being zero in all stages except one. As would be anticipated, the noise at higher frequencies is dominated by the loss in the final stage of the suspension, since the noise contributed by earlier stages in the suspension is filtered by the final stages. At very low frequencies, the noise is dominated by the stages with the greatest loss, the cantilevers, which is unfiltered at low frequencies. The evaluation of some of these curves at higher frequencies causes some numerical difficulty. This results in the irregularity of some curves in figure 5.5, which is particularly obvious in the data for loss only in the highest stage of wire (labelled 'wire 1') near 10 Hz. This irregularity is inconsequential to any of the conclusions.

The noise at 50 Hz is the crucial result for this suspension. Due to the tilt and longitudinal mode shapes, the thermal noise seen by the optical beam could vary across the surface of the test mass. By varying the impinging point on the surface, the minimum noise and corresponding point can be determined. For the triple pendulum parameters used in the above figure (and summarized in section 7.3), there is very little variation (<1%) within a few millimetres of the point level with the centre of mass. The other important result that this data offers is the amount of loss in the higher stages of the pendulum that is tolerable without compromising the total noise, with the loss in the final stage fixed at the best achievable level. The low level of loss that is required in the final stage of the suspension leads to the use of fused silica fibres and specialized methods of bonding the fibres to the test mass. If higher levels of loss can be allowed in the higher pendulum stages, relatively simple steel wires and mechanical clamps may be used in those stages. By varying the loss parameters of the higher stages in the thermal noise calculation, it may be seen that at 50 Hz the loss in both of these higher stages can easily afford to be a factor of 10^3 worse than the loss in the bottom stage. This is effectively because of the amount of filtering of the noise from the higher stages given by the 1 Hz final pendulum stage. The total pendulum thermal noise expected in the GEO 600 main suspension is therefore expected to be $1.25 \times 10^{-20}\mathrm{m}/\sqrt{\mathrm{Hz}}$ at 50 Hz.

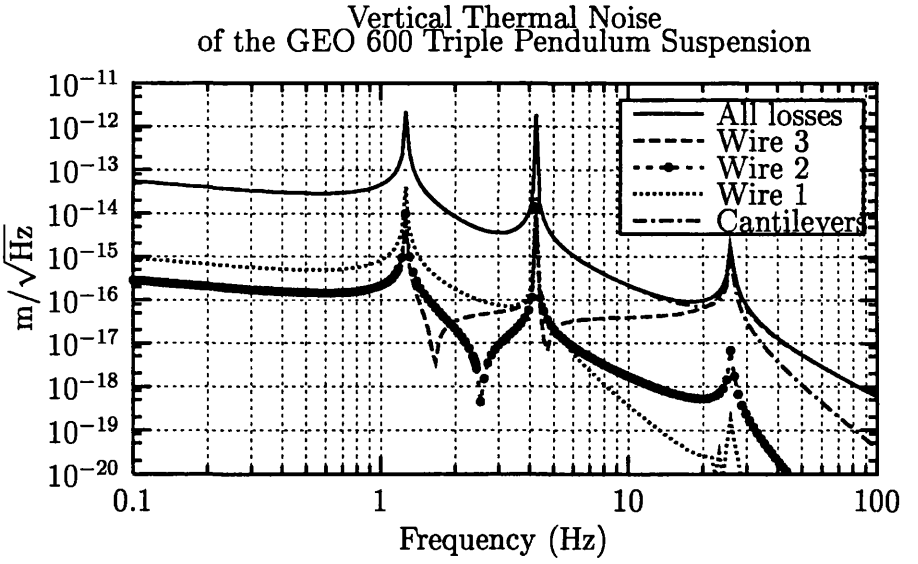

Figure 5.6: Vertical thermal noise in the GEO 600 triple pendulum suspension. The notation is as in figure 5.5.

5.3.2 Vertical

The higher vertical frequencies in the system suggest that the loss in the higher stages of the suspension system will not be filtered as much. In addition, the cantilevers, which may have a great deal more loss, affect the performance directly in the vertical direction, rather than indirectly affecting the thermal noise in the longitudinal direction through coupling from the tilt modes. Figure 5.6 shows the vertical thermal noise seen at the bottom of the GEO 600 triple pendulum suspension. In these cases, while the loss in the final stage is the most important, the loss in the cantilever stages does affect the total performance of the suspension at 50 Hz. For $\alpha_{cant} = 10^{-4}$, the total noise is observed to be $5.4 \times 10^{-18}\mathrm{m}/\sqrt{\mathrm{Hz}}$ in the vertical direction. When the loss in the cantilevers is assumed to be a factor of 10 greater, the total loss observed in the system increases nearly 20% to $6.3 \times 10^{-18}\mathrm{m}/\sqrt{\mathrm{Hz}}$.

When a 0.1% coupling from vertical to horizontal output is assumed for the system, this contribution to horizontal thermal noise from the vertical direction is $5.3 \times 10^{-21}\mathrm{m}/\sqrt{\mathrm{Hz}}$, compared to the noise predicted for the longitudinal and tilt directions of $1.25 \times 10^{-20}\mathrm{m}/\sqrt{\mathrm{Hz}}$ at 50 Hz. The uncorrelated sum of these two noise sources give the total anticipated pendulum thermal noise for the GEO 600 main suspension as $1.36 \times 10^{-20}\mathrm{m}/\sqrt{\mathrm{Hz}}$ at 50 Hz, below the target specification of $7 \times 10^{-20}\mathrm{m}/\sqrt{\mathrm{Hz}}$.

Chapter 6

Control of Interferometer Optics

The GEO 600 suspension system isolates the interferometer optics from disturbances due to ground motion at the measurement frequencies. This alone is not sufficient; while the test masses may be extremely quiet in inertial space, they still require to be measured in order to detect a gravitational wave. Therefore the suspended masses need to be controlled, both to reduce their motion at low frequencies and to reduce their relative motion with respect to the measurement device, the input laser.

This chapter will examine the philosophy of how control ought be applied to a complex mechanical system, such as the suspensions in a gravitational wave interferometer. Next, it will examine how the techniques of chapter 3 were used to design a pendulum suspension that met the low frequency control requirements of the GEO 600 detector. This is followed by a discussion of how the modelling of a single suspension requires to be expanded to include violin modes when the control of the entire interferometer is considered. The chapter concludes by examining in detail the signal commonly used in 'locking' interferometers and how this signal is affected by the long optical characteristic times associated with long base–line interferometers, compared to the usual regime of short characteristic times in table–top experiments.

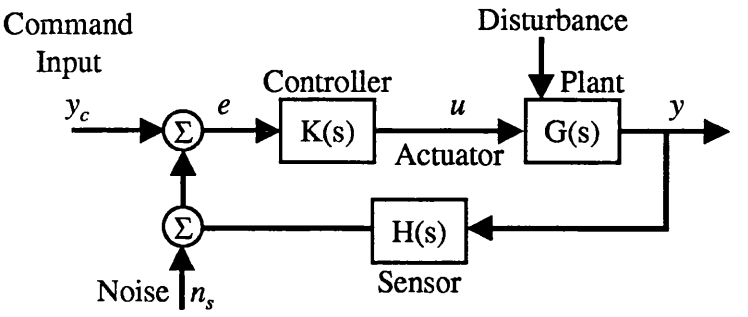

Figure 6.1: Block diagram of a control system.

6.1 Hierarchy of Control

There are four parts to any control system: the sensor, the actuator, the plant, and then the control law. It is in this order that control problems should be addressed. These components are summarized in the block diagram in figure 6.1, along with various kinds of input variables, noise sources, and outputs that are relevant to the design of a controller. Something can only be controlled as well as it can be measured, thus giving precedence to the sensing. How correction is to be applied to a system can also be a limitation, highlighting the importance of the actuation. While the design of physical systems is often constrained by many (often conflicting) requirements, it is often possible to choose a system that proves much easier to control while not compromising other requirements. Finally, a control algorithm is determined, based on the capabilities of the sensor, the actuator, and the response of the physical plant. While very clever controller design may be able to compensate for a wide variety of performance deficiencies, reliance on an intricate control algorithm usually results in a system that is not robust to changes in the system over time and, in practice, depends overly much on a highly specialized individual to maintain and update the controller. Therefore, robust and simple controller designs are preferred.

For complex systems such as gravitational wave detectors, there are many control loops. All the possible degrees of freedom have to be considered to determine the respective degree of control required. It is common that there be multiple, nested, loops acting on the most important degrees of freedom. Different loops can, for example, provide correction in different frequency bands. These loops may use multiple sensors which use different references, as appropriate for each frequency

band. Additionally, loops may act over different ranges, one loop using a large range 'coarse' actuator effect while another provides a more accurate and less noisy 'fine' control.

For the suspensions described in this work, control is typically broken into two types. The 'local' control, described in the next section, uses a non–inertial reference to sense disturbances in every degree of freedom of one pendulum mass. The relatively simple sensors and actuators can have a very wide range, compared to the signal to be detected by the interferometer, and the control is applied at frequencies well below the detection band to control the behaviour of the entire pendulum suspension. The 'global' control, discussed in section 6.3, is the fine control applied to the sensed test mass. It requires sensing the entire state of the interferometer, using an involved sensing scheme. It typically requires higher bandwidth control, but is only required in certain degrees of freedom. In particular, the longitudinal degree of freedom—the sensed direction of the interferometer—has the tightest control requirements. Variations in the angular positions of the mirrors can couple noise to the interferometer output with a coupling based on beam position. In a similar fashion, mirror displacements in directions orthogonal to the beam can cause higher order errors in the optical signal. The global control of these degrees of freedom is not discussed in detail here.

6.2 'Local' Control

The pendulum suspensions provide a seismically quiet system at higher frequencies. Below the resonant frequencies of the system, naturally, the system provides no isolation, so that the suspended optic moves exactly as much as the ground on which it rests. Exactly on resonance, the pendulums can move a great deal more than the input ground motion. By being in vacuum, and due to the high mechanical Q required for thermal noise reasons, it is guaranteed that the pendulums resonances will cause motion many ($\sqrt{Q}$) times more than the base spectrum. This leads to a large average (root mean square or rms) motion which can persist for a great deal of time. While great effort is placed into making sensors and actuators very accurate and sensitive, if a large motion were to be accommodated, the dynamic range requirements become prohibitive. As an example, even if the interferometer

signal, which is to detect motions on the scale of 10^{-19} m in a bandwidth of a few Hz, could operate over a range of 1 mm, the data would have to be recorded to $\log(10^{-3}/10^{-19}) = 16$ decimal places, and require $\log_2(10^{15}) \approx 54$ bits of analog to digital conversion. In addition, the time Q/f_0 gives a measure of how long these resonances take to decay when excited by whatever means. A Q on the order of one million in a pendulum would give a decay time on the order of twelve days. Clearly the system cannot tolerate disturbances that prevent operation on these time scales.

Thus it is important to reduce the Q, the magnitude, of these resonant peaks. The metric is a practical one; it is desired that the system quiet down for a disturbance input in a short period of time, on the order of a few seconds. Therefore, the Q of the resonances should be reduced to $\sim$5 or less.

As noted in the discussion of the fluctuation–dissipation theorem (section 2.5.1), a lower value of Q would typically cause the system to have more thermal noise in the measurement band, since the energy thermally dissipated in the suspension causes more fluctuating motion. Damping the system externally is called 'cold damping', since feedback forces are used to increase the damping without raising the noise temperature of the system. Energy is removed from the system through the external actuators rather than through frictional or other entropy increasing methods.

To reduce the motion of the system requires a reference that is quieter than the suspension to be controlled. On resonance, the ground input (or other interface to which the pendulum is attached) is much quieter than the pendulum, so measuring the position of the pendulum with respect to the ground is appropriate. This is done by mounting a light emitting diode (LED) and a photodiode on the frame surrounding the pendulum. A flag is attached to the pendulum, positioned so as to block some of the light of the diode. This sensing of each pendulum system with respect to its immediate surroundings lead to the designation 'local control'. In the GEO 600 design, this 'shadow sensor' uses a photodetector of area $(4.5\text{mm})^2$ and 50 mA to supply the LED. This gives a position measurement with sensitivity better than $3 \times 10^{-10}\text{m}/\sqrt{\text{Hz}}$. In the state-space formulation the relative motion between the ground and the moving mass can be made an output by setting, for example,

$$y_{ss} = x_1 - x_g,$$

using the $\mathbf{C}$ and $\mathbf{D}$ matrices (section 3.7). All the modelling work for the local control

simply uses $y = x_1$, because near the resonance where the control has greatest effect, $x_1 \gg x_g$.

For a one–dimensional resonance, the ideal feedback controller is simple to determine. Since the energy flow in the system is the rate of work done on the system,

$$E = \frac{d}{dt}W = F\frac{dx}{dt} = F \cdot v,$$

to quiet the system by removing energy, ideally

$$F \propto -v. \tag{6.1}$$

Of course, the ground does not provide a quiet reference at higher frequencies. In addition, the shadow sensor provides a position signal; converting this to the desired velocity involves an electronic differentiation which typically adds noise at higher frequencies. Therefore the feedback controller should not provide gain above the pendulum frequencies.

Since isolation is provided by the suspension at high frequencies, it is important not to rigidly fix the suspension to the ground. Therefore, the appropriate actuators are low impedance (soft), those which provide a correcting force, rather than high impedance (stiff), such as piezo–electric stacks which establish a position. For gravitational wave detectors, the suspensions typically use magnets attached to the suspended masses and use external coils to generate corrective forces. The simplest way to reduce the affect of actuator noise on the suspension is to make the actuator very weak. Limiting the authority in the actuator in this fashion clearly can reduce the effectiveness when large forces would be appropriate, such as for acquiring lock as described in section 6.4.

These sensors and actuators could, in principle, act at any point on the multiple stage pendulum to reduce the motion. Sensing and actuating at the same point ensures that no unmodelled dynamics can affect the performance of the loop. By proper design of the control loop, stability can be guaranteed.

These ideas were extended, in a classical control context[65], to the double pendulum suspensions to be used in GEO 600 by Killbourn[67]. The success of this control design was to be extended to the triple pendulum suspensions used for the main optics. There are a number of features that are advantageous to this design,

not the least of which is the great variety of suspensions to which it may be applied. Firstly, the controller design is simple. A rigid body exhibits motion in six degrees of freedom; to control all of these requires six sensor–actuator pairs positioned around the mass. Each sensor–actuator pair is controlled independently with a single–input, single–output (SISO) controller. This allows the full, multiple–input, multiple–output (MIMO) design to be greatly simplified. Each channel is identical, with, at most, a small change in electronic gain, reflecting the relative scale of the moments of inertia and lever arms for each degree of freedom. Secondly, the control is collocated. By feeding back each sensor signal to the corresponding actuator, rather than combining the signals of multiple sensors into, for example, the translation and rotation of each mass then decomposing the actuation signal back to the appropriate drivers, the system has all the usual advantages of collocation, such as the guarantee of stability. These two virtues lead to the most general advantage of all, the robustness of the controller. Each controller acts to damp any resonances that are in the band of approximately 0.5—5 Hz. Thus any suspension whose frequencies lie in this range can be controlled, virtually without modification.

Ideally, the suspension design would be chosen such that all modes of the system lie in this range. This is not always possible. The vertical resonant frequencies of a wire based pendulum suspension will be higher than the longitudinal resonant frequencies. The inclusion of cantilever blades in the upper stages of a suspension allow these vertical (and roll) frequencies to be reduced to fall within the local control band. As previously noted, these thermally noisy blades can not be used in the final, most sensitive stage of a pendulum suspension. Therefore, for the GEO 600 triple pendulum suspension, the vertical and roll modes that involve the differential motion of the bottom two stages of the pendulum will have higher frequencies. The roll motion couples very weakly to the interferometer performance, and therefore this mode has little effect. The entire suspension was designed to ensure that the higher frequency vertical mode is acceptable for isolation. This mode is resonant at too high a frequency to be damped but not so high a frequency that its affect on the control loops may be ignored, and the electronic feedback typically uses a notch filter at this frequency to avoid difficulties.

The important characteristics of the local control examined here are that it acts in a specific low frequency band and damps all the motion of the uppermost mass

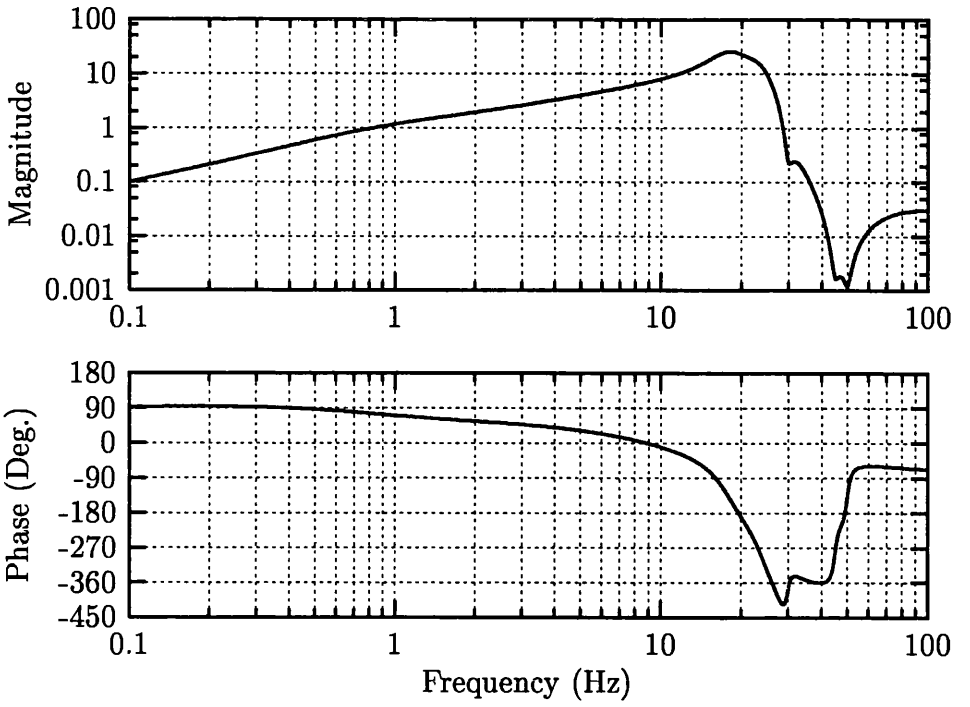

Figure 6.2: Bode response of the local controller.

in the suspension. This allows the simple extension of this control philosophy to a large variety of suspensions, both minor variations as used in all the different optics in GEO 600 (described in chapter 7) and in substantially different pendulums as may be used for advanced detectors (chapter 8). The frequency response of the local control electronics for GEO 600 is shown in figure 6.2.

6.2.1 Location of Damping Versus Noise

The difficulty in damping the motion of the test mass in a multi–stage pendulum system is that, above the resonant frequencies, the mass is very quiet. Any attempts to sense the motion of this test mass will be dominated by the noise in the sensor, n_s in figure 6.1. To not exceed the target specification of $7 \times 10^{-21}\mathrm{m}/\sqrt{\mathrm{Hz}}$ at 50 Hz (a factor of ten below the anticipated internal thermal noise of the test mass) for sensors which sensed the critical test mass with a sensitivity of $3 \times 10^{-10}\mathrm{m}/\sqrt{\mathrm{Hz}}$, the loop gain of the controller would have to be something less than 10^{-9} by 50 Hz. Since the loop gain of the controller must be of order 1 up to a few Hertz to provide damping for the longitudinal resonances of the system, the system would require to

achieve this filtering in less than two orders of magnitude of frequency. The inertia of the triple pendulum provides some of the filtering—the transfer function between force applied to the bottom mass of the GEO design to resulting displacement gives $\sim 10^{-4}$ filtering between low frequencies and 50 Hz—but the fundamental relationship between the magnitude and phase of a transfer function[79] ensures that the electronics used to achieve the remainder of the attenuation will cause some phase lag at the lower frequencies. The amount of filtering required makes this potential controller a challenging design if it is to maintain a reasonable phase margin above a few Hertz.

In addition, any noise in an actuator acting directly on the isolated test mass is applied directly to the test mass. In the electronics that drives the actuator, the final stage operational amplifier can output 10 V peak (or ~ 7 V_{rms}) with a noise of 4 $nV_{rms}/\sqrt{Hz}$, for a dynamic range of $\sim 2 \times 10^9$ in a 1 Hz band at 50 Hz. An actuator being driven by this amplifier acting directly on the test mass and having a noise less than the detector specification at 50 Hz would have a maximum range of less than one micron (allowing for the mechanical filtering).

Instead of attempting to control the sensitively isolated optic, a more viable solution is to sense and actuate on a less sensitive stage of the multi–stage pendulum—in particular, the least sensitive, or highest stage. This allows both the actuator to be made significantly stronger, by the inverse of the isolation of the final stages of the pendulum at 50 Hz, and reduces the requirements on the electronic filtering of the sensor noise, by the same factor of isolation. There is still a significant amount of electronic filtering to be done, and this filtering has been updated from that developed for the double pendulum suspension for use in the suspension of the main optics in GEO 600. The required filtering is achieved by three stages of resonant Scultéty filters[80]. This is a particular implementation of a filter consisting of a pair of resonant poles, relatively heavily damped, to cause rapid $(f_p/f_0)^2$ attenuation, followed by a lightly damped pair of filter zeros, which reduces the phase lag observed at lower frequencies. It is chosen due to its electronically quiet implementation. The transfer function of a single Scultéty filter is

$$\frac{V_{out}}{V_{in}} = k_{DC} \frac{s^2 + \frac{2s\omega_0}{2q_n} + \omega_n^2}{s^2 + \frac{2s\omega_0}{2q_p} + \omega_p^2}. \tag{6.2}$$

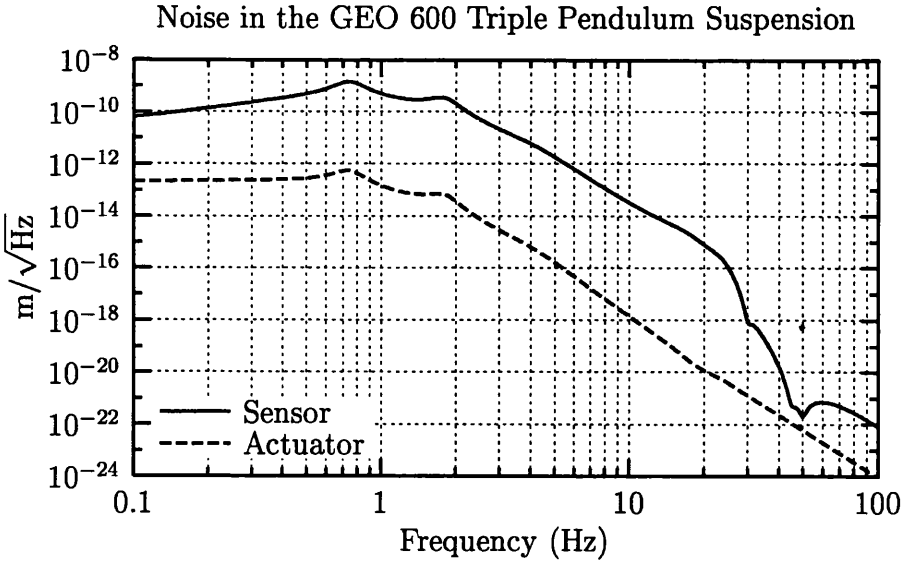

Figure 6.3: Sensor and actuator noise in GEO 600 main suspension. The effective displacement noise of the suspended mass due to sensor noise and actuator noise. At 50 Hz and above, each of these is below the internal thermal noise of the test mass, estimated to be $7 \times 10^{-20}\mathrm{m}/\sqrt{\mathrm{Hz}}$.

The parameters are chosen such that the resonant peak of each filter stage has a Q of approximately 3. The notch in each filter is tuned to account for uncontrolled resonances in the system. The lowest frequency notch is at the highest frequency vertical mode of the triple pendulum system, 25 Hz. The exact frequencies of the second and third notches are not crucial as long as sufficient electronic isolation is achieved; these notches are set at 45 and 50 Hz.

The implementation of this electronic filtering, along with the characteristics of the shadow sensor and the coil actuator, inserted into the dynamics model of the multi-stage pendulum gives the predicted levels of noise shown in figure 6.3. The contribution to the noise budget is a factor of nearly 100 below the specified level for GEO. The transfer function between the volts applied to the actuation coil (a noise of $4\mathrm{nV}/\sqrt{\mathrm{Hz}}$) and the resultant motion may be deduced from the figure; the mechanical attenuation of $\sim 10^9$ between low frequencies and 50 Hz combined with the dynamic range of the actuator gives a total actuator range greater than 1 mm. The effect of the local control on the motion of the test mass can be seen in figure 6.4. The height of the resonant peaks has been reduced (to a Q of a few), as

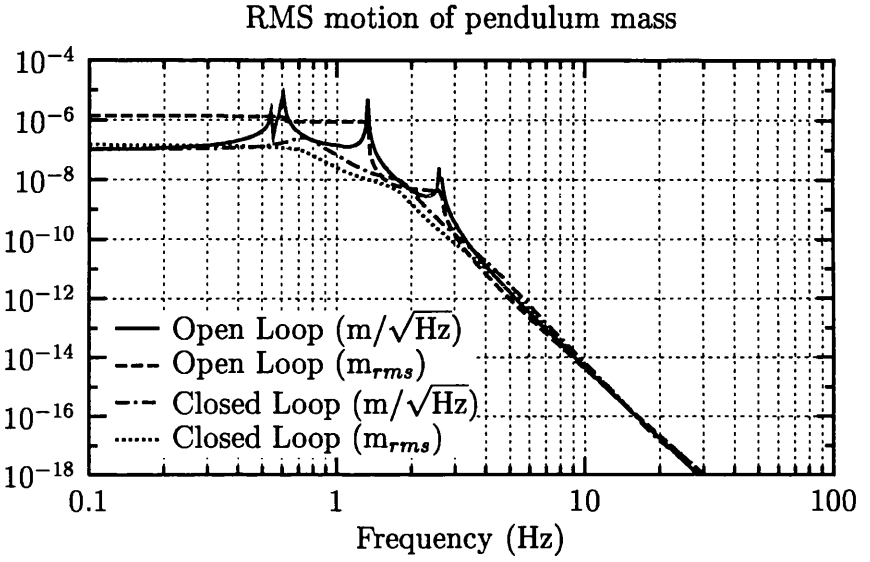

Figure 6.4: Predicted RMS motion of test mass. The spectral density (x_{sd}) of the open and closed loop performance can be compared to see the reduction of the resonant peaks due to the local control. The root mean square (*rms*) motion for both open and closed loop performance is plotted as the integral of the residual motion at that frequency and above, $x_{rms}(f) = \int_f^\infty x_{sd}^2(f)\, df$. Clearly most of the average motion comes from the resonant peaks; thus the closed loop rms motion is an order of magnitude less than the open loop rms motion.

seen in the spectral density, and the total average (rms) motion has been reduced approximately a factor of ten.

6.2.2 Mode Coupling

The choice of a triple pendulum (or any multiple–stage pendulum) adds one important complication to damping the system at the uppermost stage. The technique will successfully reduce motion of the damped stage, but it is not guaranteed to damp motion of the test mass at the lowest stage of the pendulum. The difficulty is that there may be a mode where there is a great deal of motion in the lower stages of the pendulum while there is little motion at the uppermost stage. The simplest example would be for a system where one stage has a great deal more mass than any other stage. The same forces that cause large motions of one stage would then cause little motion of the most massive stage. This aspect of the problem is avoided by having each stage of the suspension have comparable mass and moments of inertia about each axis.

The more general problem is somewhat subtler. In order for each mode of the system to be damped by a sensor–actuator pair, each mode must be both controllable and observable[81]. In practice, the requirement is that each eigenmode of the system should have a substantial component of motion on the uppermost mass. The exact relationship between observed system performance and the eigenmodes depends on the frequencies of the modes and the masses and moments. Therefore, the simplest way to verify that the mode shapes are suitable is to use the modelling techniques to calculate the open loop transfer function of each channel. Since each resonant mode of the plant is very lightly damped, and thus on the magnitude response exhibits a large peak, if the mode is sufficiently observable, it will have a large peak in the open loop transfer function of the controller channel. Achieving acceptable performance for all the modes to be controlled in the system requires some effort and iteration. Examples are shown in figure 6.5. The open loop response of one of the tilt controllers in the GEO 600 main suspension is shown in the solid curve. In contrast, the dashed line shows the same open loop controller for an arbitrary choice of one selected mechanical parameter, where $s[1,l] = s[2,u]$ has been reduced from 0.03 to 0.01 (i.e., the full separation of the wires between the uppermost and intermediate stages has been reduced from 6 cm to 2 cm). There are three resonant peaks

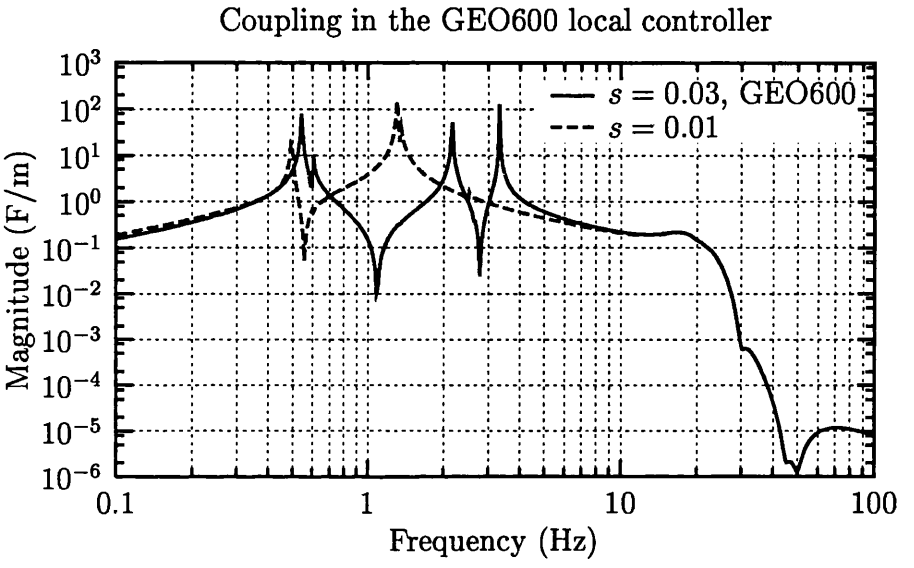

Figure 6.5: Coupling of modes in the triple pendulum suspension. The solid line illustrates the open loop signal at a representative sensor which demonstrates a large amount of gain at each resonant peak. The dashed line shows the same signal for a poor choice of pendulum parameters, where the control gain at one peak (~2.5 Hz) is much lower than at the other peaks, resulting in very little damping of that resonance.

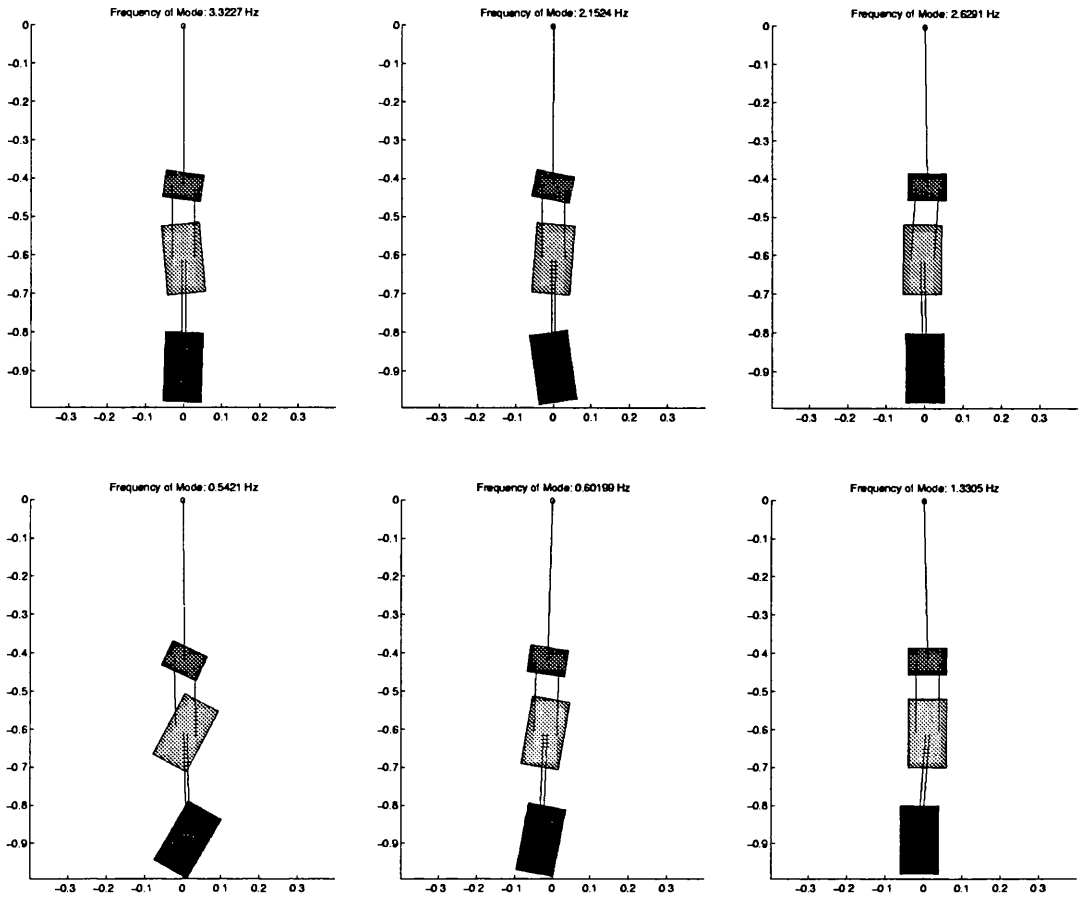

Figure 6.6: Mode shapes in the triple pendulum. The various figures show the shape of the the six longitudinal and tilt modes for the GEO 600 suspension.

observed in each magnitude plot. In the chosen design, the magnitude of each peak is large, resulting in a large loop gain at each resonant frequency and thus sufficient damping. In the alternate design, the magnitude of one of the peaks, between 2 and 3 Hz, is so small that it essentially does not appear above the baseline curve. This happens because the cantilevers between the uppermost and intermediate stages of the suspension make the tilt between these two stages very soft, such that the bottom two stages can tilt with respect to each other while the uppermost stage tilts very little unless the separation of the wires is sufficiently large. Therefore one of the modes of the system has very little loop gain and therefore little reduction of the resonant peak. The details of each case can be examined in turn, but the design iteration can be done by examining the open loop response of each of the control channels.

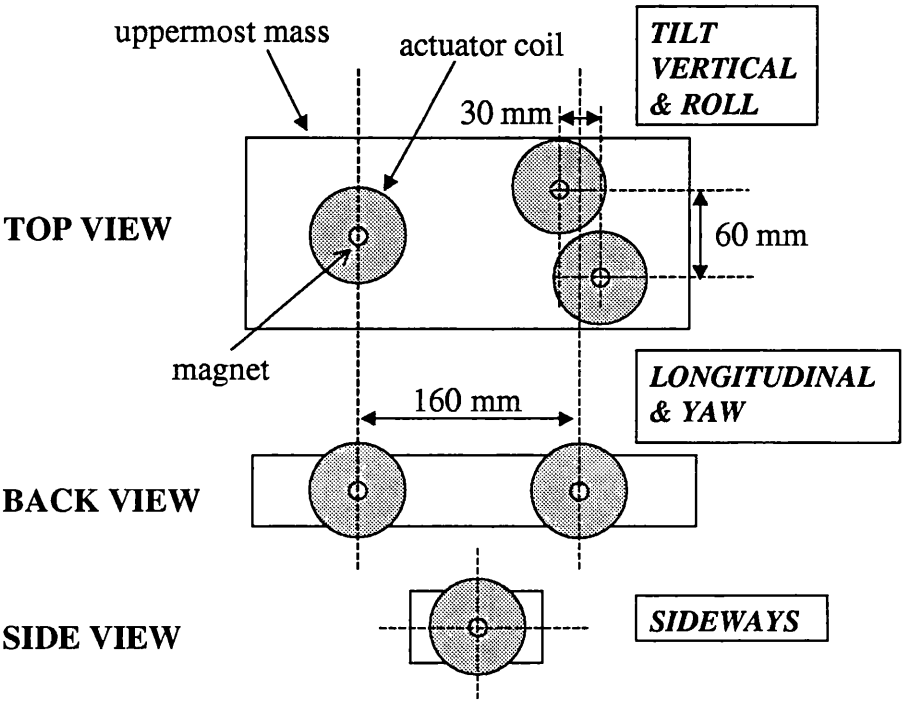

Figure 6.7: Position of the coils on the triple pendulum. Six coils allow control of all six degrees of freedom of the uppermost masss of the pendulum.

With this design tool, the mechanical parameters of the triple pendulum can be finalized. The specific longitudinal and tilt mode shapes for the GEO 600 triple pendulum are depicted in figure 6.6. The control is achieved by positioning the collocated sensor/actuator pairs to sense and control all the modes of the system. For the final design, two sensor/actuator pairs are located to provide longitudinal and yaw control, spaced 8 cm on either side of the centre of mass; one sensor/actuator is located on the side of the mass, actuating through the centre of mass; and three pairs are located on the top surface of the mass (figure 6.7). These three control vertical, pitch, and roll motion. One of these is located 8 cm away from the centre of mass in the transverse, Z, direction, acting vertically. The other two are centred about a line the same distance on the other side of the mass, one of them 6.5 cm and one 9.5 cm from the centre of mass in the Z direction, while they are each 3 cm from the centre of mass in the longitudinal direction. These positions are chosen very practically such that the coils fit together, both for a single suspension and for suspensions involving a reaction mass needed for applying the global control forces (section 6.3).

6.2.3 Verification

The operation of this local controller was demonstrated on the prototype triple suspension. Experimentally, the test of the local control with respect to the mechanical parameters of the pendulum was done before the final version of the control electronics was completed. Therefore the circuitry designed for the control of an earlier double pendulum design[67] was used. The ability to do this reflects the wide range of applicability of the control philosophy as described ealier. The only difference in the transfer functions was the final electronic filtering, which does not affect the control near the pendulum resonant frequencies. When in operation, it is visually clear that the pendulum system is well damped. Even for a large manual disturbance which saturates multiple sensors, the system appears to return to equilibrium in less than ten seconds. Each channel is well damped, with a Q on the order of 3 or less.

The two most critical degrees of freedom, longitudinal and tilt, are explicitly evaluated. The local control electronics is designed with both a 'fast' and a 'slow' input to allow various test inputs to be applied to the system. A step input was

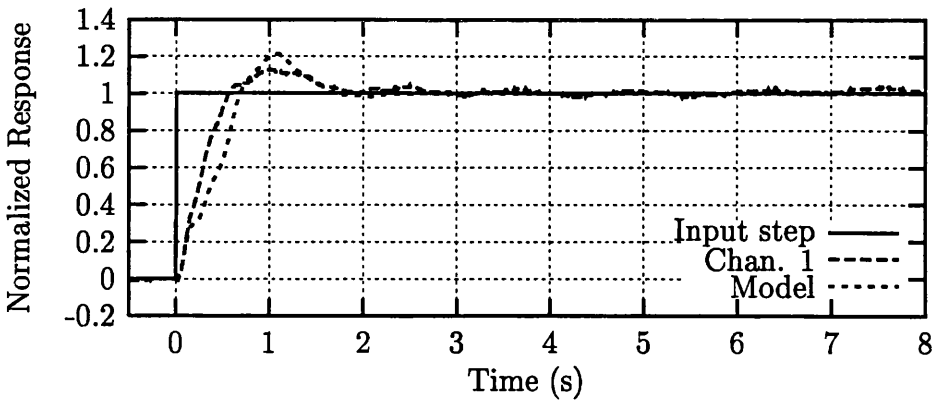

Figure 6.8: Tilt step response of the prototype suspension. The figure shows the measurement in one channel compared to the predicted response.

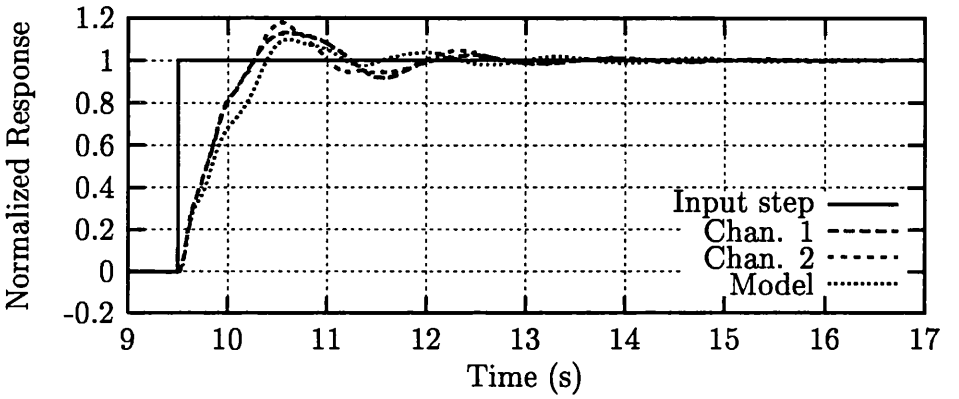

Figure 6.9: Longitudinal step response of the prototype suspension. The figure shows the measurements in both channels compared to the predicted response.

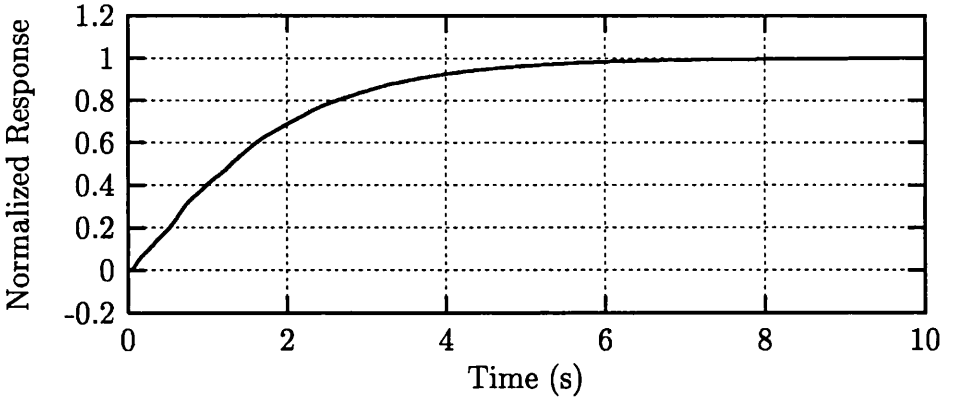

Figure 6.10: Yaw step response of the prototype suspension (theoretical).

fed into the slow input of the relevant channel, resulting in the step being fed differentially into the two appropriate coils for tilt control on top of the mass for tilt testing and the step being fed identically to the two coils at the rear of the mass for longitudinal testing. The response of one sensor of the tilt pair of channels is shown in figure 6.8, where the agreement with theory is excellent. The next figure, figure 6.9, illustrates the response of the two sensors in the longitudinal pair. This data provided an interesting test of the robustness of the control design.

The original data taken for the longitudinal step response showed a greatly different response between the two nominally identical channels. The response of one channel looked very much as predicted by the model, while the second channel showed no overshoot and seemed to be well overdamped. This was because the shadow sensor of the second channel had approximately twice the gain of the sensor in the first channel. Therefore, the same force generated in each longitudinal coil was being detected as if there were a great deal of yaw motion. The predicted yaw response to a step input is shown in figure 6.10, where it is seen that the yaw motion is overdamped. Since the same pair of actuators affects both longitudinal and yaw motion, the electronic gain in these channels is a compromise of the ideal gain for each direction. The separation of the coils provides the lever arm for the yaw direction, and a practical separation based on physical convenience yields the overdamped response which is plotted. This description of the motion in terms of the centre of mass coordinates is for observational convenience and does not affect the fact that each sensor–actuator pair acts independently. The behaviour of the system with respect to its damping and hence its rms motion was still acceptable, even with an unanticipated factor of two in one channel. It was, however, desired that the channels work identically for simplicity in setup and for calibration of alignment signals, and the electronic gains in the two channels were adjusted accordingly.

6.3 'Global' Control

The gravitational wave is detected by sensing the response of the optical system formed by the interferometer. Therefore, while the suspended masses need to be seismically quiet, so that their motion under the influence of a gravitational wave can be seen, the mirrors also need to form this optical cavity. The most basic form

of this requirement is that the laser beam which travels down the long arm of the interferometer needs to be reflected back to return to the beamsplitter. More specifically, the lengths of the interferometer arms are required to be controlled, whether to maintain the interferometer on a dark fringe or to form a cavity resonance. This alignment is always defined with respect to the optical field and thus intrinsically with respect to the other mechanical components of the system which define the optical path. Because the error signal for the position of any single optic then depends on the state of the entire system, and may most practically be measured at a large physical distance from that optic, this is called 'global' control, as opposed to the local control defined earlier.

As far as directing the path of the optical beam as it reflects off the suspended mirror, the angular orientation of the mirror in tilt and yaw are the critical degrees of freedom. Since this is fundamentally a question of equilibrium alignment, the low frequency control may be applied through the same coil–magnet actuators described as for the local control, applied at the uppermost mass of the system. For the GEO 600 main suspension, it is desired that the coils provide a capability of 10 mrad of static alignment. For the 600 m long arms of the interferometer, this means that as long as the beam initially returns down the beam tube, or as long as it still returns down the tube after the vacuum system has been evacuated, the coils have more than sufficient range to align the beam. This alignment can be detected with a generalization of the technique commonly used to sense the length of a Fabry–Perot interferometer, which will be examined in detail in section 6.4. This can provide a very high gain signal once the cavity is close to resonance, and has been demonstrated for use in GEO 600 by Morrison[82, 83].

6.3.1 Requirements

The interferometer is maintained on a dark fringe of the interferometer, as mentioned in section 1.2.2. If the interferometer is offest from a dark fringe by an amount Δx, intensity noise on the laser beam appears in the output signal of the detector as

$$\delta x = \Delta x \frac{\hat{I}}{I}, \tag{6.3}$$

where $\hat{I}$ is the intensity noise of the light. For GEO 600, the anticipated intensity noise of the Nd:YAG laser is one part in 10^7[84]. To reach the displacement sensitivity of $10^{-20}\mathrm{m}/\sqrt{\mathrm{Hz}}$ requires that the average (rms) motion of the mass to be less than 10^{-13} m. From figure 6.4, it can be seen that the rms motion of the system, even after the damping from the local controller, is on the order of 10^{-7} m. Therefore, the global control servo requires a gain of $\sim 10^6$ in the neighbourhood of 1 Hz.

6.3.2 Gain Versus Bandwidth

Achieving this amount of gain in a single control loop results in a bandwidth of $\sim$1 kHz[85]. Since this level of control is applied directly to the test mass, its noise is not filtered by any lower pendulum stages. This control then requires an actuator with much lower noise performance, such as an electrostatic drive[86]. The linear range of these actuators is typically very small, such that the motion of these actuators must now also be considered. (This is considered in detail for coil–magnet actuators by Killbourn[67].) To provide a seismically quiet base for actuation, where global control forces are to be applied there is an identical, parallel triple pendulum suspension. This 'reaction mass pendulum' design is similar to the main pendulum, although the fused silica fibres in the final stage are unnecessary. This allows the same assembly and same local control to be used, greatly simplifying the total system design.

The high gain necessary in the global control loops leads to the potential problem of exciting internal modes of the system. The internal modes of the test mass are $\geq$ 10 kHz. Since these modes are, necessarily, very high Q resonances (section 1.3.2), the loop gain at these frequencies will exceed unity magnitude and cause instability unless precautionary measures are taken. This can be done with careful notch filtering[85].

Alternatively, because of the very high gain required and the concomitant difficulty of achieving this gain through a single stage of noise–free actuation, an obvious method to consider is to use split feedback—apply actuation up to mid–frequency regions directly on the test mass while applying higher gain control with lower bandwidth further away from the test mass. This is achievable since the system is stiff at low frequencies, below the pendulum resonances. This allows, for example, a large

range, slightly noisier coil–magnet actuator to be used on the intermediate mass of the pendulum while a quieter electrostatic drive applies force directly to the test mass.

6.3.3 Split Feedback—Effects of Control 'Through' Resonances

The control loop that feeds back to the intermediate mass will have somewhat higher bandwidth than the ~5 Hz loops used for the local control. Therefore, the modes in the suspension elements (the violin modes described in section 4.5.1) may have to be included in the modelling of the transfer function. The effects of these internal modes can be modelled in a finite element fashion, using a small number of elements per wire to include the first few violin modes, or as a continuous, standing wave solution[71]. The particular solution to be discussed is a one dimensional solution, just considering motion along the beam direction, X. In this example, the wires are modelled using the second order equation for a wire under tension[70] (as opposed to the fourth order beam equation, equation 3.20),

$$\rho \frac{\partial^2 w}{\partial t^2} = T \frac{\partial^2 w}{\partial \eta^2}, \tag{6.4}$$

where ρ is the linear density, T is the tension, and w is the transverse displacement of the wire as a function of distance along the wire, η. The solution of this equation is

$$w(\eta, t) = (\alpha \sin(k\eta) + \beta \cos(k\eta)) \exp(-i\omega t) \tag{6.5}$$

where k, the wave vector, is given by

$$k = \frac{\omega}{c_s} \tag{6.6}$$

in terms of the angular frequency, ω, and the speed of sound in the wire, c_s, which in turn is

$$c_s = \sqrt{\frac{T}{\rho}}. \tag{6.7}$$

The boundary conditions are that the displacements between wire stages must match,

$$w_i(l_i, t) = w_{i+1}(0, t), \tag{6.8}$$

and Newton's second law of motion must be obeyed at each mass

$$m_i \frac{\partial^2 w_i(l_i, t)}{\partial t^2} = -T_i \frac{\partial w_i(l_i, t)}{\partial \eta} + T_{i+1} \frac{\partial w_{i+1}(0, t)}{\partial \eta}. \tag{6.9}$$

Stated properly, an equation is written for each wire, and the resultant force at any mass is the sum of the forces due to all of the wires. In equation 6.9, each mass is represented by a point mass, such that the force equals the mass times the acceleration. Because this modelling is intended to allow much higher bandwidth control to be designed, it may be necessary to include the higher frequency internal modes of the test mass. In this case, the impedance of the mass can be used to express the relationship between the force and velocity at the endpoint of the wire, rather than simply using $F = ma$. Treating the test mass as, for example, a cylinder with longitudinal modes, the relationship between force and velocity is solved using the second order equation[70]

$$E \frac{\partial^2 f}{\partial x^2} = \rho \frac{\partial^2 f}{\partial t^2}, \tag{6.10}$$

which has solution

$$f(x, t) = (f_1 \sin(k_c x + \delta) + f_2 \cos(k_c x + \delta)) \exp(i\omega t). \tag{6.11}$$

Here f is the amount of longitudinal compression, with the compressional wave vector $k_c = \omega / c_c$. The velocity of this compressional wave is $c_c = \sqrt{E/\rho}$, where E is the Young's modulus and ρ the density of the material. This expression ranges from 0, where the wires attach, to $l/2$, the distance to the front of the mass. (A similar equation could be used to describe the compression from the attachments towards the back end of the mass.) The boundary conditions are that there is no

force at the unconstrained face of the mass,

$$E\frac{\partial f(l/2,t)}{\partial x} = 0, \tag{6.12}$$

and that the force at the input is balanced as

$$-E\frac{\partial f(0,t)}{\partial x} = \frac{F}{2Area}. \tag{6.13}$$

In this expression, F is the input force and $Area$ the cross sectional area of the cylinder. The factor 2 comes from the fact that this point forms the boundary condition for both the front and the rear of the test mass. This can be solved to give the impedance at the input, the ratio between input force and velocity at that point.

Solving the set of equations, w_i, for all the stages of wires, allows the response at the wire endpoints to be calculated. The same calculation that gives the impedance of the test mass can be used to show the relationship between the motion where the wires are attached, $f(0)$, and the motion of interest at the face of the optic, $f(l/2)$. If the control to be designed is of sufficiently low bandwidth to be well below the internal modes of the test mass, then $f(l/2) = f(0)$.

By modelling in this fashion, transfer functions between inputs on higher pendulum stages and outputs on the test mass can be predicted more accurately for higher frequency bands. The Lagrangian modelling discussed previously can predict the transfer function, for example, between force applied at the upper mass of a double pendulum and the motion at the test face. Figure 6.11, which shows the same problem modelled in this standing wave fashion, clearly shows the effects of the internal modes of the suspension wires above 600 Hz, with higher harmonics extending above the frequency range plotted. This standing wave model does, however, lack the details necessary for the full dynamics and thermal noise calculations of the Lagrangian model.

This model allows a feedback loop to be designed which actuates on the intermediate mass (or higher in the system). Excitation of the internal modes of the system can be avoided by carefully notching the feedback signal at the resonant frequencies of the suspension wires. This is more difficult when the wires do not have exactly the same tension and thus different violin mode frequencies. The model described

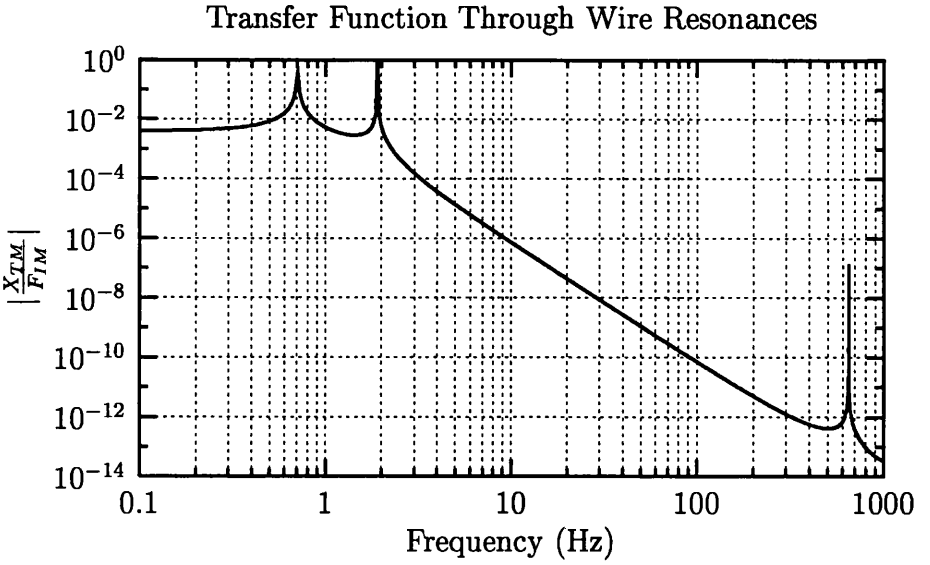

Figure 6.11: The effect of control through resonances in a double pendulum. This illustrates the transfer function from force applied at the intermediate mass to motion at the test mass, with the effect of the internal violin modes of the wires clearly visible above 600 Hz.

includes this effect by varying the tension in each individual wire. This allows the design of a proper split feedback system to begin.

It is very difficult to guarantee that the modes in the wires are not excited. When they are excited, a controller designed to position the test mass does not necessarily provide a simple manner to damp these modes. A system to damp the excitation of the violin modes has been described[87]. With this in successful operation, the possible excitation of the internal modes of the wires is much less critical, and the design of the split feedback loop may not need the level of care afforded by this model.

6.4 Lock Acquisition

To maintain the proper optical cavity resonances which allows the gravitational wave detection to be made, the longitudinal position of the mirrors with respect to the laser must be detected. This is typically done by taking advantage of the phase change of the cavity optical field through resonance. The work to be described is for

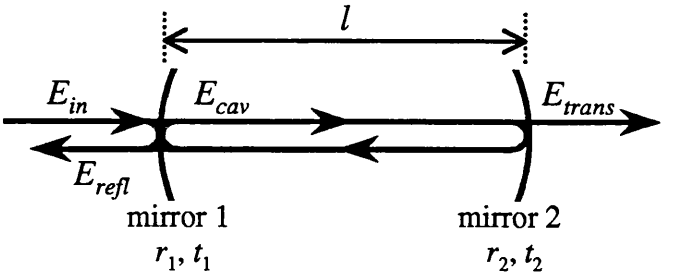

Figure 6.12: A Fabry–Perot cavity

the simplest optical cavity, a Fabry–Perot interferometer[27], but the principles are used in more complicated compound optical cavities. The difficulty is that the error signal typically derived assumes that the cavity storage time is short compared to time scales over which the mirrors move. This signal may not be a suitable error signal for control purposes when the cavity storage times are longer, as they are for long baseline interferometers. This section describes a subset of the work in Lawrence et. al.[2], with an emphasis on applications to control.

6.4.1 Optical Cavity Fields

A Fabry–Perot cavity, such as those which can used to increase the optical storage time in the arms of a gravitational wave interferometer as described in section 1.2.2, is shown in figure 6.12. The two mirrors of the cavity are a distance l apart, and the cavity is resonant with the laser field when the field acquires a $2\pi n$ phase shift in one round trip of the cavity for integer n. When the cavity is on resonance, the incoming laser light constructively interferes with the light already in the cavity, resulting in a large cavity field.

The magnitude of the steady–state electrical field just inside the cavity, E_{cav}, is equal to the same steady–state cavity field from one cavity round trip time earlier, propagated around the cavity, and added to the incoming field, $E_{in}e^{i\omega t}$, transmitted through the input mirror[88],

$$E_{cav} = it_1 E_{in} + r_1 r_2 e^{-\alpha_0 2l - i\omega 2l/c} E_{cav}. \tag{6.14}$$

In this expression, r_1 and r_2 are the field reflection coefficients of each mirror with t_1

and t_2 the corresponding transmission coefficients (such that $r_i^2 + t_i^2 = 1$ for lossless mirrors), $\mathrm{e}^{-\alpha_0 2l}$ represents the loss the field experiences in one round trip of the cavity, and ω is the optical frequency of the input beam. Therefore, the relation between the cavity field and the input field in steady–state is

$$\frac{E_{cav}}{E_{in}} = \frac{it_1}{1 - r_1 r_2 \mathrm{e}^{-\alpha_0 2l - i\omega 2l/c}}. \tag{6.15}$$

This magnitude of this expression reaches a maximum when $\mathrm{e}^{-i\omega l/c} = 1$, or $\omega l/c = 2\pi n$.

The full width–half maximum (*fwhm*) cavity linewidth is the distance in frequency between the two points on either side of the maximum transmission where the intensity falls to half of its maximum value[89]. This is given by

$$\Delta\omega_{fwhm} = \frac{\pi c}{l\mathcal{F}} \tag{6.16}$$

in radians per second, where $\mathcal{F}$ is the cavity finesse, which for low loss is given by[88]

$$\mathcal{F} = \frac{\pi\sqrt{r_1 r_2}}{1 - r_1 r_2}. \tag{6.17}$$

If the length of the cavity changes, as opposed to the input frequency changing, an alternate expression for the *fwhm* cavity linewidth may be written. Moving the mirror by $\lambda/2$ is equivalent to changing the input laser frequency by a free spectral range. Therefore the distance in cavity length between the two points on either side of the cavity resonance where the intensity falls to half of its maximum value is

$$\Delta l_{fwhm} = \frac{\lambda/2}{\mathcal{F}} = \frac{\pi c}{\omega\mathcal{F}}. \tag{6.18}$$

A useful error signal can be obtained by using the reflected cavity field in a heterodyne detection scheme[90]. The field reflected from the cavity is the superposition of the cavity field transmitted through the input mirror and the reflection of the input field. Therefore,

$$E_{refl} = r_1 E_{in} + it_1 r_2 \mathrm{e}^{-\alpha_0 2l - i\omega 2l/c} E_{cav}, \tag{6.19}$$

where the cavity field is propagated around a round trip and then transmitted

through the final mirror. For $r_1^2 + t_1^2 = 1$, equations 6.15 and 6.19 combine to give

$$\frac{E_{refl}}{E_{in}} = \frac{1}{r_1}\frac{r_1^2 - r_1 r_2 \mathrm{e}^{-\alpha_0 2l - i\omega 2l/c}}{1 - r_1 r_2 \mathrm{e}^{-\alpha_0 2l - i\omega 2l/c}}. \tag{6.20}$$

For the case where $r_1 = r_2$ and with very low loss ($\alpha_0 \ll 1$), on resonance the reflected field drops to zero, whereas far from resonance essentially the entire input field is reflected (as can also be seen by considering power conservation with respect to the transmitted field).

If the input field is phase modulated at frequency ω_m with small modulation depth δ, the resulting field can be described to first order by a central carrier field with two sidebands given by[91]

$$E_{in} = E_0 \left(\mathrm{e}^{-i\omega t} + \frac{\delta}{2}\left(\mathrm{e}^{-i(\omega+\omega_m)t} - \mathrm{e}^{-i(\omega-\omega_m)t}\right)\right). \tag{6.21}$$

When the carrier frequency, ω, is close to a resonant frequency of the cavity and the modulation frequency is significantly larger than a cavity linewidth, then the sidebands are directly reflected while the carrier builds up a cavity field. For a cavity near resonance, $\mathrm{e}^{-i\omega 2l/c} \approx 1$, such that the reflected field from equation 6.20 with the input field from 6.21 is

$$E_{refl} = E_0 r_1 \mathrm{e}^{-i\omega t}\left(1 + \frac{\delta}{2}\left(\mathrm{e}^{-i\omega_m t} - \mathrm{e}^{+i\omega_m t}\right)\right) + i t_1 r_2 E_{cav} \mathrm{e}^{-i\omega t}, \tag{6.22}$$

and a corresponding reflected intensity of

$$I_{refl} = \frac{1}{2} c\epsilon_0 E_{refl} E_{refl}^*, \tag{6.23}$$

where ϵ_0 is the permeability of free space. Detection of this reflected field with a photodetector yields a photocurrent of

$$i_{refl} = \Re(I_{refl}) = \frac{1}{2} c\epsilon_0 \mathcal{R} E_{refl} E_{refl}^*, \tag{6.24}$$

where $\mathcal{R}$ is the responsivity of the detector.

For slow changes in the cavity length, the reflected current has a DC term, a term at frequency ω_m, and a term at frequency $2\omega_m$, which may be determined by inserting

the expression for the field, equation 6.22, into the expression for the photocurrent, equation 6.24. The component of the reflected current at the modulation frequency ω_m is

$$i_{RF} = -c\epsilon_0 R t_1 r_1 r_2 \delta E_0 \Re(E_{cav}). \tag{6.25}$$

Rexamining the cavity field, equation 6.15, for small perturbations away from resonance, where $l = l_0 + \Delta l$ and l_0 satisfies the resonance condition, then

$$\frac{E_{cav}}{E_{in}} = \frac{it_1\left(1 - r_1 r_2 \mathrm{e}^{-\alpha_0 2l}\right) + r_1 r_2 t_1 \frac{2\omega\Delta l}{c}\mathrm{e}^{-\alpha_0 2l}}{\left(1 - r_1 r_2 \mathrm{e}^{-\alpha_0 2l}\right)^2 + \left(r_1 r_2 \frac{2\omega\Delta l}{c}\mathrm{e}^{-\alpha_0 2l}\right)^2}. \tag{6.26}$$

From this it can be seen that the real part of E_{cav}, and thus the detected photocurrent in equation 6.25, is proportional to Δl.

For a high finesse cavity, this provides an excellent error signal for use in locking the cavity on resonance. The signal is unambiguous, crosses zero at the desired position and can have an extremely high gain (V/nm). Any variations in input field affect the size of the output signal, but since this is centred about zero, this only affects the gain. The clear shortcoming of this signal is that it is only valid over a fairly narrow range of displacement. For mirror excursions of more than a few linewidths, there is very little field built up in the cavity and thus very little error signal.

6.4.2 Non–Steady State RF Error Signal

One potential difficulty comes from the fact that these mirrors may be moving over time scales comparable to the cavity storage time. The calculation of the cavity fields done in the previous section is a steady–state analysis. In practice, this means that the length of the cavity does not change appreciably over time scales in which the cavity field might change, which is approximately $t_s = \mathcal{F}2l/\pi c$ for a high finesse cavity. For a laboratory scale cavity, with $l \approx 1$ m, for a relatively low finesse cavity of $\mathcal{F} = 10^3$, the cavity storage time is only $t_s \approx 2\mu$s. Since for a Nd:YAG laser (wavelength = 1.064 μm) the cavity linewidth would be 0.53 nm, the mirror moving this distance over t_s yields a velocity of 0.25 mm/s, a velocity which the suspended mirrors would never exceed in normal circumstances. However, for a cavity a factor

of ten longer and with ten times greater finesse, the critical velocity would be closer to 0.25μm/s, and it is less certain that the suspended mirror would never exceed this velocity.

Consider the same Fabry–Perot cavity from figure 6.12 where the far mirror is moving. If the cavity is initially empty, the cavity field immediately after the input beam is turned on is the beam transmitted through the input mirror, such that

$$E_{cav} = it_1 E_0 \mathrm{e}^{i(kx-\omega t)}. \tag{6.27}$$

This beam is propagated around the cavity. At the far mirror, the frequency of the field changes due to the Doppler shift experienced by reflecting off the moving mirror. By the time this beam returns to the near mirror after an (unperturbed) round trip time $\tau = 2l/c$ and combines with the transmitted input light,

$$E_{cav} = it_1 E_0 \left(\mathrm{e}^{-i\omega\tau} \mathrm{e}^{i[kx-\omega(t-\tau)]} + \rho \mathrm{e}^{i\left(1+\frac{2\dot{l}_{\tau/2}}{c}\right)[kx-\omega(t-\tau)]} \right), \tag{6.28}$$

where $\rho = r_1 r_2 \mathrm{e}^{-2\alpha_0 l}$, the round trip loss factor. Here $k(1+2\dot{l}_{\tau/2}/c)$ and $\omega(1+2\dot{l}_{\tau/2}/c)$ are the wave vector and frequency after reflection from the end mirror moving with velocity $\dot{l}_{\tau/2}$ toward the input mirror.

This is extended to a recursion relationship between the cavity field at time t and the field that existed a round trip time before as

$$E_{cav}(t+\tau) = it_1 E_0 + \rho \exp\left(\frac{i2\omega L_{t+\tau/2}}{c}\right) E_{cav}(t). \tag{6.29}$$

For small offsets from resonance, the phase shift acquired by the field after one round trip, $\exp\left(i2\omega L_{t+\tau/2}/c\right)$, is approximately $1 + i(2\omega \dot{l}t/c)$, where $\dot{l}t$ is the time-varying offset from resonance. The recursion relation accurately describes the cavity field after a round-trip, including the Doppler effects. It does not account for the different phases acquired over smaller time intervals by the components that make up the cavity field from time $t-\tau, t-2\tau, \ldots$, each of which has experienced a different total Doppler phase shift.

If neither the cavity nor the input beam change significantly within a round trip

time, the relation in equation 6.29 can be rewritten as a differential equation

$$\frac{dE_{cav}}{dt} = \left(\frac{\rho - 1}{\tau} + \frac{i2\rho\omega\dot{l}}{\tau c}t\right) E_{cav} + \frac{it_1}{\tau}E_0. \tag{6.30}$$

The cavity storage time, τ_s, is the time required for a $1/e$ decay of the cavity field. For high finesse cavities, where $\rho \approx 1 - \pi/\mathcal{F}$, the storage time is

$$\tau_s \approx \frac{\mathcal{F}\tau}{\pi} = \frac{2\mathcal{F}L}{\pi c}. \tag{6.31}$$

Equation 6.30 can be normalized with respect to the cavity storage time by using $t' = t/\tau_s$, which results in

$$\frac{dE_{cav}}{dt'} = -\left(1 - i\nu_l t'\right) E_{cav} + i\frac{t_1\mathcal{F}}{\pi}E_0, \tag{6.32}$$

where ν_l, the normalized length scan rate, is given by

$$\nu_l = \frac{2\mathcal{F}\omega\dot{l}\tau_s}{\pi c}. \tag{6.33}$$

From the definition of cavity linewidth, equation 6.18, ν_l is the number of half *fwhm* cavity linewidths moved by the mirror in a cavity storage time,

$$\nu_l = \frac{\dot{l}}{\left(\Delta l_{fwhm}/2\right)/\tau_s}. \tag{6.34}$$

From equation 6.32, E_{cav} will have an oscillating component when ν_l is nonzero. These oscillations can affect the measured error signal, i_{RF}, such that the error signal does not accurately reflect the length of the cavity with respect to a feedback controller. Figure 6.13 shows the nominal error signal when a 40 m cavity with a finesse of $\sim 8 \times 10^3$, corresponding to a laboratory scale experiment with long optical storage times, passes through resonance at various speeds. For large speeds, the error signal passes through zero substantially after the cavity has passed through the resonant length. For a very large relative speed, in fact, the signal oscillates through zero for constant mirror velocity, such that the signal is no longer even monotonic.

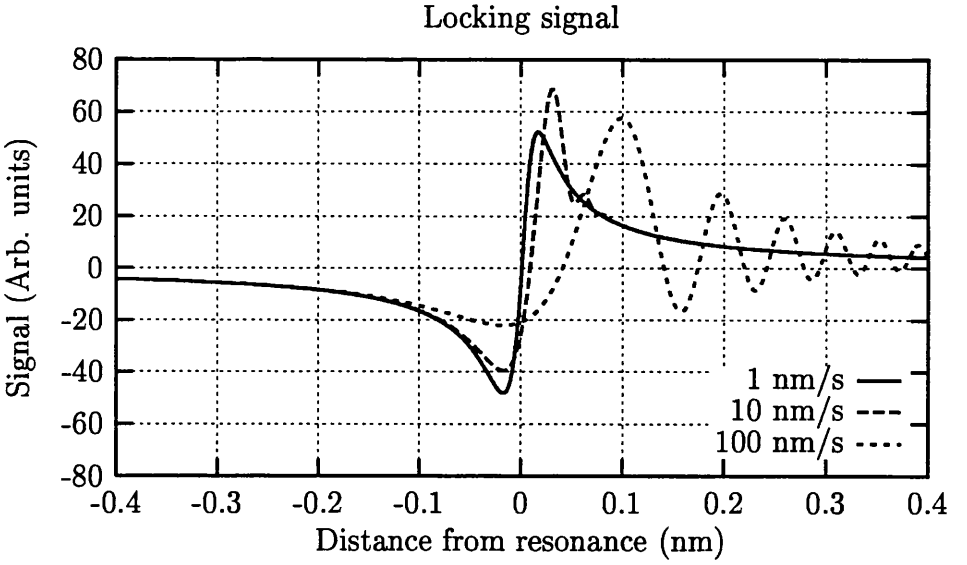

Figure 6.13: Error signal in a Fabry–Perot cavity. For a cavity of moderate length with high finesse ($L = 40, \mathcal{F} = 8 \times 10^3$), the various curves show how the standard error signal is affected by passing through the resonance at different speeds.

6.4.3 Experimental Verification

These expressions were experimentally verified to confirm the behaviour of the error signal. The setup is shown in figure 6.14. The Fabry–Perot ring cavity had a perimeter of 42 cm and finesse of 4000 for S-polarized light. The end mirror of the cavity was mounted on a piezoelectric transducer (PZT) to change the length of the cavity. The laser was a single–axial–mode 300–mW Lightwave Model 122, such that the wavelength of the laser beam was 1064 nm. (The experiment also explored the affects of variation in input laser frequency. The full details of this are covered in Lawrence[2].)

The method of sensing the reflected error signal is entirely conventional[90]. The input light was phase modulated with an electro–optic modulator (EOM) and introduced into the cavity. The light reflected from the cavity was measured by a photodetector and the resulting signal was demodulated with the local oscillator driving the phase modulator. The cavity length was changed by applying a high–voltage triangular signal to the cavity PZT. Over the times scales of the cavity passing through resonance, the input laser frequency was essentially constant.

With this apparatus, the signals from photodetectors sensing the transmitted

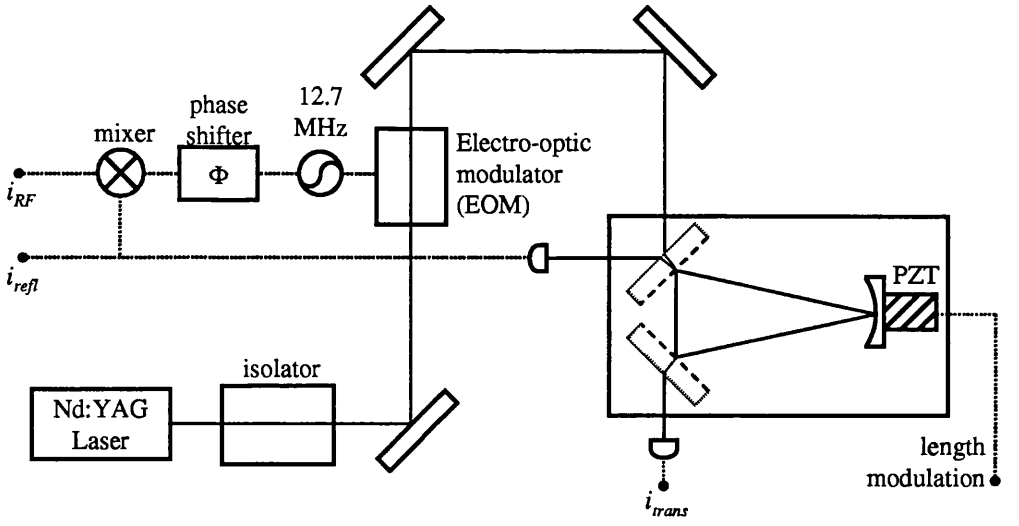

Figure 6.14: Experimental apparatus for measuring the time response of the Fabry–Perot cavity. The cavity had a round–trip length of 42 cm and a finesse of 4000. A piezoelectric actuator was used to change the cavity length.

field and the reflected field, as well as the demodulated signal from the reflected field, can be measured. Equation 6.32 is then fitted to the measurements. The cavity finesse was determined by the value that produced the best agreement for all of the experimental data acquired from the cavity. Because of differences between the photodetectors, a scaling factor and offset were determined for each detector, which were then kept constant. For this modelling to be used to generate an error signal, the measured photodetector signal would be used to calculate the mirror velocity. Therefore, the remaining free parameter used for fitting the data was the mirror velocity for each case. In all cases, the calculated mirror velocity was consistent with the velocity anticipated in the PZT due to the applied voltage ramp.

Figure 6.15 shows the experimental results and the excellent agreement between the theory and the measured data. It also again illustrates the potential difficulty with the use of the typical error signal. For very low mirror speeds, the response is essentially the well known steady–state response[88]. The response, in a very narrow range, is linear with mirror position, is centred about zero, and has a very high gain. The signal may not be used in this straightforward fashion for higher mirror velocities.

These curves are calculated for a constant velocity mirror. Typically, there is

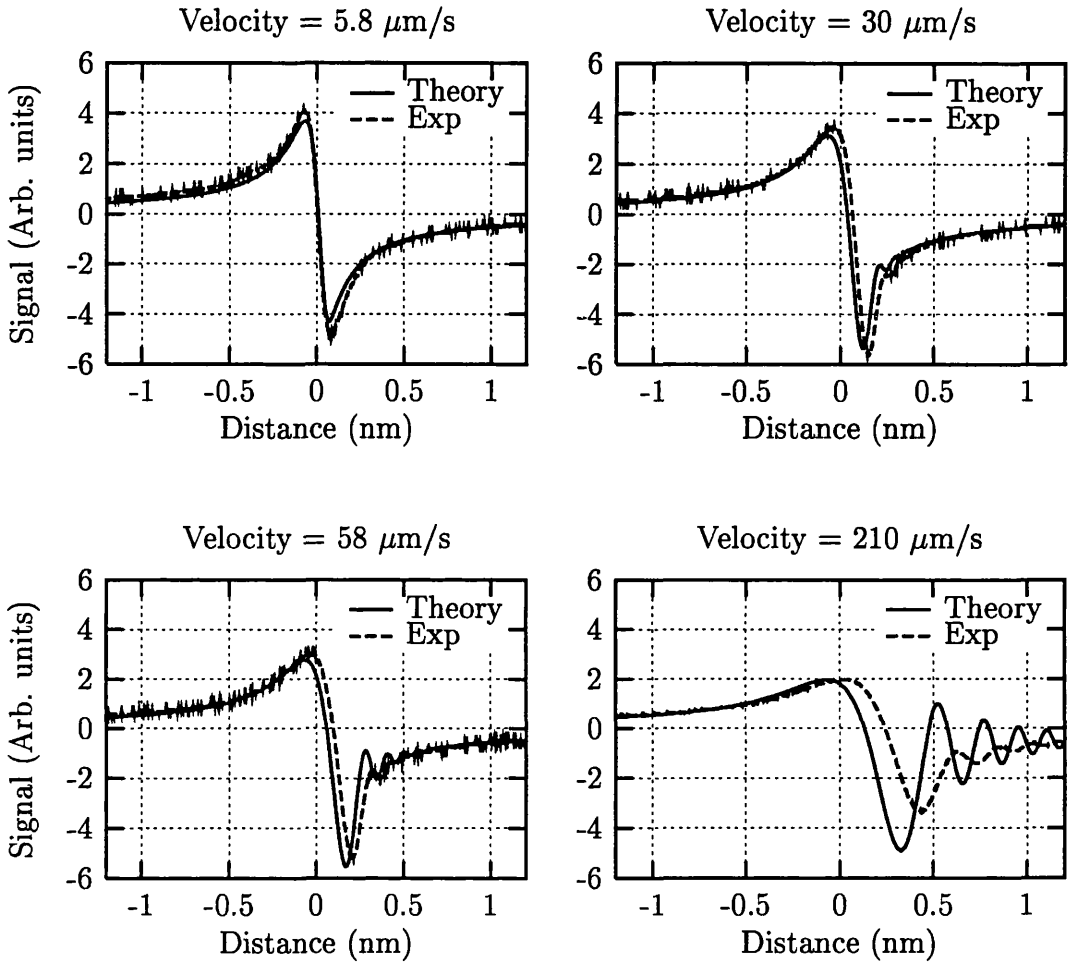

Figure 6.15: Time response of the Fabry–Perot cavity error signal. For the highest velocity case (210 μm/s), some unmodelled high frequency filtering in the detection electronics causes the agreement with theory to be compromised.

feedback on the mirror. On a table–top system where a PZT is used to control the cavity length to maintain cavity resonance[92], the fast response of the actuator cause the mirror position to be controlled before the oscillations in the error signal have any affect. However, since the strength of the actuator in these pendulum suspensions must be low in order to minimize noise, the mirror moving at high speed can pass completely through resonance without 'catching'. Since the signal can be oscillating even while the mirror continues its constant velocity sweep, the net integrated force on the mirror can be very small. In other words, the mirror can pass through resonance while the system fails to achieve lock and, in fact, very little energy may be removed from the system.

Whether this is a real problem depends on the specifics of the optical cavity, the mechanics of the suspension, and the input noise spectrum. A variety of techniques have been developed which involve 'fringe–counting'[67, 93]. These techniques use the fact that if the velocity of the mirror is low enough, the standard techniques can successfully lock the cavity and therefore seek first to reduce the velocity of the mirror. Ignoring the details which this section explicitly determines, for a cavity moving at essentially constant speed through resonance, more oscillations in the reflected field correspond to a greater velocity. These methods of lock acquisition essentially apply a force to slow down the mirror proportional to the number of oscillations of the signal. By removing enough energy from the system, on the next pass through resonance the mirror is assumed to be moving slowly enough that the usual locking techniques may be successfully used.

With the expression in equation 6.32 and more detailed modelling techniques, in principal an improved lock acquisition algorithm can be developed. The fringe counting techniques establish the direction and an approximate velocity for the mirror. With the more complete knowledge offered by the cavity equation, the velocity and position of the cavity could be determined. This would allow a more robust locking algorithm to be devised. By knowing the distance from a resonance condition, rather than simply removing energy from the system and then waiting, the mirror can be actively guided to the proper position. Upon reaching resonance, one difficulty in high power cavities, for example, will be the large jump in photon pressure on the mirror when the cavity field is suddenly amplified on resonance. By knowing exactly when this resonance is going to be reached, the locking servo can

anticipate and compensate for this disturbance.

Chapter 7

GEO 600

7.1 Description

The work described in the preceeding chapters has been applied to the development of the suspensions to be used in GEO 600. This section will summarize some of the design features of the GEO 600 detector. The following sections describe some practical constraints on the suspension design, the parameters used in the main suspension (based on the work from the earlier chapters), and the variations on this suspension used to support other optical elements in GEO.

GEO 600 is the British–German collaboration to build a 600 m long laser interferometric gravitational wave detector. It was proposed in the United Kingdom and Germany in 1994, and involves the combined efforts of research groups at the University of Glasgow, the Max–Planck–Institut für Quantenoptik at Garching and Hannover, the University of Wales (Cardiff), and the Albert Einstein Institut at Potsdam, with further contributions from the Laser–Zentrum, Hannover. It is scheduled to begin operation in autumn 2001.

The GEO 600 detector uses a four–bounce delay–line in each 600 m arm of the interferometer. It will use a 10 W stabilised diode–pumped Nd:YAG laser, which passes through two modecleaners to spatially and temporally filter the light before injection into the main interferometer[94]. The GEO 600 detector is being constructed near the German town of Ruthe, just south of Hannover. The location is an agricultural research field owned by the University of Hannover, a relatively quiet site seismically.

GEO 600 will act as part of a worldwide network of detectors which includes the American LIGO and the French–Italian VIRGO projects mentioned in the introduction. The different projects have all emphasized different aspects of the technical challenges. Knowledge developed for all three will strongly influence designs for advanced receivers for all the different projects. One example is the cantilever blades, described in detail in section 2.4.2, which were first developed by the VIRGO group and a version of which are now incorporated into the GEO 600 main suspension. Similarly, the GEO 600 group is the only group using fused silica fibres in the suspension in the first generation. GEO 600 is also the only detector which plans to initially use signal recycling as well as power recycling[95].

7.2 Design Constraints for Suspension

7.2.1 Physical Size and Space

The vacuum tanks present in GEO 600 limit the size of the isolation systems that can be used. As noted in the discussion on isolation systems, larger systems are the simplest way to get systems with lower resonant frequencies; this is not a luxury available in the design of the GEO suspension. The total height of the system, approximately 2 m from the top of the vacuum chamber to the beam height, limits the lengths of the pendulum stages, barring a substantial redesign away from simple wire pendulums.

7.2.2 Bonding and Other Restrictions

For the thermal noise reasons discussed in detail in section 2.5, the materials and methods of attachments of the pendulums have to be chosen very carefully[38]. Silicate bonding[40] will be used to attach the fused silica wires of the bottom stage pendulum between the lower two masses. To guarantee a good surface for the bonding process, the wire connections must be tangent to a flat surface. In practice, this means that the wires in the bottom stage of the pendulum must be vertical ($s[2,l] = s[3,u]$ and $n[2,l] = n[3,u]$, where all parameters are as defined in section 3.1).

The mirror cross section is chosen based on the spot size of the laser beam and

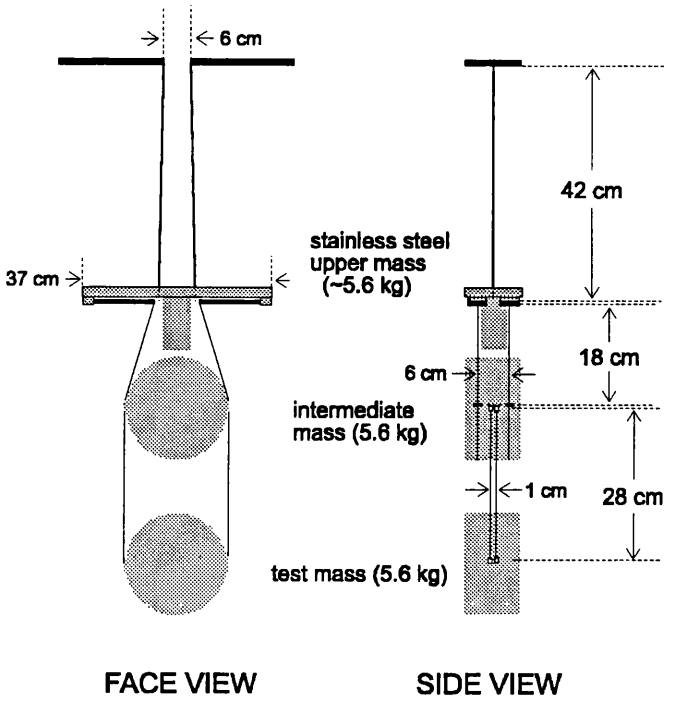

Figure 7.1: Main suspension in GEO 600

the desire to minimize the amount of light lost past the edges of the mirror. The aspect ratio of the mirror is chosen to minimize the total internal thermal noise summed over all the mirror modes (section 1.3.2). Based on the required coupling of all the modes of the multiple stage pendulum to allow the proper functioning of the local control, each mass in the pendulum has mass and moments of inertia comparable to the mirror.

7.3 Main Suspension

The primary suspension system, used for the end mirrors and with small modifications for the other large optics, will be as shown in figure 7.1.

7.3.1 Description

The support structure for the pendulum is the rotational stage, a rigid frame which allows the entire suspension to be rotated in the yaw direction for initial alignment within ten milliradians. The suspension is a triple pendulum, which includes two

		First stage		Second stage		Third stage	
	units	var	value	var	value	var	value
Mass dimensions	m	u_x	0.1	i_r	0.09	t_r	0.09
		u_y	0.3	i_x	0.1	t_i	0.1
		u_z	0.07				
Wire parameters	#		2		4		4
length	m	l_1	0.42	l_2	0.187	l_3	0.28
radius	μm	r_1	350	r_2	175	r_3	154
Cantilevers	#		2		4		
spring constants	N/m	$k_{c,u}$	739	$k_{c,l}$	498		
Half wire separations							
in X-Y plane	m	$s[0]$	0	$s[1,l]$	0.03	$s[2,l]$	0.005
		$s[1,u]$	0	$s[2,u]$	0.03	$s[3,u]$	0.005
in X-Z plane	m	$n[0]$	0.03	$n[1,l]$	0.045	$n[2,l]$	i_r+ 0.0065[a]
		$n[1,u]$	0.04	$n[2,u]$	i_r+ 0.0065[a]	$n[3,u]$	t_r+ 0.0065[a]
Vertical offsets	m	$d[0]$	0	$d[1,l]$	0.001	$d[2,l]$	0.001
of wires ($\|\|$ Y)		$d[1,u]$	0.001	$d[2,u]$	0.001	$d[3,u]$	0.001

[a] Wire position is at the mass radius − the width of the flat on side of mass (0.0035) + a breakoff (0.01)

Table 7.1: Parameters for the GEO 600 main suspension. The wire spacing parameters are as defined in section 3.2. The first stage is the uppermost stage and the third stage is the sensitive optic.

stages of cantilever blades. The top pair of cantilevers attachs to the rotation stage. This allows the entire system to be very soft in tilt. A second set of four cantilevers attach to the uppermost mass of the pendulum, supporting the lower two stages.

7.3.2 Pendulum Parameters

The specific parameters of the GEO 600 main suspension are summarized in table 7.1. The definitions of the wire spacings are as defined in the modelling section (section 3.2) and summarized in figure 3.2. The cantilever blades are all basically triangular and similar to the design shown in figure 2.11. The upper set of blades are 24 cm long, 2 mm thick, with a 6 cm wide base. The lower cantilevers are 12.4 cm in length, 1 mm thick, with a 2.8 cm wide base.

The lowest mass (the optic) and the intermediate mass are modelled as cylinders.

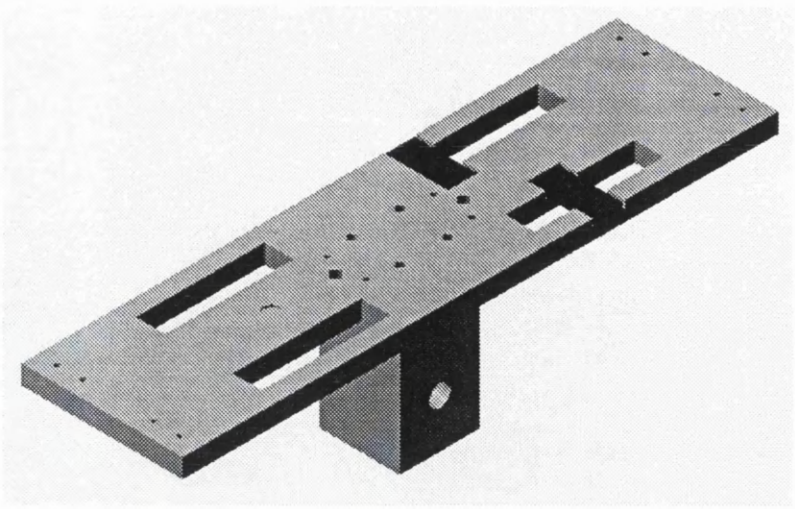

Figure 7.2: Uppermost mass in the GEO 600 suspension. The slots allow the cantilever blades to be mounted without being stressed. Other details of the design allow attachment of the cantilevers and the local control magnets.

The actual masses have vertical flats polished on opposite sides of a diameter of each mass to allow the bonding of the wire attachments. The wire spacing parameters reflect this and are set equal to the radius of the mass minus the thickness of the flat plus the thickness of the bonding piece. The small amount of removed mass has a negligible effect on the calculated moments of inertia.

7.3.3 Uppermost Mass

For design purposes, the upper two masses of the pendulum suspension have been treated as rigid bodies. Only the mass and moments of inertia of these masses have been important. For appropriately sized cubical or cylindrical masses, the internal modes of the masses are very high (comparable to the internal modes of the test mass, in the 10's of kHz). However, the uppermost mass in the GEO main suspension must be sized to support the lower set of cantilever blades. The initial design of the upper mass is shown in figure 7.2. Based on the length of the cantilevers, this mass has long 'wings' extending from a central block. The mass is designed such that the two main components, the long thin top piece and the short lower piece, add to give approximately the desired mass and moment of inertia.

One concern of this design is that these long 'wings' might lead to internal

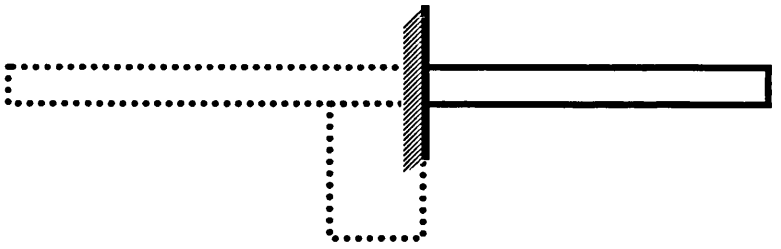

Figure 7.3: Internal mode of uppermost mass, modelled as a cantilever. A schematic section of the uppermost mass from figure 7.2 illustrates the long wing of the mass which is to be modelled as a cantilever, as well as showing the fixed boundary condition used at the central block of the mass.

resonances with unacceptably low frequencies. These frequencies are estimated by treating the ends of the mass as unsupported cantilevers, as in figure 7.3. The resonant frequency for a beam, fixed at one end, is given by[70]:

$$\omega_n = (k_n l)^2 \frac{a}{2\sqrt{3}l^2} \left(\frac{E}{\rho}\right)^{1/2} \tag{7.1}$$

for a rectangular bar of thickness a, length l, Young's Modulus E, density ρ. The values for $k_n l$ are the numeric solutions, the first few of which are $k_n l \approx 1.875, 4.694, 7.853, \ldots$. For the parameters of the GEO 600 uppermost mass, namely $a = 0.012$ m, $l = 0.160$ m, $E_{SS} = 1.65 \times 10^{11}\text{N/m}^2$, and $\rho = 7870\text{kg/m}^3$, the first resonant frequency is $f_1 \approx 350$ Hz. While this is likely an optimistic estimate for a real GEO 600 uppermost mass—the clamps for the intermediate stage cantilever blades will add mass at the end of this beam, plus the slots used for assembly effectively add mass at the tip without corresponding stiffness—having the frequency well over 300 Hz in a fundamentally vertical mode and thus coupling to the interferometer at a lower order, suggests that this frequency is sufficiently high.

7.3.4 Wires

The suspension wires are chosen to be stressed at ~25% of their breaking stress in order to maximize the internal 'violin' modes in the wires. The wires in the upper two stages are steel, with a breaking stress of ~1.5 GPa, which gives the wire radii given in the table. The breaking stress of the silica fibres is an active topic

of research; the size of the fibres which comprise the third stage in the GEO 600 suspension were chosen based on an anticipated strength of the fibres. This size has been used to finalize the design of the local control electronics based on the resulting mode frequencies (section 6.2.1). Based on these numbers, the first violin modes of the three stages will be, from the top down, approximately 200, 500, and 500 Hz. The modes of the lowest stage will have the strongest coupling to the output signal, since they are not filtered by lower pendulum stages. These parameters would cause only the first $\sim$2 harmonics of the lowest stage violin modes to be within the measurement band.

7.3.5 Assembly and Adjustment

Having established that the theoretical performance of the pendulum suspension is suitable for GEO 600, the remaining challenge is to design an achievable suspension. The practical difficulties in assembling the suspension are foremost the cantilevers, which deflect up to 5 cm between their unloaded and loaded positions, and allowing for correction of any imbalances in the system due to slight differences between the cantilevers, the mounting clamps, or other mechanical parts.

Ideally, all the components in the suspension would be perfectly matched. In practice, the masses may have a static angular misalignment on assembly. This could come, for example, from the lower cantilevers not all having the exact same static deflection. In the same manner, the error could be in the lengths of the wires. As much as it would be theoretically desirable to allow adjustment of every parameter of the system, this is very difficult.

The uppermost mass (figure 7.2) has been designed with slots cut into the top surface, which allows the cantilevers to be firmly mounted to the mass without being stressed. The wires that are to be attached to these cantilevers are mounted to their respective clamps, again, unstressed, before these clamps are attached to the cantilevers. This affords the best chance of having these pieces all attached consistently. For any adjustment that is required, small shims—calibrated thin flat pieces—will be used between the clamps of the cantilevers to adjust the height of the cantilevers. For any small errors, this is adequate adjustment to compensate any variety of error.

The suspended optic must be properly oriented to form the proper optical path.

The rotational stage previously mentioned allows the mirror to be aligned in the yaw direction to within 10 mrad. The actuators for the local control have sufficient range to allow final alignment within this range after the vacuum tank has been evacuated. Similarly, the triple pendulum has been designed to be soft in tilt, allowing simple mechanical counter–balances attached to the uppermost mass to provide initial alignment, and again, the local control actuators can provide the final alignment.

7.4 Other Suspension Variations

The same process that was applied to the design of the suspension for the main optics can be applied to the design of other suspensions in the total GEO 600 system. The optical layout of the entire interferometer is shown in figure 7.4. This layout is not examined here in any detail, simply shown to illustrate the great variety of optical components involved in the system. The requirements for each of the components are often similar to those of the main suspension. Therefore, simple modifications of the process described in the preceeding chapters can achieve the required designs.

7.4.1 Reaction Mass Pendulum

To provide a quiet base of actuation, the actuation for the global control (section 6.3) is applied from a reaction mass pendulum. The setup within the vacuum tanks is as shown in figure 7.5, which applies to the tanks labelled *TCE* and *TCN* in figure 7.4. The requirement is that any relative motion of the actuators does not cause any excess noise on the sensitive optic through non–linear action of the actuators. Therefore the isolation and thermal noise requirements on the reaction mass are less stringent than on the main suspension. Based on ealier work on the electromagnetic coils used to drive the sensitive stage in a double pendulum, the displacement of the coils is allowed to be approximately 1000 times that of the test mass[67]. For ease in design and construction, and to allow the reaction mass pendulum to be easily aligned with respect to the main suspension, the reaction mass pendulum will be very similar to the main triple pendulum, although without the need for the fused silica final stages.

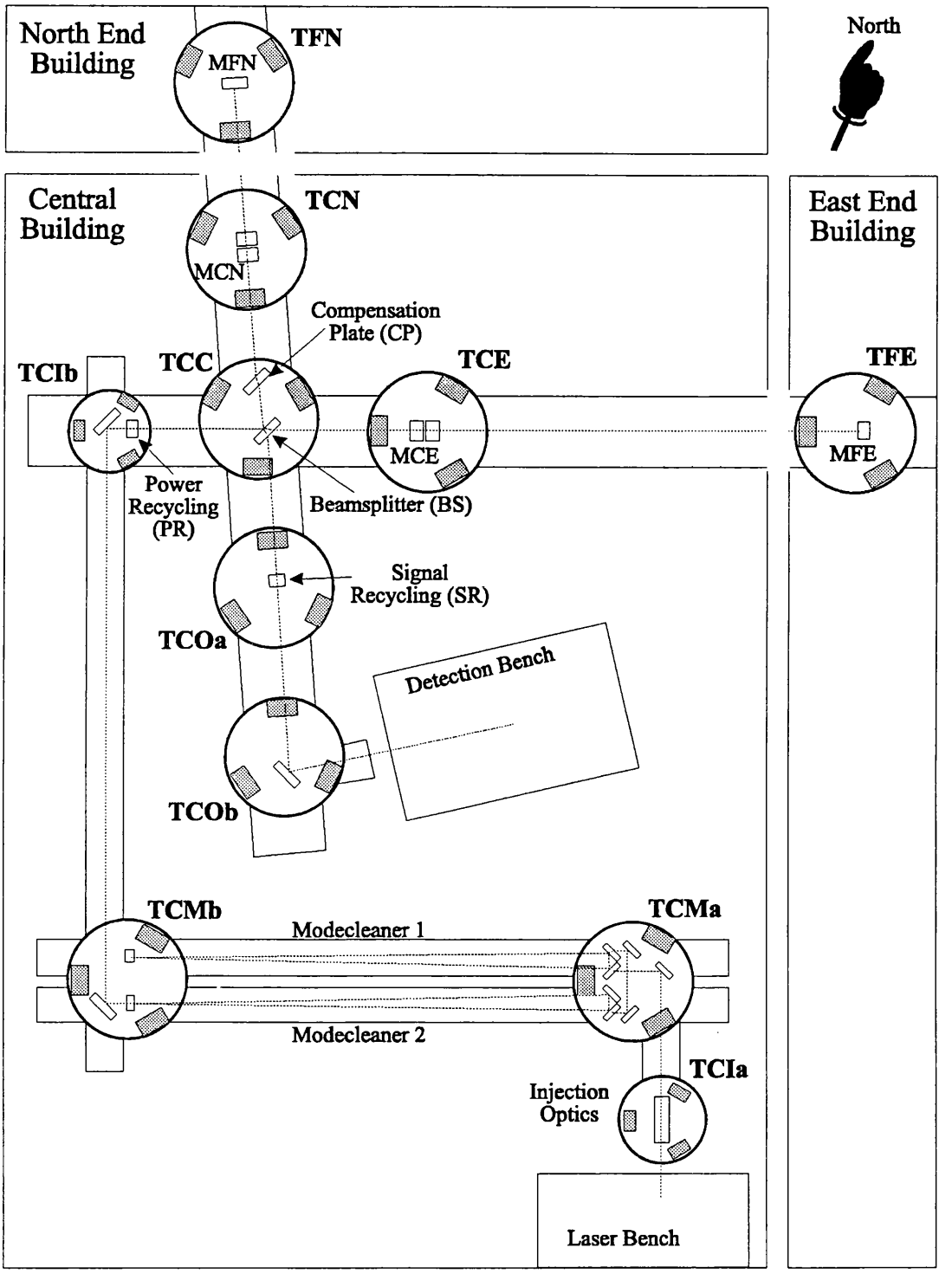

Figure 7.4: The optical layout of GEO 600. The full details of the optical layout may be examined on the GEO 600 website at *www.geo600.uni-hannover.de/geo600/project/optical.shtml* (adapted from Casey[85]).

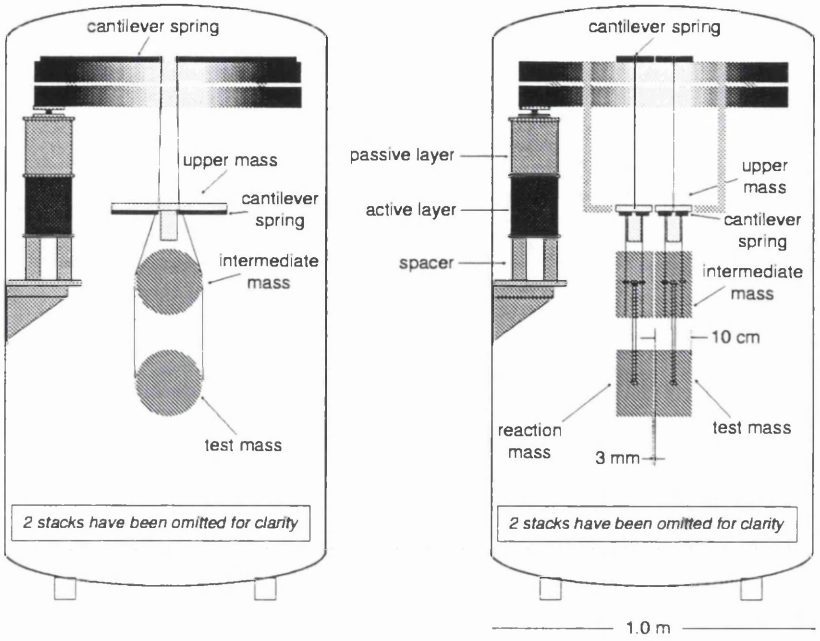

Figure 7.5: Reaction mass pendulum in GEO 600. The main mirror pendulum has a reaction mass pendulum hanging immediately behind it in both inboard tanks.

7.4.2 Other Optics

The suspended components in the main interferometer are shown in table 7.2. Based on where in the optical path an element may be, whether or not the position of the optic is sensed or if the optic is used in transmission, and so forth, most of the suspended components do not need the full isolation of a full triple pendulum suspension. Similarly, only the suspended components that are to be actuated to maintain global 'lock' of the interferometer require a reaction mass pendulum to be suspended alongside them. The details of the displacement noise requirements on each component, as well as the number of stages, also affects the number of stage of cantilevers that are necessary.

The two other optics that are supported on triple pendulum suspensions are the beam splitter, in tank *TCC*, and the signal recycling mirror (section 1.2.2), in tank *TCOa*. The displacement noise requirement on each of these suspensions is similar to that of the main suspension. However, by being at different points in the optical path, the size of the beam, and thus the size of the optic, is different. With different mass, the behaviour of the local control from section 6.2 has to be re–examined. The

Description		Num. of pendulums	Num. of cantilever stages	Size of Optic	Suspension material	Intermediate mass material	Lower reaction mass material	Intermediate reaction mass material
Far end suspension	$MF_{n,e}$	3	2	18 cmϕ× 10 cm	silica	silica	—	—
Near end suspension	$MC_{n,e}$	3	2	18 cmϕ× 10 cm	silica	silica	silica	aluminum
Power recycling	MPR	2	1	15 cmϕ× 7.5 cm	steel wire	aluminum	aluminum	aluminum
Beam splitter	BS	3	2	26 cmϕ× 8 cm	silica	silica	—	—
Compensation plate	CP	2	1	26 cmϕ× 8 cm	steel wire	aluminum	—	—
Signal recycling	SR	3	2	15 cmϕ× 7.5 cm	steel/silica[a]	aluminum/silica[a]	silica	aluminum
Reference cavity		1	1	N/A	steel wire	—	—	—

[a] Depending on specific application

Table 7.2: Summary of the suspended masses in GEO 600

Beam Splitter Suspension

		First stage		Second stage		Third stage	
	units	var	value	var	value	var	value
Mass dimensions	m	u_x	0.1 (Al)	i_r	0.12	t_r	0.12
		u_y	0.07	i_x	0.08	t_x	0.08
		u_z	0.2				
Wire parameters	#		2		4		4
length	m	l_1	0.545	l_2	0.187	l_3	0.28
radius	μm	r_1	350	r_2	230	r_3	140
Cantilevers	#		2		4		
spring constants	N/m	$k_{c,u}$	298	$k_{c,l}$	909		
Half wire separations							
in X-Y plane	m	$s[0]$	0	$s[1,l]$	0.03	$s[2,l]$	0.005
		$s[1,u]$	0	$s[2,u]$	0.03	$s[3,u]$	0.005
in X-Z plane	m	$n[0]$	0.03	$n[1,l]$	0.04	$n[2,l]$	i_r+ 0.0065[a]
		$n[1,u]$	0.04	$n[2,u]$	i_r+ 0.0065[a]	$n[3,u]$	t_r+ 0.0065[a]
Vertical offsets	m	$d[0]$	0	$d[1,l]$	0.001	$d[2,l]$	0.001
of wires ($\parallel Y$)		$d[1,u]$	0.002	$d[2,u]$	0.001	$d[3,u]$	0.001

Table 7.3: Parameters for the GEO 600 beam splitter suspension. The first stage is made out of aluminium.

Signal Recyling Mirror Suspension

		First stage		Second stage		Third stage	
	units	var	value	var	value	var	value
Mass dimensions	m	u_x	0.1	i_r	0.075	t_r	0.075
		u_y	0.07	i_x	0.075	t_x	0.075
		u_z	0.22				
Wire parameters	#		2		4		4
length	m	l_1	0.445	l_2	0.287	l_3	0.28
radius	μm	r_1	350	r_2	230	r_3	75
Cantilevers	#		2		4		
spring constants	N/m	$k_{c,u}$	457	$k_{c,l}$	333		
Half wire separations							
in X-Y plane	m	$s[0]$	0	$s[1,l]$	0.03	$s[2,l]$	0.005
		$s[1,u]$	0	$s[2,u]$	0.03	$s[3,u]$	0.005
in X-Z plane	m	$n[0]$	0.03	$n[1,l]$	0.04	$n[2,l]$	i_r+ 0.0065[a]
		$n[1,u]$	0.04	$n[2,u]$	i_r+ 0.0065[a]	$n[3,u]$	t_r+ 0.0065[a]
Vertical offsets	m	$d[0]$	0	$d[1,l]$	0.001	$d[2,l]$	0.001
of wires ($\parallel Y$)		$d[1,u]$	0.001	$d[2,u]$	0.001	$d[3,u]$	0.001

[a] Wire position is at the mass radius − the width of the flat on side of mass (0.0035) + a breakoff (0.01)

Table 7.4: Parameters for the GEO 600 signal recycling mirror suspension

final parameters for these two suspension variations are summarized in tables 7.3 and 7.4, with the definition of the parameters being the same as for the main suspension.

Chapter 8

Future Work

There is a constant effort to make ground based gravitational wave detectors sensitive at lower frequencies. They are limited at low frequencies by transmitted seismic noise, thermal noise in the pendulum suspension, and noise from the low frequency control electronics. The work presented here, which was specifically directed toward the GEO 600 detector, addresses all of these issues. The modelling code can predict the pendulum thermal noise for a multi–stage pendulum suspension, fully considering all the rigid body modes of the system. By calculating sensitivities to misalignments, the work quantifies the required vertical seismic isolation, as well as providing an improved model of the cantilever blades often used to achieve this isolation. Finally, the application of the local control to the uppermost mass eases the noise requirements on the sensors and actuators.

Construction of a number of long baseline interferometric detectors is well underway. With the completion of these first generation long baseline interferometers and the anticipated success of first detection, experimental efforts are likely to increase. New developments are already being studied to improve the sensitivity of next generation detectors. Better sensitivity will increase the 'range' at which these detectors can see events, and allowing a greater rate of detection events and better signal to noise, allowing more detailed information about the waveforms to be obtained. Extending the most sensitive band of these detectors to lower frequencies will permit binary inspirals to be observed for a longer time before the final coalescence.

The results of the work explored in the preceding chapters has been applied

specifically to the design on the main suspension system in the GEO 600 detector. The modelling work of chapter 3 is done in a general fashion, allowing some straightforward extensions for the design work required for higher sensitivity detectors. Examples include the general problem of replacing cylindrical wires with ribbons and the specific proposals for the suspension for the upgraded American LIGO detector (LIGO II).

8.1 Advanced Detectors—Suspensions in LIGO II

The GEO 600 project is a member of the LIGO Science Community (LSC), and as such its members are intimately involved in the discussions on how to construct a second generation gravitational wave detector. There are a number of steps to be taken to improve the sensitivity of the initial long–baseline gravity wave interferometers. Upgrading the input laser to higher power will improve the shot noise; implementation of signal recycling schemes will allow tuned performance not available in the first generation of LIGO; and new mirror and suspension materials should allow improved thermal noise performance. One primary goal for the second generation will be a push toward lower frequency sensitivity.

At the present time, the GEO team has agreed to design a multiple stage pendulum suspension (possibly quadruple) for application in the LIGO II detector. Because the interferometer arms are longer than in GEO 600 (4 km), the beam size and thus the suspended mirrors are larger. In addition, there is more room in the LIGO vacuum tanks than is available in the GEO system. However, the design principles are exactly as outlined in these preceeding chapters. In particular, the local control is designed to sense and actuate on the uppermost mass of the multi–stage pendulum.

It is impractical to get vastly improved seismic isolation from simple wire pendulums. To extend the detection band down toward 10 Hz, much more isolation is required of the overall system. The pendulum suspension does not have an explicit vibration isolation goal; instead, it will have as much isolation as is possible while achieving the required control objectives and thermal noise performance. The local control algorithms described in this thesis will work with minimal modification to act on slightly lower frequency bands. The sensor noise may have to be improved slightly

from that of the GEO sensor design. The overall isolation goal will be achieved by a combination of the pendulum system and a replacement of the current isolation stacks potentially consisting of a combination of passive and active elements. The initial LIGO detector is to begin operation in 2001; an upgraded detector would be entering prototype stages at that time, in anticipation of installation in the main facility in 2005[44].

The modelling of such a quadruple pendulum suspension is a straightforward extension of the work presented here and is already in progress.

8.2 Flexures

All of the work discussed here has involved pendulums hanging on round wires or fibres of constant cross–section along their functional length. One obvious change is to vary the size and shape of the elements doing the suspending, which could reduce the effects of the violin modes and possibly provide improved thermal noise performance.

Since the softness in bending of a wire occurs over a characteristic bending length (section 3.4.3), typically much shorter than the total length, the bending element could be made very short (comparable to this bending length). The rest of the pendulum length could be made of, for example, a lightweight, stiff tube. This would likely involve a short soft element at both the top and bottom of the suspension element to prevent over constraining tilt motion. Such a design would allow the same pendulum modes while the tube structure would ensure very high internal modes, although there would be the additional mode of the tube moving out of phase with the suspended mass.

Either the short bending elements as just described or the entire length of the suspension element could be made round, as in conventional wires, or as thin as possible in the bending direction, as in a flexure. The cross–sectional area of a flexure would have to be comparable to that of the wires in order to keep the stress in the material at the same level. However, since this flexure could be made wide in one dimension and narrow in the bending direction, the flexure could actually be made much softer in the critical direction than the wire it replaces. Since the loss and therefore the thermal noise observed in the pendulum mode comes from the energy stored in bending, reducing this bending stiffness could reduce the observed

thermal noise. Since a single flexure is stiff in three degrees of freedom—transverse motion, vertical motion, and roll—as opposed to the single degree of freedom of a round wire (vertical), a simple flexure system is inherently a reduced degree–of–freedom suspension (section 4.4). A system using more than one flexure must be carefully aligned, since if the bending degrees of freedom of the multiple flexures do not align, the system will be kinematically over–constrained. One way to avoid this would be to have flexures with their long dimension transverse to the beam at the suspension point (soft in bending in the longitudinal direction) which twist partway along their length. The long dimension of the flexure would then be in the longitudinal direction where the flexure attaches to the mass.

The modelling work presented in this thesis could readily be extended to the study of the use of such flexures and investigation of their potential for improving the performance of upgraded long baseline detectors.

Appendix A

Lagran.mws

Lagrangian for Compound pendula

MEH 8/9/98

CIT, JH, NAR

A.1 Introduction

6-Degree-of-Freedom Lagrangian for up to a 3-stage pendulum, involving vertical motion (y), yaw (phi), longitudinal (x), tilt (theta), transverse (z), and roll (psi). Solve for equations of motion, initially to check resonant frequencies. Derives equations of motion to first order in the center of mass coordinates of the suspended masses and converts the equations to a state space (1st order) format.

In the nominal case, the top mass of the pendulum is hung by two wires, each from its own cantilever blade. The second mass hangs by four wires, either each from its own cantilever or each pair (left and right) from one blade. The third mass hangs by four wires.

The spring constants for the cantilevers are input in N/m. The rest of the constants (wire spring constants [extension and torsion], moments of inertia) are calculated from physical parameters such as dimensions and material properties.

Method In the Lagrangian, we need to calculate the kinetic and potential energies of the system then take the appropriate derivatives. As the only kinetic energies

considered are the motions of the test masses, very little time is spent on this half of the calculation. This does mean there are no 'internal modes', either in the masses or the suspension elements (wires).

The first portion of the code sets up the physical system based on the input parameters.

The next large section of the code determines the contributions of various forms of potential energy to the system, including the gravitational potential energy of the masses and the elastic energy stored in the stretching, bending, and twisting of the wires. These are calculated independently, which for these small motions will be valid, with the caveat that while stretching is calculated properly in 3 dimensions, bending is calculated in the 2 non-vertical directions. (This means that for wires sloped at extreme angles from vertical, vertical motion should cause some bending of the wires, which this will ignore.)

NOTE: This is being adjusted as of version 6.7 29/4/99. Bending and stretching are now coupled in terms of the wire shape. These notes will be updated once I resolve the situation–MEH

This total potential energy is minimized to calculate the equilibrium position of the system. This is solved numerically for vertical motions (the 'symmetric' case) then expanded quadratically in the neighborhood and iterated. The full Lagrangian is re-written in terms of small differentials about these equilibrium coordinates, and the appropriate derivatives are taken. This expression gives the differential equation, which involves only the approximations expressed above (ie, could be expanded to higher order); it is then manually Taylor expanded to first order in the relevant variables. The case parameters are then substituted to get numerical results. (Unfortunately, the full expressions for the general case are so complicated as to make symbolic intuition very difficult; if desired, the definition of the potential energy (section A.5.2) may have specific terms commented. This allows parts of the equation to be explored symbolically. One note is that both the gravitational term and the stretching term must be included to get 'Tension', and that the solution to the fourth order beam equation for the wires under tension requires a tension value to be correctly evaluated. Thus to examine the bending term, run the full potential energy until the point where the tensions are evaluated, then back up, redefine the potential energy, then run the last part of the program.)

There are a few lines of code which are more necessary for testing than for use. Also, there are portions which are build-ins for the evolution of the program. For example the last few pages calculate the cross-coupling between various degrees of freedom that are, virtually by definition, zero for these cases. Finally, many of the intermediate results are printed; the convention in Maple to suppress output is to end the statement with a colon(:), whereas a semi-colon(;) shows the output, and these may be adjusted without affecting the results of the program.

NB: The program continues to be numerically sensitive when solving for the initial cantilever offsets. The initial unloaded (i.e., bent) position of the cantilevers is defined (section A.4.3) to be where yc = 0. One of the first steps of the program is to calculate the loaded positions of the cantilevers, yc0 (which would typically be flat). Because in the general case this offset might be anything in a large range (up to 30cm in these cases vs. approximately 1mm for a wire), the numerical solution range is specified as quite large. In the full, 3x6-DOF program with misalignments, it should not be a problem, since uneven cantilevers will contribute in directions other than vertically. Here, it tends to find non-physical solutions where the cantilevers are uneven. This can be solved by using a tighter solution range, although I'd prefer a wide solution range to allow the most general cases.

The other point to mention is that for esthetic sake, I have frequently used subscripts for denoting which stage, wire, etc. Maple interprets subscripts as vector or matrix indicies. Because of this, if certain parts of the code are re-run, it believes there is a recursive definition and will fail. To avoid this, my notation is not completely consistent, but I trust it will still be understandable.

This code was developed using Maple V Release 4.00a on a PC compatible platform. There are a few features, primarily formatting and hyperlinks, that may not be compatible across platforms. Ken Strain has been good enough to test the code in Maple V Release 5, and assures me the only changes are a small number of warning messages concerning a new use of matricies.

Version 7.5 8/9/99.

A.2 Instructions for use

At the moment, the code is intended as stand-alone, not as a subroutine to be included. This means, for example, that every time it is run it clears the Maple workspace. This is neceassary for two reasons–firstly, the problem of redefining certain terms, and secondly on this platform there is occasionally a memory leak, causing the program to 'forget' certain variables. Clearing the workspace is the simplest way of avoiding this.

The outputs of the system are A matrices, although not strictly the A matrices of state space formulation. As there is no loss included, this solves the second order differential equations

```
> diff(X(t),t,t) = A*X(t);
```

where x is the vector of center of mass coordinates (displacements and rotations).

$$\frac{\partial^2}{\partial t^2}\mathrm{X}(t) = A\,\mathrm{X}(t)$$

In the nominal cases, only certain degrees of freedom are coupled. Thus, it returns A matrices for

- vertical,
- rotational (yaw),
- longitudinal and tilt (pitch), and
- sideways and roll.

These elements may be converted to the lower-left quadrant of appropriate state-space A matrices. The program also returns the eigenvalues or resonant frequencies of the system. Using these uncoupled degrees of freedom, the mode shapes should be obvious; if it is required to see the shapes of these modes, the Maple language command *linalg[eigenvects]* is the appropriate one to use after the calculation of the A matrices.

Definitions of the all input and some derived parameters are in section A.4 titled Variables.

It would be difficult to implement all possible misalignments; at this point each misalignment must be input individually at the proper point in the code. Where and how this is done are shown by example, including:

- Varying the extension spring constant (section A.5.2)
- Misalignment of wire connections (section A.5.3)

A.2.1 Categories

Section A.3 entitled Setup describes the system to be modeled, including number of stages and numbers of cantilevers at the top two stages. While the program in principle can use any number of wires, to ease in setup the nominal setup is left-right symmetric. To get the desired tilt couplings, the lower two stages will use 4 wires.

A.2.2 Inputs

There are two parts to the Variables section: the part described under Common Variables (A.4.1) are typically those derived quantities that are in common for any spacings, lengths, and material choices of wires or simple changes in mass dimensions. Rather than repeat these for each case, they are grouped at the front. Cases are where the specifics of the run are input, including material properties, (sectionA.4.1,Cases) sizes and shapes of the components, and dimensions for the spacings. All units are mks(SI).

```
> restart;
```

```
> sttime := time():
```

Means no annotation on assumed variables, for compactness.

```
> interface(showassumed=0);
```

```
> Digits := 20:
```

```
> with(linalg):
```

```
Warning, new definition for norm
```

```
Warning, new definition for trace
```

```
> readlib(mtaylor):
```

Initialization:

```
> stable_system := 1:
```

A.3 Setup

Basic setup parameters of the system.

Functional choices are shown in parenthesis with the nominal case in bold brackets [x].

For any fully x- and z-symmetric case, the calculations are much, much faster. This should not effect the results, but setting symmetric to 1 will speed up the program (0, [1]).

```
> Symmetric := 0:
```

Number of stages of pendulum: (1,2,[3]):

```
> NumPen := 1:
```

(Numbered from top to bottom) NB: If there are fewer than 3 stages, the program will just ignore the variables for the other stages, so they may be excluded or just ignored when copying over cases. The program will return frequencies of zero for the non-existent stages.

Number of cantilevers at upper (or first) stage (0,[2],4):

```
> NumCanU := 0:
```

Number of cantilevers at intermediate (second) stage (0,2,[4]):

```
> NumCanM := 0:
```

The typical setups use either 2, 4, and 4 wires or 4, 4, and 4 wires. Using 1, 2, or 4 wires, the assumed symmetries can be taken care of by setting either the x and/or the z separations to zero.

```
> '# of wires,u' := 4:
'# of wires,m' := 0:
'# of wires,l' := 0:
```

A.4 Variables

Definitions of variables:

y, ydot = vertical displacement/velocity, positive upwards *(0 = unstretched wire)*

x, xdot = longitudinal displacement/velocity, along beam, positive toward incoming beam

z, zdot = transverse displacement/velocity

x0, y0, z0, theta0 = translations of the top plate/attachment point While using rotations about the center of mass of each stage is sensible for the pendulum stages, it's not clear what the 'center of mass' is for the top plate. What should probably be used as an input is the angle of the top plate off the isolation stacks. Theta0 assumes rotation about the center point of the wire attachments.

phi, phidot = yaw angle/angular velocity *(0 = aligned with beam)*

theta, thetadot = pitch angle (tilt)/angular velocity, positive tilted upwards

psi, psidot = roll angle/angular velocity, positive clockwise facing into beam

massi = mass (numbered top to bottom)

Iyaw, Ipitch, Iroll = Moment of Inertia for yaw/pitch/roll *(at the moment, derived from physical dimensions)*

s0, s[i,u/l] = distance of wire attachment, upper and lower, from center of mass, along direction of the beam

n0, n[i,j] = distance of wire attachment, upper and lower, from center of mass, along direction perpendicular to the beam

Lengthi = length of wire *(nominally unstretched; in practice, probably stretched)*

d[i,j] = vertical distance from attachment of wire to mass to center of mass (positive is above/below CM)

Hi = vertical distance from center of mass one stage to the next (unstretched wires) *(H = dl+sqrt[length^2 - dn^2 - ds^2] + dd)*

ks = spring constant of wire in stretching = *E*pi*(rwire)^2/length*

kt = spring constant of wire in torsion = *E*pi*(rwire)^4/[4*(1+PR)*length]*

Ewire = Young's Modulus of wire sigma = Poisson's Ratio for wire

Iwire = area moment of inertia of wire = *1/4*pi*r^4 for round wire*

rwire = radius of wire g = gravitational constant *(9.8 m/s^2)*

kcant = cantilever spring constants *(N/m)*

kappa = characteristic bending length of wire *(derived)*

Ten = nominal tension in the wire *(derived)*

alpha_wire.i = loss in wire, as an imaginary part of Young's Modulus, as a function of frequency

A.4.1 Common variables

Often derived quantities, these are the variables used in the system for every choice of parameters, such as wire spring constant as a function of wire size and material. Therefore there are some implicit assumptions, including:

- Each wire is round and of constant material property
- The upper mass is a rectangular parallelpiped (a box)
- The middle and lower masses are cylinders of the same dimensions

These assumptions can be adjusted, but the definitions in this section and in the vars definitions must be changed.

```
> vars_equations :=
'Iroll[2]'='mass[2]'*ir^2/2,'Iroll[3]'='mass[3]'*tr^2/2,
'Ipitch[2]'='mass[2]'*(ir^2/4+ix^2/12),
'Ipitch[3]'='mass[3]'*(tr^2/4+tx^2/12),
'Iyaw[2]'='mass[2]'*(ir^2/4+ix^2/12),
'Iyaw[3]'='mass[3]'*(tr^2/4+tx^2/12),
#'Iroll[1]'='mass[1]'*(uy^2+uz^2)/12,
#'Ipitch[1]'='mass[1]'*(uy^2+ux^2)/12,
##'Iyaw[1]'='mass[1]'*(ux^2+uz^2)/12, # Cube
#'Iroll[1]'='mass[1]'*(ur^2)/2,
#'Ipitch[1]'='mass[1]'*(ur^2/4+ux^2/12),
#'Iyaw[1]'='mass[1]'*(ur^2/4+ux^2/12), # Cylinder
#'Iroll[2]'='mass[2]'*(tr^2)/2,
#'Ipitch[2]'='mass[2]'*(tr^2/4+tx^2/12),
#'Iyaw[2]'='mass[2]'*(tr^2/4+tx^2/12), # Cylinder
'Iroll[1]'='mass[1]'*(tr^2)/2,
'Ipitch[1]'='mass[1]'*(tr^2/4+tx^2/12),
'Iyaw[1]'='mass[1]'*(tr^2/4+tx^2/12), # Cylinder
'H[1]'=(Length[1]^2 - ('s[1,u]'-'s[0]')^2 -
('n[1,u]'-'n[0]')^2)^(1/2) + 'd[1,u]',
'H[2]'=(Length[2]^2 - ('s[2,u]'-'s[1,1]')^2 -
('n[2,u]'-'n[1,1]')^2)^(1/2) + 'd[2,u]' + 'd[1,1]',
'H[3]'=(Length[3]^2 - ('s[3,u]'-'s[2,1]')^2 -
('n[3,u]'-'n[2,1]')^2)^(1/2) + 'd[3,u]' + 'd[2,1]',
ks1=E[wire1]*(Pi*r[wire1]^2)/Length[1],
ks2=E[wire2]*(Pi*r[wire2]^2)/Length[2],
ks3=E[wire3]*(Pi*r[wire3]^2)/Length[3],
```

```
k[t1]=E[wire1]*Pi*r[wire1]^4/(4*(1+sigma[1])*Length[1]),
k[t2]=E[wire2]*Pi*r[wire2]^4/(4*(1+sigma[2])*Length[2]),
k[t3]=E[wire3]*Pi*r[wire3]^4/(4*(1+sigma[3])*Length[3]),
k[cant,u]=739*(1+I*alpha_cantU),
# N/m, numerically to match uncoupled frequencies
k[cant,l]=498*(1+I*alpha_cantL),
# N/m, numerically to match uncoupled frequencies
Iwire[1]=(1/4)*Pi*r[wire1]^4,Iwire[2]=(1/4)*Pi*r[wire2]^4,
Iwire[3]=(1/4)*Pi*r[wire3]^4;
```

$$vars\_equations := Iroll[2] = \frac{1}{2}\, mass[2]\, ir^2,\ Iroll[3] = \frac{1}{2}\, mass[3]\, tr^2,$$

$$Ipitch[2] = mass[2]\,(\frac{1}{4}\, ir^2 + \frac{1}{12}\, ix^2),\ Ipitch[3] = mass[3]\,\%1,$$

$$Iyaw[2] = mass[2]\,(\frac{1}{4}\, ir^2 + \frac{1}{12}\, ix^2),\ Iyaw[3] = mass[3]\,\%1,$$

$$Iroll[1] = \frac{1}{2}\, mass[1]\, tr^2,\ Ipitch[1] = mass[1]\,\%1,\ Iyaw[1] = mass[1]\,\%1,$$

$$H[1] = \sqrt{Length_1{}^2 - (s[1,u] - s[0])^2 - (n[1,u] - n[0])^2} + d[1,u],$$

$$H[2] = \sqrt{Length_2{}^2 - (s[2,u] - s[1,l])^2 - (n[2,u] - n[1,l])^2} + d[2,u] + d[1,l],$$

$$H[3] = \sqrt{Length_3{}^2 - (s[3,u] - s[2,l])^2 - (n[3,u] - n[2,l])^2} + d[3,u] + d[2,l],$$

$$ks1 = \frac{E_{wire1}\,\pi\, r_{wire1}{}^2}{Length_1},\ ks2 = \frac{E_{wire2}\,\pi\, r_{wire2}{}^2}{Length_2},\ ks3 = \frac{E_{wire3}\,\pi\, r_{wire3}{}^2}{Length_3},$$

$$k_{t1} = \frac{1}{4}\,\frac{E_{wire1}\,\pi\, r_{wire1}{}^4}{(1+\sigma_1)\, Length_1},\ k_{t2} = \frac{1}{4}\,\frac{E_{wire2}\,\pi\, r_{wire2}{}^4}{(1+\sigma_2)\, Length_2},$$

$$k_{t3} = \frac{1}{4}\,\frac{E_{wire3}\,\pi\, r_{wire3}{}^4}{(1+\sigma_3)\, Length_3},\ k_{cant,u} = 739 + 739\, I\, alpha\_cantU,$$

$$k_{cant,l} = 498 + 498\, I\, alpha\_cantL,\ Iwire_1 = \frac{1}{4}\,\pi\, r_{wire1}{}^4,\ Iwire_2 = \frac{1}{4}\,\pi\, r_{wire2}{}^4,$$

$$Iwire_3 = \frac{1}{4}\,\pi\, r_{wire3}{}^4$$

$$\%1 := \frac{1}{4}\, tr^2 + \frac{1}{12}\, tx^2$$

Cases:

Different sample cases follow below. As in many computer languages, Maple uses the last definition of "vars". In other words, set the desired parameters equal to "vars" and any following definitions to some dummy name (such as "vars1"). Each

should begin with "vars_equations" in order to include the above definitions.

Case 1:

2+4+4 wires:

```
> vars := vars_equations,
E[wire1] = 1.65e11*(1+I*alpha_wire1), # N/m^2
E[wire2] = 1.65e11*(1+I*alpha_wire2),
E[wire3] = 7e10*(1+I*alpha_wire3), # Fused Silica
r[wire1] = 350e-6, r[wire2] = 175e-6, r[wire3] = 154e-6,
sigma[1] = 0.29, sigma[2] = 0.29, sigma[3] = 0.29,
`s[0]`=`s[1,u]`,`s[1,u]`=0,`s[1,1]`=`s[2,u]`,
`s[2,u]`=0.03,`s[2,1]`=`s[3,u]`,`s[3,u]`=0.005,
`n[0]`=0.03,`n[1,u]`=0.04,`n[1,1]`=0.045,
`n[2,u]`=ir-0.0035+0.01,`n[2,1]`=`n[3,u]`,`n[3,u]`=tr-0.0035+0.01,
`d[1,u]`=0.001,`d[1,1]`=0.001,
`d[2,u]`=0.001,`d[2,1]`=0.001,`d[3,u]`=0.001,
g=9.81,`mass[1]`=ux*uy*uz*2700,
`mass[2]` = ix*Pi*(ir^2)*2202, `mass[3]` = tx*Pi*(tr^2)*2202,
Length[1]=0.42, Length[2] = 0.187, Length[3] = 0.28,
`Iyaw[1]`=0.1134, `Ipitch[1]`=0.1134,
ux = 0.1, uy=0.07, uz=0.3,
ix=0.1, ir=0.09, tx=0.1, tr=0.09,
IcanU=mass_canU*LCanU^2/18,
IcanM=mass_canM*LCanM^2/18,
mass_canU=1/2*(0.04+0.0045)*LCanU*(0.002)*7800,
mass_canM=1/2*(0.028+0.0038)*LCanM*(0.001)*7800,
LCanU=0.24,LCanM=0.124;
```

$$vars := Iroll[2] = \frac{1}{2}\, mass[2]\, ir^2,\ Iroll[3] = \frac{1}{2}\, mass[3]\, tr^2,$$

$$Ipitch[2] = mass[2]\,(\frac{1}{4}\, ir^2 + \frac{1}{12}\, ix^2),\ Ipitch[3] = mass[3]\,\%1,$$

$$Iyaw[2] = mass[2]\,(\frac{1}{4}\, ir^2 + \frac{1}{12}\, ix^2),\ Iyaw[3] = mass[3]\,\%1,$$

$$Iroll[1] = \frac{1}{2}\, mass[1]\, tr^2,$$

$$Ipitch[1] = mass[1]\,\%1,\ Iyaw[1] = mass[1]\,\%1,$$

$$H[1] = \sqrt{Length_1{}^2 - (s[1,u] - s[0])^2 - (n[1,u] - n[0])^2} + d[1,u],$$

$$H[2] = \sqrt{Length_2{}^2 - (s[2,u] - s[1,l])^2 - (n[2,u] - n[1,l])^2} + d[2,u] + d[1,l],$$

$$H[3] = \sqrt{Length_3{}^2 - (s[3,u] - s[2,l])^2 - (n[3,u] - n[2,l])^2} + d[3,u] + d[2,l],$$

$$ks1 = \frac{E_{wire1}\,\pi\, r_{wire1}{}^2}{Length_1},\ ks2 = \frac{E_{wire2}\,\pi\, r_{wire2}{}^2}{Length_2},\ ks3 = \frac{E_{wire3}\,\pi\, r_{wire3}{}^2}{Length_3},$$

$$k_{t1} = \frac{1}{4}\,\frac{E_{wire1}\,\pi\, r_{wire1}{}^4}{(1+\sigma_1)\, Length_1},\ k_{t2} = \frac{1}{4}\,\frac{E_{wire2}\,\pi\, r_{wire2}{}^4}{(1+\sigma_2)\, Length_2},$$

$$k_{t3} = \frac{1}{4}\,\frac{E_{wire3}\,\pi\, r_{wire3}{}^4}{(1+\sigma_3)\, Length_3},\ k_{cant,u} = 739 + 739\, I\ alpha\_cantU,$$

$$k_{cant,l} = 498 + 498\, I\ alpha\_cantL,\ Iwire_1 = \frac{1}{4}\,\pi\, r_{wire1}{}^4,\ Iwire_2 = \frac{1}{4}\,\pi\, r_{wire2}{}^4,$$

$$Iwire_3 = \frac{1}{4}\,\pi\, r_{wire3}{}^4,\ E_{wire1} = .165\,10^{12} + .165\,10^{12}\, I\ alpha\_wire1,$$

$$E_{wire2} = .165\,10^{12} + .165\,10^{12}\, I\ alpha\_wire2,$$

$$E_{wire3} = .7\,10^{11} + .7\,10^{11}\, I\ alpha\_wire3,$$

$$r_{wire1} = .000350,\ r_{wire2} = .000175,\ r_{wire3} = .000154,$$

$$\sigma_1 = .29,\ \sigma_2 = .29,\ \sigma_3 = .29,\ s[0] = s[1,u],\ s[1,u] = 0,$$

$$s[1,l] = s[2,u],\ s[2,u] = .03,\ s[2,l] = s[3,u],\ s[3,u] = .005,$$

$$n[0] = .03,\ n[1,u] = .04,\ n[1,l] = .045,\ n[2,u] = ir + .0065,\ n[2,l] = n[3,u],$$

$$n[3,u] = tr + .0065,\ d[1,u] = .001,\ d[1,l] = .001,\ d[2,u] = .001,$$

$$d[2,l] = .001,\ d[3,u] = .001,\ g = 9.81,\ mass[1] = 2700\, ux\, uy\, uz,$$

$$mass[2] = 2202\, ix\, \pi\, ir^2,\ mass[3] = 2202\, tx\, \pi\, tr^2,\ Length_1 = .42,$$

$$Length_2 = .187,\ Length_3 = .28,\ Iyaw[1] = .1134, Ipitch[1] = .1134,\ ux = .1,$$

$$uy = .07,\ uz = .3, ix = .1,\ ir = .09,\ tx = .1,\ tr = .09,$$

$$IcanU = \frac{1}{18}\, mass\_canU\ LCanU^2,\ IcanM = \frac{1}{18}\, mass\_canM\ LCanM^2,$$

$$mass\_canU = .347100000000\, LCanU,\ mass\_canM = .124020000000\, LCanM,$$

$$LCanU = .24,\ LCanM = .124\%1 := \frac{1}{4}\, tr^2 + \frac{1}{12}\, tx^2$$

Case 2: Single Pendulum cases.

```
> vars1 := vars_equations,
E[wire1] = 7e10*(1+I*alpha_wire1), # N/m^2 Fused silica
r[wire1] = 140e-6,
sigma[1] = 0.29,
`s[0]`=`s[1,u]`,`s[1,u]`=0.005,
`n[0]`=0,`n[1,u]`=tr-0.0035+0.01,
`d[1,u]`=0.001,
g=9.81,`mass[1]`=tx*Pi*(tr^2)*2700,
Length[1]=0.28,
tx=0.09, tr=0.10:
```

Case 3: Thermal Noise per Sheila

```
> vars1 := vars_equations,
E[wire1] = 7e10*(1+I*alpha_wire1), # N/m^2 Fused silica
r[wire1] = 500e-6/2, # 500 micron diameter
sigma[1] = 0.29, # Poisson's Ratio
`s[0]`=`s[1,u]`,`s[1,u]`= 0, #0.005, # 1cm full separation
`n[0]`=`n[1,u]`,`n[1,u]`= tr, # Attached at mirror radius
`d[1,u]`= 0.001, # 1mm
g=9.81,
`mass[1]`=10.8, # kg
Length[1]=0.25, # 25cm
tr=0.25/2, tx=0.10,
IcanU=mass_canU*LCanU^2/18,
IcanM=mass_canM*LCanM^2/18,
mass_canU=1/2*(0.04+0.0045)*LCanU*(0.002)*7800,
mass_canM=1/2*(0.028+0.0038)*LCanM*(0.001)*7800,
LCanU=0.24,LCanM=0.124;
```

$$vars1 := Iroll[2] = \frac{1}{2}\, mass[2]\, ir^2,\ Iroll[3] = \frac{1}{2}\, mass[3]\, tr^2,$$

$$Ipitch[2] = mass[2]\,(\frac{1}{4}\, ir^2 + \frac{1}{12}\, ix^2),\ Ipitch[3] = mass[3]\,\%1,$$

$$Iyaw[2] = mass[2]\,(\frac{1}{4}\, ir^2 + \frac{1}{12}\, ix^2),\ Iyaw[3] = mass[3]\,\%1,$$

$$Iroll[1] = \frac{1}{2}\, mass[1]\, tr^2,$$

$$Ipitch[1] = mass[1]\,\%1,\ Iyaw[1] = mass[1]\,\%1,$$

$$H[1] = \sqrt{Length_1{}^2 - (s[1,u] - s[0])^2 - (n[1,u] - n[0])^2} + d[1,u],$$

$$H[2] = \sqrt{Length_2{}^2 - (s[2,u] - s[1,l])^2 - (n[2,u] - n[1,l])^2} + d[2,u] + d[1,l],$$

$$H[3] = \sqrt{Length_3{}^2 - (s[3,u] - s[2,l])^2 - (n[3,u] - n[2,l])^2} + d[3,u] + d[2,l],$$

$$ks1 = \frac{E_{wire1}\,\pi\, r_{wire1}{}^2}{Length_1},\ ks2 = \frac{E_{wire2}\,\pi\, r_{wire2}{}^2}{Length_2},\ ks3 = \frac{E_{wire3}\,\pi\, r_{wire3}{}^2}{Length_3},$$

$$k_{t1} = \frac{1}{4}\,\frac{E_{wire1}\,\pi\, r_{wire1}{}^4}{(1+\sigma_1)\, Length_1},\ k_{t2} = \frac{1}{4}\,\frac{E_{wire2}\,\pi\, r_{wire2}{}^4}{(1+\sigma_2)\, Length_2},$$

$$k_{t3} = \frac{1}{4}\,\frac{E_{wire3}\,\pi\, r_{wire3}{}^4}{(1+\sigma_3)\, Length_3},\ k_{cant,u} = 739 + 739\, I\, alpha\_cantU,$$

$$k_{cant,l} = 498 + 498\, I\, alpha\_cantL,\ Iwire_1 = \frac{1}{4}\,\pi\, r_{wire1}{}^4,\ Iwire_2 = \frac{1}{4}\,\pi\, r_{wire2}{}^4,$$

$$Iwire_3 = \frac{1}{4}\,\pi\, r_{wire3}{}^4,\ E_{wire1} = .7\,10^{11} + .7\,10^{11}\, I\, alpha\_wire1,$$

$$r_{wire1} = .00025000000000000,\ \sigma_1 = .29,\ s[0] = s[1,u],\ s[1,u] = 0,$$

$$n[0] = n[1,u],$$

$$n[1,u] = tr,\ d[1,u] = .001,\ g = 9.81,\ mass[1] = 10.8,\ Length_1 = .25,$$

$$tr = .125000000000000,\ tx = .10,\ IcanU = \frac{1}{18}\, mass\_canU\, LCanU^2,$$

$$IcanM = \frac{1}{18}\, mass\_canM\, LCanM^2,\ mass\_canU = .347100000000000\, LCanU,$$

$$mass\_canM = .124020000000000\, LCanM,\ LCanU = .24,\ LCanM = .124$$

$$\%1 := \frac{1}{4}\, tr^2 + \frac{1}{12}\, tx^2$$

Case 4: 2 wire–one front right, one back left:

```
> vars1 := vars_equations,
E[wire1] =
7e10*(1+I*alpha_wire1), # N/m^2 Fused silica
r[wire1] = evalf(sqrt(2))*500e-6/2, # 500 micron diameter
sigma[1] = 0.29, # Poisson's Ratio
`s[0]`=`s[1,u]`,`s[1,u]`= 0.005, # 1cm full separation
```

```
'n[0]'='n[1,u]','n[1,u]'= tr, # Attached at mirror radius
'd[1,u]'= 0.001, # 1mm
g=9.81,
'mass[1]'=10.8, # kg
Length[1]=0.25, #0.02, # 25cm
tr=0.25/2, tx=0.10:
```

A.4.2 Loss

Structural (or viscous) loss in the wires.

Viscous loss, *alpha = phi0 * omega*

```
> loss :=
alpha_wire1 = 1e-6*omega,
alpha_wire2 = 1e-6*omega,
alpha_wire3 = 1e-6*omega;
```

$$loss := alpha\_wire1 = .1\,10^{-5}\,\omega,\ alpha\_wire2 = .1\,10^{-5}\,\omega,\ alpha\_wire3 = .1\,10^{-5}\,\omega$$

Structural loss, *alpha = phi0*

```
> loss :=
alpha_wire1 = 3.3e-8,
alpha_wire2 = 3.3e-8,
alpha_wire3 = 3.3e-8;
```

$$loss := alpha\_wire1 = .33\,10^{-7},\ alpha\_wire2 = .33\,10^{-7},\ alpha\_wire3 = .33\,10^{-7}$$

Structural material loss + Thermoelastic damping

While this depends on properties that are defined in 'vars', getting the substitution order correct is a chore, so just put in numerically here.

tau = 7.37e-2*rho*c*d^2/k

Delta = E*alpha^2*Temp/(rho*c)

phi_Thermoelastic = Delta*omega*tau /(1 + omega^2*tau^2)

phi = phi_intrinsic + phi_Thermoelastic

```
> loss :=
alpha_cantU = 1.0e-4,
alpha_cantL = 1.0e-4,
alpha_wire1 = 1.0e-5,
```

```
alpha_wire2 = 1.0e-6,
alpha_wire3 = 3.3e-8 + (7e10*(5e-7)^2*300/( (2.2e3)*(772) ))*
omega*(7.37e-2*(2.2e3)*(772)*(500e-6)^2/1.38)/
(1+omega^2*(7.37e-2*(2.2e3)*(772)*(500e-6)^2/1.38)^2);
#alpha_wire3 = proc (omega)
# local tau,Delta,alpha1;
#
# tau := 7.37e-2*(2.2e3)*(772)*(500e-6)^2/1.38:
# Delta := 7e10*(5e-7)^2*300/( (2.2e3)*(772) ):
#
# alpha1 := Delta*omega*tau/(1+omega^2*tau^2);
#
# RETURN(3.3e-8 + alpha1);
#end;
```

$$loss := alpha\_cantU = .00010,\ alpha\_cantL = .00010,\ alpha\_wire1 = .000010,$$
$$alpha\_wire2 = .10\,10^{-5},\ alpha\_wire3 = .33\,10^{-7} + .70095108695652173913\,10^{-7}\,\frac{\omega}{1 + .00051420557693782818736\,\omega^2}$$

```
> loss :=
alpha_wire1 = 3.3e-8 +
(7e10*(5e-7)^2*300/( (2.2e3)*(772)
))*omega*(7.37e-2*(2.2e3)*(772)*(500e-6)^2/1.38)/
(1+omega^2*(7.37e-2*(2.2e3)*(772)*(500e-6)^2/1.38)^2);
```

$$loss := alpha\_wire1 = .33\,10^{-7} + .70095108695652173913\,10^{-7}\,\frac{\omega}{1 + .00051420557693782818736\,\omega^2}$$

A dummy zero-loss function, for calculation of static conditions and zero-loss resonant frequencies.

```
> loss0 :=
alpha_wire1=0,alpha_wire2=0,alpha_wire3=0,
alpha_cantU=0,alpha_cantL=0;
```

$$loss0 := alpha\_wire1 = 0,\ alpha\_wire2 = 0,\ alpha\_wire3 = 0,\ alpha\_cantU = 0,\ alpha\_cantL = 0$$

```
> lossVars :=
[alpha_wire1,alpha_wire2,alpha_wire3,alpha_cantU,alpha_cantL];
```

$$lossVars := [alpha\_wire1,\ alpha\_wire2,\ alpha\_wire3,\ alpha\_cantU,\ alpha\_cantL]$$

A.4.3 Simplifications

```
> input_vars := x0,y0,z0,theta0;
```

$$input\_vars := x0,\ y0,\ z0,\ \theta 0$$

```
> inputs0 := seq(ii=0,ii=input_vars):
```

Used for expansions

```
> readlib(coeftayl): readlib(mtaylor):
```

For expansion about nominal:

```
> allDOF0 := inputs0,
seq(op([x.ii=0,y.ii=0,z.ii=0,phi.ii=0,theta.ii=0,psi.ii=0]),
ii=1..NumPen),
seq(`yc[u,`.ii.`]`=0,ii=1..NumCanU),
seq(`yc[l,`.ii.`]`=0,ii=1..NumCanM):
```

A 'list' versus a 'set' ([ ] vs. { }) so it will stay ordered:

```
> all_vars := [
seq(op([x.ii,y.ii,z.ii,theta.ii,phi.ii,psi.ii]),ii=1..NumPen),
seq(`yc[u,`.ii.`]`,ii=1..NumCanU),
seq(`yc[l,`.ii.`]`,ii=1..NumCanM),
input_vars];
```

$$all\_vars := [x1,\ y1,\ z1,\ \theta 1,\ \phi 1,\ \psi 1,\ x0,\ y0,\ z0,\ \theta 0]$$

```
> CantOffs0 := UCantOff=0,MCantOff=0;
```

$$CantOffs0 := UCantOff = 0,\ MCantOff = 0$$

```
> CantOffs := CantOffs0:
if (NumCanU>0) then
CantOffs := evalf(op([
UCantOff=subs(vars,loss0,add(`mass[`.ii.`]`,
ii=1..NumPen)*g/(NumCanU*k[cant,u])) ]) );
if (NumCanM>0) then
CantOffs := CantOffs,
evalf(op([MCantOff=subs(vars,loss0,add(`mass[`.ii.`]`,
ii=2..NumPen)*g/(NumCanM*k[cant,l])) ]) );
fi:
fi:
CantOffs;
```

$$UCantOff = 0,\ MCantOff = 0$$

To simplify expressions further on (usually sqrt(L^2)=L):

```
> assume(x0,real,y0,real,z0,real,theta0,real,
x1,real,y1,real,z1,real,theta1,real,phi1,real,psi1,real,
x2,real,y2,real,z2,real,theta2,real,phi2,real,psi2,real,
x3,real,y3,real,z3,real,theta3,real,phi3,real,psi3,real,
y10,real,y20,real,y30,real,
alpha_wire1,real,alpha_wire2,real,alpha_wire3,real,
alpha_cantU,real,alpha_cantL,real);

> additionally(`n[0]`,real,`s[0]`,real):
additionally(`n[1,u]`,real,`s[1,u]`,real,`d[1,u]`,real);
additionally(`n[1,l]`,real,`s[1,l]`,real,`d[1,l]`,real);
additionally(`n[2,u]`,real,`s[2,u]`,real,`d[2,u]`,real);
additionally(`n[2,l]`,real,`s[2,l]`,real,`d[2,l]`,real);
additionally(`n[3,u]`,real,`s[3,u]`,real,`d[3,u]`,real);
additionally(`yc[u,1]`,real,`yc[u,2]`,real,`yc[u,3]`,real,
`yc[u,4]`,real);
additionally(`yc[l,1]`,real,`yc[l,2]`,real,`yc[l,3]`,real,
`yc[l,4]`,real);
additionally(`H[1]`,real,`H[2]`,real,`H[3]`,real);
additionally(UCantOff,real,MCantOff,real);
additionally(`H[1]`-`d[1,u]`>0,`H[1]`-`d[1,u]`-y1>0);
additionally(`H[1]`-`d[1,u]`-y10>0);
additionally(`H[2]`-`d[2,u]`-`d[1,l]`>0,
```

```
'H[2]'-'d[2,u]'-'d[1,1]'+y1-y2>0);
```

Because Maple is sometimes too dense to set (a-b)^2 = (b-a)^2:

```
> simple := ('s[1,u]'-'s[0]')^2 =
('s[0]'-'s[1,u]')^2, ('n[1,u]'-'n[0]')^2 = ('n[0]'-'n[1,u]')^2,
('s[2,u]'-'s[1,1]')^2 = ('s[1,1]'-'s[2,u]')^2,
('n[2,u]'-'n[1,1]')^2 = ('n[1,1]'-'n[2,u]')^2,
('s[3,u]'-'s[2,1]')^2 = ('s[2,1]'-'s[3,u]')^2,
('n[3,u]'-'n[2,1]')^2 = ('n[2,1]'-'n[3,u]')^2:
```

Some useful substitutions for intermediate steps when calculating the *delta_l* due to gravity (and thus tensions):

```
> delta_gs0 :=
seq(delta[g1.ii]=0,ii=1..'# of wires,u'):
if (NumPen>1) then
delta_gs0 := delta_gs0, seq(delta[g2.ii]=0,ii=1..'# of wires,m'):
if (NumPen>2) then
delta_gs0 := delta_gs0, seq(delta[g3.ii]=0,ii=1..'# of wires,l'):
fi:
fi:
```

```
> lgsEQl0s :=
seq(lg[1,ii]=l0[1,ii],ii=1..'# of wires,u'):
if (NumPen>1) then
lgsEQl0s := lgsEQl0s, seq(lg[2,ii]=l0[2,ii],ii=1..'# of wires,m'):
if (NumPen>2) then
lgsEQl0s := lgsEQl0s, seq(lg[3,ii]=l0[3,ii],ii=1..'# of wires,l'):
fi:
fi:
```

To replace the initial variables with their equilibrium positions:

```
> allDOFq0 := seq(op([x.ii=x.ii.0,y.ii=y.ii.0,z.ii=z.ii.0,
theta.ii=theta.ii.0,phi.ii=phi.ii.0,psi.ii=psi.ii.0]),
ii=1..NumPen),
seq('yc[u,'.ii.']'='yc[u,'.ii.']0',ii=1..NumCanU),
seq('yc[l,'.ii.']'='yc[l,'.ii.']0',ii=1..NumCanM);
```

$$allDOFq0 := x1\tilde{} = x10,\ y1\tilde{} = y10\tilde{},\ z1\tilde{} = z10,\ \theta 1\tilde{} = \theta 10,\ \phi 1\tilde{} = \phi 10,\ \psi 1\tilde{} = \psi 10$$

To use the dynamic variables while solving for the equilibrium condition:

```
> allq0eq0 :=
seq(op([x.ii.0=0,y.ii.0=0,z.ii.0=0,
theta.ii.0=0,phi.ii.0=0,psi.ii.0=0]),ii=1..NumPen),
seq(`yc[u,`.ii.`]0`=0,ii=1..NumCanU),
seq(`yc[l,`.ii.`]0`=0,ii=1..NumCanM);
```

$$allq0eq0 := x10 = 0,\ y10\tilde{} = 0,\ z10 = 0,\ \theta 10 = 0,\ \phi 10 = 0,\ \psi 10 = 0$$

A.5 Lagrangian

L = Kinetic Energy - Potential Energy

A.5.1 Kinetic Energy

6 DOF for a single stage pendulum:

```
> KE[1] := 1/2*(`mass[1]`*dot.y1^2) +
1/2*(`Iyaw[1]`*dot.phi1^2)
+ 1/2*(`mass[1]`*dot.x1^2) + 1/2*(`Ipitch[1]`*dot.theta1^2)
+ 1/2*(`mass[1]`*dot.z1^2) + 1/2*(`Iroll[1]`*dot.psi1^2);
```

$$KE_1 := \frac{1}{2} mass[1]\, doty1\tilde{}^2 + \frac{1}{2} Iyaw[1]\, dotphi1\tilde{}^2 + \frac{1}{2} mass[1]\, dotx1\tilde{}^2 + \frac{1}{2} Ipitch[1]\, dottheta1\tilde{}^2 + \frac{1}{2} mass[1]\, dotz1\tilde{}^2 + \frac{1}{2} Iroll[1]\, dotpsi1\tilde{}^2$$

And the second and third stages:

```
> if (NumPen>1) then
KE[2] := 1/2*(`mass[2]`*dot.y2^2) + 1/2*(`Iyaw[2]`*dot.phi2^2)
+ 1/2*(`mass[2]`*dot.x2^2) + 1/2*(`Ipitch[2]`*dot.theta2^2)
+ 1/2*(`mass[2]`*dot.z2^2) + 1/2*(`Iroll[2]`*dot.psi2^2):
if (NumPen>2) then
KE[3] := 1/2*(`mass[3]`*dot.y3^2) + 1/2*(`Iyaw[3]`*dot.phi3^2)
+ 1/2*(`mass[3]`*dot.x3^2) + 1/2*(`Ipitch[3]`*dot.theta3^2)
+ 1/2*(`mass[3]`*dot.z3^2) + 1/2*(`Iroll[3]`*dot.psi3^2):
fi:
fi:
```

```
> KE := sum('KE[j]','j'=1..NumPen):
```

Kinetic energy of the cantilevers (translational):

```
> KE := KE +
add(1/2*mass_canU*(dotXCanU.ii)^2,ii=1..NumCanU)+
add(1/2*mass_canM*dotXCanM.ii^2,ii=1..NumCanM):
```

Rotational:

```
> KE := KE +
add(1/2*IcanU*(dotThCanU.ii)^2,ii=1..NumCanU)+
add(1/2*IcanM*dotThCanM.ii^2,ii=1..NumCanM);
```

$$KE := \frac{1}{2}\,mass[1]\,doty1^{\sim 2} + \frac{1}{2}\,Iyaw[1]\,dotphi1^{\sim 2} + \frac{1}{2}\,mass[1]\,dotx1^{\sim 2} + \frac{1}{2}\,Ipitch[1]\,dottheta1^{\sim 2} + \frac{1}{2}\,mass[1]\,dotz1^{\sim 2} + \frac{1}{2}\,Iroll[1]\,dotpsi1^{\sim 2}$$

A.5.2 Potential Energy

First used to determine the equilibrium positions of the suspension.

Gravitation potential.

Stretching of wires.

Twisting of wires.

Bending of wires.

Cantilevers.

Potential Energy from gravity.

```
> PEgravity := sum(''mass['.j.']'*g*(y.j)','j'=1..NumPen);
```

$$PEgravity := mass[1]\,g\,y1^{\sim}$$

Potential Energy for extension of 4 wires.

Wires are symmetric and the wires opposite each other (1&2, 3&4) experience the same extension/compression for y and phi motions.

Wire pairs front and back (1&3, 2&4) experience same extension/compression for x and theta motions, and etc.

In the initial calculation of the equilibrium position, we end up solving for the (DC) tension, so we need two forms of the stretching energy.

```
> PE[stretching,1] :=
seq(1/2*ks1*delta[l1.j]^2,j=1..'# of wires,u');
PE[stretching_eq,1] :=
subs(delta=delta_eq,add(ii,ii={PE[stretching,1]}));
```

$$PE_{stretching,1} := \frac{1}{2} ks1\ \delta_{l11}{}^2, \frac{1}{2} ks1\ \delta_{l12}{}^2, \frac{1}{2} ks1\ \delta_{l13}{}^2, \frac{1}{2} ks1\ \delta_{l14}{}^2$$

$$PE_{stretching\_eq,1} := \frac{1}{2} ks1\ delta\_eq_{l11}{}^2 + \frac{1}{2} ks1\ delta\_eq_{l12}{}^2 + \frac{1}{2} ks1\ delta\_eq_{l13}{}^2 + \frac{1}{2} ks1\ delta\_eq_{l14}{}^2$$

```
> if (NumPen>1) then
PE[stretching,2] := seq(1/2*ks2*delta[l2.j]^2
# *'if'(j=1,1.3,1)
# For a variation in the spring constant of one wire
# use a line something like this
,j=1..'# of wires,m'):
PE[stretching_eq,2] :=
subs(delta=delta_eq,add(ii,ii={PE[stretching,2]}));
if (NumPen>2) then
PE[stretching,3] := seq(1/2*ks3*delta[l3.j]^2,
j=1..'# of wires,l'):
PE[stretching_eq,3] :=
subs(delta=delta_eq,add(ii,ii={PE[stretching,3]})); fi:
fi:
```

```
> PEstretching :=
seq(PE[stretching,k],k=1..NumPen);
PEstretching_eq := sum('PE[stretching_eq,k]','k'=1..NumPen):
```

$$PEstretching := \frac{1}{2} ks1\ \delta_{l11}{}^2, \frac{1}{2} ks1\ \delta_{l12}{}^2, \frac{1}{2} ks1\ \delta_{l13}{}^2, \frac{1}{2} ks1\ \delta_{l14}{}^2$$

Potential Energy for twisting of wires.

```
> PEtwisting :=
1/2*'# of wires, u'*(k[t1]*phi1^2) +
```

```
sum('1/2*'if'(j=2,'# of wires,m','# of wires,1')*
(k[t.j]*(phi.j-phi.(j-1))^2)','j'=2..NumPen);
```

$$PEtwisting := 2\,k_{t1}\,\phi 1^{\sim 2}$$

Potential Energy from cantilevers

```
> PEcant[u] := sum('1/2*k[cant,u]*'yc[u,'.j.']'^2
# *'if'(j=1,1.1,1)'
# For a variation in the spring constant of one cantilever
# use a line something like this
','j'=1..NumCanU);
```

$$PEcant_u := 0$$

```
> PEcant[m] :=
sum('1/2*k[cant,1]*'yc[1,'.j.']'^2','j'=1..NumCanM);
```

$$PEcant_m := 0$$

```
> PEcantilevers := PEcant[u] +
'if'(NumPen>1,PEcant[m],0):
```

Potential Energy from bending of wires

This really serves as a place holder for the bending energy terms; these are the equations used, but as called fuctions further along.

```
> PEbending[u] :=
Sum('(1/2)*E[wire1]*int(Iwire[1]*
((diff(eta[u](zeta),zeta,zeta)^2)+
diff(chi[u](zeta),zeta,zeta)^2),zeta=0..Length[1])',
'j'=1..'# of wires,u');
```

$$PEbending_u := \sum_{j=1}^{4} \left(\frac{1}{2} E_{wire1} \int_0^{Length_1} Iwire_1 \left(\left(\frac{\partial^2}{\partial \zeta^2} \eta_u(\zeta) \right)^2 + \left(\frac{\partial^2}{\partial \zeta^2} \chi_u(\zeta) \right)^2 \right) d\zeta \right)$$

```
> PEbending[m] :=
Sum('(1/2)*E[wire2]*int(Iwire[2]*
((diff(eta[m](zeta),zeta,zeta)^2)+
```

```
diff(chi[m](zeta),zeta,zeta)^2),zeta=0..Length[2])',
'j'=1..'# of wires,m'):
```

```
> PEbending[1] :=
Sum('(1/2)*E[wire3]*int(Iwire[3]*
((diff(eta[1](zeta),zeta,zeta)^2)+
diff(chi[1](zeta),zeta,zeta)^2),zeta=0..Length[3])',
'j'=1..'# of wires,1'):
```

A Maple note: in *'PEbending[u]'*, the ' quote allows delayed evaluation. While it still allows *PEbend* to equal *PEbending[u]*, it does not substitute the definition from above, allowing us to redefine this term later.

```
> PEbend := seq('if'(ii=1,'PEbending[u]',
'if'(ii=2,'PEbending[m]','PEbending[1]')),ii=1..NumPen);
```

$$PEbend := PEbending_u$$

The potential energy of the system, specifically for the equilibrium position calculation:

```
> PE_eq := PEgravity + PEstretching_eq
+ PEtwisting
+ PEcantilevers;
#+ 'PEbend';
```

$$PE\_eq := mass[1]\, g\, y1\tilde{} + \frac{1}{2}\, ks1\ delta\_eq_{l11}{}^2 + \frac{1}{2}\, ks1\ delta\_eq_{l12}{}^2 + \frac{1}{2}\, ks1\ delta\_eq_{l13}{}^2 + \frac{1}{2}\, ks1\ delta\_eq_{l14}{}^2 + 2\, k_{t1}\, \phi 1\tilde{}^2$$

A.5.3 Wire Lengths

For convenience in stretching of wires:

```
> dist := proc (x1::vector,x2::vector)
norm(x1-x2,2);
simplify(",abs);
end;
```

$$dist := \mathbf{proc}(x1::vector,\ x2::vector)\ \mathrm{norm}(x1 - x2,\ 2)\,;\ \mathrm{simplify}(",\ \mathrm{abs})\ \mathbf{end}$$

Position of Top Connections

Matrix of locations of connections of top wires.

Co-ordinates go in as x (along beam), y (vertical), and z (transverse).

Points are numbered (looking down on system) 1 is front right, 2 is back left, 3 is front left, and 4 is back right. This allows simplest input of 2 wire systems (either one wire loop or one wire in front of the other).

```
> TopPlate := matrix('# of wires,u',3):
```

```
> row(TopPlate,1) :=
vector([x0+'s[0]',y0+'if'(NumCanU>0,'yc[u,1]'+UCantOff,0)+
's[0]'*theta0,z0+'n[0]']);
```

$$\mathrm{row}(TopPlate, 1) := [x0\tilde{} + s[0]\tilde{},\ y0\tilde{} + s[0]\tilde{}\,\theta 0\tilde{},\ z0\tilde{} + n[0]\tilde{}]$$

```
> row(TopPlate,2) := vector([x0-'s[0]',
y0+'if'(NumCanU>0,'yc[u,2]'+UCantOff,0)-'s[0]'*theta0,z0-'n[0]']);
```

$$\mathrm{row}(TopPlate, 2) := [x0\tilde{} - s[0]\tilde{},\ y0\tilde{} - s[0]\tilde{}\,\theta 0\tilde{},\ z0\tilde{} - n[0]\tilde{}]$$

```
> row(TopPlate,3) :=
vector([x0+'s[0]',y0+'if'(NumCanU>0,'yc[u,'.(2+
'if'(NumCanU>2,1,0)).']'+UCantOff,0)+'s[0]'*theta0,z0-'n[0]']);
```

$$\mathrm{row}(TopPlate, 3) := [x0\tilde{} + s[0]\tilde{},\ y0\tilde{} + s[0]\tilde{}\,\theta 0\tilde{},\ z0\tilde{} - n[0]\tilde{}]$$

```
> row(TopPlate,4) := vector([x0-'s[0]',y0+
'if'(NumCanU>0,'yc[u,'.(1+ 'if'(NumCanU>2,3,0)).']'+UCantOff,0)-
's[0]'*theta0,z0+'n[0]']);
```

$$\mathrm{row}(TopPlate, 4) := [x0\tilde{} - s[0]\tilde{},\ y0\tilde{} - s[0]\tilde{}\,\theta 0\tilde{},\ z0\tilde{} + n[0]\tilde{}]$$

Position of Top Mass

Upper Connection

```
> Mass1u := matrix('# of wires,u',3):
```

```
> row(Mass1u,1) :=
vector([`s[1,u]`*cos(phi1)*cos(theta1)-
`d[1,u]`*sin(theta1)+`n[1,u]`*sin(phi1)+x1,
-`H[1]`+`d[1,u]`*cos(theta1)*cos(psi1)+
`s[1,u]`*sin(theta1)-`n[1,u]`*sin(psi1)+y1,
`n[1,u]`*cos(phi1)*cos(psi1)+`d[1,u]`*sin(psi1)-
`s[1,u]`*sin(phi1)+z1] );
```

$$\mathrm{row}(Mass1u,\,1) := [\,s[1,u]^{\sim}\cos(\phi 1^{\sim})\cos(\theta 1^{\sim}) - d[1,u]^{\sim}\sin(\theta 1^{\sim}) + n[1,u]^{\sim}\sin(\phi 1^{\sim}) + x1^{\sim},\; -H[1]^{\sim} + d[1,u]^{\sim}\cos(\theta 1^{\sim})\cos(\psi 1^{\sim}) + s[1,u]^{\sim}\sin(\theta 1^{\sim}) - n[1,u]^{\sim}\sin(\psi 1^{\sim}) + y1^{\sim},\; n[1,u]^{\sim}\cos(\phi 1^{\sim})\cos(\psi 1^{\sim}) + d[1,u]^{\sim}\sin(\psi 1^{\sim}) - s[1,u]^{\sim}\sin(\phi 1^{\sim}) + z1^{\sim}]$$

```
> row(Mass1u,2) :=
vector([-`s[1,u]`*cos(phi1)*cos(theta1)-
`d[1,u]`*sin(theta1)-`n[1,u]`*sin(phi1)+x1,
-`H[1]`+`d[1,u]`*cos(theta1)*cos(psi1)-
`s[1,u]`*sin(theta1)+`n[1,u]`*sin(psi1)+y1,
-`n[1,u]`*cos(phi1)*cos(psi1)+`d[1,u]`*sin(psi1)+
`s[1,u]`*sin(phi1)+z1 ]):

> row(Mass1u,3) :=
vector([`s[1,u]`*cos(phi1)*cos(theta1)-`d[1,u]`*sin(theta1)-
`n[1,u]`*sin(phi1)+x1,
-`H[1]`+`d[1,u]`*cos(theta1)*cos(psi1)+`s[1,u]`*sin(theta1)+
`n[1,u]`*sin(psi1)+y1,
-`n[1,u]`*cos(phi1)*cos(psi1)+`d[1,u]`*sin(psi1)-
`s[1,u]`*sin(phi1)+z1 ]):

> row(Mass1u,4) :=
vector([-`s[1,u]`*cos(phi1)*cos(theta1)-
`d[1,u]`*sin(theta1)+`n[1,u]`*sin(phi1)+x1,
-`H[1]`+`d[1,u]`*cos(theta1)*cos(psi1)-
`s[1,u]`*sin(theta1)-`n[1,u]`*sin(psi1)+y1,
`n[1,u]`*cos(phi1)*cos(psi1)+`d[1,u]`*sin(psi1)+
`s[1,u]`*sin(phi1)+z1] ):
```

Lower Connection

Same co-ordinates as for top wire connection points, except using var[1,l] instead of var[1,u], and changing the sign of d[1] where it appears, since d[1,l] is defined positive downward whereas d[1,u] is defined positive upwards.

```
> Mass1l := matrix(4,3):

> row(Mass1l,1) :=
vector([`s[1,l]`*cos(phi1)*cos(theta1)+`n[1,l]`*sin(phi1)+x1
+(`d[1,l]`-`if`(NumCanM>0,`yc[l,1]`+MCantOff,0))*sin(theta1),
# -0.00X,
# For a Xmm misalignment in the wire attachment
# use a line like this
-`H[1]`+`s[1,l]`*sin(theta1)-`n[1,l]`*sin(psi1)+y1-
(`d[1,l]`-`if`(NumCanM>0,`yc[l,1]`+MCantOff,0))*
cos(theta1)*cos(psi1),
`n[1,l]`*cos(phi1)*cos(psi1)-`s[1,l]`*sin(phi1)+z1
-(`d[1,l]`-`if`(NumCanM>0,`yc[l,1]`+MCantOff,0))*sin(psi1)]);
```

row(*Mass1l*, 1) := [
$s[1,l]^{\sim}\cos(\phi 1^{\sim})\cos(\theta 1^{\sim}) + n[1,l]^{\sim}\sin(\phi 1^{\sim}) + x1^{\sim} + d[1,l]^{\sim}\sin(\theta 1^{\sim})$,
$-H[1]^{\sim} + s[1,l]^{\sim}\sin(\theta 1^{\sim}) - n[1,l]^{\sim}\sin(\psi 1^{\sim}) + y1^{\sim} - d[1,l]^{\sim}\cos(\theta 1^{\sim})\cos(\psi 1^{\sim})$,
$n[1,l]^{\sim}\cos(\phi 1^{\sim})\cos(\psi 1^{\sim}) - s[1,l]^{\sim}\sin(\phi 1^{\sim}) + z1^{\sim} - d[1,l]^{\sim}\sin(\psi 1^{\sim})$]

```
> row(Mass1l,2) :=
vector([-`s[1,l]`*cos(phi1)*cos(theta1)+
(`d[1,l]`-`if`(NumCanM>0,`yc[l,2]`+MCantOff,0))*sin(theta1)-
`n[1,l]`*sin(phi1)+x1,
-`H[1]`-`s[1,l]`*sin(theta1)+`n[1,l]`*sin(psi1)+y1-
(`d[1,l]`-`if`(NumCanM>0,`yc[l,2]`+MCantOff,0))
*cos(theta1)*cos(psi1),
-`n[1,l]`*cos(phi1)*cos(psi1)+`s[1,l]`*sin(phi1)+z1
-(`d[1,l]`-`if`(NumCanM>0,`yc[l,2]`+MCantOff,0))*sin(psi1)]):

> which_cantL :=
`if`(NumCanM>0,`yc[l,`.(2+`if`(NumCanM>2,1,0)).`]`+MCantOff,0):
row(Mass1l,3) :=
vector([`s[1,l]`*cos(phi1)*cos(theta1)-`n[1,l]`*sin(phi1)+x1
+(`d[1,l]`-which_cantL)*sin(theta1),
```

```
-`H[1]`+`s[1,l]`*sin(theta1)+`n[1,l]`*sin(psi1)+y1
-(`d[1,l]`-which_cantL)*cos(theta1)*cos(psi1),
-`n[1,l]`*cos(phi1)*cos(psi1)-`s[1,l]`*sin(phi1)+z1
-(`d[1,l]`-which_cantL)*sin(psi1)]):

> which_cantL := `if`(NumCanM>0,`yc[l,`.(1+
`if`(NumCanM>2,3,0) ).`]`+MCantOff,0):
row(Mass1l,4) :=
vector([-`s[1,l]`*cos(phi1)*cos(theta1)+`n[1,l]`*sin(phi1)+x1
+(`d[1,l]`-which_cantL)*sin(theta1),
-`H[1]`-`s[1,l]`*sin(theta1)-`n[1,l]`*sin(psi1)+y1
-(`d[1,l]`-which_cantL)*cos(theta1)*cos(psi1),
`n[1,l]`*cos(phi1)*cos(psi1)+`s[1,l]`*sin(phi1)+z1
-(`d[1,l]`-which_cantL)*sin(psi1)]):
```

Position of Second Mass

As per top mass, except var[2,u] instead of var[1,u], the independent variables are var2, and the vertical distance is (essentially) the sum of the top 2 masses.

Upper Connection

```
> if (NumPen>1) then

> Mass2u := matrix(4,3):

> row(Mass2u,1) :=
vector([`s[2,u]`*cos(phi2)*cos(theta2)-
`d[2,u]`*sin(theta2)+`n[2,u]`*sin(phi2)+x2,
-`H[1]`-`H[2]`+`d[2,u]`*cos(theta2)*cos(psi2)+
`s[2,u]`*sin(theta2)-`n[2,u]`*sin(psi2)+y2,
`n[2,u]`*cos(phi2)*cos(psi2)+`d[2,u]`*sin(psi2)-
`s[2,u]`*sin(phi2)+z2] ):

> row(Mass2u,2) :=
vector([-`s[2,u]`*cos(phi2)*cos(theta2)-
`d[2,u]`*sin(theta2)-`n[2,u]`*sin(phi2)+x2,
-`H[1]`-`H[2]`+`d[2,u]`*cos(theta2)*cos(psi2)-
`s[2,u]`*sin(theta2)+`n[2,u]`*sin(psi2)+y2,
-`n[2,u]`*cos(phi2)*cos(psi2)+`d[2,u]`*sin(psi2)+
`s[2,u]`*sin(phi2)+z2]):
row(Mass2u,3) :=
```

```
vector([`s[2,u]`*cos(phi2)*cos(theta2)-
`d[2,u]`*sin(theta2)-`n[2,u]`*sin(phi2)+x2,
-`H[1]`-`H[2]`+`d[2,u]`*cos(theta2)*cos(psi2)+
`s[2,u]`*sin(theta2)+`n[2,u]`*sin(psi2)+y2,
-`n[2,u]`*cos(phi2)*cos(psi2)+
`d[2,u]`*sin(psi2)-`s[2,u]`*sin(phi2)+z2 ]):

> row(Mass2u,4) :=
vector([-`s[2,u]`*cos(phi2)*cos(theta2)-
`d[2,u]`*sin(theta2)+`n[2,u]`*sin(phi2)+x2,
-`H[1]`-`H[2]`+`d[2,u]`*cos(theta2)*cos(psi2)-
`s[2,u]`*sin(theta2)-`n[2,u]`*sin(psi2)+y2,
`n[2,u]`*cos(phi2)*cos(psi2)+`d[2,u]`*sin(psi2)+
`s[2,u]`*sin(phi2)+z2]):
fi:
```

Lower Connection

```
> if (NumPen>2) then Mass2l := matrix(4,3):

> row(Mass2l,1) :=
vector([`s[2,l]`*cos(phi2)*cos(theta2)+
`d[2,l]`*sin(theta2)+`n[2,l]`*sin(phi2)+x2,
-`H[1]`-`H[2]`-`d[2,l]`*cos(theta2)*cos(psi2)+
`s[2,l]`*sin(theta2)-`n[2,l]`*sin(psi2)+y2,
`n[2,l]`*cos(phi2)*cos(psi2)-
`d[2,l]`*sin(psi2)-`s[2,l]`*sin(phi2)+z2]):
row(Mass2l,2) :=
vector([-`s[2,l]`*cos(phi2)*cos(theta2)+
`d[2,l]`*sin(theta2)-`n[2,l]`*sin(phi2)+x2,
-`H[1]`-`H[2]`-`d[2,l]`*cos(theta2)*cos(psi2)-
`s[2,l]`*sin(theta2)+`n[2,l]`*sin(psi2)+y2,
-`n[2,l]`*cos(phi2)*cos(psi2)-`d[2,l]`*sin(psi2)+
`s[2,l]`*sin(phi2)+z2 ]):

> row(Mass2l,3) :=
vector([`s[2,l]`*cos(phi2)*cos(theta2)+
`d[2,l]`*sin(theta2)-`n[2,l]`*sin(phi2)+x2,
-`H[1]`-`H[2]`-`d[2,l]`*cos(theta2)*cos(psi2)+
`s[2,l]`*sin(theta2)+`n[2,l]`*sin(psi2)+y2,
-`n[2,l]`*cos(phi2)*cos(psi2)-`d[2,l]`*sin(psi2)-
```

```
's[2,1]'*sin(phi2)+z2 ]):

> row(Mass2l,4) :=
vector([-'s[2,1]'*cos(phi2)*cos(theta2)+
'd[2,1]'*sin(theta2)+'n[2,1]'*sin(phi2)+x2,
-'H[1]'-'H[2]'-'d[2,1]'*cos(theta2)*cos(psi2)-
's[2,1]'*sin(theta2)-'n[2,1]'*sin(psi2)+y2,
'n[2,1]'*cos(phi2)*cos(psi2)-'d[2,1]'*sin(psi2)+
's[2,1]'*sin(phi2)+z2]):
fi:
```

Position of Test Mass

Again, as before except with var[3] and vertical distance is the total distance.

Upper Connection

```
> if (NumPen>2) then Mass3u := matrix(4,3):

> row(Mass3u,1) :=
vector(['s[3,u]'*cos(phi3)*cos(theta3)-
'd[3,u]'*sin(theta3)+'n[3,u]'*sin(phi3)+x3,
-'H[1]'-'H[2]'-'H[3]'+'d[3,u]'*cos(theta3)*cos(psi3)+
's[3,u]'*sin(theta3)-'n[3,u]'*sin(psi3)+y3,
'n[3,u]'*cos(phi3)*cos(psi3)+'d[3,u]'*sin(psi3)-
's[3,u]'*sin(phi3)+z3] ):

> row(Mass3u,2) :=
vector([-'s[3,u]'*cos(phi3)*cos(theta3)-
'd[3,u]'*sin(theta3)-'n[3,u]'*sin(phi3)+x3,
-'H[1]'-'H[2]'-'H[3]'+'d[3,u]'*cos(theta3)*cos(psi3)-
's[3,u]'*sin(theta3)+'n[3,u]'*sin(psi3)+y3,
-'n[3,u]'*cos(phi3)*cos(psi3)+'d[3,u]'*sin(psi3)+
's[3,u]'*sin(phi3)+z3 ]):

> row(Mass3u,3) :=
vector(['s[3,u]'*cos(phi3)*cos(theta3)-'d[3,u]'*sin(theta3)-
'n[3,u]'*sin(phi3)+x3,
-'H[1]'-'H[2]'-'H[3]'+'d[3,u]'*cos(theta3)*cos(psi3)+
's[3,u]'*sin(theta3)+'n[3,u]'*sin(psi3)+y3,
-'n[3,u]'*cos(phi3)*cos(psi3)+'d[3,u]'*sin(psi3)-
's[3,u]'*sin(phi3)+z3]):
```

```
> row(Mass3u,4) :=
vector([-`s[3,u]`*cos(phi3)*cos(theta3)-`d[3,u]`*sin(theta3)+
`n[3,u]`*sin(phi3)+x3,
-`H[1]`-`H[2]`-`H[3]`+`d[3,u]`*cos(theta3)*cos(psi3)-
`s[3,u]`*sin(theta3)-`n[3,u]`*sin(psi3)+y3,
`n[3,u]`*cos(phi3)*cos(psi3)+`d[3,u]`*sin(psi3)+
`s[3,u]`*sin(phi3)+z3]):
fi:
```

Extension of Wires

Extension of Upper Wires

Initial length for each of the 4 wires.

```
> lgeom[1,1] := dist(row(TopPlate,1),row(Mass1u,1));
```

$$lgeom_{1,1} := ($$
$$(x0\tilde{} + s[0]\tilde{} - s[1,u]\tilde{}\cos(\phi 1\tilde{})\cos(\theta 1\tilde{}) + d[1,u]\tilde{}\sin(\theta 1\tilde{}) - n[1,u]\tilde{}\sin(\phi 1\tilde{})$$
$$- x1\tilde{})^2 + (y0\tilde{} + s[0]\tilde{}\,\theta 0\tilde{} + H[1]\tilde{} - d[1,u]\tilde{}\cos(\theta 1\tilde{})\cos(\psi 1\tilde{})$$
$$- s[1,u]\tilde{}\sin(\theta 1\tilde{}) + n[1,u]\tilde{}\sin(\psi 1\tilde{}) - y1\tilde{})^2 + (z0\tilde{} + n[0]\tilde{}$$
$$- n[1,u]\tilde{}\cos(\phi 1\tilde{})\cos(\psi 1\tilde{}) - d[1,u]\tilde{}\sin(\psi 1\tilde{}) + s[1,u]\tilde{}\sin(\phi 1\tilde{}) - z1\tilde{})^2)^{1/2}$$

```
> l0[1,1] :=
subs(allDOF0,CantOffs0,lgeom[1,1]):l0[1,1] :=
simplify(l0[1,1],geom);
```

$$l0_{1,1} := \sqrt{(s[0]\tilde{} - s[1,u]\tilde{})^2 + (H[1]\tilde{} - d[1,u]\tilde{})^2 + (n[0]\tilde{} - n[1,u]\tilde{})^2}$$

**********This is the big change in 6.7********** The shape of the wire, which is determined by the bending terms, gives the correct length of the wire, and thus the amount the wire stretches. This is the function–it looks an awful lot like the function for calculating the bending energy stored in the wire.

It uses the geometrical distance calculated above as the 'straight' length of the wire. Then integrates along this length, using as boundary conditions 0 displacement at each end and angles of wires relative to the 'straight' wire.

This should use int(sqrt(1 + (dx/du)^2 + (dz/du)^2))–by integrating along the 'straight' wire can use int(1 + 1/2*(dx/du)^2 + 1/2*(dz/du)^2)

```
> lenwire := proc (j,w)
local eta,chi,first_theta,first_psi,which1,which2,wire_shapex,
wire_shapez,answx,answz,DetaDzeta,DchiDzeta,bcs,lentemp,
len1,len2;
eta := proc (zeta,w)
a*exp(kappa*zeta) + b*exp(-kappa*zeta) + c*zeta + d:
end:
chi := proc (zeta,w)
e*exp(kappa*zeta) + f*exp(-kappa*zeta) + g*zeta + h:
end:
if (w=1) then
first_theta := theta0;
first_psi := 0;
which1 := `TopPlate`;
which2 := `Mass1u`;
else
first_theta := theta.(`w`-1);
first_psi := psi.(`w`-1);
if (w=2) then
which1 := `Mass1l`;
which2 := `Mass2u`;
else
which1 := `Mass2l`;
which2 := `Mass3u`;
fi;
fi;
bcs := DetaDzeta = (row(which2,j)[1]-row(which1,j)[1]) /
(row(which2,j)[2]-row(which1,j)[2]),
DchiDzeta = (row(which2,j)[3]-row(which1,j)[3]) /
(row(which2,j)[2]-row(which1,j)[2]);
wire_shapex := {eta(0,w) = 0,
subs(zeta=0,diff(eta(zeta,w),zeta))= -DetaDzeta - first_theta,
eta(lentemp,w) = 0,
subs(zeta=lentemp,diff(eta(zeta,w),zeta)) =
-DetaDzeta - theta.`w`};
wire_shapez := {chi(0,w) = 0,
subs(zeta=0,diff(chi(zeta,w),zeta))= -DchiDzeta + first_psi,
chi(lentemp,w) = 0,
subs(zeta=lentemp,diff(chi(zeta,w),zeta)) =
```

```
-DchiDzeta + psi.`w`};
answx := solve(wire_shapex,{a,b,c,d});
answz := solve(wire_shapez,{e,f,g,h});
len1 := expand(1+ (1/2) *( diff(eta(zeta,w),zeta) )^2 +
(1/2) *(diff(chi(zeta,w),zeta) )^2);
len2 := int(len1,zeta=0..lentemp );
len2 := subs(answx,answz,len2);
len2 := subs(bcs,lentemp=lgeom[w,j],len2);
RETURN( subs(kappa=sqrt(Ten[w,j]/(E[wire.w]*Iwire[w])),len2) ):
end;
```

```
lenwire := proc(j, w)
    local η, χ, first_theta, first_psi, which1, which2, wire_shapex, wire_shapez,
     answx, answz, DetaDzeta, DchiDzeta, bcs, lentemp, len1, len2;
       η := proc(ζ, w) aexp(κζ) + bexp(−κζ) + cζ + d end;
       χ := proc(ζ, w) eexp(κζ) + fexp(−κζ) + gζ + h end;
       if w = 1 then first_theta := θ0; first_psi := 0; which1 := TopPlate;
    which2 := Mass1u
       else
          first_theta := θ.(w − 1);
          first_psi := ψ.(w − 1);
          if w = 2 then which1 := Mass1l; which2 := Mass2u
          else which1 := Mass2l; which2 := Mass3u
          fi
       fi;
       bcs := DetaDzeta =
          (row(which2, j)1 − row(which1, j)1) /(row(which2, j)2
          − row(which1, j)2),
          DchiDzeta =
          (row(which2, j)3 − row(which1, j)3) /(row(which2, j)2
          − row(which1, j)2);
       wire_shapex := {η(0, w) = 0, subs(ζ = 0,
          diff(η(ζ, w), ζ)) = −DetaDzeta − first_theta, η(lentemp, w) = 0,
          subs(ζ = lentemp, diff(η(ζ, w), ζ)) = −DetaDzeta − θ.w};
       wire_shapez := {χ(0, w) = 0, subs(ζ = 0,
          diff(χ(ζ, w), ζ)) = −DchiDzeta + first_psi, χ(lentemp, w) = 0,
          subs(ζ = lentemp, diff(χ(ζ, w), ζ)) = −DchiDzeta + ψ.w};
       answx := solve(wire_shapex, {b, a, d, c});
       answz := solve(wire_shapez, {f, e, g, h});
       len1 := expand(1 + 1/2diff(η(ζ, w), ζ)^2 + 1/2diff(χ(ζ, w), ζ)^2);
       len2 := int(len1, ζ = 0..lentemp);
       len2 := subs(answx, answz, len2);
       len2 := subs(bcs, lentemp = lgeom_{w,j}, len2);
       RETURN(subs(κ = sqrt(Ten_{w,j} /(E_{wire.w} Iwire_w)), len2))
    end
```

```
> l[1,1] := lenwire(1,1):
```

Wire 1 is the forward right wire (from above). The length is to be defined as L(vars) - L(0) = [L(vars) - L(equilibrium)] + [L(equilibrium) - L(0)]. The equilibrium position corresponds to 'Tension'–the term that represents the stored energy in the gravitational field, it does not have an associated loss.

```
> delta[l11] := l[1,1] - lg[1,1] + delta[g11]:
delta_eq[l11] :=
subs(Ten[1,1]=ks1*(lgeom[1,1]-l0[1,1]),delta_gs0,
lgsEQl0s,delta[l11]):

> for ii from 2 to `# of wires,u` do
lgeom[1,ii] := dist(row(TopPlate,ii),row(Mass1u,ii)):
l0[1,ii] :=
subs(allDOF0,CantOffs0,lgeom[1,ii]):l0[1,ii]:=
simplify(l0[1,ii],geom)+
`if`(ii=4,0.0005,0):
l[1,ii] := lenwire(ii,1):
delta[l1.ii] := l[1,ii] - lg[1,ii] + delta[g1.ii]:
delta_eq[l1.ii] :=
subs(Ten[1,ii]=ks1*(lgeom[1,ii]-l0[1,ii]),delta_gs0,
lgsEQl0s,delta[l1.ii]):
od:
```

Extension of Middle Wires

Initial length for each of the 4 wires.

```
> if (NumPen>1) then
for ii from 1 to `# of wires,m` do
lgeom[2,ii] := dist(row(Mass1l,ii),row(Mass2u,ii)):
l0[2,ii] :=
subs(allDOF0,CantOffs0,lgeom[2,ii]):l0[2,ii]:=
simplify(l0[2,ii],geom):
l[2,ii] := lenwire(ii,2):
delta[l2.ii] := l[2,ii] - lg[2,ii] + delta[g2.ii]:
delta_eq[l2.ii] :=
subs(Ten[2,ii]=ks2*(lgeom[2,ii]-l0[2,ii]),delta_gs0,
lgsEQl0s,delta[l2.ii]):
```

```
od:
fi:
```

Extension of Lower Wires

Initial length for each of the 4 wires.

```
> if (NumPen>2) then
for ii from 1 to '# of wires,l' do
lgeom[3,ii] := dist(row(Mass2l,ii),row(Mass3u,ii)):
l0[3,ii] :=
subs(allDOF0,CantOffs0,lgeom[3,ii]):l0[3,ii]:=
simplify(l0[3,ii],geom):
l[3,ii] := lenwire(ii,3):
delta[l3.ii] := l[3,ii] - lg[3,ii] + delta[g3.ii]:
delta_eq[l3.ii] :=
subs(Ten[3,ii]=ks3*(lgeom[3,ii]-l0[3,ii]),delta_gs0,
lgsEQl0s,delta[l3.  ii]):
od:
fi:
```

A.5.4 Bending of Wires

This function calculates the potential energy for one wire. j indicates the # of the wire, 'w' indicates 'which' (1=upper, etc.).

```
> bendwire := proc (j,w)
local eta,chi,first_theta,first_psi,which1,which2,
wire_shapex,wire_shapez,answx,answz,lentemp;
eta := proc (zeta,w)
a*exp(kappa*zeta) + b*exp(-kappa*zeta) + c*zeta + d:
end:
chi := proc (zeta,w)
e*exp(kappa*zeta) + f*exp(-kappa*zeta) + g*zeta + h:
end:
if (w=1) then
first_theta := theta0;
first_psi := 0;
which1 := 'TopPlate';
which2 := 'Mass1u';
```

```
else
first_theta := theta.(`w`-1);
first_psi := psi.(`w`-1);
if (w=2) then
which1 := `Mass1l`;
which2 := `Mass2u`;
else
which1 := `Mass2l`;
which2 := `Mass3u`;
fi;
fi;
wire_shapex := {eta(0,w) = row(which1,j)[1],
subs(zeta=0,diff(eta(zeta,w),zeta))= first_theta,
eta(lentemp,w) = row(which2,j)[1],
subs(zeta=lentemp,diff(eta(zeta,w),zeta)) = theta.`w`};
wire_shapez := {chi(0,w) = row(which1,j)[3],
subs(zeta=0,diff(chi(zeta,w),zeta))= first_psi,
chi(lentemp,w) = row(which2,j)[3],
subs(zeta=lentemp,diff(chi(zeta,w),zeta)) = psi.`w`};
answx := solve(wire_shapex,{a,b,c,d});
answz := solve(wire_shapez,{e,f,g,h});
(1/2)*E[wire.`w`]*int(Iwire[w]*
((diff(eta(zeta,w),zeta,zeta))^2 +
(diff(chi(zeta,w),zeta,zeta))^2),
zeta=0..lentemp);
subs(answx,answz,lentemp=(row(which1,j)[2]-row(which2,j)[2]),"):
RETURN(subs(kappa=sqrt(Ten[w,j]/(E[wire.`w`]*Iwire[w])),")):
end;
```

bendwire := **proc**(j, w)
localη, χ, *first_theta*, *first_psi*, *which1*, *which2*, *wire_shapex*, *wire_shapez*, *answx*, *answz*, *lentemp*;
η := **proc**(ζ, w) $a\exp(\kappa\zeta) + b\exp(-\kappa\zeta) + c\zeta + d$ **end**;
χ := **proc**(ζ, w) $e\exp(\kappa\zeta) + f\exp(-\kappa\zeta) + g\zeta + h$ **end**;
if $w = 1$ **then** *first_theta* := $\theta 0$; *first_psi* := 0; *which1* := *TopPlate*;
which2 := *Mass1u*
else
first_theta := $\theta.(w-1)$;
first_psi := $\psi.(w-1)$;
if $w = 2$ **then** *which1* := *Mass1l*; *which2* := *Mass2u*
else *which1* := *Mass2l*; *which2* := *Mass3u*
fi
fi;
wire_shapex := {$\eta(0, w) = \mathrm{row}(which1, j)_1$, subs($\zeta = 0$,
diff($\eta(\zeta, w), \zeta$)) = *first_theta*, η(*lentemp*, w) = row(*which2*, j)$_1$,
subs(ζ = *lentemp*, diff($\eta(\zeta, w), \zeta$)) = $\theta.w$};
wire_shapez := {$\chi(0, w) = \mathrm{row}(which1, j)_3$, subs($\zeta = 0$,
diff($\chi(\zeta, w), \zeta$)) = *first_psi*, χ(*lentemp*, w) = row(*which2*, j)$_3$,
subs(ζ = *lentemp*, diff($\chi(\zeta, w), \zeta$)) = $\psi.w$};
answx := solve(*wire_shapex*, {b, a, d, c});
answz := solve(*wire_shapez*, {f, e, g, h});
1/2
$E_{wire.w}$int($Iwire_w$(diff($\eta(\zeta, w), \zeta, \zeta)^2$ + diff($\chi(\zeta, w), \zeta, \zeta)^2$),
$\zeta = 0..lentemp$);
subs(*answx*, *answz*, *lentemp* = row(*which1*, j)$_2$ − row(*which2*, j)$_2$, "");
RETURN(subs(κ = sqrt($Ten_{w,j}$ /($E_{wire.w} Iwire_w$)), ""))
end

Bending of Upper Wires

```
> PEbending[u] :=
sum('bendwire(j,1)','j'=1..'# of wires,u'):
```

Bending of Middle Wires

```
> if (NumPen>1) then
PEbending[m] := sum('bendwire(j,2)','j'=1..'# of wires,m'): fi:
```

Bending of Lower Wires

```
> if (NumPen>2) then
PEbending[1] := sum('bendwire(j,3)','j'=1..'# of wires,1'): fi:
```

```
> PEbend:
```

```
> PE_eq:
```

A.6 Offsets

Offsets to give steady state condition, where stretching of wires and bending of cantilevers counters the gravitational potential. Minimizes potential energy with respect to y1,y2,y3, and the yc's. Then, for non-symmetric cases, iterates to find the potential mininum for x's, z's, etc. These become the offsets which we expand about in the differential equations. We can then also expand the yc's in terms of the other variables, to remove them as independent variables.

A.6.1 Gravitational Offset (Tension)

```
> solve_varsY := {seq(y.j,j=1..NumPen),
seq('yc[u,1]',j=1..NumCanU),seq('yc[1,1]',j=1..NumCanM)};
```

$$solve\_varsY := \{y1\tilde{}\}$$

```
> vert_only := x0=0,y0=0,z0=0,theta0=0,
x1=0,x2=0,x3=0,z1=0,z2=0,z3=0,
theta1=0,theta2=0,theta3=0,
phi1=0,phi2=0,phi3=0,psi1=0,psi2=0,psi3=0:
```

```
> solve_vars :=
[seq(x.j,j=1..NumPen),seq(y.j,j=1..NumPen),seq(z.j,j=1..NumPen),
seq(theta.j,j=1..NumPen),seq(phi.j,j=1..NumPen),
seq(psi.j,j=1..NumPen),
seq('yc[u,'.j.']',j=1..NumCanU),seq('yc[1,'.j.']',j=1..NumCanM)];
```

$$solve\_vars := [x1\tilde{}, y1\tilde{}, z1\tilde{}, \theta 1\tilde{}, \phi 1\tilde{}, \psi 1\tilde{}]$$

```
> PE_eq := evalf(subs(vars,CantOffs,loss0,PE_eq)):
> PE_eq := subs(inputs0,PE_eq):
> PE_eqY := subs(vert_only,PE_eq):
> PE_eqY :=
subs(seq(`yc[u,`.jj.`]`=`yc[u,1]`,jj=2..NumCanU),
seq(`yc[1,`.jj.`]`=`yc[1,1]`,jj=2..NumCanM), PE_eqY):
> gravity_eqsY := {seq( diff(PE_eqY,jj), jj=solve_varsY )}:
```

Sometimes it seems to need this, sometimes it doesn't.

```
> #gravity_eqsY := simplify(gravity_eqsY):
```

NOTE: Solving for the proper offsets is very dependent on giving the correct range. Otherwise, the program will find non-physical solutions [primarily involving using sqrt(L^2) = -L]. The easiest way to check for this is to see, for example, that all the cantilever offsets are approximately equal.

```
> offset_values := fsolve(gravity_eqsY, solve_varsY,
{ y1=-0.2..0,y2=-0.2..-0.0,y3=-0.2..0,`yc[u,1]`=-0.2..0 });
```

$$offset\_values := \{y1\tilde{} = -.0006849139904000000004\}$$

Often most memory efficient to solve for the equilibrium position (to this point) and save the equilibrium position, then restart and state this equilibrium with solving (i.e., comment out the *fsolve* line).

```
> #offset_values := {y2 = -.6779872077364094171077955989 58e-3,
y3 = -.1058881078756817580373101721 40e-2,
y1= #-.4953853874673927195196694397 66e-3,
`yc[1,1]` = -.5519018821795889862131518003 46e-1,
`yc[u,1]` = -.1120172902098607077494315552 29};
> offset_values := {op(offset_values),
seq(`yc[u,`.jj.`]`=subs(offset_values,`yc[u,1]`),jj=2..NumCanU),
seq(`yc[1,`.jj.`]`=subs(offset_values,`yc[1,1]`),jj=2..NumCanM)}:
> offset_values := {op(offset_values),
seq(x.j=0,j=1..NumPen),seq(z.j=0,j=1..NumPen),
```

```
seq(phi.j=0,j=1..NumPen),seq(theta.j=0,j=1..NumPen),
seq(psi.j=0,j=1..NumPen)}:

> if (Symmetric=0) then
`deltaPE%` := 1;
offset_values1 := offset_values:
PENum0 := fnormal(evalf(subs(offset_values,PE_eq)),15);
PENum1 := PENum0:
# while (`deltaPE%`>(5e-16)) do
# For most cases, one iteration is sufficient
# and it is MUCH faster
offset_values := offset_values1;
PENum0 := PENum1;
PE_MT2 := mtaylor(PE_eq,[op(offset_values)],3):
PE_MT2 := expand(collect(PE_MT2,[x1,x2,x3,y1,y2,y3,z1,z2,z3,
theta1,theta2,theta3,phi1,phi2,phi3,psi1,psi2,psi3,
`yc[u,1]`,`yc[u,2]`,`yc[u,3]`,`yc[u,4]`,
`yc[l,1]`,`yc[l,2]`,`yc[l,3]`,`yc[l,4]`])):
Qtest := array(1..nops(solve_vars),1..nops(solve_vars)):
for ii from 1 to nops(solve_vars) do
for jj from 1 to nops(solve_vars) do
Qtest[ii,jj] := fnormal(op(1,
select(has,PE_MT2,
op(ii,solve_vars)*op(jj,solve_vars))))/(`if`(ii=jj,1,2)):
od:
od:
Vtest := array(1..nops(solve_vars)):
for ii from 1 to nops(solve_vars) do
Vtest[ii] := subs(allDOF0,coeff(PE_MT2,op(ii,solve_vars))):
od:
Qtestinv := inverse(Qtest):
offset_valuesTEMP := evalm(-Qtestinv &* Vtest/2):
offset_values1 := fnormal(
{ seq( (op(jj,solve_vars) =
offset_valuesTEMP[jj]),jj=1..nops(solve_vars))} );
PENum1 := evalf(subs(offset_values1,PE_eq));
`deltaPE%` := (PENum0-PENum1)/abs(PENum0)*100:
print(`deltaPE%`);
# od:  # The iterations, when necessary
offset_values := offset_values1; # COMMENT OUT IF ITERATING
```

```
fi:
```

5.0845242228311064243

```
> tensions_temp :=
seq(Ten[1,ii]=evalf(subs(inputs0,vars,loss0,offset_values,
CantOffs,ks1*delta_eq[l1.ii])),ii=1..'# of wires,u'):
if (NumPen>1) then
tensions_temp := tensions_temp,
seq(Ten[2,ii]=evalf(subs(inputs0,vars,loss0,offset_values,
CantOffs,ks2*delta_eq[l2.ii])),ii=1..'# of wires,m');
if (NumPen>2) then
tensions_temp := tensions_temp,
seq(Ten[3,ii]=evalf(subs(inputs0,vars,loss0,offset_values,
CantOffs,ks3*delta_eq[l3.ii])),ii=1..'# of wires,l');
fi:
fi:
```

lg is the length of the wire in the equilibrium position; *delta[g]* is the change in the length of wire from the starting position to the equilibrium position. Using this equilibrium position to calculate tensions:

```
> lgEq :=
seq(lg[1,ii]=simplify(evalf(subs(offset_values,inputs0,vars,
CantOffs,loss0,tensions_temp,l[1,ii]))),ii=1..'# of wires,u'):
delta_gs := seq(delta[g1.ii]= subs(vars,lgEq,lg[1,ii]-l0[1,ii]),
ii=1..'# of wires,u'):
tensions := seq(Ten[1,ii]=
evalf(subs(vars,loss0,delta_gs,ks1*delta[g1.ii])),ii=1..
'# of wires,u'):
if (NumPen>1) then
lgEq := lgEq,
seq(lg[2,ii]=simplify(evalf(subs(offset_values,inputs0,vars,
CantOffs,loss0,tensions_temp,l[2,ii]))),
ii=1..'# of wires,m'):
delta_gs := delta_gs, seq(delta[g2.ii]=
subs(vars,lgEq,lg[2,ii]-l0[2,ii]), ii=1..'# of wires,m'):
tensions := tensions, seq(Ten[2,ii]=
evalf(subs(vars,loss0,delta_gs,ks2*delta[g2.ii])),ii=1..
'# of wires,m'):
```

```
if (NumPen>2) then
lgEq := lgEq,
seq(lg[3,ii]=simplify(evalf(subs(offset_values,inputs0,vars,
CantOffs,loss0,tensions_temp,l[3,ii]))),
ii=1..'# of wires,l'):
delta_gs := delta_gs, seq(delta[g3.ii]=
subs(vars,lgEq,lg[3,ii]-l0[3,ii]), ii=1..'# of wires,l'):
tensions := tensions, seq(Ten[3,ii]=
evalf(subs(vars,loss0,delta_gs,ks3*delta[g3.ii])),ii=1..
'# of wires,l'):
fi:
fi:
```

Replacing the dynamic *q[i]* with their equilibrium *q[i]0*:

```
> offset_values := subs( allDOFq0,offset_values);
```

$$offset\_values := \{x10 = .0007488428247477619626 5,$$
$$y10^{\sim} = -.0006849139904000450685 0, z10 = -.0001171684016270730332 9,$$
$$\theta 10 = .0082313890617863095540, \phi 10 = .72966752035554638490\,10^{-5},$$
$$\psi 10 = .0012882910979480565168\}$$

Now, adjust the Lagrangian to normalize and expand about the nominal: (such as x1=x1+x10, etc.)

```
> #PE := PEgravity + PEtwisting
#+ PEcantilevers
#+ PEbend
#+ PEstretching:
```

```
> loopcount := 3 + NumPen + '# of wires,u'
+ 'if'(NumPen>1,'# of wires,m',0)
+ 'if'(NumPen>2,'# of wires,l',0);
```

$$loopcount := 8$$

```
> PEnum1 := 'PEgravity+PEtwisting':
```

```
> PEnum2 := PEcant[u]:
```

```
> PEnum3 := PEcant[m]:
```

```
> PEnum4 := 'PEbending[u]':

> kk := 5:
if (NumPen>1) then
PEnum5 := 'PEbending[m]':
kk := kk+1:
if (NumPen>2) then
PEnum6 := 'PEbending[l]':
kk := kk+1:
fi:
fi:

> for ll in [PEstretching] do
PEnum.kk := ll:
kk := kk+1:
od:

> #PE := ['PEgravity+PEtwisting',
# 'PEcantilevers',
# 'PEbend',
# 'PEstretching'];

> #L := KE - PE:

> about_nominal :=
seq(op([x.ii=x.ii+x.ii.0,y.ii=y.ii+y.ii.0,z.ii=z.ii+z.ii.0,
theta.ii=theta.ii+theta.ii.0,phi.ii=phi.ii+phi.ii.0,
psi.ii=psi.ii+psi.  ii.0]),ii=1..NumPen),
seq(`yc[u,`.ii.`]`=`yc[u,`.ii.`]`+`yc[u,`.ii.`]0`,ii=1..NumCanU),
seq(`yc[l,`.ii.`]`=`yc[l,`.ii.`]`+`yc[l,`.ii.`]0`,ii=1..NumCanM);
```

$$about\_nominal := x1\tilde{} = x1\tilde{} + x10,\ y1\tilde{} = y1\tilde{} + y10\tilde{},\ z1\tilde{} = z1\tilde{} + z10,$$
$$\theta 1\tilde{} = \theta 1\tilde{} + \theta 10, \phi 1\tilde{} = \phi 1\tilde{} + \phi 10,\ \psi 1\tilde{} = \psi 1\tilde{} + \psi 10$$

```
> about_values :=
op(subs(offset_values,{about_nominal}));
```

$$
\begin{aligned}
about\_values := \; & z1\tilde{} = z1\tilde{} - .000117168401627073029, \\
& \theta 1\tilde{} = \theta 1\tilde{} + .008231389061786309 5540, \\
& \phi 1\tilde{} = \phi 1\tilde{} + .72966752035554638490\,10^{-5}, \\
& \psi 1\tilde{} = \psi 1\tilde{} + .0012882910979480565168, \\
& x1\tilde{} = x1\tilde{} + .0007488428247477619 6265, \\
& y1\tilde{} = y1\tilde{} - .0006849139904000 4506850
\end{aligned}
$$

```
> #L := subs(about_nominal,L):
```

```
> #PE := subs(about_nominal,PE):
```

This line allows algebraic substitutions in the equations of motion, when *k*delta_l* is set equal to tension (=*k*delta_l* at DC or no loss). In practice, the way to do it is to replace *delta[g]* with *Ten/k[s]*, such that *k[s]*delta[g]* becomes *Ten*.

```
> tension_subs :=
seq(delta[g1.ii]=Ten[1,ii]/ks1,ii=1..`# of wires,u`):
if (NumPen>1) then
tension_subs := tension_subs,
seq(delta[g2.ii]=Ten[2,ii]/ks2,ii=1..`# of wires,m`):
if (NumPen>2) then
tension_subs := tension_subs,
seq(delta[g3.ii]=Ten[3,ii]/ks3,ii=1..`# of wires,l`):
fi:
fi:
```

```
> print(loopcount);
for kk from 1 to loopcount do
print(kk);
PEnum.kk :=
evalf(subs(tension_subs,vars,CantOffs,tensions,lgEq,PEnum.kk)):
PEnum.kk := evalf(subs(about_values,PEnum.kk)):
od:
```

8
1
2
3
4
5

6
7
8

A.7 Cantilevers

A.7.1 Cantilever Velocity (Translational)

Rather than substitue for the cantilever co-ordinates, as done previously, will instead keep cantilever positions as states. To do this, require extra parts of the kinetic energy term.

```
> allCants0 :=
seq(`yc[u,`.ii.`]`=0,ii=1..NumCanU),
seq(`yc[l,`.ii.`]`=0,ii=1..NumCanM );
```

$$allCants0 :=$$

```
> time_vars := seq(ii=ii(t),ii=all_vars):
vel_time_vars := seq(dot.ii=dot.ii(t),ii=all_vars):

> no_time_vars := seq(ii(t)=ii,ii=all_vars):
no_vel_time_vars := seq(dot.ii(t)=dot.ii,ii=all_vars):

> all_vel0 := seq(dot.ii=0,ii=all_vars):
```

For a triangular blade, the center of mass lies 2/3 of the way from the tip of the blade towards the base. The base of the blade is equivalent to the tip of the blade with yc's=0 and n-> n+Lblade.

```
> for ii from 1 to NumCanU do
XCanU.ii := evalm(
2/3*subs(`n[0]`=`n[0]`+LCanU,CantOffs0,allCants0,
row(TopPlate,ii)) + 1/3*row(TopPlate,ii) ):
od:

> for ii from 1 to NumCanM do
XCanM.ii := evalm(
2/3*subs(`n[1,l]`=`n[1,l]`+LCanM,CantOffs0,allCants0,
```

```
row(Mass1l,ii)) + 1/3*row(Mass1l,ii) ):
od:
```

Substituting in values for these points.

```
> for ii from 1 to NumCanU do
XCanU.ii := map2(subs,{about_values,CantOffs},XCanU.ii);
XCanU.ii := subs(vars,op(XCanU.ii));
XCanU.ii := subs(time_vars,op(XCanU.ii));
od:
```

```
> for ii from 1 to NumCanM do
XCanM.ii := map2(subs,{about_values,CantOffs,vars},XCanM.ii);
XCanM.ii := subs(vars,op(XCanM.ii));
XCanM.ii := subs(time_vars,op(XCanM.ii));
od:
```

```
> velocity_subs := seq(diff(ii(t),t)=dot.ii,ii=all_vars):
```

```
> acc_subs := seq(diff(dot.ii(t),t)=dotdot.ii,ii=all_vars):
```

The velocity of each point is the time derivative of the position:

```
> for ii from 1 to NumCanU do
dotXCanU.ii := map(diff,XCanU.ii,t);
dotXCanU.ii := subs(velocity_subs,op(dotXCanU.ii)):
dotXCanU.ii.Sq := dotprod(dotXCanU.ii,dotXCanU.ii):
od:
```

```
> for ii from 1 to NumCanM do
dotXCanM.ii := map(diff,XCanM.ii,t);
dotXCanM.ii := subs(velocity_subs,op(dotXCanM.ii)):
dotXCanM.ii.Sq := dotprod(dotXCanM.ii,dotXCanM.ii):
od:
```

A.7.2 Cantilever Velocity (Rotational)

The kinetic energy due to rotation of the blades.

The blades angular position is equal to the rotation of the mass they are attached to plus the relative rotation of the blade. Note that for our purposes, the blades only rotate in roll (*psi*)–this is equivalent to just allowing pure vertical motion of the tips of the blades. (To be totally correct, should add the relevant moments of inertia

to the other 2 directions, but as long as the blade can't rotate in those directions, this just adds this moment to the respective moments of the masses, and has little effect.)

In particular, angle = (y_tip - y_base)/L, and y_tip - y_base = yc.

Can ignore sign for upper, as will be squared.

```
> for ii from 1 to NumCanU do
dotThCanU.ii := dot.(`yc[u,`.ii.`]`)/LCanU;
od;
for ii from 1 to NumCanM do
dotThCanM.ii := (dot.(`yc[l,`.ii.`]`) +
dot.psi1*(-1)^iquo(ii,2))/LCanM;
od;
```

Expanding the kinetic energy:

```
> KE := subs(vars,KE):
```

```
> KE := evalf(subs(
seq(dotXCanU.ii^2=dotXCanU.ii.Sq,ii=1..NumCanU),
seq(dotXCanM.ii^2=dotXCanM.ii.Sq,ii=1..NumCanM), KE)):
```

```
> for ii in all_vars do
LHS.ii := diff(KE,dot.ii):
LHS.ii := subs(vel_time_vars,LHS.ii):
LHS.ii := diff(LHS.ii,t):
LHS.ii := subs(acc_subs,velocity_subs,LHS.ii):
LHS.ii := subs(no_time_vars,no_vel_time_vars,LHS.ii):
od:
```

*We have not **proved** that every term in the states (positions or velocities) is higher order; it is true for the example cases, and should be true in general. If this is a concern, the place to check is right here. To eliminate the 'higher order' terms, we assume those terms involve the states, and set those states to zero. Can take first order terms here:

```
> for ii in all_vars do
LHS.ii := subs(allDOF0,all_vel0,LHS.ii):
od:
```

```
> NumEqs := nops(all_vars); NumInputs := nops([inputs0]);
```

$$NumEqs := 10$$
$$NumInputs := 4$$

Note, too, that if we use cantilever states, then d/dt(y0) is required to get the proper kinetic energy. This means that y0 is not a proper input; instead, must use d^2/dt^2(y0) as the input, and d/dt(y0) and y0 will be used as (additional) states.

In either case, the terms that go as the (acceleration of) the inputs are not differential equations, and thus do not go on the 'left' side of the equation, but rather as driving terms on the right side.

```
> MassMatrix := matrix(NumEqs,NumEqs);
```

$$MassMatrix := \text{array}(1..10, 1..10, [])$$

```
> NegStiffMatrix := matrix(NumEqs,NumEqs);
```

$$NegStiffMatrix := \text{array}(1..10, 1..10, [])$$

```
> for ii from 1 to (NumEqs-NumInputs) do
for jj from 1 to (NumEqs-NumInputs) do
MassMatrix[ii,jj] :=
fnormal(coeff(LHS.(op(ii,all_vars)),dotdot.(op(jj,all_vars)))):
od:
for jj from 1 to NumInputs do
MassMatrix[ii,(NumEqs-NumInputs)+jj] := 0:
od:
od:
for ii from 1 to NumInputs do
for jj from 1 to NumEqs do
MassMatrix[(NumEqs-NumInputs)+ii,jj] :=
`if`(jj=ii+(NumEqs-NumInputs),1,0):
od:
od:
```

Negative, since this will be taken to the opposite side of the equal sign:

```
> InputsMatrix := matrix(NumEqs,NumInputs);
for ii from 1 to NumInputs do
for jj from 1 to (NumEqs-NumInputs) do
InputsMatrix[jj,ii] :=
```

```
-fnormal(coeff(LHS.(op(jj,all_vars)),
dotdot.(op(ii+NumEqs-NumInputs,all_vars)))):
od:
for jj from 1 to NumInputs do
InputsMatrix[NumEqs-NumInputs+jj,ii] := 'if'(ii=jj,1,0):
od:
od:
```

$$InputsMatrix := \text{array}(1..10,\ 1..4,\ [])$$

This forms the left hand side of the (set of) equations, [M] d^2/dt^2[x] = [-K][x]. The potential energies are used, below, to generate [-K].

A.8 Equations of Motion

D/Dt(dL/d(qdot)) - dL/dq = 0

For each variable: y(1,2,3), phi(1,2,3), x(1,2,3), theta(1,2,3), z(1,2,3), psi(1,2,3). This is entirely historical.

A.8.1 Equation for y (Vertical)

Left hand side of "y" equations:

```
>  #for ii from 1 to NumPen do
# assume('mass['.ii.']',constant):
# y.ii.LHS := D(diff(KE,y.ii.dot));
#od;
```

Right hand side of "y1" equation:

```
>  #y1RHS := diff(L,y1):
```

```
>  #if (NumPen>1) then
# y2RHS := diff(L,y2):
# if (NumPen>2) then
# y3RHS := diff(L,y3):
# fi:
#fi:
```

A.8.2 Equation for phi (Rotation)

Left and right hand side of the "phi" equations:

```
> #for ii from 1 to NumPen do
# assume('Iyaw['.ii.']', constant):
# phi.ii.LHS := D(diff(KE,phi.ii.dot));
# phi.ii.RHS := diff(L,phi.ii):
#od:
```

A.8.3 Equation for x (Longitudinal)

Left and right hand sides of the "x1" equation:

```
> #for ii from 1 to NumPen do
# x.ii.LHS := D(diff(KE,x.ii.dot));
# x.ii.RHS := diff(L,x.ii):
#od:
```

A.8.4 Equation for theta (Tilt)

Left and right hand sides of the "theta" equations:

```
> #for ii from 1 to NumPen do
# assume('Ipitch['.ii.']', constant):
# theta.ii.LHS := D(diff(KE,theta.ii.dot)):
# theta.ii.RHS := diff(L,theta.ii):
#od:
```

A.8.5 Equation for z (Sideways)

Left and right hand sides of the "z" equations:

```
> #for ii from 1 to NumPen do
# z.ii.LHS := D(diff(KE,z.ii.dot)):
# z.ii.RHS := diff(L,z.ii):
#od:
```

A.8.6 Equation for psi (Roll)

Left and right hand sides of the "psi" equation:

```
> #for ii from 1 to NumPen do
# assume('Iroll['.ii.']',constant):
# psi.ii.LHS := D(diff(KE,psi.ii.dot)):
# psi.ii.RHS := diff(L,psi.ii):
#od:
```

A.9 Coefficients of A matrix for y, phi, x, theta, z, psi

These equations of motion are typically used in a state-space formulation for control and simulation. This puts the differential equations in a series of first order differential equations in the form d/dt(x^) = [A]x^ + [B]u^, y^ = [C]x^ + [D]u^. The equations determined above are expanded to first order in the variables to find the [A] matrix.

Higher order terms or sensitivities to parameters may also be calculated.

Setting the initial elements to zero so we can sum the contributions of the parts of the potential energy.

```
> for ii in all_vars do
for jj in all_vars do
A[ii,jj]:=0;
od;
od:
```

```
> time()-sttime;
```

$$812.903$$

```
> done_vars := {};
```

$$done\_vars := \{\}$$

A.9.1 Vertical Motion

Nominally decoupled from all other degrees of freedom.

Y1

```
> #diff_vars := {seq(op([y.ii=0]),ii=0..NumPen)};

> #diff_vars_only := (all_vars_subs minus diff_vars);

> #statime := time():
#for ii from 1 to loopcount do
# PEnumDiff.ii := evalf(subs(diff_vars_only,PEnum.ii)):
#od:
```

Then expanding this about y=0 (the substituted y), phi=0, x=0, theta=0, z=0, and psi =0, for the other Y variables and the ground inputs:

```
> statime := time():
for kk from 1 to loopcount do
print(kk);
qiRHS := -diff(PEnum.kk,y1):
#print('qy1');
#print(time()-statime);
if Symmetric=1 then
coup_vars := {seq(y.ii,ii=0..NumPen),
seq(`yc[u,`.ii.`]`,ii=1..NumCanU),
seq(`yc[l,`.ii.`]`,ii=1..NumCanM)}:
else # If non-symmetric
coup_vars := {op(all_vars)}:
fi:
coup_vars := coup_vars minus done_vars:
for ii in coup_vars do
diff_vars := {ii=0};
diff_vars_only := {allDOF0} minus diff_vars;
qiRHSqi := evalf(subs(diff_vars_only,qiRHS)):
qiRHSqi := diff(qiRHSqi,ii):
qiRHSqi := evalf(subs(diff_vars,qiRHSqi)):
#print('qi,qi1');
qiRHSqi := mtaylor(qiRHSqi,lossVars,2);
#print('qi,qi1,loss');
#print(time()-statime);
A[y.1,ii] := A[y.1,ii] + fnormal(simplify(qiRHSqi),12);
#simplify(qiRHSqi):
A[ii,y.1] := A[y.1,ii]:
```

```
od:
od:
done_vars := done_vars union {y1}:
time()-statime;
time()-sttime;
```

$$1$$
$$2$$
$$3$$
$$4$$
$$5$$
$$6$$
$$7$$
$$8$$
$$66774.888$$
$$67587.820$$

```
> 1=1;
```

$$1 = 1$$

```
> #DEBUG();
> #quit
```

Y2, Y3

As above for the other masses:

```
> statime := time():
for ii from 2 to NumPen do
for kk from 1 to loopcount do
print(ii,kk);
qiRHS := -diff(PEnum.kk,y.ii):
if Symmetric=1 then
coup_vars := {seq(y.ii,ii=1..NumPen),
seq(`yc[u,`.ii.`]`,ii=1..NumCanU),
seq(`yc[l,`.ii.`]`,ii=1..NumCanM)}:
else # If non-symmetric
coup_vars := {op(all_vars)}:
fi:
```

```
coup_vars := coup_vars minus done_vars:
for ll in coup_vars do
diff_vars := {ll=0};
diff_vars_only := {allDOF0} minus diff_vars;
qiRHSqi := evalf(subs(diff_vars_only,qiRHS));
qiRHSqi := diff(qiRHSqi,ll);
qiRHSqi := evalf(subs(diff_vars,qiRHSqi));
#print('qi,qi');
qiRHSqi := mtaylor(qiRHSqi,lossVars,2);
#print('qi,qi,loss');
#print(time()-statime);
A[y.ii,ll] := A[y.ii,ll] + simplify(qiRHSqi);
A[ll,y.ii] := A[y.ii,ll]:
od:
od:
done_vars := done_vars union {y.ii}:
od:
time()-statime;
```

A.9.2 Rotational Motion

Again, nominally decoupled from the other degrees of freedom:

Phi[i]'s

```
> statime := time():
for ii from 1 to NumPen do
for kk from 1 to loopcount do
print(ii,kk);
qiRHS := -diff(PEnum.kk,phi.ii):
#print(time()-statime);
if Symmetric=1 then
coup_vars := {seq(phi.ii,ii=1..NumPen),
seq(`yc[u,`.ii.`]`,ii=1..NumCanU),
seq(`yc[l,`.ii.`]`,ii=1..NumCanM)}:
else # If non-symmetric
coup_vars := {op(all_vars)}:
fi:
coup_vars := coup_vars minus done_vars:
```

```
for ll in coup_vars do
diff_vars := {ll=0};
diff_vars_only := {allDOF0} minus diff_vars;
qiRHSqi := evalf(subs(diff_vars_only,qiRHS));
qiRHSqi := diff(qiRHSqi,ll);
qiRHSqi := evalf(subs(diff_vars,qiRHSqi)):
#print('qi,qi');
qiRHSqi := mtaylor(qiRHSqi,lossVars,2);
#print('qi,qi,loss');
#print(time()-statime);
A[phi.ii,ll] := A[phi.ii,ll] + simplify(qiRHSqi);
A[ll,phi.ii] := A[phi.ii,ll];
od:
od:
done_vars := done_vars union {phi.ii};
od:
time()-statime;
```

1, 1
1, 2
1, 3
1, 4
1, 5
1, 6
1, 7
1, 8
50075.597

A.9.3 Longitudinal and Tilt

These two are coupled in the nominal case.

X[i]

```
> statime := time():
for ii from 1 to NumPen do
for kk from 1 to loopcount do
print(ii,kk);
qiRHS := -diff(PEnum.kk,x.ii):
#print('qi');
```

```
if Symmetric=1 then
coup_vars :=
{seq(x.ii,ii=0..NumPen),seq(theta.ii,ii=0..NumPen),
seq('yc[u,'.ii.']',ii=1..NumCanU),
seq('yc[l,'.ii.']',ii=1..NumCanM)}:
else # If non-symmetric
coup_vars := {op(all_vars)}:
fi:
coup_vars := coup_vars minus done_vars:
for ll in coup_vars do
diff_vars := {ll=0};
diff_vars_only := {allDOF0} minus diff_vars;
qiRHSqi := evalf(subs(diff_vars_only,qiRHS));
qiRHSqi := diff(qiRHSqi,ll);
qiRHSqi := evalf(subs(diff_vars,qiRHSqi));
#print('qi,qx');
qiRHSqi := mtaylor(qiRHSqi,lossVars,2);
#print('qi,qi,loss');
#print(time()-statime);
A[x.ii,ll] := A[x.ii,ll] + simplify(qiRHSqi);
A[ll,x.ii] := A[x.ii,ll];
od:
od:  # kk, Loop on PE
done_vars := done_vars union {x.ii};
od:
time()-statime;
```

1, 1
1, 2
1, 3
1, 4
1, 5
1, 6
1, 7
1, 8
43980.689

Theta[i]'s

```
> statime := time():
for ii from 1 to NumPen do
for kk from 1 to loopcount do
print(ii,kk);
qiRHS := -diff(PEnum.kk,theta.ii):
#print('qi');
if Symmetric=1 then
coup_vars :=
{seq(x.ii,ii=0..NumPen),seq(theta.ii,ii=0..NumPen),
seq(`yc[u,`.ii.`]`,ii=1..NumCanU),
seq(`yc[l,`.ii.`]`,ii=1..NumCanM)}:
else # If non-symmetric
coup_vars := {op(all_vars)}:
fi:
coup_vars := coup_vars minus done_vars:
for ll in coup_vars do
diff_vars := {ll=0};
diff_vars_only := {allDOF0} minus diff_vars;
qiRHSqi := evalf(subs(diff_vars_only,qiRHS));
qiRHSqi := diff(qiRHSqi,ll);
qiRHSqi := evalf(subs(diff_vars,qiRHSqi));
#print('qi,qx');
qiRHSqi := mtaylor(qiRHSqi,lossVars,2);
#print('qi,qi,loss');
#print(time()-statime);
A[theta.ii,ll] := A[theta.ii,ll] + simplify(qiRHSqi);
A[ll,theta.ii] := A[theta.ii,ll];
od:
od:  # kk, Loop on PE
done_vars := done_vars union {theta.ii};
od:
time()-statime;
```

$$1, 1$$
$$1, 2$$
$$1, 3$$
$$1, 4$$
$$1, 5$$

1, 6
1, 7
1, 8
47562.272

A.9.4 Sideways and Roll

Once again, nominally coupled.

Z[i]'s

```
> statime := time():
for ii from 1 to NumPen do
for kk from 1 to loopcount do
print(ii,kk);
qiRHS := -diff(PEnum.kk,z.ii):
#print(qi):
if Symmetric=1 then
coup_vars := {seq(z.ii,ii=0..NumPen),
seq(psi.ii,ii=1..NumPen),
seq(`yc[u,`.ii.`]`,ii=1..NumCanU),
seq(`yc[l,`.ii.`]`,ii=1..NumCanM)}:
else # If non-symmetric
coup_vars := {op(all_vars)}:
fi:
coup_vars := coup_vars minus done_vars:
for ll in coup_vars do
diff_vars := {ll=0};
diff_vars_only := {allDOF0} minus diff_vars;
qiRHSqi := evalf(subs(diff_vars_only,qiRHS));
qiRHSqi := diff(qiRHSqi,ll):
qiRHSqi := evalf(subs(diff_vars,qiRHSqi)):
qiRHSqi := mtaylor(qiRHSqi,lossVars,2):
A[z.ii,ll] := A[z.ii,ll] + qiRHSqi; #simplify(qiRHSqi):
A[ll,z.ii] := A[z.ii,ll]:
#print(qiz):
od:
od:  # Loop on PE
done_vars := done_vars union {z.ii};
od:
```

1, 1
1, 2
1, 3
1, 4
1, 5
1, 6
1, 7
1, 8

Psi[i]'s

Again, expanding about the equilibrium to first order:

```
> statime := time():
for ii from 1 to NumPen do
for kk from 1 to loopcount do
print(ii,kk);
qiRHS := -diff(PEnum.kk,psi.ii):
#print(qi):
if Symmetric=1 then
coup_vars := {seq(z.ii,ii=0..NumPen),
seq(psi.ii,ii=1..NumPen),
seq(`yc[u,`.ii.`]`,ii=1..NumCanU),
seq(`yc[l,`.ii.`]`,ii=1..NumCanM)}:
else # If non-symmetric
coup_vars := {op(all_vars)}:
fi:
coup_vars := coup_vars minus done_vars:
for ll in coup_vars do
diff_vars := {ll=0};
diff_vars_only := {allDOF0} minus diff_vars;
qiRHSqi := evalf(subs(diff_vars_only,qiRHS));
qiRHSqi := diff(qiRHSqi,ll):
qiRHSqi := evalf(subs(diff_vars,qiRHSqi)):
qiRHSqi := mtaylor(qiRHSqi,lossVars,2):
A[psi.ii,ll] := A[psi.ii,ll] + qiRHSqi; #simplify(qiRHSqi):
A[ll,psi.ii] := A[psi.ii,ll]:
#print(qiz):
od:
od:  # Loop on PE
done_vars := done_vars union {psi.ii};
```

```
od:
```

$$1, 1$$
$$1, 2$$
$$1, 3$$
$$1, 4$$
$$1, 5$$
$$1, 6$$
$$1, 7$$
$$1, 8$$

Cantilevers

```
> statime := time():
for ii from 1 to NumCanU do
for kk from 1 to loopcount do
print(ii,kk);
qiRHS := -diff(PEnum.kk,`yc[u,`.ii.`]`):
#print(qi):
if Symmetric=1 then
coup_vars :=
{seq(`yc[u,`.ii.`]`,ii=1..NumCanU),
seq(`yc[l,`.ii.`]`,ii=1..NumCanM),
input_vars}:
else # If non-symmetric
coup_vars := {op(all_vars)}:
fi:
coup_vars := coup_vars minus done_vars:
for ll in coup_vars do
diff_vars := {ll=0};
diff_vars_only := {allDOF0} minus diff_vars;
qiRHSqi := evalf(subs(diff_vars_only,qiRHS));
qiRHSqi := diff(qiRHSqi,ll):
qiRHSqi := evalf(subs(diff_vars,qiRHSqi)):
qiRHSqi := mtaylor(qiRHSqi,lossVars,2):
A[`yc[u,`.ii.`]`,ll] := A[`yc[u,`.ii.`]`,ll] + qiRHSqi;
#simplify(qiRHSqi):
A[ll,`yc[u,`.ii.`]`] := A[`yc[u,`.ii.`]`,ll]:
#print(qiz):
```

```
od:
od:  # Loop on PE
done_vars := done_vars union {`yc[u,`.ii.`]`};
od:

> statime := time():
for ii from 1 to NumCanM do
for kk from 1 to loopcount do
print(ii,kk);
qiRHS := -diff(PEnum.kk,`yc[l,`.ii.`]`):
#print(qi):
if Symmetric=1 then
coup_vars :=
{seq(`yc[u,`.ii.`]`,ii=1..NumCanU),
seq(`yc[l,`.ii.`]`,ii=1..NumCanM)
}:
else # If non-symmetric1
coup_vars := {op(all_vars)}:
fi:
coup_vars := coup_vars minus done_vars:
for ll in coup_vars do
diff_vars := {ll=0};
diff_vars_only := {allDOF0} minus diff_vars;
qiRHSqi := evalf(subs(diff_vars_only,qiRHS));
qiRHSqi := diff(qiRHSqi,ll):
qiRHSqi := evalf(subs(diff_vars,qiRHSqi)):
qiRHSqi := mtaylor(qiRHSqi,lossVars,2):
A[`yc[l,`.ii.`]`,ll] := A[`yc[l,`.ii.`]`,ll] + qiRHSqi;
#simplify(qiRHSqi):
A[ll,`yc[l,`.ii.`]`] := A[`yc[l,`.ii.`]`,ll]:
#print(qiz):
od:
od:  # Loop on PE
done_vars := done_vars union {`yc[l,`.ii.`]`};
od:
time()-statime;
```

A.9.5 Stiffness Matrix

```
> for ii from 1 to (NumEqs-NumInputs) do
for jj from 1 to NumEqs do
NegStiffMatrix[ii,jj] := A[op(ii,all_vars),op(jj,all_vars)]:
od:
od:
for ii from 1 to NumInputs do
for jj from 1 to NumEqs do
NegStiffMatrix[NumEqs-NumInputs+ii,jj] := 0:
od:
od:
```

```
> invMK := matrix(NumEqs,NumEqs);
```

$$invMK := \text{array}(1..10,\ 1..10,\ [])$$

```
> invMass := inverse(MassMatrix):
```

```
> invMass := map(fnormal,invMass);
```

$$invMass := \begin{bmatrix} .17846283747871781632 & 0 & 0 & 0 & 0 & 0 & 0 & 0 & 0 & 0 \\ 0 & .17846283747871781632 & 0 & 0 & 0 & 0 & 0 & 0 & 0 & 0 \\ 0 & 0 & .17846283747871781632 & 0 & 0 & 0 & 0 & 0 & 0 & 0 \\ 0 & 0 & 0 & 62.43597812666512523 & 9 & 0 & 0 & 0 & 0 & 0 & 0 \\ 0 & 0 & 0 & 0 & 62.43597812666512523 & 9 & 0 & 0 & 0 & 0 & 0 \\ 0 & 0 & 0 & 0 & 0 & 44.06489814289328797 & 7 & 0 & 0 & 0 & 0 \\ 0 & 0 & 0 & 0 & 0 & 0 & 1. & 0 & 0 & 0 \\ 0 & 0 & 0 & 0 & 0 & 0 & 0 & 1. & 0 & 0 \\ 0 & 0 & 0 & 0 & 0 & 0 & 0 & 0 & 1. & 0 \\ 0 & 0 & 0 & 0 & 0 & 0 & 0 & 0 & 0 & 1. \end{bmatrix}$$

```
> invMK := evalm(invMass &* NegStiffMatrix):
invMK := map(fnormal,invMK,14);
```

$$
\begin{aligned}
&\mathit{invMK} := \\
&\quad [[-35.318812192440 - .19091015796722\, I\, \mathit{alpha\_wire1}^{\sim}, \\
&\quad .00040478294044744 - .083594322498618\, I\, \mathit{alpha\_wire1}^{\sim}, \\
&\quad -.26744642444341\, 10^{-9} + .16764740598133\, 10^{-9}\, I\, \mathit{alpha\_wire1}^{\sim}, \\
&\quad .088278840112331 + .026951239894845\, I\, \mathit{alpha\_wire1}^{\sim}, \\
&\quad .00031334925327275 + .35626226693750\, 10^{-5}\, I\, \mathit{alpha\_wire1}^{\sim}, \\
&\quad -.00026676192885280 - .00026850144755726\, I\, \mathit{alpha\_wire1}^{\sim}, \\
&\quad 35.318812192440 + .19091015796734\, I\, \mathit{alpha\_wire1}^{\sim}, \\
&\quad -.00040478294044399 + .083594322498617\, I\, \mathit{alpha\_wire1}^{\sim}, \\
&\quad .26744642444341\, 10^{-9} - .16764740598234\, 10^{-9}\, I\, \mathit{alpha\_wire1}^{\sim}, \\
&\quad .052984416627300 + .026784585686546\, I\, \mathit{alpha\_wire1}^{\sim}], \\
&\quad [.00040478294044744 - .083594322498618\, I\, \mathit{alpha\_wire1}^{\sim}, \\
&\quad -13296.554200983 - 13296.554203273\, I\, \mathit{alpha\_wire1}^{\sim}, \\
&\quad .000038394879635326 + .0045904221360322\, I\, \mathit{alpha\_wire1}^{\sim}, \\
&\quad .11052982986076 + .13426521926695\, I\, \mathit{alpha\_wire1}^{\sim}, \\
&\quad .00026751751261964 + .00026931623216167\, I\, \mathit{alpha\_wire1}^{\sim}, \\
&\quad .0060214749158941 + .0073145408409210\, I\, \mathit{alpha\_wire1}^{\sim}, \\
&\quad -.00040478294044744 + .083594322498797\, I\, \mathit{alpha\_wire1}^{\sim}, \\
&\quad 13296.554200983 + 13296.554203273\, I\, \mathit{alpha\_wire1}^{\sim}, \\
&\quad -.000038394879635326 - .0045904221360322\, I\, \mathit{alpha\_wire1}^{\sim}, \\
&\quad -.00012949352024709 - .00019703103175665\, I\, \mathit{alpha\_wire1}^{\sim}], \\
&\quad [-.26744642444341\, 10^{-9} + .16764740598133\, 10^{-9}\, I\, \mathit{alpha\_wire1}^{\sim}, \\
&\quad .000038394879635326 + .0045904221360322\, I\, \mathit{alpha\_wire1}^{\sim}, \\
&\quad -35.318812196334 - .19091015507376\, I\, \mathit{alpha\_wire1}^{\sim}, \\
&\quad -.75587349845810\, 10^{-6} - .81497793686898\, 10^{-6}\, I\, \mathit{alpha\_wire1}^{\sim}, \\
&\quad .00030649819291337 + .93531645429161\, 10^{-6}\, I\, \mathit{alpha\_wire1}^{\sim}, \\
&\quad -.034731875588975 + .00040223534629417\, I\, \mathit{alpha\_wire1}^{\sim}, \\
&\quad .26744642444340\, 10^{-9} - .16764740598203\, 10^{-9}\, I\, \mathit{alpha\_wire1}^{\sim}, \\
&\quad -.000038394879635398 - .0045904221360317\, I\, \mathit{alpha\_wire1}^{\sim}, \\
&\quad 35.318812196334 + .19091015507373\, I\, \mathit{alpha\_wire1}^{\sim}, \\
&\quad .75564466503484\, 10^{-6} + .77683486971723\, 10^{-6}\, I\, \mathit{alpha\_wire1}^{\sim}],
\end{aligned}
$$

[30.884725403731 + 9.4290052110244 *I alpha_wire1~*,
38.669328231170 + 46.973254554036 *I alpha_wire1~*,
−.00026444553881916 − .00028512347645562 *I alpha_wire1~*,
−124.95129462147 − 118.91498741370 *I alpha_wire1~*,
.0011377926517916 + .00058678248019933 *I alpha_wire1~*,
.00007721816178566 4 + .000065168837615292 *I alpha_wire1~*,
−30.884725403731 − 9.4290052110244 *I alpha_wire1~*,
−38.669328231895 − 46.973254561547 *I alpha_wire1~*,
.00026444553881916 + .00028512347645556 *I alpha_wire1~*,
116.24880715864 + 116.25785450894 *I alpha_wire1~*],

[.10962656091175 + .0012463986015306 *I alpha_wire1~*,
.093592132694919 + .094221422330614 *I alpha_wire1~*,
.10722968848281 + .00032722441549561 *I alpha_wire1~*,
.0011377926517916 + .00058678248019933 *I alpha_wire1~*,
−115.39651758459 − .64502244724294 *I alpha_wire1~*,
−.0012898284165657 + .27230517901136 *I alpha_wire1~*,
−.10962656091179 − .0012463986075199 *I alpha_wire1~*,
−.093592132694811 − .094221422328873 *I alpha_wire1~*,
−.10722968848281 − .00032722441505193 *I alpha_wire1~*,
−.00066781159953618 − .00077739453567748 *I alpha_wire1~*],

[−.065867142926616 − .066296653717842 *I alpha_wire1~*,
1.4867839298504 + 1.8060594668941 *I alpha_wire1~*,
−8.5757717503641 + .099317369455350 *I alpha_wire1~*,
.000054497591548319 + .000045993644654414 *I alpha_wire1~*,
−.00091031100181492 + .19218246173024 *I alpha_wire1~*,
−30579.127381233 − 30574.880080559 *I alpha_wire1~*,
.065867142926616 + .066296653717860 *I alpha_wire1~*,
−1.4867842692593 − 1.8060592407731 *I alpha_wire1~*,
8.5757717503641 − .099317369455352 *I alpha_wire1~*,
.000052806331126026 + .000079378897846151 *I alpha_wire1~*],

$$[0,0,0,0,0,0,0,0,0,0],$$
$$[0,0,0,0,0,0,0,0,0,0],$$
$$[0,0,0,0,0,0,0,0,0,0],$$
$$[0,0,0,0,0,0,0,0,0,0]]$$

```
> invMInputs := evalm(invMass &* InputsMatrix);
```

$$invMInputs := \begin{bmatrix} 0 & 0 & 0 & 0 \\ 0 & 0 & 0 & 0 \\ 0 & 0 & 0 & 0 \\ 0 & 0 & 0 & 0 \\ 0 & 0 & 0 & 0 \\ 0 & 0 & 0 & 0 \\ 1. & 0 & 0 & 0 \\ 0 & 1. & 0 & 0 \\ 0 & 0 & 1. & 0 \\ 0 & 0 & 0 & 1. \end{bmatrix}$$

```
> 1=1;
```

$$1 = 1$$

~17 hours for GEO numbers

```
> time()-sttime;
```

277258.398

A.9.6 Resonant Frequencies

For y, phi, since they are uncoupled to first order from the other variables, can calculate their resonant frequencies from the qiRHSqj terms. For coupled degrees of freedom, need to calculate the (sub)matrix and find the eigenvalues.

```
> invMK0 := map2(subs,[loss0],invMK):
> Freqs_omega := [eigenvals(invMK0)]:
> Freqs_omega := map(sqrt,-Freqs_omega);
```

Freqs_omega := [201.44661570824887056, 132.37847506020080438, 24.142463731684817928, 5.3643287817954678076, 10.792456624324310125, 5.9647488221081273455, 0, 0, 0, 0]

```
> Freqs := evalf(Freqs_omega/(2*Pi));
```

Freqs := [32.061224659101258013, 21.068688664798145004, 3.8423924413144443021, .85375944199287391115, 1.7176728198660844167, .94931925934006874325, 0, 0, 0, 0]

The vertical resonant frequencies in Hz:

```
> freq_vars :=
{seq(y.ii,ii=1..NumPen),seq(`yc[u,`.ii.`]`,ii=1..NumCanU),
seq(`yc[l,`.ii.`]`,ii=1..NumCanM)};
dim_freq := nops(freq_vars):
AFreqsY := matrix(dim_freq,dim_freq):
```

$$freq\_vars := \{y1^{\sim}\}$$

```
> which_vars := {}:
for ii from 1 to NumEqs do
if ({op(ii,all_vars)} intersect freq_vars)<>{}
then which_vars := which_vars union {ii} fi:
od:
which_vars := sort([op(which_vars)]):
```

```
> for ii from 1 to dim_freq do
for jj from 1 to dim_freq do
AFreqsY[ii,jj] := invMK0[op(ii,which_vars),op(jj,which_vars)]:
od:
od:
```

```
> FrequencysY := [eigenvals(AFreqsY)]:
```

```
> if (max(op(FrequencysY))>0) then
stable_system := 0:
ERROR(`UNSTABLE in y.`):
else fi:
```

```
> FrequencysY := evalf(map(sqrt,-FrequencysY)/(2*Pi)):
```

```
> temp_freqs := {op(FrequencysY)}:
for ii in FrequencysY do
if (abs(ii)>500) then
temp_freqs := temp_freqs minus {ii} fi:
od:
FrequencysY := sort([op(temp_freqs)]);
```

$$FrequencysY := [21.066577042357931220]$$

The rotational (yaw) resonant frequencies in Hz:

```
> freq_vars :=
{seq(phi.ii,ii=1..NumPen),
seq(`yc[u,`.ii.`]`,ii=1..NumCanU),
seq(`yc[l,`.ii.`]`,ii=1..NumCanM)};
dim_freq := nops(freq_vars):
AFreqsPhi := matrix(dim_freq,dim_freq):
```

$$freq\_vars := \{\phi 1\tilde{}\}$$

```
> which_vars := {}:
for ii from 1 to NumEqs do
if ({op(ii,all_vars)} intersect freq_vars)<>{}
then which_vars := which_vars union {ii} fi:
od:
which_vars := sort([op(which_vars)]):

> for ii from 1 to dim_freq do
for jj from 1 to dim_freq do
AFreqsPhi[ii,jj] := invMK0[op(ii,which_vars),op(jj,which_vars)]:
od:
od:

> FrequencysPhi := [eigenvals(AFreqsPhi)]:

> if (max(op(FrequencysPhi))>0) then
stable_system := 0:
ERROR(`UNSTABLE in phi.`):
else fi:

> FrequencysPhi := evalf(map(sqrt,-FrequencysPhi)/(2*Pi)):
```

```
> temp_freqs := {op(FrequencysPhi)}:
for ii in FrequencysPhi do
if (abs(ii)>500) then
temp_freqs := temp_freqs minus {ii} fi:
od:
FrequencysPhi := sort([op(temp_freqs)]);
```

$$FrequencysPhi := [1.7176507978694903821]$$

Giving longitudinal and tilt frequencies in Hz of:

```
> freq_vars :=
{seq(x.ii,ii=1..NumPen),seq(theta.ii,ii=1..NumPen),
seq(`yc[u,`.ii.`]`,ii=1..NumCanU),
seq(`yc[l,`.ii.`]`,ii=1..NumCanM)};
dim_freq := nops(freq_vars):
AFreqsXTheta := matrix(dim_freq,dim_freq):
```

$$freq\_vars := \{\theta 1\tilde{}, x1\tilde{}\}$$

```
> which_vars := {}:
for ii from 1 to NumEqs do
if ({op(ii,all_vars)} intersect freq_vars)<>{}
then which_vars := which_vars union {ii} fi:
od:
which_vars := sort([op(which_vars)]):

> for ii from 1 to dim_freq do
for jj from 1 to dim_freq do
AFreqsXTheta[ii,jj] :=
invMK0[op(ii,which_vars),op(jj,which_vars)]:
od:
od:

> FrequencysXTheta := [eigenvals(AFreqsXTheta)]:

> if (max(op(FrequencysXTheta))>0) then
stable_system := 0:
ERROR(`UNSTABLE in x/theta.`):
else fi:

> FrequencysXTheta := evalf(map(sqrt,-FrequencysXTheta)/(2*Pi)):
```

```
> temp_freqs := {op(FrequencysXTheta)}:
for ii in FrequencysXTheta do
if (abs(ii)>500) then
temp_freqs := temp_freqs minus {ii} fi:
od:
FrequencysXTheta := sort([op(temp_freqs)]);
```

$$FrequencysXTheta := [.85438955831540808240, 3.8539619432088401669]$$

Sideways and roll frequencies are, in Hz:

```
> freq_vars :=
{seq(z.ii,ii=1..NumPen),seq(psi.ii,ii=1..NumPen),
seq(`yc[u,`.ii.`]`,ii=1..NumCanU),
seq(`yc[l,`.ii.`]`,ii=1..NumCanM)};
dim_freq := nops(freq_vars):
AFreqsZPsi := matrix(dim_freq,dim_freq):
```

$$freq\_vars := \{\psi 1\tilde{}, z1\tilde{}\}$$

```
> which_vars := {}:
for ii from 1 to NumEqs do
if ({op(ii,all_vars)} intersect freq_vars)<>{}
then which_vars := which_vars union {ii} fi:
od:
which_vars := sort([op(which_vars)]):

> for ii from 1 to dim_freq do
for jj from 1 to dim_freq do
AFreqsZPsi[ii,jj] :=
invMK0[op(ii,which_vars),op(jj,which_vars)]:
od:
od:

> FrequencysZPsi := [eigenvals(AFreqsZPsi)]:

> if (max(op(FrequencysZPsi))>0) then
stable_system := 0:
ERROR(`UNSTABLE in z/psi.`):
else fi:

> FrequencysZPsi := evalf(map(sqrt,-FrequencysZPsi)/(2*Pi)):
```

```
> temp_freqs := {op(FrequencysZPsi)}:
for ii in FrequencysZPsi do
if (abs(ii)>500) then
temp_freqs := temp_freqs minus {ii} fi:
od:
FrequencysZPsi := sort([op(temp_freqs)]);
```

$$FrequencysZPsi := [.94935921241067477385, 32.061206790908636184]$$

```
> if (stable_system =0) then
print(`\n ***********************************\n
SYSTEM IS IN UNSTABLE EQUILIBRIUM\n
***********************************\n\n`)
else
print(`\n SYSTEM IS STABLE\n\n`):
fi;
```

SYSTEM IS STABLE

29,600sec., ~490min., ~8.5 hours for GEO600 numbers (no cantilevers)

```
> time()-sttime;
```

277259.503

```
> #DEBUG();
> #quit
> #save invMK, MassMatrix, invMInputs, loss0, loss, `11july.m`:
> #save invMK, MassMatrix, invMInputs, loss0, loss, `11july.txt`:
```

A.9.7 Cross terms

Original code solved the 'coupled' variables first, then, for a non-symmetric case, solved every variable (the extra cross couplings) here. Now, the code solves for

all 'coup_vars' which, for a symmetric case, is just the obvious couplings (plus the cantilevers, where appropriate) and for a non-symmetric case is equal to all variables. Thus, this separate section is no longer necessary.

A.10 General System Dynamics

```
> UpperRight := array(identity,1..NumEqs,1..NumEqs):
UpperLeft := array(sparse,1..NumEqs,1..NumEqs):

> additionally(alpha_wire1,real,alpha_wire2,
real,alpha_wire3,real,alpha_cantU,real,alpha_cantL,real);

> ReInvMK := copy(invMK):
for ii from 1 to NumEqs do
for jj from 1 to NumEqs do
ReInvMK[ii,jj] := Re(ReInvMK[ii,jj]):
od:
od:

> ImInvMK := copy(invMK):
for ii from 1 to NumEqs do
for jj from 1 to NumEqs do
ImInvMK[ii,jj] := Im(ImInvMK[ii,jj])/omega:
od:
od:

> Adynam :=
blockmatrix(2,2,UpperLeft,UpperRight,ReInvMK,ImInvMK):

> sIminusA := charmat(Adynam,omega*I):
```

A.10.1 Input vectors

Sample input vectors-from motion of the top plate, x0, y0, z0, and theta0: First column is x0, then y0, z0, theta0.

```
> Btemp := array(sparse,1..NumEqs,1..1):
Bdynam := blockmatrix(2,1,Btemp,col(invMInputs,1)):
```

A.10.2 Output Vectors

Sample out put vectors-basically, motions of the test mass (bottom mass) in each direction.

```
> Cdynam := array(sparse,1..2*NumEqs):
Cdynam[(NumPen-1)*6+1] := 1:
print(Cdynam);
```

$$[1, 0, 0, 0, 0, 0, 0, 0, 0, 0, 0, 0, 0, 0, 0, 0, 0, 0, 0, 0]$$

Output perpendicular to the test mass face, i.e., correcting for non-zero yaw angle:

```
> CdynamXTMFace := matrix(1,6*(2*NumPen),
[seq(0, jj=1..6*(NumPen-1)),
subs(offset_values,1*cos(phi.NumPen.0)),0,
subs(offset_values,-1*sin(phi.NumPen.0)),0,0,0,
seq(0, jj=1..6*NumPen)]);
```

$$CdynamXTMFace := [\cos(.72966752035554638490\,10^{-5}), 0, -\sin(.72966752035554638490\,10^{-5}), 0, 0, 0, 0, 0, 0, 0, 0, 0]$$

A.10.3 Straight Through Term

For most cases of interest,

```
> Ddynam := matrix(1,1,0);
```

$$Ddynam := \begin{bmatrix} 0 \end{bmatrix}$$

As a reminder of the previously calculated frequencies, to compare to the full calculation:

```
> FrequencysY; FrequencysPhi; FrequencysXTheta; FrequencysZPsi;
```

$$[21.066577042357931220]$$
$$[1.7176507978694903821]$$
$$[.85438955831540808240, 3.8539619432088401669]$$

[.94935921241067477385, 32.061206790908636184]

2/8/99, Full run, 58600 sec., 977 min., ~16.3 hours

```
> time()-sttime;
```

277260.129

```
> DEBUG();
```

```
277260.129
```

```
> quit
```

```
Warning, computation interrupted
```

A.11 Functional Outputs

Based on these system dynamics, we can generate useful outputs to study the system. For simple systems, with no loss and no bending terms included, we can take the *[A,B,C,D]* matricies and calculate the relevant transfer functions as *C(sI-A)^(-1)B + D*. For more complicated systems, it is very computational difficult to symbolically invert the matricies, so the most convenient thing to do is to set up a function that calculates as much as it can, then for each frequency point, numerically does the matrix math.

The general idea is shown below.

Note that for plotting, the automatic plotting routines will have trouble with such a function. As such, you may wish to provide your own plotting vector.

```
> Aplot := copy(sIminusA):
```

Note: Inputs are accelerations, so to get proper transfer functions, must use accerleration as output.

```
> TF := proc (f) local ii,jj:
global Aplot:
for ii from 1 to NumEqs do
Aplot[ii,ii] := evalf(subs(omega=2*Pi*f,sIminusA[ii,ii])):
od:
```

```
for ii from (NumEqs+1) to (NumEqs+NumEqs) do
for jj from (NumEqs+1) to (NumEqs+NumEqs) do
Aplot[ii,jj] :=
evalf(subs(test,loss,omega=2*Pi*f,sIminusA[ii,jj])): od:
od:
evalf(-(2*Pi*f)^2)*evalm(Cdynam &* inverse(Aplot) &* Bdynam +
Ddynam)[1,1];
end;
```

$TF :=$ **proc**(f)
local ii, jj;
global $Aplot$;
for ii **to** $NumEqs$ **do** $Aplot_{ii,ii} :=$ evalf(subs$(\omega = 2\pi f,\ sIminusA_{ii,ii})$) **od**;
for ii **from** $NumEqs + 1$ **to** $2NumEqs$ **do**
for jj **from** $NumEqs + 1$ **to** $2NumEqs$ **do**
$Aplot_{ii,jj} :=$ evalf(subs$(test,\ loss,\ \omega = 2\pi f,\ sIminusA_{ii,jj})$)
od
od;
evalf$(-4\pi^2 f^2)$evalm$(((Cdynam\ \&*\ (\text{inverse}(Aplot)))\ \&*\ Bdynam)+$
$Ddynam)_{1,1}$
end

```
> min_f := 0.1:
max_f := 100:
num_f := 30:
delta_f := (max_f/min_f)^(1/(num_f-1)):
f_vec := [seq(min_f*delta_f^(ii-1),ii=1..num_f)]:
> data_vec := [seq(TF(ii),ii=f_vec)]:
> mag_data := zip((x,y)->[x,abs(y)],f_vec,data_vec):
> with(plots):
> mag_plot := loglogplot(mag_data,color=red):
> #display(mag_plot,axes=boxed);
```

A Maple note: For variables, y=x sets the value of y equal to the value of x. Later changing x does not change y.

For matricies, Y=X sets a pointer; later changing X *does* change Y. Use 'copy' to get a new version of the matrix.

'Aplot0' and 'Bplot0' will be dummy matricies we can substitute specific values for frequency without changing *Adynam* and *Bdynam.*

```
> Aplot0 := copy('sI-ATotal'):

> Bplot0 := matrix(6*(2*NumPen),1,
[seq(0, jj=1..6*NumPen), 1/(subs(vars,'mass[1]')), 0,0, 0,0,0]);

> Cplot := matrix(1,6*(2*NumPen),
[1,0,0,0,0,0, seq(0, jj=1..6*NumPen)]);

> Dplot := copy(Ddynam);
```

We do all the substituting we can before the function call; as this step is slow, there is an output to reassure the user it hasn't stopped.

```
> for ii from 1 to (2*DOFtot) do
if (ii=1) then print('1 out of '.(2*DOFtot)):
else print(ii): fi:
for jj from 1 to (2*DOFtot) do
Aplot0[ii,jj] := evalf(subs(loss,Aplot0[ii,jj]));
od:
Bplot0[ii,1] := evalf(subs(loss,Bplot0[ii,1]));
od:
Aplot := copy(Aplot0):
Bplot := copy(Bplot0):
```

Function of omega (not f):

```
> TFTot := proc(x) local ii,jj;
global Aplot,Bplot,Cplot,Dplot;
for ii from 1 to (2*DOFtot) do
for jj from 1 to (2*DOFtot) do
Aplot[ii,jj] := subs(omega=x,Aplot0[ii,jj]);
Aplot[ii,jj] := evalf(Aplot[ii,jj]);
od:
Bplot[ii,1] := subs(omega=x,Bplot0[ii,1]);
Bplot[ii,1] := evalf(Bplot[ii,1]);
od:
```

```
RETURN(evalm(Cplot &* inverse(Aplot) &* Bplot + Dplot)[1,1]);
end;
```

In Hz:

```
> TargetFreq := 1e-4;
> TF0 := TFTot(2*TargetFreq);
> Im(TF0)/Re(TF0);
> Elapsed := time()-sttime;
> Elapsed/60;
```

Appendix B

Blade Equations

Transfer Function of Cantilever Blades

MEH, 28/5/99

As ideal (massless) springs, as an element with mass & inertia, and in a coupled system.

z0 = input

zEnd = motion at end of blade

z1 = motion of mass1 (at bottom of wire)

```
> Digits := 20;
```

Digits := 20

```
> KE := 1/2*Mass1*z1dot^2 # For the mass
+ 1/2*MassBlade*( (2*z0dot + zEnddot)/3)^2
# From geometry, translation of the blade
+ 1/2*JBlade/Lblade^2*(zEnddot-z0dot)^2:
# From geometry, rotation of blade;
```

```
> PE := 1/2*kcant*(z0-zEnd)^2 + 1/2*kwire1*(z1-zEnd)^2:
```

```
> L1 := KE - PE;
```

$$L1 := \frac{1}{2}\,Mass1\;z1dot^2 + \frac{1}{2}\,MassBlade\,(\frac{2}{3}\,z0dot + \frac{1}{3}\,zEnddot)^2 + \frac{1}{2}\,\frac{JBlade\,(zEnddot - z0dot)^2}{Lblade^2} - \frac{1}{2}\,kcant\,(z0\tilde{} - zEnd)^2 - \frac{1}{2}\,kwire1\,(z1\tilde{} - zEnd)^2$$

Really d/dt(diff(*)), but we'll clean that up in the Lagrangian:

```
> Eqs1 := {diff(L1,zEnddot) = diff(L1,zEnd),
diff(L1,z1dot) = diff(L1,z1)}:
```

```
> Eqs1 := subs(zEnddot=s^2*zEnd, z1dot=s^2*z1,
z0dot=s^2*z0,Eqs1);
```

$$Eqs1 := \{\frac{1}{3}\,MassBlade\,(\frac{2}{3}\,s^2\,z0\tilde{} + \frac{1}{3}\,s^2\,zEnd) + \frac{JBlade\,(s^2\,zEnd - s^2\,z0\tilde{})}{Lblade^2} = kcant\,(z0\tilde{} - zEnd) + kwire1\,(z1\tilde{} - zEnd),\ Mass1\;s^2\,z1\tilde{} = -kwire1\,(z1\tilde{} - zEnd)\}$$

```
> Soln1 := solve(Eqs1,{z1,zEnd}):
```

```
> vars := kcant = omega0^2*Mass1,
omega0 = sqrt(1.86E11*b*h^3/(4*alpha*Mass1)/Lblade^3),
Mass1=5.6/NumBlades,kwire1=1.7e11*evalf(Pi)*rwire^2/LenWire,
JBlade=MassBlade*Lblade^2/18,MassBlade=1/2*(b+a)*Lblade*h*7800,
alpha=(3/(2*(1-beta))*(3-(2/(1-beta))*(1+(beta^2*ln(beta)
/(1-beta))))),
beta=a/b;
```

$$vars := kcant = \omega0^2\;Mass1,$$

$$\omega0 = 215638.58652847824675\,\sqrt{\frac{b\,h^3}{\alpha\;Mass1\;Lblade^3}},$$

$$Mass1 = \frac{5.6}{NumBlades},\ kwire1 = .53407075111026485055\,10^{12}\,\frac{rwire^2}{LenWire},$$

$$JBlade = \frac{1}{18}\;MassBlade\;Lblade^2,\ MassBlade = 3900\,(b+a)\;Lblade\;h,$$

$$\alpha = 3\,\frac{3 - 2\,\dfrac{1 + \dfrac{\beta^2 \ln(\beta)}{1-\beta}}{1-\beta}}{2 - 2\,\beta},\ \beta = \frac{a}{b}$$

```
> UpperBlades := NumBlades=2,b=0.04,a=0.0045,h=0.002,
Lblade=0.24,LenWire=0.42,rwire=350 e-6:
LowerBlades := NumBlades=4,b=0.028,a=0.0038,h=0.001,
Lblade=0.124,LenWire=0.187,rwire= 175e-6:
```

```
> print('alphaUpper = '+evalf(subs(vars,UpperBlades,alpha)));
print('alphaLower = '+evalf(subs(vars,LowerBlades,alpha)));
```

$$alphaUpper = +1.3803223482783266058$$

$$alphaLower = +1.3614241824553639503$$

```
> TF0to1 := subs(Soln1,z0=1,z1);
```

$$TF0to1 := -kwire1\,(2\,MassBlade\,s^2\,Lblade^2 - 9\,JBlade\,s^2 - 9\,kcant\,Lblade^2)$$
$$/(MassBlade\,s^4\,Lblade^2\,Mass1 + MassBlade\,s^2\,Lblade^2\,kwire1$$
$$+ 9\,JBlade\,s^4\,Mass1 + 9\,JBlade\,s^2\,kwire1 + 9\,kcant\,Lblade^2\,Mass1\,s^2$$
$$+ 9\,kcant\,Lblade^2\,kwire1 + 9\,kwire1\,Lblade^2\,Mass1\,s^2)$$

```
> TF0to1Upper := evalf(subs(vars,UpperBlades,s=I*omega,
omega=2*Pi*f,TF0to1));
```

$$TF0to1Upper := -155770.63574049391474($$
$$-.28414455264979704475\,f^2 - 404.25339827033324521)/$$
$$(31.409216466633643562\,f^4 - .901518313499094595 77\,10^7\,f^2 +$$
$$.629708088488248927 03\,10^8)$$

```
> TF0to1Lower := evalf(subs(vars,LowerBlades,s=I*omega,
omega=2*Pi*f,TF0to1)):
```

```
> fsolve(1/TF0to1Upper,f=0..5);
fsolve(1/TF0to1Upper,f=100..5000);
```

2.6429420687406739352

535.73921961531450801

```
> fsolve(1/TF0to1Lower,f=0..5);
fsolve(1/TF0to1Lower,f=100..5000);
```

3.0012206882376742346

933.23304759607086041

```
> with(plots):

> MagUpper1 := loglogplot(abs(TF0to1Upper),f=0.1..1000,
numpoints=300,title='Single Stage TF: Upper Blade plus Wire'):
Mag1UUC := loglogplot(abs(1/(1-(f/subs(vars,UpperBlades,
omega0/(2*Pi)))^2)),f=0.1 ..1000,numpoints=200,color=blue):

> MagLower1 := loglogplot(abs(TF0to1Lower),f=0.1..1000,
numpoints=300,title='Single Stage TF: Lower Blade plus Wire'):
Mag1LUC := loglogplot(abs(1/(1-(f/subs(vars,LowerBlades,
omega0/(2*Pi)))^2)),f=0.1 ..1000,numpoints=200,color=blue):

> display([MagUpper1,Mag1UUC],view=[-1..3,-3..2 ]);
```

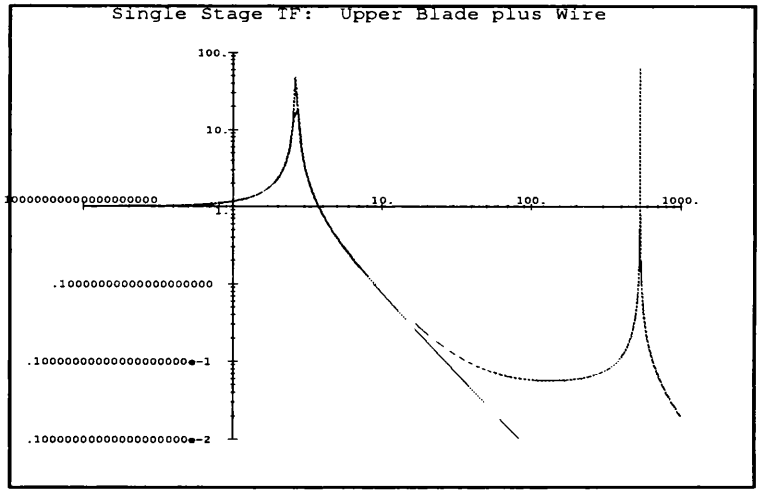


```
> (evalf(subs(vars,UpperBlades,omega0/(2*Pi)))/ 50)^2;
abs(subs(f=50,TF0to1Upper));"/"";
```

.002821830412545989 3876

.007793291943039764510 3

2.761786076296585970 0

```
> display([MagLower1,Mag1LUC],view=[-1..3,-3..2 ]);
```

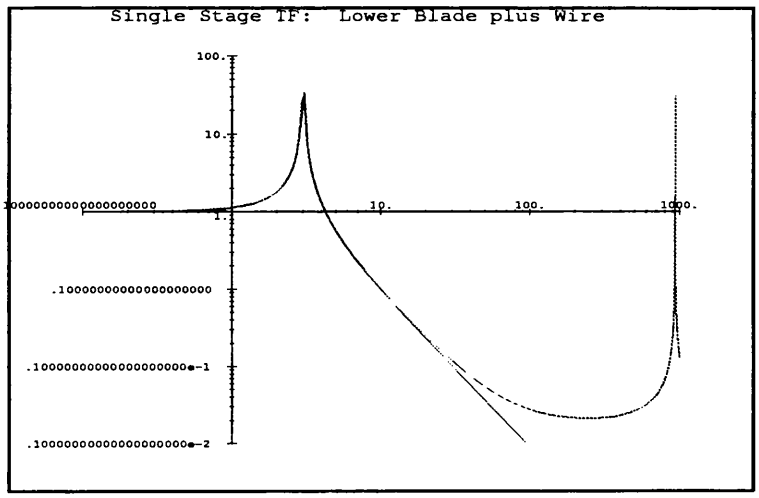


```
> abs(subs(f=50,TF0to1Lower));
(evalf(subs(vars, LowerBlades,omega0/(2*Pi)))/50)^2; ""/";
```

.005455231338350940922 0

.003630150973101007308 4

1.502756050305776519 1

Bibliography

[1] M. E. Husman, C. I. Torrie, N. A. Robertson, K. A. Strain, and J. Hough, "Modelling of compound pendula: Triple pendulum in GEO 600," *Review of Scientific Instruments*, 2000. in press.

[2] M. J. Lawrence, B. Wilke, M. E. Husman, E. K. Gustafson, and R. L. Byer, "Dynamic response of a Fabry–Perot interferometer," *Journal of the Optical Society of America*, vol. 16, April 1999.

[3] A. Einstein, "Die Grundlage der Algemeinen Relativitätstheorie," *Annalen der Physik*, 1916.

[4] R. Hulse and J. Taylor *Astrophysics Journal*, 1975.

[5] J. Taylor *Review of Modern Physics*, 1994.

[6] S. Bonazzola and J.-A. Marck, "Astrophysical sources of gravitational radiation," *Annual Review of Nuclear and Particle Science*, 1994.

[7] B. F. Schutz, "The detection of gravitational waves," in *Proceedings 1995 Houches School on Astrophysical Sources of Gravitational Radiation* (J. Marck and J. Lasota, eds.), Springer, Berlin, 1996.

[8] J. A. Lobo, "Sources of gravitational waves," in *General Relativity, Proceedings of the 46th Scottish Universities Summer School in Physics, Aberdeen* (G. S. Hall and J. R. Pulham, eds.), 1995.

[9] B. F. Schutz, "Determining the Hubble constant from gravitational wave observations," *Nature*, September 1986.

[10] K. S. Thorne, "Gravititional waves," in *Proceedings of the Snowmass 94 Summer Study on Particle and Nuclear Astrophysics and Cosmology in the Next Millenium* (E. Kolb and R. Peccei, eds.), World Scientific, Singapore, 1995.

[11] J. Hough, "GEO 600 proposal for a 600 m laser interferometric gravitational wave antenna," September 1994.

[12] R. V. Wagoner, "Gravitational radiation from accreting neutron stars," *The Astrophysical Journal*, vol. 278, 1984.

[13] L. Bildsten, "Gravitational radiation and rotation of accreting neutron stars," *The Astrophysical Journal*, vol. 501, 1998.

[14] K. Danzmann, et. al., "GEO 600: Proposal for a 600 m laser interferometric gravitational wave antenna," Report 190, Max–Planck–Institut für Quantenoptik, Garching, Germany, 1994.

[15] J. Weber, "Detection and generation of gravitational waves," *Physical Review*, vol. 117, no. 1, 1960.

[16] Z. K. Geng, W. O. Hamilton, W. W. Johnson, E. Mauceli, S. Merkowitz, A. Morse, and N. Solomonson, "Operation of the ALLEGRO detector at L.S.U.," in *First Eduardo Amaldi Conference on Gravitational Wave Experiments*, World Scientific, Singapore, 1995.

[17] P. Astone, et. al., "Long–term operation of the Rome "Explorer" cryogenic gravitaional wave detector," *Physical Review D*, vol. 47, no. 2, 1993.

[18] N. Solomonson, O. Aguiar, Z. Geng, W. O. Hamilton, W. W. Johnson, S. Merkowitz, B. Price, B. Xu, and N. Zhu, "The 1991 LSU gravitational radiation detector: modifications, performance, and prospects," in *Proceedings of Sixth Marcel Grossman Meeting on General Relativity* (H. Sato and A. Nakamura, eds.), (Singapore), World Scientific Publishing Co. Pte. Ltd., 1992.

[19] G. V. Pallottino, "The cryogenic gravitational wave antennas Explorer and Nautilus," in *Proceedings of VIRGO 96* (Cascina, ed.), World Scientific, 1996.

[20] A. Abromovici, P. Bender, and R. Drever, et. al., "Gravitational wave astrophysics," in *Proceedings Snowmass 94 Summer Study on Particle and Nuclear*

Astrophysics and Cosmology in the Next Millenium (E. W. Kolb and R. Peccei, eds.), World Scientific, Singapore, 1995.

[21] "http://www.lnf.infn.it/esperimenti/rog/NAUTILUS/current.html."

[22] A. D. Waard, "MiniGRAIL a small (60 cm) spherical antenna," in *3rd Edoardo Amaldi Conference on Gravitational Waves*, July 1999.

[23] R. L. Forward, "Wideband laser–interferometer gravitational–radiation experiment," *Physical Review D*, vol. 17, no. 2, 1978.

[24] R. Weiss, "Quarterly progress report no. 105," tech. rep., M.I.T., 1972.

[25] W. Winkler, "A Michelson interferometer using delay lines," in *The Detection of Gravitational Waves* (D. G. Blair, ed.), Cambridge: Cambridge University Press, 1991.

[26] D. Shoemaker, R. Schilling, L. Schnupp, W. Winkler, K. Maischberger, and A. Rüdiger, "Noise performance of the Garching 30 m prototype gravitational–wave detector," *Physical Review D*, vol. 38, no. 2, 1988.

[27] C. Fabry and A. Perot, "Théorie et applications d'une nouvelle méthode de Spectroscopie Interférentielle," *Ann. de Chim. et de Phys.*, vol. 16, 1899.

[28] R. W. P. Drever, G. M. Ford, J. Hough, I. M. Kerr, A. J. Munley, J. R. Pugh, N. A. Robertson, and H. Ward, "A Gravity–Wave Detector Using Optical Cavity Sensing," in 9th *International Conference on General Relativity and Gravitation, Jena 1980* (E. Schmutzer, ed.), VEC Deutscher Verlag der Wissenschaften, Berlin, 1983.

[29] D. Sigg, N. Mavalvala, J. Giaime, P. Fritschel, and D. Shoemaker, "Signal extraction in a power–recycled Michelson interferometer with Fabry–Perot arm cavities by use of a multiple–carrier frontal modulation scheme," *Applied Optics*, vol. 37, no. 24, 1998.

[30] D. I. Robertson, E. Morrison, J. Hough, S. Killbourn, B. Meers, G. P. Newton, N. A. Robertson, K. Strain, and H. Ward, "The Glasgow 10 m prototype laser interferometric gravitational wave detector," *Review of Scientific Instruments*, vol. 66, no. 9, 1995.

[31] R. L. Savage, Jr., "Status of the LIGO 40–m interferometer," in *Proceedings of the Seventh Marcel Grossman Meeting on General Relativity* (R. T. Jantzen and G. Mac Keiser, eds.), World Scientific, Singapore, 1996.

[32] B. J. Meers, "Recycling in laser–interferometric gravitational–wave detectors," *Physical Review D*, vol. 38, no. 8, 1988.

[33] K. Danzmann and LISA Study Team, "Lisa—a gravitational wave observatory in heliocentric orbit," in *Gravitational Wave Detection* (K. Tsubono, M.-K. Fujimoto, and K. Kuroda, eds.), no. 20 in Frontiers Science Series, 1996 TAMA International Workshop, Universal Academy Press, Inc., 1997.

[34] S. A. Hughes and K. S. Thorne, "Seismic gravity–gradient noise in interferometric gravitational–wave detectors," *Physical Review D*, vol. 5812, 1998.

[35] P. R. Saulson, "Terrestrial gravitational noise on a gravitational wave antenna," *Physical Review D*, vol. 30, no. 4, 1984.

[36] R. Spero, "Prospects for ground based detectors of low frequency gravitational radiation," in *Proceedings of the Los Alamos Conference* (M. M. Nieto, et. al., ed.), (New York), AIP, 1983.

[37] M. Hewitson, 1999. Private communication.

[38] S. M. Twyford, *Developments Towards Low Loss Suspensions for Laser Interferometric Gravitational Wave Detectors.* PhD thesis, University of Glasgow, September 1998.

[39] G. I. Gonzalez and P. R. Saulson, "Brownian motion of a mass suspended by an anelastic wire," *Journal of the Acoustical Society of America*, vol. 96, no. 1, 1994.

[40] S. Rowan, S. Twyford, J. Hough, D.-H. Gwo, and R. Route, "Mechanical losses associated with the technique of hydroxide–catalysis bonding of fused silica," *Physics Letters A*, vol. 246, 1998.

[41] J. E. Logan, J. Hough, and N. A. Robertson, "Aspects of the thermal motion of a mass suspended as a pendulum by wires," *Physics Letters A*, vol. 183, 1993.

[42] J. Hough, H. Walther, B. F. Schutz, J. Ehlers, H. Welling, I. F. Corbett, and V. Kose, et. al., "Proposal for a Joint German–British Interferometric Gravitational Wave Detector," Report 147 and GWD/137/JH(89), Max–Planck–Institut für Quantenoptik, 1989.

[43] R. J. Shine, A. J. Alfrey, and R. L. Byer, "40–W CW, TEM(00)–mode, diode–laser–pumped, Nd:YAG miniature–slab laser," *Optics Letters*, vol. 20, no. 5, 1995.

[44] E. Gustafson, D. Shoemaker, K. Strain, and R. Weiss, "LSC white paper on detector research and development," Report T990080-00-D, LIGO, LIGO, September 1999.

[45] E. Coccia, "Bars in action," in *3rd Edoardo Amaldi Conference on Gravitational Waves*, July 1999.

[46] B. F. Schutz, "Gravitational wave astronomy," *Classical and Quantum Gravity*, vol. 16, December 1999.

[47] J. Hough, R. Hutchins, J. E. Logan, A. McLaren, M. Plissi, N. A. Robertson, S. Rowan, K. A. Strain, and S. M. Twyford, "Developments in isolation, suspension and thermal noise issues for GEO 600," in *Gravitational Waves: Sources and Detectors* (I. Ciufolini and F. Fidecaro, eds.), vol. 2 of *Edoardo Amaldi Foundation Series*, World Scientific, March 1996.

[48] M. V. Plissi, C. I. Torrie, M. E. Husman, K. A. Strain, N. A. Robertson, H. Ward, and J. Hough, "GEO 600 triple pendulum suspension system: Seismic isolation and control," *Review of Scientific Instruments*, 2000. Submitted.

[49] M. V. Plissi, C. I. Torrie, N. A. Robertson, S. Killbourn, S. Rowan, S. M. Twyford, H. Ward, K. D. Skeldon, and J. Hough, "Aspects of the suspension system for GEO 600," *Review of Scientific Instruments*, vol. 69, no. 8, 1998.

[50] C. I. E. Torrie, *Development of Suspensions for the GEO 600 Gravitational Wave Detector*. PhD thesis, University of Glasgow, November 1999.

[51] M. Beccaria, M. Bernardini, S. Braccini, C. Bradaschia, G. Cagnoli, C. Casciano, G. Cella, E. Cuoco, V. Dattilo, G. De Carolis, R. De Salvo, A. Di Virgilio,

G. T. Feng, I. Ferrante, F. Fidecaro, F. Frasconi, A. Gaddi, L. Gammaitoni, A. Gennai, A. Giazotto, L. Holloway, J. Kovalik, P. La Penna, G. Losurdo, S. Malik, S. Mancini, F. Marchesoni, J. Nicolas, F. Palla, H. B. Pan, F. Paoletti, A. Pasqualetti, D. Passuello, R. Poggiani, P. Popolizio, M. Punturo, F. Raffaelli, V. Rubino, R. Valentini, A. Vicere, F. Waharte, and Z. Zhang, "The creep problem in the VIRGO suspensions: a possible solution using Maraging steel," *Nuclear Instruments & Methods in Physics A*, vol. 404, 1998.

[52] R. De Salvo, "Second generation suspensions for LIGO," in *Proceedings of the Rencontres de Moriond in Gravitational Waves and Experimental Gravity* (F. Hammer, T. X. Thuân, V. Cayatte, B. Guiderdoni, and J. T. T. Vân, eds.), (Les Arcs 1800, France), Editions Frontières, 1999. in press.

[53] M. Plissi, 1999. Private communication.

[54] C. Kittel and H. Kroemer, *Thermal Physics.* W. H. Freeman and Company, 2nd ed., 1980.

[55] H. B. Callen and T. A. Welton, "Irreversibility and generalized noise," *Physical Review*, vol. 83, no. 1, 1951.

[56] H. B. Callen and R. F. Greene, "On a theorem of irreversible thermodynamics," *Physical Review*, vol. 86, no. 5, 1952.

[57] V. B. Braginsky, V. P. Mitrofanov, and V. I. Panov, *Systems with small dissipation.* Chicago and London: University of Chicago Press, 1985.

[58] G. Cagnoli, November 1999. Private communication.

[59] S. Traeger, B. Willke, and K. Danzmann, "Monolithically suspended fused silica substrates with very high mechanical Q," *Physics Letters A*, vol. 225, 1997.

[60] A. L. Kimball and D. E. Lovell, "Internal friction in solids," *Physical Review*, vol. 30, 1927.

[61] C. Torrie, G. Cagnoli, J. Hough, M. Husman, S. McIntosh, D. Palmer, M. Plissi, N. Robertson, S. Rowan, P. Sneddon, K. A. Strain, and H. Ward, "Suspension system for the main optics for GEO 600," in *Proceedings of the Rencontres de*

Moriond in Gravitational Waves and Experimental Gravity (F. Hammer, T. X. Thuân, V. Cayatte, B. Guiderdoni, and J. T. T. Vân, eds.), (Les Arcs 1800, France), Editions Frontières, 1999. in press.

[62] L. D. Landau and E. M. Lifshitz, *Mechanics*, vol. 1 of *Course in Theoretical Physics*. Pergamon Press, 1976.

[63] Waterloo Maple Inc., "Maple V Release 4.00a."

[64] L. D. Landau and E. M. Lifshitz, *Theory of Elasticity*, vol. 7 of *Course in Theoretical Physics*. Pergamon Press, 1986.

[65] G. F. Franklin, J. D. Powell, and A. Emami-Naeini, *Feedback Control of Dynamic Systems*. Addison-Wesley Publishing Company, 1986.

[66] The Mathworks Inc., "MATLAB." "bode.m" is a function supplied with the control toolbox.

[67] S. Killbourn, *Double Pendulum Suspensions for Terrestrial Interferometric Gravitational Wave Detectors*. PhD thesis, University of Glasgow, 1997.

[68] G. C. Limited, "http://www.goodfellow.com." Stainless Steel-AISI 302.

[69] A. L. Fetter and J. D. Walecka, *Theoretical Mechanics of Particles and Continua*. International Series in Pure and Applied Physics, McGraw–Hill Book Company, 1980.

[70] N. W. McLachlan, *Theory of Vibrations*. New York: Dover Publications, 1951.

[71] N. A. Robertson, *Experiments relating to the detection of gravitational radiation and to the suppression of seismic noise in sensitive measurements*. PhD thesis, University of Glasgow, 1981.

[72] K. Precision, 1999. Private communication.

[73] G. Cagnoli, November 1999. Private communication.

[74] G. W. McMahon, "Experimental study of the vibrations of solid, isotropic, elastic cylinders," *Journal of the Acoustical Society of America*, vol. 36, no. 1, 1964.

[75] A. M. Gretarsson and G. M. Harry, "Dissipation of mechanical energy in fused silica fibers," *Review of Scientific Instruments*, vol. 70, October 1999.

[76] C. Zener, "Internal friction in solids," *Physical Review*, vol. 52, 1937.

[77] A. S. Nowick and B. S. Barry, *Anelastic Relaxation in Crystalline Solids.* Academic Press, Inc., 1972.

[78] W. J. Startin, M. A. Beilby, and P. R. Saulson, "Mechanical quality factors of fused silica resonators," *Review of Scientific Instruments*, vol. 69, no. 10, 1998.

[79] H. W. Bode, *Network analysis and feedback amplifier design.* D. Van Nostrand Company, Inc., 1955.

[80] M. Herpy and J.-C. Berka, *Active RC Filter Design.* Amsterdam Oxford: Elsevier, 1986.

[81] T. Kailath, *Linear Systems.* Prentice–Hall, 1980.

[82] E. Morrison, B. J. Meers, D. I. Robertson, and H. Ward, "Automatic alignment of optical interferometers," *Applied Optics*, vol. 33, 1994.

[83] E. Morrison, B. J. Meers, D. I. Robertson, and H. Ward, "Experimental demonstration of an automatic alignment system for optical interferometers," *Applied Optics*, vol. 33, 1994.

[84] S. Rowan, *Aspects of Lasers for the Illumination of Interferometric Gravitational Wave Detectors.* PhD thesis, University of Glasgow, July 1995.

[85] M. M. Casey, *Developments Towards Autonomous Operation of Laser Interferometric Gravitational Wave Detectors.* PhD thesis, University of Glasgow, 1999.

[86] S. Grasso, C. Altucci, F. Barone, V. Ragozzino, S. Solimento, Pham-Tu, J.-Y. Vinet, and R. Abbate, "Electrostatic systems for fine control of mirror orientation in interferometric GW antennas," *Physics Letters A*, vol. 244, July 1998.

[87] S. D. Killbourn, K. D. Skeldon, D. I. Robertson, and H. Ward, "Active damping of suspension wire violin modes in gravitational wave detectors," *Physics Letters A*, vol. 261, 1999.

[88] A. E. Siegman, *Lasers.* Oxford University Press, 1986.

[89] M. Born and E. Wolf, *Principles of Optics.* Pergamon, Oxford, 1980.

[90] R. W. P. Drever, J. L. Hall, F. V. Kowalski, J. Hough, G. M. Ford, A. J. Munley, and H. Ward, "Laser phase and frequency stabilization using an optical resonator," *Applied Physics B: Photophys. Laser Chem.*, vol. 31, 1983.

[91] A. Yariv, *Optical Electronics.* Holt, Rinehart & Winston, 1985.

[92] T. Day, E. K. Gustafson, and R. L. Byer, "Active frequency stabilization of a 1.062–μm, Nd:GGG, diode–laser–pumped nonplanar ring oscillator to less than 3 Hz of relative linewidth," *Optics Letters*, vol. 15, 1990.

[93] J. Camp, L. Sievers, R. Bork, and J. Hefner, "Guided lock acquisition in a suspended Fabry–Perot cavity," *Optics Letters*, vol. 20, 1995.

[94] K. D. Skeldon, K. A. Strain, A. I. Grant, and J. Hough, "Test of an 18–m–long suspended modecleaner cavity," *Review of Scientific Instruments*, vol. 67, no. 7, 1996.

[95] G. Heinzel, K. A. Strain, J. Mizuno, K. D. Skeldon, B. Willke, W. Winkler, R. Schilling, A. Rüdiger, and K. Danzmann, "Experimental demonstration of a suspended dual recycling interferometer for gravitational wave detection," *Physical Review Letters*, vol. 81, no. 25, 1998.